Final Report

Maritime Drone Swarm

AE3200: Design Synthesis (2022/2023 Q4)
DSE Group 6

Delft University of Technology

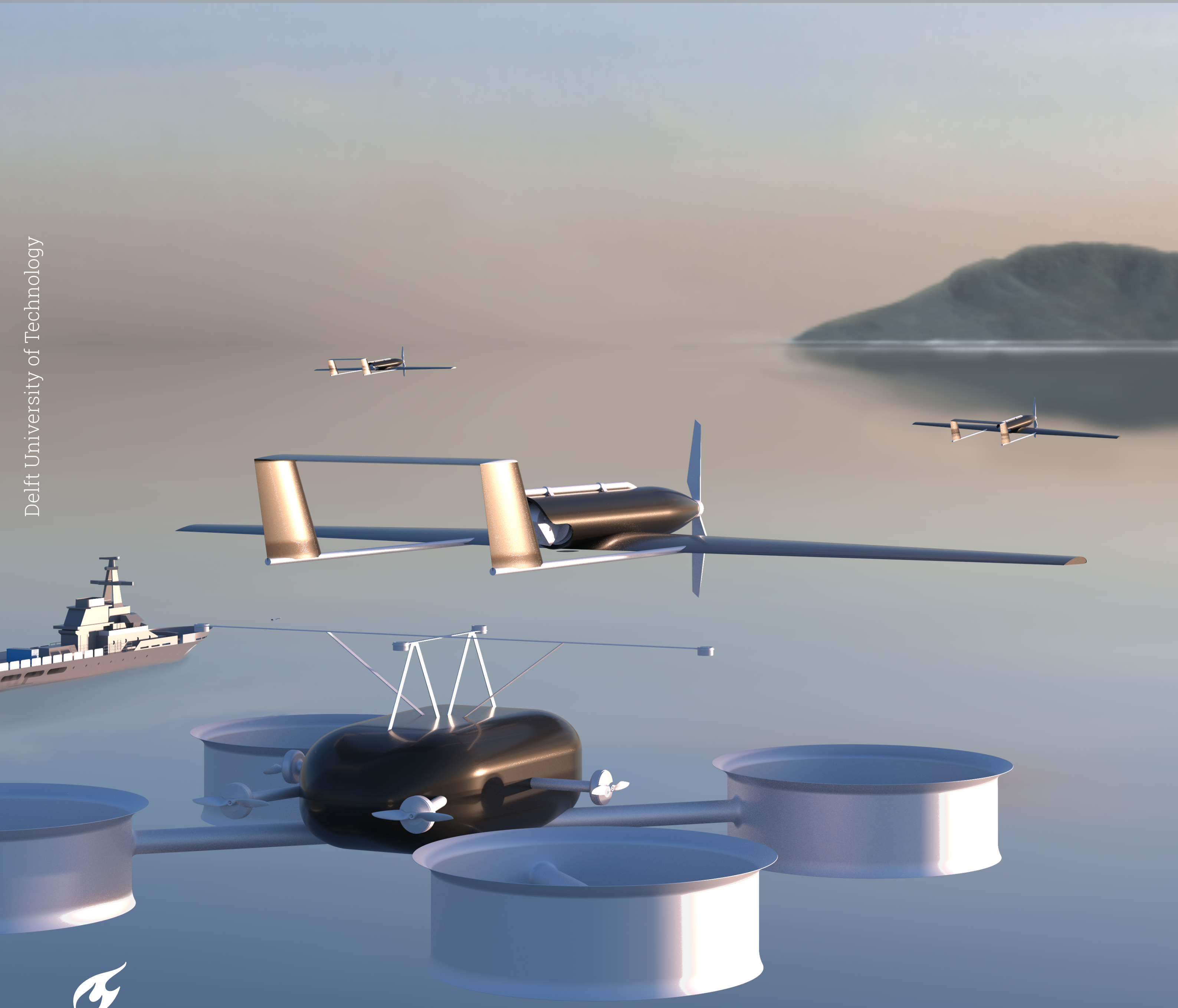

Final Report

Maritime Drone Swarm

by

DSE Group 6

Student Name	Student Number
Doruk Çelebi	5332427
Marnix de Bruijn	5314348
Jarno de Wit	5327156
Pablo Garcia de Vinuesa Garcia	5270944
Olivier Heukelom	5009448
Jorge Louro Fuentes	4838467
Max Rombouts	5309735
Mathieu van Opstal	5034515
Jan IJmte Verhoeff	5090253
Marley Wolf	5063078

Tutor:	Ir. Bart Remes
Coaches:	Dr. Bianca Giovanardi
	Ir. Sven Westerbeek
Teaching Assistant:	Kim Regnery
Project Duration:	10 weeks
Faculty:	Faculty of Aerospace Engineering, Delft

Version: Draft, V.1
Cover: Own Work
Style: TU Delft Report Style, with modifications by Daan Zwaneveld

Preface

This report presents the final design of the autonomous drone swarm that can perform search and rescue operations in stormy conditions. This report is the final result of the Design Synthesis Exercise (DSE) for the bachelor aerospace engineering at the Delft University of Technology. The DSE offers a team of ten aerospace engineering students a way to utilize all the skills they have acquired during the bachelor of aerospace engineering.

We had the honour to work on a very unique, but challenging drone project. During the DSE project, the team was faced with many challenges regarding project management, effectively using our knowledge and insights to come up with feasible concepts, providing sufficient detail and correct analysis. After all our hard work, we are proud to present our STORM system.

We want to thank our tutor Ir. B. Remes, and our coaches Ir. S. Westerbeek and Dr. B. Giovanardi for their support, guidance and time. Furthermore, we want to thank the representative for the Dutch Navy and J. Kodde from the KNRM for providing us more detail about the mission profile and insights on the use of a drone swarm. We also want to thank M.K. Altes from Avalor.ai for informing us about their software programme for an autonomous drone swarm, and J. Hatenboer for aiding us with insight on the energy management of our drone swarm, and giving helpful information on general drone operations. Furthermore, we want to thank J. L. van den Hove d'Ertsenryck MSc for his help on the clamping system and Prof. B. Çağlar for his insights in material and manufacturing considerations.

DSE Group 6
Delft, June 2023

Executive Summary

Maritime search and rescue operations can have a great impact on the lives of thousands of people that are subject to catastrophes at sea every year. The main objective in search and rescue missions is to reduce the time to find a survivor, by scanning a desired search area as quickly as possible. This report aims to provide a detailed design of a maritime drone swarm capable of performing search and rescue operations at sea, autonomously in stormy conditions. The report focuses on the design of the swarm, the search algorithm of the swarm, the interaction between the drones within it, but also a detailed design and analysis of the drones that form part of this swarm.

Mission and Operations

The mission need statement and project objective statements, as derived from user requirements and conversations with multiple clients and stakeholders are as follows:

- **Mission Need Statement:** The Coast Guard is in need of a system that autonomously performs search and rescue operations over large operational areas in harsh environmental conditions.
- **Project Objective Statement:** DSE group 6, a team of 10 students, will design a storm-resistant maritime drone swarm capable of landing autonomously on ship decks, over a design phase of 10 weeks

The mission will be fulfilled by a swarm that can autonomously perform search and rescue operations. The swarm should take off and land autonomously on a ship platform during sea state 5 and wind force 7. To ensure the success of the mission, 3 different nodes were designed, which will interact together in operation.

- Storage node: the START system has the function of storing the drones, and enabling the rapid take-off of the Fixed-Wings through the use of a catapult.
- Scanning node: Fixed-Wings have the function of performing the search part of the mission, these are optimised to obtain maximum endurance.
- Docking node: Quadcopter that intercepts Fixed-Wing, docks it onto itself and lands it back on the storage node.

The mission can be divided into 6 different phases.

- **Phase 1:** Pre-flight: After a distress signal has been given, phase 1 consists of determining the search area, the number of targets, and the algorithm initialises optimising the search pattern.
- **Phase 2:** Launch: During this phase, the scanning nodes are placed onto the launch catapult and launched.
- **Phase 3:** Search: After being launched the scanning nodes travel to the search area, and begin scanning following the search pattern. Constant communication is established with the ship such that the drones can send back abnormalities that will be analysed and the START system can update the Fixed-Wing with changes in the search pattern.
- **Phase 4:** Docking: The docking node takes off from the top of the storage node, approaches the scanning node and docks onto the Fixed-Wing using electromagnets.
- **Phase 5:** Rescue: In this phase, the swarm works together with units from the KNRM and/or coast guard know about the location of targets.
- **Phase 6:** End-of-Mission & Post-flight : recharging drones, checking them and preparing them for the next mission.

Drone Swarm

To determine the configuration of the drone swarm, it is first necessary to find the number of drones required to scan a search area, the scanning pattern, and the orientation of the pattern with respect to the wind. To determine these parameters, an extensive simulation was developed, this simulation accounts for the dynamics of the scanning nodes, the movement of the boat, the scanning width, the drift of the ocean, and the wind speed and direction.

The simulation was run repeatedly, with different initial conditions and different parameters, the results are then analysed. It is determined that the optimal number of scanning nodes is 10 nodes, as seen in the left figure in Figure 1. Additionally, it was determined the choice between a spiral and rectangular search pattern depends on the initial search area; if the area resembles a circle, a spiral search pattern is the most optimal. These results can be seen in Figure 1.

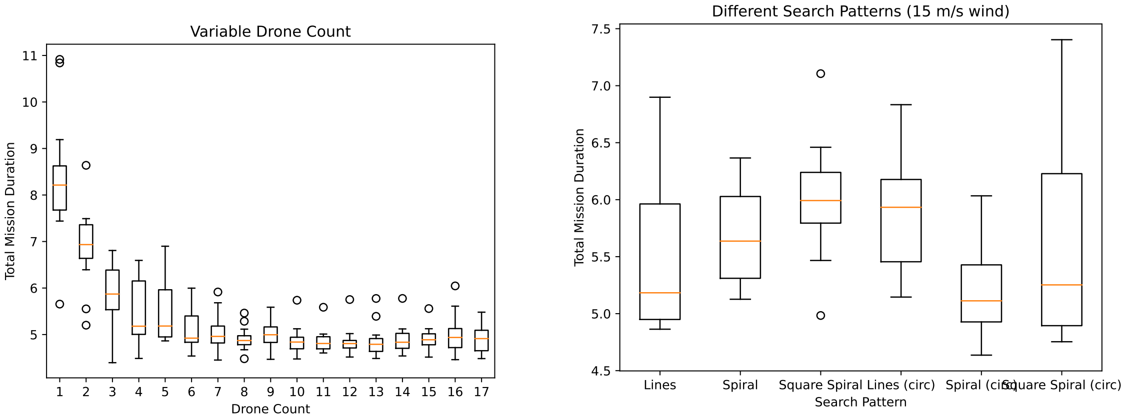

(a) Drone count impact on search effectiveness with three targets.

(b) Search pattern comparison with 15 [ms^{-1}] wind.

Figure 1: Search pattern comparison

Fixed-Wing

The main function of the Fixed-Wing is to scan the search area for as long as possible, following a predetermined pattern to perform the search operation. First, the Fixed-Wing is sized similar to a traditional aircraft. Then the aerodynamic, stability and structural characteristics are determined, in order to finalise the first stage of the design.

Wing Sizing

The next step is to determine the wing sizing. To do this, a loading diagram is plotted using the stall speed, cruise speed, climb gradient, and climb rate sizing equations. From this diagram, the wing surface area is determined, which can be used along with other relations to determine all the wing geometric parameters. These are summarized in Table 1.

Table 1: Wing geometric parameters summary table.

Parameter	Symbol	Value	Units
Wing Surface Area	S	0.845	[m^2]
Wing Span	b	3	[m]
Aspect Ratio	AR	10.7	[-]
Taper Ratio	λ	0.4	[-]
Wing Sweep	$\Lambda_{c/2}$	0	[°]
Wing Twist	α_{twist}	-3	[°]
Dihedral Angle	$\Gamma_{c/2}$	5	[°]
Thickness-to-Chord Ratio	t/c	0.117	[-]
Root Chord Thickness	t_r	0.072	[m]
Tip Chord Thickness	t_{tip}	0.029	[m]
Root Chord Length	c_r	0.401	[m]
Tip Chord Length	c_t	0.161	[m]
Mean Aerodynamic Chord	c_{MAC}	0.298	[m]
Span-wise MAC location	y_{MAC}	0.644	[m]

In addition to the wing parameters, high lift devices and ailerons are also sized. Only Kruger flaps are selected for the leading edge HLDs since split flaps for the trailing edge HLDs are no longer required after increasing the recovery drone top speed. The layout of these is shown in Figure 2.

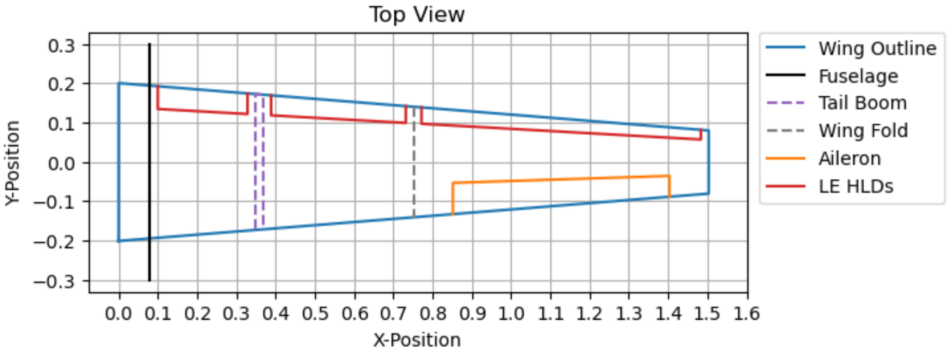

Figure 2: Top view of wing with final layout of the control surfaces.

Fuselage Sizing
Sizing of the fuselage is done by taking into account all the necessary internal components of the Fixed-Wing, placing them next to each other, and placing a casing around it to improve aerodynamic characteristics.

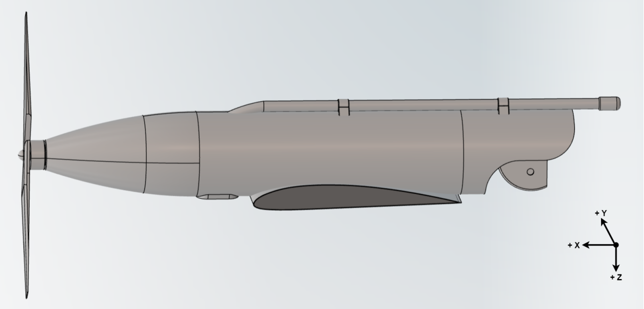

Figure 3: External view of fuselage.

Empennage Sizing
The empennage sizing is necessary, as the empennage is used for longitudinal stability, as well as yaw and pitch control. To size it the centre of gravity of all the components of the aircraft has to be identified, and then sizing relations are used to obtain the horizontal and vertical stabiliser parameters.

Table 2: Horizontal and vertical stabiliser size parameters.

Empennage parameter	**Horizontal stabiliser**	**Vertical stabiliser**
Aspect ratio [-]	4.0	1.5
Taper ratio [-]	1.0	0.5
Surface area [m^2]	0.13	0.052
Span [m]	0.72	0.279
Root chord [m]	0.18	0.248
Tip chord [m]	0.18	0.124
Leading edge sweep angle [°]	0	25

Finally, a trade-off is performed to select the tail configuration, and a high boom tail was chosen to avoid obstruction of the payload and for more effective use of the control surfaces.

Aerodynamic Analysis
The aerodynamic analysis is one of the most important aspects of the Fixed-Wing design. This aircraft should generate a high lift-to-drag ratio and have a high endurance. The first step is to select an airfoil with the best characteristics. To do this, different airfoils are simulated in XFLR5, and the best one is selected, the Clark Y. The next step is to analyse the wing with the correct size and airfoil. The wing is modelled in XFLR5, and then the following graphs are produced:

- C_L vs α curve
- C_L vs C_D curve
- C_m vs α curve
- C_L/C_D vs α curve

The final step is to analyse the aerodynamic characteristics of the wing and empennage together. The results of this analysis can be observed in Figure 4.

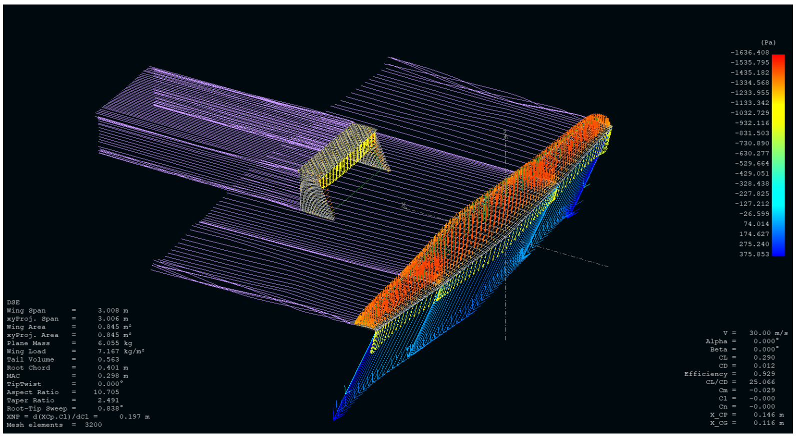

```
DSE
Wing Span       =     3.008 m
xyProj. Span    =     3.006 m
Wing Area       =     0.845 m²
xyProj. Area    =     0.845 m²
Plane Mass      =     6.055 kg
Wing Load       =     7.167 kg/m²
Tail Volume     =     0.563
Root Chord      =     0.401 m
MAC             =     0.298 m
TipTwist        =     0.000°
Aspect Ratio    =    10.705
Taper Ratio     =     2.491
Root-Tip Sweep  =     0.838°
XNP = d(XCp.Cl)/dCl =     0.197 m
Mesh elements  =  3200
```

```
         V =   30.00 m/s
     Alpha =    0.000°
      Beta =    0.000°
        CL =    0.290
        CD =    0.012
Efficiency =    0.929
     CL/CD =   25.066
        Cm =   -0.029
        Cl =   -0.000
        Cn =   -0.000
      X_CP =    0.146 m
      X_CG =    0.116 m
```

Figure 4: Visualisation of the wing and empennage in a stream flow.

Stability Analysis

The stability analysis begins by identifying the two prerequisites for longitudinal stability:

- $C_{m_\alpha} < 0$
- $C_m > 0$ at lift (L) = 0

Then the 5 eigenmotions for the aircraft can be described, and stability analysis is run on XFLR5 to identify the eigenvalues corresponding to these eigenmotions. After analysis of these eigenvalues, it was concluded that this Fixed-Wing is both dynamically and statically stable.

Power and Propulsion

The propulsion subsystem for the Fixed-Wing is designed for cruise, meaning the required thrust for the propeller is 17.57 [N] and the required power is 840 [W]. With this information, it is possible to use statistical relations to size the propeller diameter and choose a propulsion system based on the thrust output, the propeller diameter, the power consumption and the efficiency

Table 3: A table showcasing the relevant propulsion parameters and its values.

Parameter	Value
$C_{l_{cruise}}$	0.5974
$C_{d_{cruise}}$	0.0394
Motor Efficiency	0.80
Propeller Efficiency	0.75
T_{req}	17.57 [N]
Motor Power	878.55 [W]
Battery Mass	11.70 [kg]
Battery Volume	4.12 [L]
Endurance	5.39 [h]
Excess Power	97.62 [W]

Additionally, the Amprius Lithium-Ion Silicon battery is chosen as it outperforms all other commercially available battery technologies. For this system, the battery needs to be 11.70 [kg] in mass with 4.12 [L] in volume.

Structural Analysis
The structural analysis performed on the wing showed that the selected carbon fibre composite can withstand all stresses (shear, axial, bending) except for buckling. Therefore a buckling analysis is performed, showing that a stringer is needed to prevent buckling. The spar improved the maximum buckling stress from 3.74 $[MPA]$ to 171.5 $[MPa]$. The bending stress analysis was performed using a discretization of the airfoil and the shear analysis was analysed using a simplified section. Regarding the fuselage, a boom analysis was used to simplify the calculation for the maximum bending stress and the maximum shear stress. All the calculated stresses, apart form buckling, was far below the maximum allowable stress of the used material. The internal structure effectively support the major structural components and aid the stiffness and strength of those components.

Multicopter

A comprehensive landing mechanism was developed to address the challenge of landing the Fixed-Wing in the given adverse weather conditions. This involved the design of a specialized multicopter capable of safely capturing the Fixed-Wing in mid-air. The landing procedure encompasses three distinct phases: the Ascension Phase, Docking Phase, and Descending Phase.

The most complicated stage of the landing phase is the interception of the Fixed-Wing. This process requires high precision due to the fact that the clamping mechanism in itself requires high accuracy. Once the Fixed-Wing approaches the ship, it will enter a loitering track. To ensure effective tracking between the two drones, a Real-Time Kinematic (RTK) GPS system is implemented, significantly enhancing the accuracy of positioning compared to standard GPS systems by a factor of 10. To facilitate the Fixed-Wing's interception, powerful electromagnets were employed, creating a strong magnetic attraction between the fixed-wing and multicopter, that will work as clamping, without the need for mechanical components. The integration of the magnets onto the Multicopter was carefully considered to ensure that their presence did not compromise the stability of the Multicopter.

After completing the design of the clamping mechanism, the next step was to design the Multicopter itself. It was determined that an untethered Quadcopter configuration would be most suitable for this purpose. The sizing of the propellers and battery was carefully considered to ensure optimal performance and endurance during storm conditions. As a result, the Quadcopter was equipped with a total of eight rotors, with four facing upward to provide vertical lift, two positioned sideways to enable lateral movement, and two positioned forward to facilitate forward propulsion. This configuration was chosen to ensure the Quadcopter could match the movement of the Fixed-Wing mid-air with 6-axis control, allowing for precise interception and successful clamping. The final Quadcopter with its clamping mechanism can be seen in Figure 5.

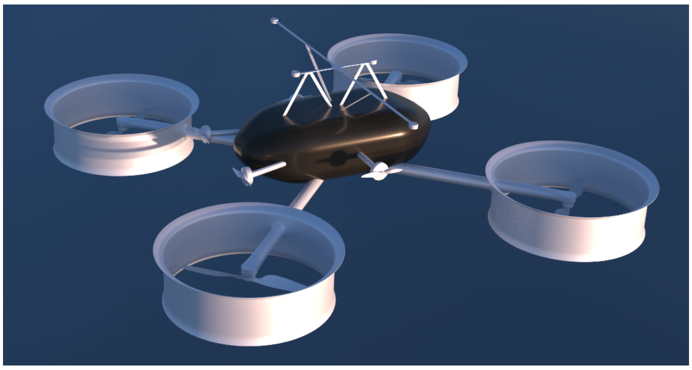

Figure 5: Final quadcopter design with its clamping mechanism to catch the Fixed-Wing.

Risk Analysis
Risk analysis is an integral part of every design project, aimed at identifying potential vulnerabilities and assessing associated risks. A total of 26 risks were identified by the team. Eight of them need a mitigation strategy since they were identified as potential threats to the outcome of the project. Additionally, a contingency plan was formulated to address any unforeseen risks that may arise during the course of the project.

Financial Analysis

Financial analysis plays a crucial role in determining the viability of the system and its potential for commercialization. It assesses whether the cost requirements are met and evaluates the feasibility of selling the drone swarm. An accurate understanding of the entire cost breakdown is essential for successful sales. The costs of the project can be categorized into several groups, including Design and Development Costs, Component Costs, Manufacturing Costs, Operations Costs, and End-of-life Costs. Each category contributes to the overall financial assessment and helps determine the pricing and profitability of the drone swarm.

After conducting a thorough cost analysis, a market analysis was performed to identify potential markets for sales. In the context of search and rescue operations, the market segment is estimated to be valued at USD 547.6 million in 2023. Analyzing the global perspective, Europe holds the largest market share with 35.4%, followed closely by North America with 30.12%. These regions present significant opportunities for the sale of drone swarm systems in search and rescue applications. Lastly,a Return on Investment analysis was performed.

After identifying the potential markets, the selling price of both systems was calculated. The total unit costs for the Fixed-Wing and Quadcopter are estimated to be EUR 83,903.6 thousand and EUR 35,781.4 thousand, respectively, considering manufacturing, component, and end-of-life costs.

Sustainable Development

In order to ensure the long-term sustainability of the drone swarm project, the team has implemented strategies to mitigate unsustainable practices and assess the project's current sustainability. This can be separated into three parts, each focusing on a different aspect of sustainability. The first aspect is economic sustainability which is outlined in section 10.1. The second aspect is social sustainability, discussed in section 10.2. Lastly, environmental sustainability will be covered in section 10.3.

For economic sustainability, the team will use sustainable manufacturing processes and materials. For materials, the team will reduce the amount of waste by choosing reusable materials and avoid using materials that can generate toxic waste. Regarding manufacturing processes, the sustainable principle lean manufacturing is the central principle. A good alternative that coincides with this principle is additive manufacturing given the fact that this produces low waste and a low amount of tools.

For social sustainability, the mission profile, the simulation, the power & propulsion of the system and the modularity of the system were the main factors that were taken into consideration when making the operations of the drone swarm compatible with society's needs.

For environmental sustainability, as the drone is sustainably powered and does not release emissions the main contributor to project emission's is the manufacturing of the drone itself. It is estimated that 1.7-2.2 [kg] of carbon dioxide equivalent (CO2e) per kilogram of aluminum and 2-7 kg of CO2e per kilogram of carbon fiber. This includes the energy requirements for mining, refining, and smelting processes.In addition, the specific energy consumption for primary aluminum production can range from approximately 13 to 17 [$MJ \cdot kg^{-1}$] of aluminum produced however, the energy consumption for aluminum recycling can be as low as 2-10 [$MJ \cdot kg^{-1}$]. Likewise, the energy consumption for carbon fiber production ranges from 150- 350 [$MJ \cdot kg^{-1}$] (CO2e) [28].

Verification and Validation

The verification and validation during the development of the system involved the use of debugging techniques, unit testing, system testing and limit testing to ensure the system behaves as follows. The V&V procedures are carried out on all simulations and all calculations, including the simulation of the swarm, Swarm.py and the state space of the coupled system. Additionally, a V&V plan is developed for the remainder of the project. The final products must be verified against the compliance matrix using verification methods such as inspection, analysis, demonstration, and testing.

Contents

Nomenclature

Abbreviations

Abbreviation	Definition
e.g.	For Example
DOT	Design Option Tree
ESC	Electronic Speed Controller
FBS	Functional Breakdown Structure
FFD	Functional Flow Diagram
HD	High Definition
HR	Human Resources
MNS	Mission Need Statement
PM/SE	Project Management and Systems Engineering
POS	Project Objective Statement
RDT	Requirements Discovery Tree
SWOT	Strength Weakness Opportunity Threat
WBD	Work Breakdown Structure
WFD	Work Flow Diagram
ADCS	Attitude Determination and Control System
UAV	Unmanned Aerial Vehicle
RDT	Requirement Discovery Tree
DOT	Design Option Tree
CCC	Command and Control Center
VTOL	Vertical Takeoff and Landing
VTO	Vertical Takeoff
FBD	Free Body Diagram
IMU	Inertial Measurement Unit
FW	Fixed-Wing
LLT	Lifting Line Theory
VLM	Vortex lattice Method
EMI	Electromagnetic Interference
CoG	Centre of gravity
EM	Electromagnetic
RTK	Real-Time Kinematics
DGPS	Differential Global Positioning System
COTS	Commercially Off The Shelf
SAR	Search and Rescue
CAGR	Compound Annual Growth Rate
HLD	High Lift Device
FBD	Free Body Diagram
DSE	Design Synthesis Exercise

Symbols

Symbol	Definition	Unit
A	Area	$[m^2]$
AR	Aspect Ratio	[-]
b	Wingspan/Spacing	[m]
c	Chord Length	[m]
C	Buckling Ratio	[-]
C_d	Drag Coefficient	[-]
C_L	Lift Coefficient	[-]
C_m	Moment Coefficient	[-]
D	Drag	[N]

Symbol	Definition	Unit
e	Oswald Efficiency Number	[-]
E	Young's Modulus	[Pa]
FOV	Field of View	[º]
h	Height	[m]
I_{ii}	Area moment of inertia around the i axis	[m^4]
l	Length	[m]
L	Lift	[N]
m	Mass	[kg]
M_i	Moment around the i axis	[Nm]
res	Resolution	[px,px]
P	Power	[W]
S	Surface Area	[m^2]
t	Thickness	[-]
T	Thrust	[N]
v	Poisson Ratio	[-]
V	Velocity	[$\frac{\text{m}}{\text{s}}$]
w	Width	[m]
W	Weight	[N]
η	Efficiency	[-]
Γ	Dihedral angle	[º]
σ	Axial Stress	[Pa]
ρ	Density of Air	[$\frac{\text{kg}}{\text{m}^3}$]
$\Lambda_{c/4}$	Quarter Chord Sweep	[º]
λ	Taper Ratio	[-]
τ	Shear Stress	[Pa]

1

Introduction

In the years 2016 to 2022, almost 40,000 lives have been saved through Search and Rescue (SAR) operations in the Mediterranean Sea [1]. Unfortunately, in this same period, the lives lost at sea have been estimated to be around 23,000. The beneficial effect of search and rescue missions is represented by the large amount of humans being saved, however, it also becomes apparent that there is still room for improvement in these operations. With populations increasing in the coming years, as well as an ever inter-connected world, travel over the ocean is expected to increase; whether it is migration, leisure, or transport [2]. Therefore, it is safe to say that search and rescue operations need to be become more effective. Major difficulties of search and rescue operations include lack of visibility, and resources being heavily taxed [6]. In addition to this, the operational conditions in which search and rescue missions are performed are most of the time very harsh. In stormy conditions, the strong winds and high waves have a huge impact on the efficiency of the operation as a whole. The reduced visibility, rocking motion of the vessel, and the constrained deployment of personnel impose serious limitations on successfully carrying out search and rescue missions.

The aforementioned limitations and obstacles present a compelling engineering problem, this report aims to provide a solution to this. The goal of this report is to perform an initial design iteration of an autonomous drone swarm aiding in stormy maritime search and rescue operations. The drone swarm will effectively enhance the visual capabilities during missions using state of the art payload systems, and lower the burden on the employees as the swarm shall operate autonomously.

This report is divided into several different chapters, commencing with chapter 2 explaining the mission in detail and representing the corresponding requirements of the entire mission. Chapter 3 aims at presenting the operations and logistics of the different phases involved in the mission. Additionally, the integrated START system responsible for autonomous command and control of the drone swarm, and physically launching the Fixed-Wing systems is also highlighted in chapter 3. Chapter 4 explains the functioning of the drone swarm profile in detail and its corresponding characteristics, in this chapter a swarm configuration is done based on the analysis of an in-house simulation tool. chapter 5 describes the design of the scanning nodes, the sizing of all the subsystems, and a performance analysis is performed to determine the structural, aerodynamic and stability characteristics of this drone. Chapter 6 describes the design of the multicopter system used for the landing procedure and the procedure itself. Additionally, this chapter looks at the coupled system its control and stability characteristics. chapter 7 analyses the risks of the project, chapter 8 describes the design and development plan. Chapter 9 contains the market analysis and other financial aspects of the product. chapter 10 deals with the sustainability of the project. Finally, chapter 11 deals with the verification and validation done during the development of this report, as well as the tests that should be done in future stages of the product development.

---

[1] URL: https://en.sosmediterranee.org/about-us/ [Cited: 19-06-2023]

[2] URL: https://education.nationalgeographic.org/resource/global-network/ [Cited: 19-06-2023]

2

Mission Architecture

This chapter serves as a mission overview, providing a high-level outline of the entire search and rescue mission. It lays the foundation for the design project by establishing the fundamental requirements and outlining the interactions with external stakeholders. Firstly, in section 2.1 the requirements are listed and the meetings with external persons are provided. In section 2.2, the Mission Need Statement and Project Objective are provided together with the mission characteristics. Lastly, in section 2.3, the various components of the swarm are introduced, as well as other systems involved in rescue operations.

2.1. Fundamentals & Relevance

An autonomous drone swarm has numerous advantages over the systems currently at use for maritime operations. Drone swarms allow for a larger coverage of an area, reduce the risk for operators, as they do not have to deal with the elements, and they can reduce the costs and duration of certain missions.

2.1.1. Top Level Requirements

The following list of top level user requirements are the starting point of the project.

Table 2.1: System requirements.

Requirement ID	Requirement Description
REQ-STK-MIS-01	The drone system shall operate in a swarm configuration
REQ-STK-MIS-02	The drone system shall be able to operate in at least wind force 7
REQ-STK-MIS-03	The drone system shall be able to operate in at least sea state 5
REQ-STK-MIS-04	The drone system shall be able to take-off autonomously from the ship deck
REQ-STK-MIS-05	The drone system shall be able to land autonomously from the ship deck
REQ-STK-SAR-01	The system shall not have a single point of failure
REQ-STK-SAR-02	The system shall not require any personnel near the drone during the operational time
REQ-STK-SUS-01	The system shall not employ any form of combustion power system
REQ-STK-SYS-01	The swarm shall be of heterogeneous nature
REQ-STK-SYS-02	The individual nodes shall not have a dimension larger than 3 meters
REQ-STK-SYS-03	The individual nodes shall not have a total operational weight exceeding 25 kilograms
REQ-STK-SYS-04	The node shall have a minimal cruise speed of 25 meters per second
REQ-STK-SYS-05	The node shall be able to deploy a maximum payload of 3 kilograms
REQ-STK-SYS-06	The system shall provide real-time HD video streaming to the Command and Control Center (CCC)
REQ-STK-SYS-07	The system shall be able to provide captured imagery to the Command and Control Center (CCC) over a minimum distance of 100 kilometers
REQ-STK-COS-01	The total costs of one individual node shall not exceed 100,000 euros

2.1.2. Mission Stakeholder

In the beginning phases of the project, meetings were conducted with various external parties from industry in order to decide on the primary stakeholder of the system. In order to make this decision, a thorough understanding was needed of the current systems in place and their shortcomings. During the meetings, valuable insights were gained related to possible applications of a maritime drone swarm. These insights were used to define the primary mission stakeholder, mission profile and other project parameters. The following is a brief summary of the meetings held with each external party:

Royal Netherlands Navy
In the first week of the project, the team had a meeting with an officer from the Royal Netherlands Navy. The navy has a drone in use called the X-300 Integrator [1] from Boeing-Insitu whose launching system takes a lot of space on the ship deck of navy ships, covering the helipad. This is something which is preferably to be avoided for future drone systems. A mission profile for the Navy would primarily consist of surveillance. The most important takeaway from the meeting was that it would be impossible to modify the deck of a navy ship, but it was suggested that the hangar could be used. Due to the limited space, there would have to be a trade-off between having many low-endurance drones or having fewer high-endurance drones.

KNRM
Another meeting was with Jeroen Kodde from the KNRM. The main useful application of a drone swarm for the KNRM would be search and rescue missions in the North Sea. Currently, only small DJI quadcopters are used, which provide very useful visualisation but have limited takeoff and landing capability, require a operational crew, and have limited endurance of around 30 minutes. During a search and rescue mission, a system would work together with rescue helicopters and rescue boats. The main takeaway from this meeting was that a drone swarm would be very useful in the context of a search and rescue mission.

Innovation consultant UMCG & ANWB Medical Drone Service
This meeting was held with Jaap Hatenboer, a drone specialist involved with the Medical Drone Service[2], a joint initiative currently in development by the ANWB and PostNL for accessible healthcare through delivery drones. The meeting with Jaap Hatenboer was useful to gain insight into a drone application in a different field. More importantly, the team learned what aspects to consider when making the change from a mission performed solely by operators, to an autonomous mission performed by unmanned aircraft. In addition, valuable insight was gained on the difficulty of VTOL operations in adverse weather conditions.

Avalor.ai
Finally, the team met with Maurits Kortes-Altes, an entrepreneur from Avalor.ai. This meeting was useful to gather information about search operations. It gave the team insight into the interaction between drones within a swarm, as well as dynamic search patterns and scanning for military operations.

Following the meetings, it was decided that the Netherlands Coastguard would be the primary mission stakeholder. This is because the Coastguard plays a crucial role in maritime safety and security of vessels and personnel at sea. The mission profile related to this stakeholder would be search and rescue, working together with helicopters and boats, and in some cases replacing them. In addition, the Coastguard has the capability to house a large drone system on its maritime vessels. While the Coastguard is the primary stakeholder, the system would work closely with the KNRM during search and rescue operations.

2.2. Mission Profile

After choosing search and rescue for the Netherlands Coastguard as the primary mission profile and mission stakeholder, the mission profile was specified. The initial Mission Need Statement and Project Objective Statement are provided below:

- **Mission Need Statement:** The Navy/Coastguard is in need of a drone swarm system that autonomously performs search and rescue operations over operational areas ranging from a few to tens of kilometers in stormy environmental conditions.

- **Project Objective Statement:** DSE group 6, a team of 10 students, will design a storm-resistant maritime drone swarm capable of landing autonomously on ship decks, over a design phase of 10 weeks.

---

[1] URL: https://www.defensie.nl/onderwerpen/materieel/vliegtuigen-en-helikopters/x-300-integrator-onbemand-verkenningssysteem [Cited 19-06-2023]

[2] URL: https://medicaldroneservice.nl/en/ [Cited 19-06-2023]

The Coastguard has been chosen as the primary stakeholder of the maritime drone swarm design as it is the most limiting case and closely aligns with the mission objective. The mission is in collaboration with the Coastguard, whose ship will be used for both landing and take-off purposes and the KNRM, who work together with the swarm during the rescue part of the search and rescue mission. The mission characteristics and their descriptions are shown in Table 2.2.

Table 2.2: Mission characteristics.

Mission Characteristic	Description
Mission Duration	The total duration of the mission is 48 hours. The duration is based on the expected survival time of a human overboard. This is based on a meeting of the STORM team with Koninklijke Nederlandse Redding Maatschappij (KNRM).
Collaborative Units	During the mission, the Coastguard works closely together with the KNRM, which has deployed lifeboats. The drone swarm must be able to work together with the relevant external units employed by these organizations keeping an eye on the safety of all parties involved in the rescue operation.
Weather Conditions	The drone swarm must operate in wind force 7 and sea state 5, which is equivalent to a wind speed of a maximum of 17.1 m/s and a maximum wave height of 4 metres.
Storage Unit	The drone swarm is stored in a container with dimensions 6.06 x 2.44 x 2.59 metres. The container is placed on the ship deck and used for take-off and landing.
Oceanic Drift	The oceanic drift due to wind and current is incorporated in the mission as it will change the search area over time. Simulation tools are available and known to the Coastguard and KNRM.
Autonomous Control	The drone swarm operates autonomously during the entirety of the operation meaning that the drone should land, take off and operate without human input.
Search Area	The initial search area is a square of 20 [km] by 20 [km]. The search area is updated continuously with respect to the oceanic drift and wind force and direction. The ship is located at most 100 [km] from the centre of the search area.
Ship	The boat that is used for take-off and landing is the Coastguard's "Multraship Commander". The dimensions are 58.55 [m] in length, 14.80 [m] in width and 7.65 [m] in height. The ship travels with a ground speed of 17.5 knots.
Assets	The drone is not used as a rescue vehicle but instead is used to pinpoints the location. Once the drones identify the target or person, it relays the information to supporting rescue assets. These assets can include manned helicopters, boats, or emergency tow vehicles that can carry out the rest of the mission.

2.2.1. Assumptions

To refine the mission various assumptions have been made. These assumptions are listed below:

- **ASP-01. The drone swarm has 24hr availability:**
  Since it is unknown when a search and rescue procedure is necessary, the drone swarm must be able to operate at any point throughout the day, and must not rely on daylight for visibility. This implies that the drone swarm must be on stand-by at all times and have the ability to become operational on short notice.
- **ASP-02. The search area drift and expansion over time is characterized by limited accuracy:**
  Simulation tools are available by the swarm operators that provide real-time data about the oceanic current and wind speed which cause search area drift and expansion over time. These simulation tools contain some uncertainties which increase the size of the search area over time.
- **ASP-03. The initial search area will have a rectangular/square shape:**
  The initial search area, as indicated by the first distress call, uses a rectangular/shape to make a first-order prediction of the mission providing a starting point for mission planning. Throughout the mission, (which includes the time required for the swarm to arrive at the search location) the search area will take a more conical shape due to the dynamic behaviour of the sea current. The search area will be closely monitored and adjusted where necessary.
- **ASP-04. Take-off and landing of the drone swarm will be performed on sea:**
  This project will assume the worst-case scenario in which the closest available drone swarm is located on a ship during a storm; coastal take-off and landing are considered outside of the scope of this project.

2.3. Mission Elements

The safe retrieval of a person at sea requires the collaboration of multiple systems. While the drone swarm plays a crucial role in locating the individual, there are additional steps involved in ensuring their safety. In this section, the various components of the swarm, as well as other systems involved in the rescue operation will be elaborated on. Together, these interconnected nodes work together to successfully locate, assist, and bring the person to safety.

2.3.1. Nodes

The STORM system consists of three different nodes. These include the following:

- **Storage node** The drone swarm, consisting of both the fixed-wing and multicopter drones, will be housed in a specially designed standard size 20ft container known as the START system. An example of such a container can be seen in Figure 2.1. START stands for Storage and Assisted Rapid Take-Off, highlighting the purpose and functionality of the container. The choice of utilizing a standard 20ft container is advantageous due to its widespread availability and compatibility with existing infrastructure. By integrating the drone system within this container, it enables convenient storage, transport, and operation of the drones. Both the fixed-wing and multicopter drones will take off and land directly from the START system making the system autonomous which will be further elaborated on in section 3.2.

Figure 2.1: Standard 20 feet sea container [9].

- **Scanning node** The scanning node of the swarm is a long range fixed wing drone equipped with a thermal imaging payload, as shown in Figure 2.2. This node will be referred to as the Fixed-Wing. It is responsible for conducting the scanning operations to locate the target. The Fixed-Wing is specifically optimized for enhanced endurance, ensuring that it can remain operational at sea for extended periods of time while actively searching for the target. By maximizing its endurance capabilities, the Fixed-Wing plays a crucial role in increasing search efficiency and maximizing the chances of successfully locating the target in a timely manner. This will be further elaborated on in chapter 5.

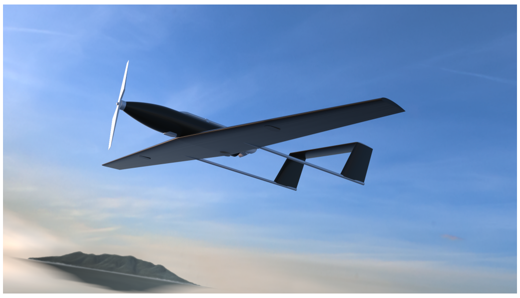

Figure 2.2: Render of scanning node

- **Docking node** The docking node in the swarm serves the purpose of facilitating the landing operations of the scanning nodes. Due to the high power requirements for take-off and landing, it was determined, based on a trade-off analysis conducted in [11], that it would be impractical for the Fixed-Wing drone to perform these maneuvers. Performing take-off and landing operations would significantly reduce the overall endurance of the Fixed-Wing drone, which is undesirable for prolonged search missions. To overcome this challenge, an additional docking node, in the form of a multicopter, is introduced. This docking node is responsible for safely capturing and landing the scanning node (Fixed-Wing drone) in midair. By utilizing the capabilities of the multicopter, the Fixed-Wing drone can safely land and dock, preserving its enhanced endurance capabilities. A render of the multicopter is shown in Figure 2.3. The details of this multicopter with its docking mechanism and its implementation will be elaborated upon in chapter 6.

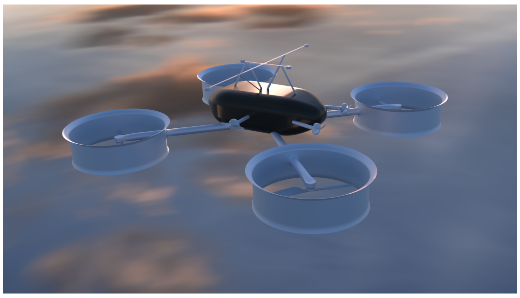

Figure 2.3: Render of docking node

2.3.2. External Systems

To efficiently locate and rescue a lost person at sea, various systems must collaborate effectively. These systems include the ship, the drone swarm, and additional resources such as search and rescue helicopters and boats. As mentioned in section 2.3, the drones are stored on a container box called the START system on the Coastguards' ”Multraship Commander”. Details regarding the specifications of the Multraship Commander can be found in Figure 2.4. This vessel serves as a crucial platform for launching and controlling the drone swarm, enabling efficient search and rescue missions at sea.
An example of a helicopter commonly used for search and rescue operations is the NH90 helicopter (Figure 2.5a). This helicopter is equipped with advanced navigation and surveillance systems, enabling it to operate effectively in various weather conditions. It has the capability to swiftly transport rescue personnel and necessary equipment to the location where the person has been found.

In addition to helicopters, lifeboats play a vital role in maritime search and rescue operations. An example of a lifeboat commonly employed by the KNRM is the NH1816 boat (Figure 2.5b). These boats are specifically designed for efficient rescue missions, equipped with advanced navigation systems, emergency medical equipment, and capabilities to operate in the challenging sea conditions. They enable rescue teams to reach the person at sea and provide necessary assistance or transport them to a safe location.

Both helicopters and lifeboats are crucial assets in maritime search and rescue operations, ensuring the safe retrieval of individuals at sea after the drones have found a target at sea.

MULTRASHIP TOWAGE & SALVAGE MAKES THE DIFFERENCE

MULTRASHIP COMMANDER

CALL SIGN	: PCBN
YEAR BUILT	: 2006
CLASSIFICATION	: DNV-GL 100 A5 E2 Offshore Service Vessel MC E2 AUT FF(1)
FLAG	: Dutch
HOMEPORT	: Terneuzen-Netherlands
IMO NR	: 9344966

DIMENSIONS

L.O.A.	: 58.55 m
L.B.P.	: 52.29 m
B.O.A.	: 14.80 m
Depth to maindeck	: 7.65 m
Max. draught	: 5.82 m
Deadweight	: 1.694 mt
Gross tonnage	: 1.767 mt
Nett. tonnage	: 530 mt
Cargo deck area	: 220 sqm
Deck load	: 10 mt / sqm max.
Chain locker capacity	: 2 x 33 cbm

PERFORMANCE

Bollard pull	:192 mt cont.
Max. speed	:17,5 knots

MACHINERY

Main engines	: 14.000 kW / 750 rpm 2 x 7.000 kW MAN B&W 14V32/40
Propellers	: 2 x CPP 3.800 mm in nozzle
Rudders	: High performance Becker rudders
Bow thrusters	: 2 x 400 kW tunnel thrusters, CPP
Stern thrusters	: 1 x 400 kW tunnel thruster, CPP
Generators	: 2 x 500 ekW, 50Hz auxiliary generators 2 x 1.500 ekW, 50Hz shaft generators 1 x emergency generator

TANK CAPACITIES

Ballast water	: 140 cbm
Fresh water	: 77 cbm
Marine gas oil	: 131 cbm
Heavy fuel oil / marine gas oil	: 1.132 cbm

TOWING / ANCHOR HANDLING

Towing winch	: Electr. driven 100/200 mt @ 15/7,5 m / min
Brake holding load	: 300 mt drum's 1st layer
Drums	: 2 x 1.600 m, 76 mm
Control	: Remote controlled from bridge
Cable lifters	: 1 x 76 mm and 1 x 126 mm
Tow wire	: 1 x 1.600 m, 76 mm 1 x 300 m, 76 mm
Storage reel	: 1 x 1.200 m, 76 mm
Stern roller	: 300 mt SWL, 3,00 m length / 2,00 m diameter
Tugger winches	: 2 x 10 mt @ 15 m / min
Towing pins	: 2 x Karmoy, 300 mt SWL
Karm forks	: 2 x Karmoy, 650 mt SWL, various inserts

ACCOMMODATION

Total capacity	: 21 persons
Cabins	: Single berth 13 Double berth 2 Four berth 1
Hospital	: Single berth

MULTRASHIP.COM Tel: +31 (0) 115 645000 (24/7)

Figure 2.4: Multraship commander ship of the Coastguard with the specifications which is the boat that is used for the search and rescue mission [40].

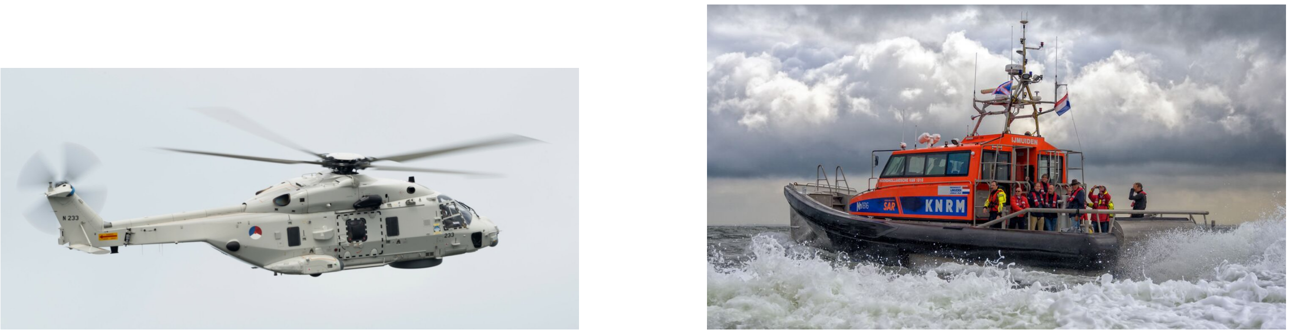

(a) NH90 Helicopter [31].

(b) NH1816 boat [32].

Figure 2.5: Two systems that are used for the search and rescue mission after the target has been found at sea already used by the KRNM.

2.4. Conclusion

This chapter served as a starting point for the design project by establishing the fundamental elements of the search and rescue mission. It introduced the key requirements that shape the design process and outlined the various components that are present in the mission. Building upon this foundation, chapter 3 will provide the mission operations and logistics. It will provide an overview of the different phases of the mission and present a conceptual starting system for the drone swarm.

3
Mission Operations and Logistics

The operations and logistics of the mission play a crucial role in identifying and understanding the different phases involved in the overall mission. In section 3.1, the operations and logistics plan will provide detailed information with regards to all the phases. In section 3.2, the housing of the docking and scanning nodes will be provided.

3.1. Operations and Logistics Plan

This chapter covers the operations and logistics of a search and rescue mission of project STORM. It is assumed that the mission starts from a START system as described in section 2.3 at sea and a search area is provided by the KNRM or Coastguard. The mission can be split up into 6 phases as shown in image Figure 3.1. The phases will be briefly explained in the following sections. Prior to the start of the search and rescue mission phases, the drones are stored within the START system.

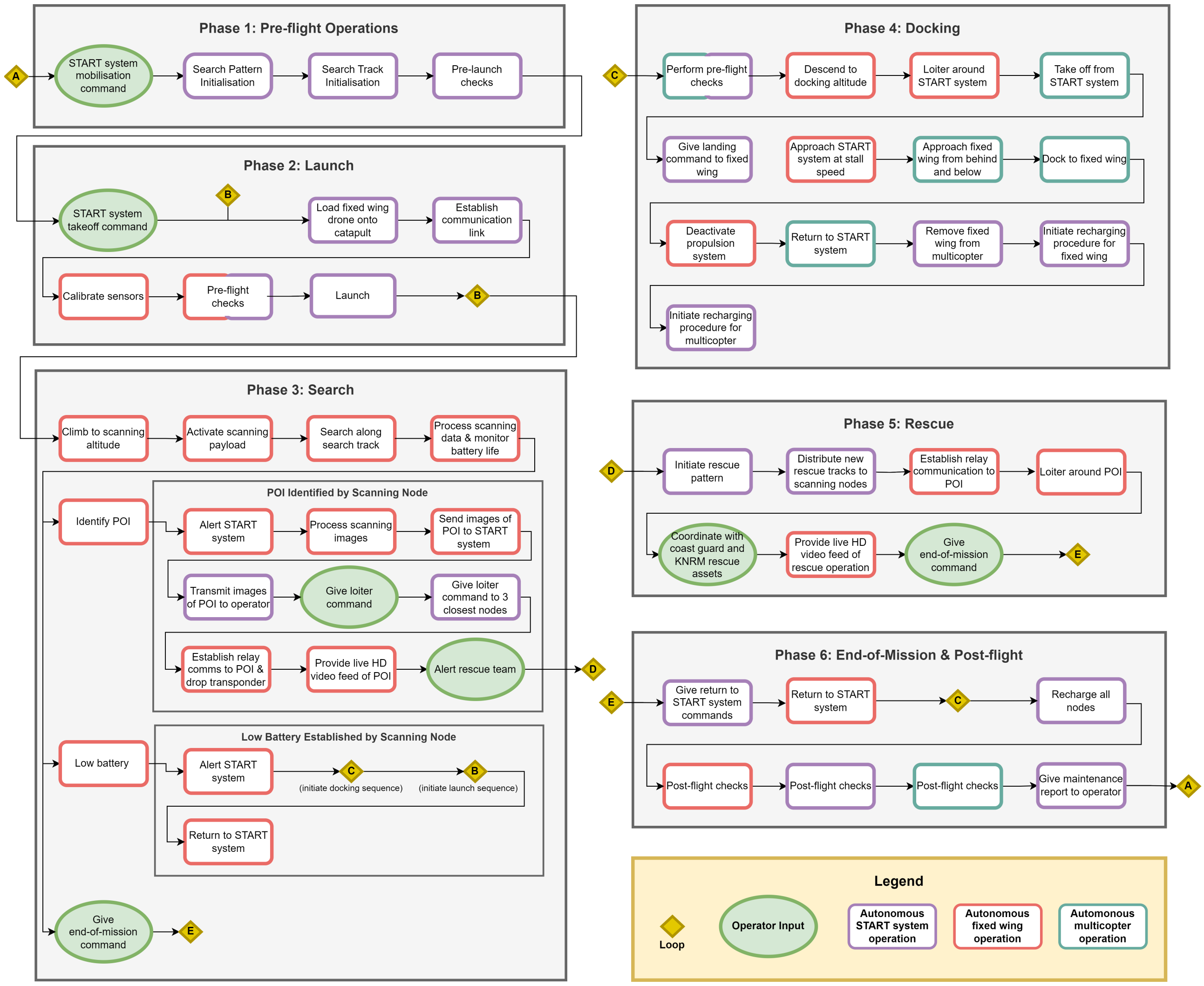

Figure 3.1: Operations and logistics flow diagram containing the six operational phases of the STORM system.

3.1.1. Phase 1: Pre-flight

The pre-flight phase of the mission contains all operations that have to be completed after a mobilisation command has been given to the swarm and prior to takeoff of the Fixed-Wing. A mobilisation command consists of communication from a command and control center to the system with a request for launch, an area that needs to be searched, and the amount and type of targets that need to be rescued. Once a mobilisation command is given by the Coastguard, the START system initialises a search pattern over the search area. The search area is split up into a search pattern to maximise the scanning speed of the search area which will be elaborated on further in chapter 4. Following the search pattern initialisation, pre-launch checks are performed to ensure nominal operation of the START system.

3.1.2. Phase 2: Launch

During the launch phase, the swarm of scanning nodes is initialised and launched from the START system on a ship. This is triggered by a takeoff command from the operator in the command and control center. Once the takeoff command is received by the START system, the swarm will autonomously takeoff from the ship by following a set of launch steps for each Fixed-Wing.

First, the Fixed-Wing is loaded onto the launch catapult. Next, a communication link is established between the START system and the Fixed-Wing, and the Fixed-Wing sensors are calibrated. Next, the node is allocated a unique search track within the search pattern. Following this, the Fixed-Wing performs its final pre-flight checks and sends back an OK status. Lastly, the START system launches the Fixed-Wing and repeats the launch procedure for the remaining Fixed-Wing drones.
In the span of several minutes, the Fixed-Wing scanning drones are launched from the start system by use of the catapult and start making their way to the scanning area. Once a node is launched, it keeps a two-way communication link with the start system to keep an accurate view on its continually shifting search track.

3.1.3. Phase 3: Search

During the search phase, the Fixed-Wing drones climb to the scanning altitude, travel to the search area, and perform a search over the search area with its thermal IR imaging payload. Each Fixed-Wing drone scans its allocated part of the search area. Upon arrival at the center of the search area, one scanning node will drop a transponder to track the oceanic drift and thus characterise and anticipate the change in shape and size of the designated search area. Concurrently, the drone swarm engages in scanning the area through the use of infrared and electro-optical sensors. The collected data is processed, compressed and analysed by the Fixed-Wing . Images of potential points of interest are transmitted via the START system to the operator in the command and control center. The operator can use visual inspection or artificial intelligence algorithms to determine if a HD video is needed or if the rescue teams need to be alerted. If the target is located, a transponder is dropped at the initial target location and concurrently the target location is filmed and a HD video is directly transmitted to the operator on the ground ship. Depending on the environmental conditions, other nearby drones can be called in to help keep track of the target, to ensure that the target is not lost again in the conditions. The exact number of drones that are called in would depend on multiple factors such as the environmental conditions and the progress of the search, since any drone that is circling a target can not be used to actively search for other yet unlocated targets. There is also a possibility that the mission duration may exceed the endurance of the drones. In this case drone scheduling algorithm makes sure that a drone is automatically replaced when it returns to the start system before running out of battery to ensure continuous operation of the swarm.

3.1.4. Phase 4: Docking

Upon returning to the start system, the Fixed-Wing loiters at its stall speed of 18 $[m \cdot s^{-1}]$. The start system detects an incoming Fixed-Wing and gives a takeoff command to the Multicopter docking drone. Once in the air, the Multicopter docking drone approaches the scanning node from behind and below, matching its velocity. When sufficiently close, it initiates the docking procedure, eventually coming close enough such that the docking electromagnets attach to the docking plates of the fixed wing. Once secured, the Multicopter returns to the start system such that the Fixed-Wing can recharge.

3.1.5. Phase 5: Rescue

Once the target has been found and the location is made known to the rescue teams, the rescue procedure is started. This will be done by the Coastguard or KNRM. Rescue vehicles approach the designated target location. As the rescue vehicles are manned, the drone swarm will be at a specified safe distance from the target to ensure the safety of the personnel. The swarm will continue to provide a live video feed of the operation by forming a relay to the ship. The rest of the swarm will return to the ship or continue scanning if there are still targets to be found.

3.1.6. Phase 6: End-of-Mission & Post-flight

In the post-flight phase, once all nodes have successfully landed and are stored back in the start system, they are recharged and manually checked to ensure that they can be used for a next mission. Post-flight checks are performed to check whether repair or any replacement is necessary. After the ground ship arrives back to land, the start system is stored and maintenance for the drones can be performed.

3.2. START System

An integral part of the STORM system operations is the system which houses the scanning and docking nodes, acts as the primary command and control center for autonomous operations of the drone swarm, and physically launches the scanning nodes into the air. This system is contained within a standard 20ft container and is called the START system.

3.2.1. Storage and Transport

The START system offers convenient storage and transport capabilities as it is stored in a standardized 20 ft container. The system can accommodate for a total of 10 Fixed-Wing drones and 2 Multicopter drones fit in per START system. The setup allows for efficient deployment and retrieval of the drones enhancing the performance of the system.

3.2.2. Autonomous Operations

A critical function of the drone swarm is that its operations are fully autonomous. By making sure that no people have to be present during a mission, it ensures that the system is not limited by weather and human life is not risked at the expense of putting people in dangerous situations during the storm on deck. During a storm storing the drone of the drone swarm product being designed is that it should be fully autonomous. This introduces heavy constraints on the take-off and landing procedures. Along with that, carrying out these procedures on a ship in sea state 5 imposes even further complications. As a result, extensive thought had to be put into landing and take-off. This chapter highlights the design of a compatible take-off system in section 3.3 and a landing system in section 6.1.

3.3. Take-off procedure for the Fixed-Wing

The initial phase of the take-off for the Fixed-Wing is situated in the START system. The Fixed-Wing is put on a specially designed elevator using a feeding system, which brings the drone to the top-level of the START system. Thereafter, the Fixed-Wing is loaded onto the catapult. The catapult system shoots the Fixed-Wing into the air after which the Fixed-Wing trades in a part of its launch velocity to rapidly gain altitude. The internal layout of the START System is shown in Figure 3.2. The external layout of the START is shown in Figure 3.3.

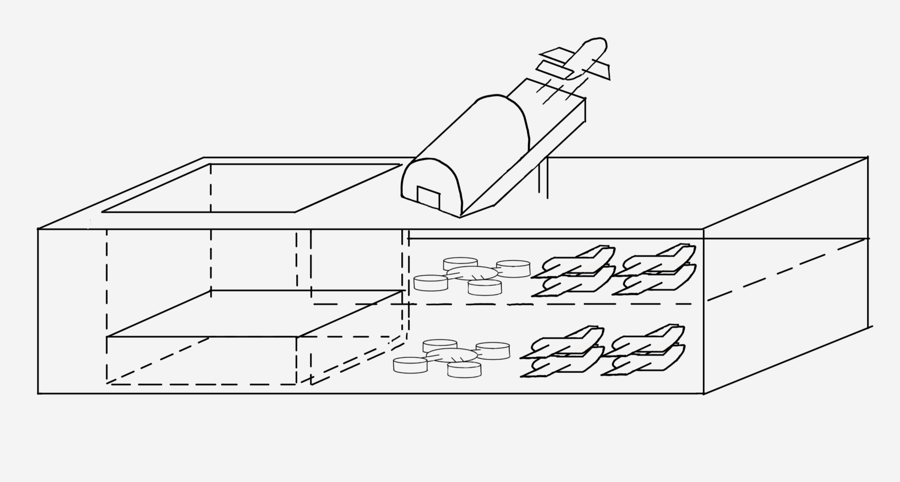

Figure 3.2: The internal layout of the START System

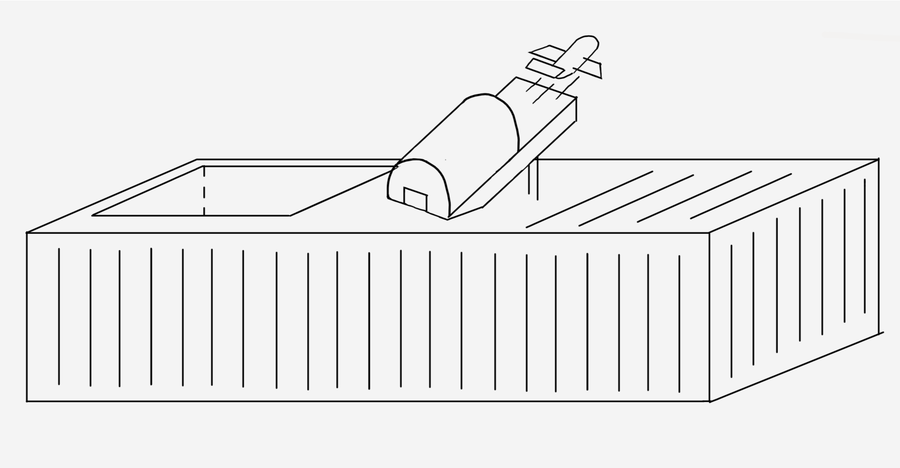

Figure 3.3: The external layout of the START System

In section 6.1, it is explained how the retrieving of the drone is executed. After the fixed wing is successfully retrieved, the batteries of the fixed wing can be recharged. The batteries are charged using wireless charging.

3.4. Conclusion

In conclusion, the sections have provided an overview of the START system, highlighting its role in the storing of Fixed-Wing and Multicopter drones and enabling the launching and recharging of the scanning nodes. In the next chapter, the drone swarm characteristics will be explored and refined in more detail. The initial swarm characteristics will be used as the building block for the subsequent design activities.

4
Drone Swarm

This chapter aims at presenting the characteristics of the drone swarm. By understanding the overall swarm behavior and performance, the specific drones can be designed more effectively. In section 4.1, a performance analysis of the swarm will be conducted, where the scanning height and simulation behaviour will be explored. section 4.2, explores the methodology and simulation of ocean drift, leading to the identification of optimal searching patterns and the required number of scanning drones. Lastly, in section 4.3, the communication flow and software diagram will be provided, illustrating the interaction between the drones in the swarm and the START system.

4.1. Performance Analysis

The performance analysis of the drone compares the results of the simulation of the search and rescue given different initial conditions. In such a way, it is possible to determine the optimal search pattern given the search area shape, the optimal number of scanning drones, and the optimal angle with respect to the wing among other parameters. These parameters are useful to optimise the search algorithm and improve the efficiency of the search and rescue mission.

4.1.1. Scanning Height

The primary driving factor for the scanning height at which the drones fly, is the resolution and field of view of the camera used, along with the amount of pixels required to pick out a person from the water. When a person is floating in the water, it cannot be assumed that their entire body is visible. Instead, only their head, shoulders and arms might be visible above the water, with the rest of their body being fully below the waterline. This means that the drones will need to detect a target that is potentially no larger than 60 cm by 60 cm. To reliably detect a target in the water using an infrared camera, it was determined that the target would need to have a size of at least 4 pixels for the longest dimension. This may seem small, however, the 4 by 4-pixel surface detected by the infrared camera will be double-checked by the electro-optical camera with a higher resolution. From this, it can be found that the ground resolution required would need to be at least 0.15 [px·m^{-1}]. In [11], it was decided to use the Mantis i45N camera. This camera has a resolution of 640 [px] wide and a field of view of $10.8°$[34]. Calculating the swath width results in a maximum swath width of 96 [m] while flying at an altitude of 400 [m].

A wider effective field of view can however be achieved without giving up ground resolution by panning the camera back and forth during flight. This allows the camera to cover more area without the drone having to fly more distance. However, when doing so, one gives up a temporal resolution over the scanned area. It is therefore important to ensure that there is still overlap between the different frames taken along the entire scanned width to ensure no area is skipped. Furthermore, to maintain the minimum ground resolution, it is required to reduce the flight altitude of the drone to compensate for the stretching distortion of the image due to the lower angle of incidence when the camera is facing sideways. As the camera span angle increases, the required flight height decreases. In addition, increasing the field of view also reduces the required scan height required to detect a person. However, the larger the pan angle, the larger the area that can be scanned at a time, therefore it is important to determine the optimal scan height that allows the drones to scan the largest possible width.

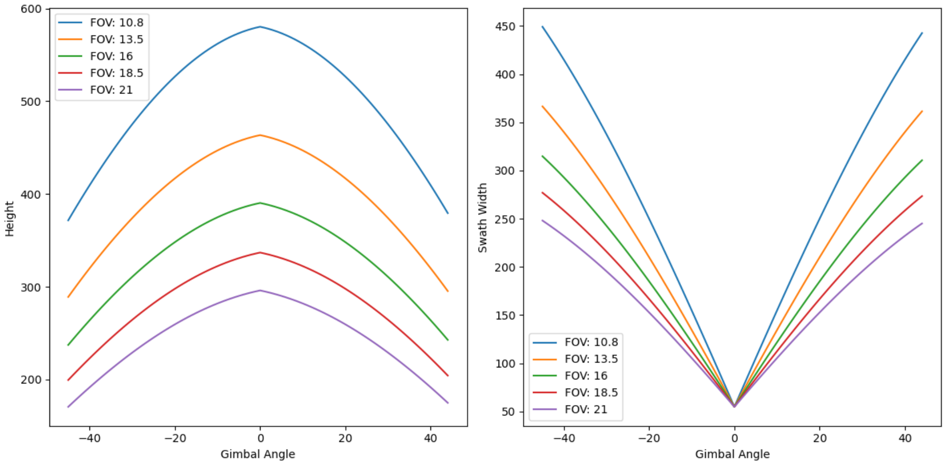

Figure 4.1: Minimum scanning height vs gimbal angle and maximum scan half-width vs gimbal angle for multiple FOVs.

Figure 4.1 shows two figures. On the left, one can observe the minimum required height for a given gimbal angle for a set of fields of view. From this plot it is clear that the smaller the field of view, the higher the minimum flight height. In addition, the plot on the right shows the scan width for a given gimbal angle for different fields of view. In order to maximise the scanned area, one must use the smallest field of view, this area is achieved with a gimbal rotation of 45º or more, however, the flight height for this drastically reduces, as seen on the plot on the left. Therefore, a gimbal rotation of 40º was selected, which yields a high scan area, while staying at a flight height of approximately 400 m.

Another aspect that must be considered is that the drone is travelling perpendicular to the camera rotation, so the camera must pan fast enough to ensure the whole area is scanned as the drone travels forward. If the drone has a groundspeed of 50 [m/s], the camera should be able to scan quickly enough to cover the required -40º to 40º pan.

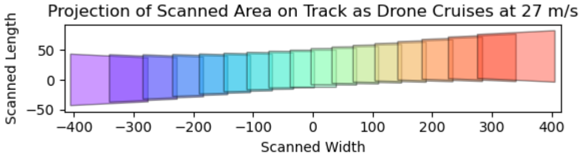

Figure 4.2: Scanned frames at 5 [º] intervals for one track.

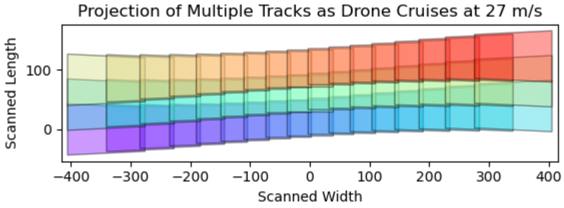

Figure 4.3: Scanned frames at 5 [º] intervals for three tracks.

Figure 4.2 shows the different scans that could be done if the gimbal has a rotational speed of approximately 90 [º/s]. Figure 4.3 shows multiple tracks, and one can observe the overlap between them.

4.1.2. Simulation Behaviour

To compare the impact of different parameters in the swarm behaviour, a 2D swarm searching simulation written in python was developed. In this simulation, the rescue ship with the drones is initially situated 100 [km] away from the center of the search area, being either a square 20 x 20 [km] area, or a circular shape with the same surface area. From this ship, drones are then launched towards the search area at a 5 minute interval. Each drone is then assigned a specific track in the search area, as divided using the patterns described above, in which they will search for potential survivors. When a survivor is found, it is then required to maintain contact with the target to ensure it can not get lost before the ship can pick them out of the water. For this purpose, up to 3 drones are directed to keep loitering any found target to keep its position up to date. Once the ship arrives to rescue the target out of the water, the drones will continue their search effort to find other targets within the search area. If a drone runs low on battery while searching, it will be required to return to the ship to land and get its batteries recharged. The threshold for returning to the ship is defined such that the drone will return when it has 1.5 times the energy expected to be needed to return to the ship, with a margin on top of that of 10 minutes to allow for recovery of the drone. As soon as it arrives back at the ship, a new drone is launched to replace it. Once all targets have been found, the drones return to the ship and the mission is finished. During this simulation, multiple parameters can be varied, such as the number of drones, the wind strength and direction, the search area and pattern used, and the number of survivors. Similarly, a variety of parameters is tracked during the simulation, such as the total mission duration and rescue times of the targets. When drift simulation is enabled in the simulation, every hour the search area is recomputed considering potential drift that might have occurred during the previous hour. At this point, the search patterns are also rebuilt to properly cover the search area again. This process is repeated until the entire area has been searched, or all targets have been found. A view of the simulation with the line sweep search pattern can be seen in Figure 4.4, whereas figure Figure 4.5 shows the spiral search pattern.

Figure 4.4: A view of the two-dimensional simulation used to analyse the swarm behaviour for the line-sweep search pattern.

The green outline represents the perimeter of the search area that still needs to be scanned, the horizontal red lines represent the current flight path assigned to each scanning drone, the small red trapeziums represent the specific area that is being scanned at that exact instant by the camera, the pink circle represents a survivor and the black outlines are the drones and the ship. At the top right of the window one can observe the vectors representing wind and the sea current and the top left one can see the time settings such as the time elapsed since the beginning of the simulation and the time-warp. Finally there is also a bar representing the scale.

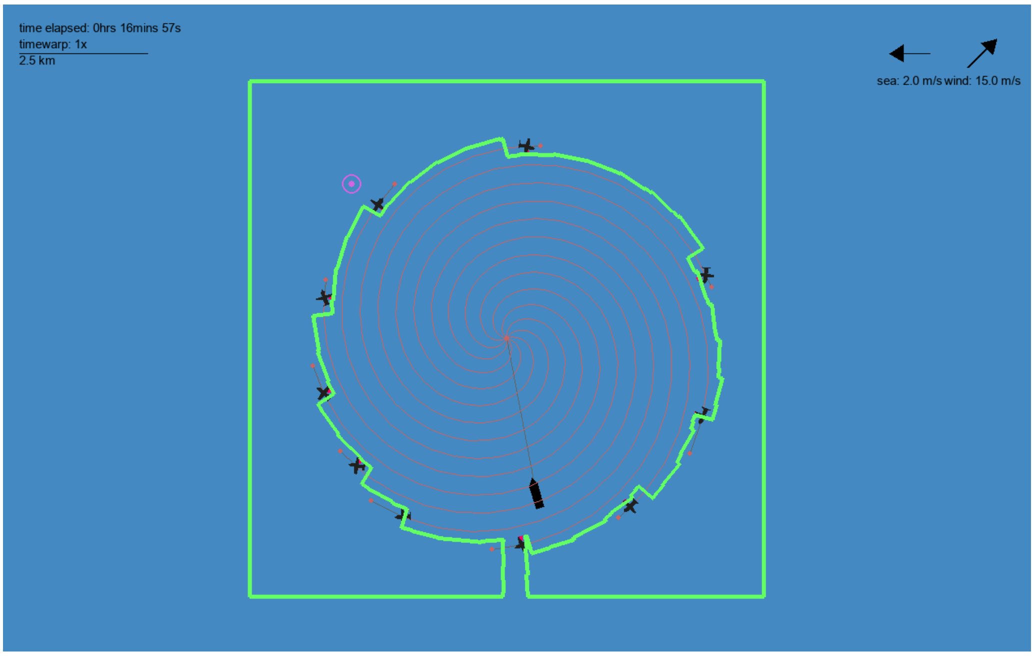

Figure 4.5: A view of the two-dimensional simulation used to analyse the swarm behaviour for the spiral search pattern.

4.2. Ocean Drift

To implement oceanic drift into the simulation, the Leeway model as implemented into the opendrift Python library is used. Leeway is an open source oceanic drift simulation model that was developed by the United States Coastguard in 1999[5][4]. The Leeway model is based on empirical data collected by the U.S. Coastguard on the oceanic drift behaviour of many seaborne objects including people in water, life rafts, and boats in various states. To implement the Leeway model into the simulation, every hour in the simulation, a grid of points is generated based on the area that still has to be searched. This grid is then input into the Leeway model and allowed to drift for a time period of 1 hour. After this time, the resultant grid can be used to reconstruct the search area that has not been covered yet. For this new area, the search pattern can then be rebuilt, after which the drones can continue to search their area. The 1 hour figure was chosen as a middle-ground between simulation accuracy and search and simulation performance. Choosing a too large time step between drift simulations would result in the scanning drones working with potentially outdated data, reducing their effectiveness and potentially allowing them to miss targets. To limit the error, during the 1 hour interval, a linear translation is applied to the search area to ensure it roughly matches the drifting search area. Additionally, the different tracks in the search pattern are constructed such that there is some overlap at the edges of each track to ensure that a small amount of deformation does not instantly lead to missed areas. Taking a too small time step however would lead to a reduced effectiveness of the drone swarm. Every time the search area and search pattern are recomputed, the drones lose scanning time as they will no longer be on a scanning track and have to navigate to their new search track again. Furthermore, if the drifting offset is too small, there is a higher chance of the reconstructed search pattern containing many sections which only cover a very small area making it inefficient to fly these patterns. Therefore, the 1 hour mark was found to provide a good middle ground between searching accuracy and searching efficiency. It is however advisable that in areas with large current and wind gradients, the search area is recomputed more often since in these areas, the searching accuracy would otherwise drop off rather quickly.

4.2.1. Search Pattern Determination

When searching a large area for points of interest, an important parameter is the choice of the search pattern that will be followed to find the final target. For the STORM drone swarm, a selection of parameters has been considered. Firstly, there is a standard line sweeping pattern. In this pattern, the search target area is divided into straight parallel segments, which are then divided among the available drones. For this search pattern, it is possible to orient the strips in any direction while covering the entire field. The optimal value of this parameter will be discussed in subsection 4.2.2. The second search pattern that is considered is a spiraling search pattern.

In this pattern, the search area is covered in a set number of outward spiraling line segments. When a segment of the spiral extends beyond the search area, this segment will then be discarded to prevent spending time searching areas which do not contain any target anyway. The determination of the optimal number of tracks will be discussed in subsection 4.2.3. The last pattern that will be considered is a square shaped spiral. For this pattern, a singular track will spiral outwards making 90° turns whenever it reaches the end of its segment. This last pattern will for simplicity be referred to as the ”squiral” search pattern throughout the rest of the report. Although it is possible to include multiple spiraling tracks for this pattern, this variation is considered to be sufficiently covered for the true spiral track in subsection 4.2.3, such that it would add little value to repeat the same process for this pattern. Furthermore, although more patterns exist than are treated in this report, this selection of patterns is deemed sufficient to provide a good knowledge basis from which better experiments and comparisons can be performed in later stages of the design.

For the comparison of the search patterns described above, all tests are run with the same environmental set-up. Within the search area, three targets are positioned at random (albeit the same for each pattern) positions, with the wind blowing towards blowing head-on during the journey towards the search area with a speed of 15 [ms^{-1}]. During the simulation, the drone limit is set to 6, meaning no more than 6 drones will be in the air at any given time. The tests were run both with drift being modeled, and without. During the test, the line sweep search pattern was oriented such that its tracks are at 90° relative to the wind the direction, and the spiral search is set to have the same number of tracks as drones, with 6 outward spiraling tracks.

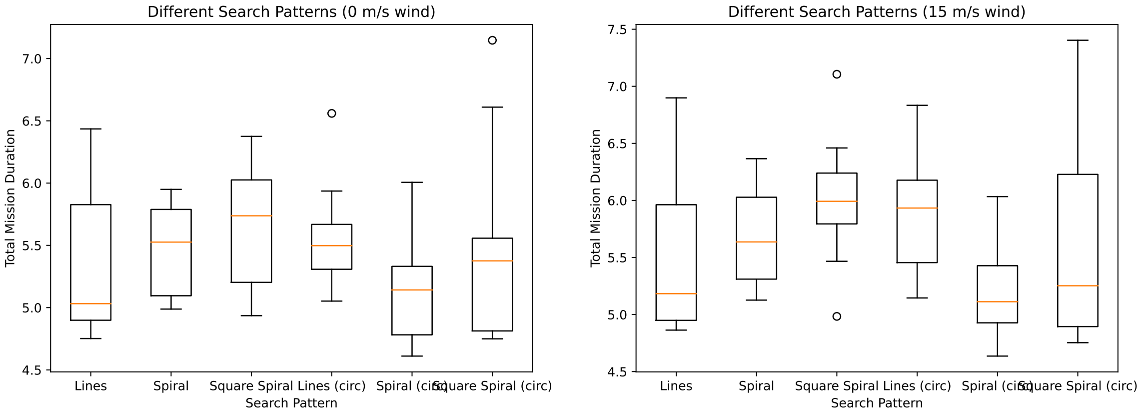

(a) Search pattern comparison with 0 [ms^{-1}] wind.

(b) Search pattern comparison with 15 [ms^{-1}] wind.

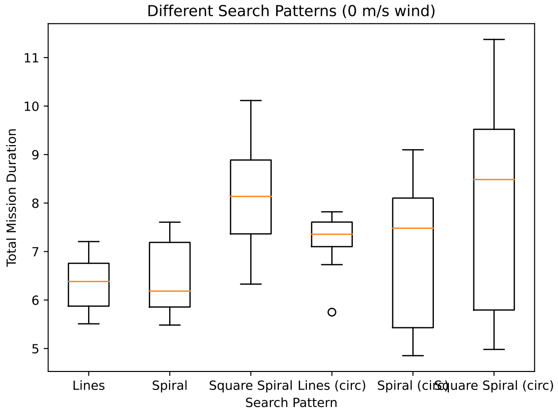

(c) Search pattern comparison with drift implementation with 0 [ms^{-1}] wind.

Figure 4.6: Search pattern comparison.

From the results, shown in Figure 4.6a, it can be seen that in the baseline test with no wind on a square search area, the line sweep search pattern performs the best. Although the spiral search pattern has more consistent results, it takes on average longer to locate all targets using this search pattern. The squiral performs consistently slightly worse than either of the two search patterns. This is likely caused by the difficulties in distributing the search area segments between drones leading to drones not always getting assigned connected segments which in turn leads to a significant time loss as the drones fly between segments. When the search area has a more circular shape, the spiral search pattern can be observed to have better performance than any of the other search patterns. This can be explained by the fact that in the spiral pattern, many segments of the track are connected directly onto the previous segment. Especially when the pattern properly matches the search area such as is the case for a circular search area, and therefore there are no disconnected segments along each spiral track, the drones do not lose time flying between segments and can therefore spend the majority of their time scanning new areas.

In the case where wind is introduced, as shown in Figure 4.6b, it can be seen that the squiral performs significantly worse in the case of a square search area. This is likely caused by the many potentially straight upwind segments present in this search pattern, giving the drones a relatively low average ground speed. For a circular search area however, it can be seen that the average performance is now significantly better than that of the linear sweep pattern and only slightly worse than that of the spiral, although in this scenario its performance is still fairly inconsistent making it a notably worse search pattern in scenarios when quick rescue is absolutely mandatory. Regardless of the search area shape, the spiral search pattern can be seen to lose significantly less performance than the line sweep and squiral search patterns. This is likely caused by the spiral search pattern having less straight upwind sections, allowing the drones to maintain a higher average ground speed throughout the mission. Nonetheless, for a square search area, the line sweep search pattern still comes out on top, although for a circular search area the line sweep loses a significant amount of performance, meaning that in this situation the spiral is now indisputably the best performing search pattern.

Lastly, in the case where drift is introduced, as shown in Figure 4.6c, a different noteworthy trend can be seen. When drift is applied, it can be seen that the line sweep search pattern has significantly more predictable performance than any of the other two search patterns. Due to the methodical nature of the line sweep, which leads to only a small boundary length, the of the search pattern due to drift has a relatively tame impact on the size of the search area. Especially the squiral search pattern however seems to suffer significantly from the implementation of drift into the model, seeing an increase in scanning duration of almost 50%. The spiral search pattern seems to suffer from a slightly more unpredictable impact from the drift implementation. Although with drift its average search time compared to the line sweep search pattern improved for the square search area, it seems to suffer significantly more for the spiral search pattern, although even in this case its best performance remained relatively similar to the case without drift.

In conclusion, both the line sweep and spiral search patterns have strong and weak points. In the case that the spiral properly matches the search area, it can be expected to perform very competitively compared to a simple line sweep. If the search area however is a more irregular shape, the line sweep's simplicity allows it to cover the search area with minimal complex drone behaviour and planning, allowing it to more efficiently search the entire search area. In the case where drift is considered, the line sweep's simplicity especially allows it to outperform all other options. The squiral search pattern does not seem to be particularly good for searching any area regardless of the circumstances.

4.2.2. Optimal Scanning Orientation

A potentially important parameter for the line sweep search pattern is the orientation of the lines with respect to the wind direction. From Figure 4.7a, it can be observed that, with the original ship positioned 100 [km] away from the centre of the search area, there is only minimal variations in the time taken to complete the mission. When the ship is however originally placed at a distance of only 20 [km], as shown in Figure 4.7b, away from the center of the search area, a more pronounced trend can be seen. From this result, it can be seen that the line sweep search pattern performs best whenever the the pattern is at a 90 [°] angle with respect to the wind direction. This result can be mathematically explained by calculating the expected time to fly a specific distance in windy conditions. It can be found that the ground speed V_g of the drone in windy conditions can be calculated using Equation 4.1.

$$V_g = V_{wind} \cdot cos(\alpha_{wind}) + \sqrt{(V_{wind} \cdot cos(\alpha_{wind}))^2 - (V_{wind}^2 - V_{air}^2)} \tag{4.1}$$

In this equation, α_{wind} is the angle between the required course over the ground and the wind direction, V_{wind} is the wind speed, and V_{air} is the airspeed of the drone. Using this equation to calculate the round trip time for a back and forth journey between two points, it can be found that the shortest round trip time is achieved when flying perpendicular to the wind, with the longest round trip time occurring when the section is oriented at a 0 [°] relative to the wind. Since the primary flight direction of the drones is along the searching lines of the track, with comparatively less distance being flown between line segments. Therefore, it is to be expected that the search pattern performs optimally when oriented at 90 [°] relative to the wind direction, which matches the data in Figure 4.7b.

The reason why the case with the original ship position being 100 [km] away in Figure 4.7a does not show this trend, is likely caused by the drones spending significantly more time waiting for the ship to arrive to pick up the target. This waiting time then likely overshadows the time difference due to a difference in efficiency of the search pattern. It can however not be excluded that more pronounced differences will be visible in other scenarios such as with a different drone swarm size or a different number of targets in the water.

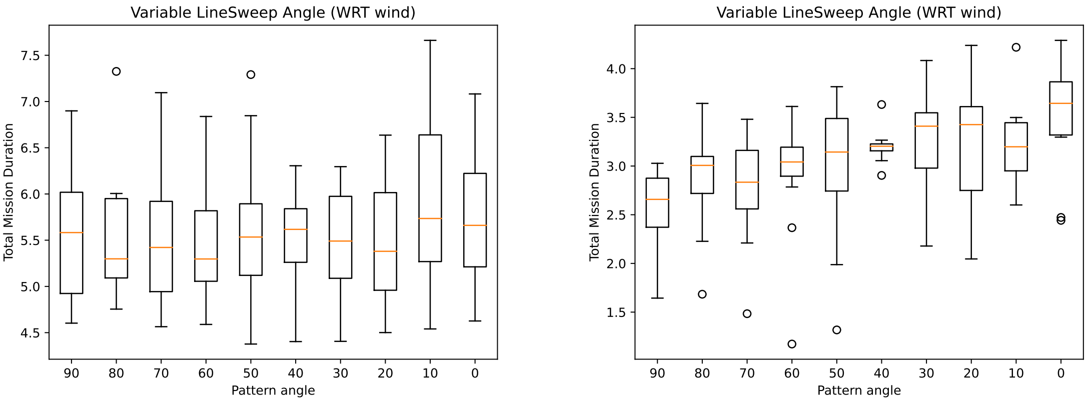

(a) Line sweep with original ship position 100 [km] away.

(b) Line sweep with original ship position 20 [km] away.

Figure 4.7: Line sweep effectiveness with variable angle w.r.t. wind.

4.2.3. Optimal Spiral Track Count

For the spiral search pattern, the primary variable is the number of outward spiraling tracks within the search pattern. For this test, 6 drones were active simultaneously. In Figure 4.8a it can be seen that the spiral performs best when the number of spiral tracks is one less than the total number of drones. Once the track count exceeds the number of drones, the time to search the entire search area increases significantly. A likely explanation for this phenomenon is that once the track count only marginally exceeds the number of drones searching the area, when each drone is done searching its designated track, all drones will start competing for different segments of the last remaining track. This means that this track will not be searched optimally as many segments will get covered multiple times by different drones. When the track count is one less than the number of drones, one drone will automatically be designated to filling in the corner sections, where the spiral tracks have been clipped, which can lead to better performance compared to exactly matching the number of spirals to the number of drones. Similarly, the performance drastically improves again once the number of tracks approaches the next integer multiple of the number drones in the swarm, after which the same pattern appears to repeat as the drone count exceeds this integer multiple.

From Figure 4.8b it can be seen that when the spiral pattern is applied to a circular area, the track count is less important than for a square area. Nonetheless, a trend can be seen that when the track count is slightly less than the number of drones in the swarm, the system performs most optimal. It is however notably less efficient to exactly match the number of drones directly to the number of spirals. A likely cause for this result is that for the circular pattern, once a drone finds a target, they will halt their search pattern until the target is picked up. In this case, these drones will get out of sync with the rest of the swarm searching the area, meaning that once the drones resume searching for remaining survivors they might no longer have a track assigned only to themselves. Especially due to the lack of small segments in the corners which are present in the square search area, tracking conflicts are more likely to occur.

In the case where drift is implemented, as shown in Figure 4.8c, it can be seen that the performance dependence on track count, although leading to larger overall changes in the search pattern performance, has significantly more variance than in the case without drift. This is likely caused by the more chaotic nature of the drifting of the search area, which means that after the renewed generation of the search pattern every hour, the spiral tracks might no longer properly align with the searched area leading to drones potentially searching inefficient tracks. A notable effect of applying the drift is that the optimum spiral count seems to shift more toward the lower end of the number of drones. The large performance gain approaching the 2n track count now occurs one spiral earlier. This is likely to be caused by the drift, after all, drones have completed a full outward spiral track, growing the search area such that on either side of the searched area another search track is added. Therefore initially having two fewer tracks than the number of drones allows these two ”spare” drones to pick up at these newly formed tracks once they begin to appear.

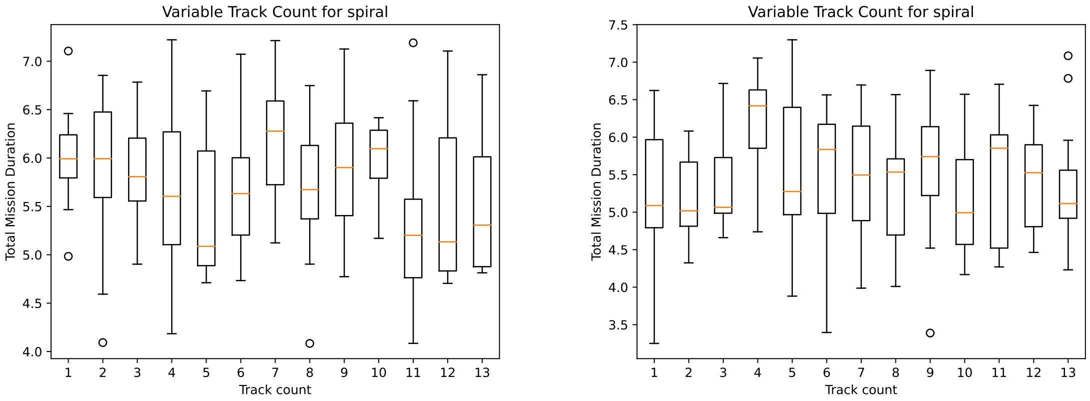

(a) Spiral effectiveness with variable spiral count on a square area. **(b)** Spiral effectiveness with variable spiral count on a circular area.

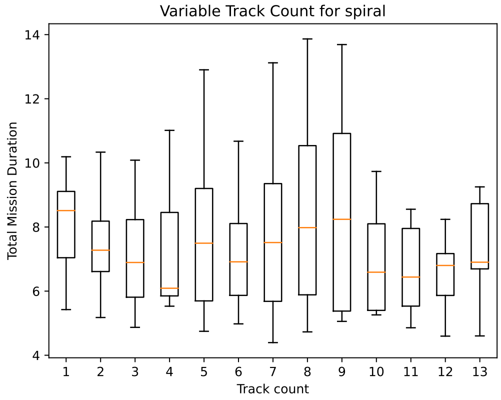

(c) Spiral effectiveness with implemented drift on a square area.

Figure 4.8: Spiral effectiveness with variable spiral count values.

In conclusion, it can be said that the performance of the spiral search pattern is optimal when the number of tracks is slightly lower than an integer multiple of the number of drones. Even so, the optimal number of tracks depends on multiple other factors such as the shape of the search area.

4.2.4. Number of Scanning Drones

Regardless of the search pattern used, the number of drones in the swarm is an important parameter that can be varied to change the performance of the swarm. To compare the impact of a different number of drones, the line sweep search pattern is used as a baseline due to its independence from the number of drones as opposed to the spiral, as explained in subsection 4.2.3. From Figure 4.9, it can be seen that when very few drones are active, the total search duration is significantly higher than when multiple drones are active. In the case with three targets in the water, as shown in Figure 4.9a, it can be seen that the total search duration keeps reducing up until a limit of approximately 10 simultaneous scanning drones in the air. After this point adding more drones to the searching swarm does not significantly affect the effectiveness of the swarm in scanning the area. A likely cause for this observation could be the limited speed at which the ship is capable of sailing to and rescuing the targets. Therefore, once the drones are capable of finding all targets before the ship gets into range of the search area, there is little benefit of launching more drones.

In the case of only one target in the water, as shown in Figure 4.9b, it can be seen that the optimal drone limit occurs around the same point, at a swarm size of up to 9 scanning drones. For this test, the ship has been positioned at an original position of only 20 [km] away from the search area to better show the difference in scanning speed between different swarm sizes.

Another notable observation, that can be seen in both simulations is that for the case with only 1 drone maximum in the swarm, there appears to be a hard cut-off for the mission around the 4 hour and 45 minute mark. This cut-off is caused by the battery lifetime of the drone. As the drone runs out of battery and is no longer able to track the target, if it has not been rescued yet at this point, the target will once again be lost and become harder to find again. Due to this, the mission ends prematurely even if no target has been found. In reality, this cut-off would not happen as the operation would be able to continue with the latest known position, which would allow for a new search area to be constructed, this is not possible with the current implementation of the simulation. It can however still be determined that any number of drones less than 4 has a fairly limited performance. The most optimal point for both cases seems to occur around 10 drones, after which adding more drones does not add much value anymore. Therefore, the drone swarm has been determined to consist of 10 active scanning nodes for missions with an equally sized search area. When however more targets are in the water, it is anticipated that adding more drones could improve the performance as more drones would be stuck circling found targets. In this case however, more ships should also be added to more quickly alleviate the drones such that they can continue their searching operations.

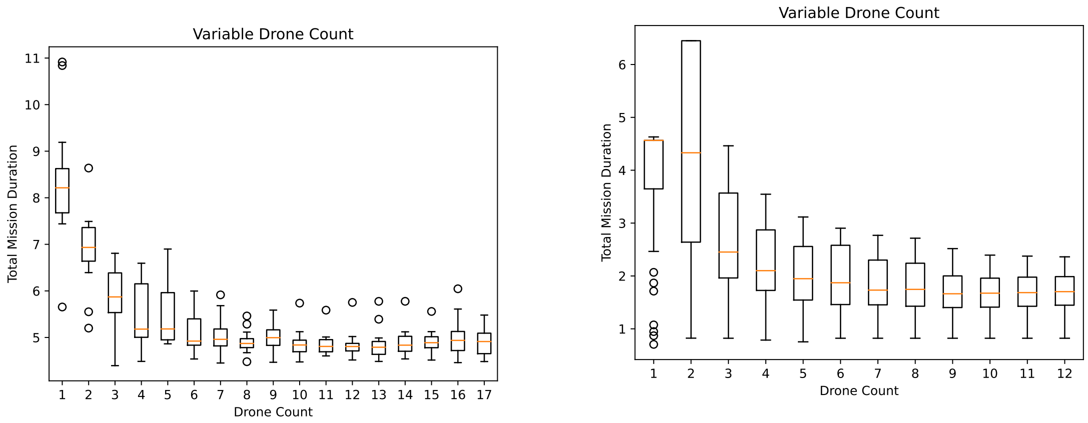

(a) Drone count impact on search effectiveness with three targets.

(b) Drone count impact on search effectiveness with one target at 20 [km].

Figure 4.9: Drone count impact on search effectiveness.

4.3. Communication and Software Diagrams

This section presents the communication flow diagram of the entire swarm, illustrating the communication system comprising three main components: the ground station located on the ship (START system), the two drones, and the operator responsible for controlling the autonomous drones. Effective communication is essential for the smooth operation of the swarm. Inter-drone communication is crucial to facilitate collaborative decision-making and ensure autonomous landing of the drones. The data handling in Figure 5.44 and Figure 6.12 can be used to see how the data from the communication is processed and translated into actions within each of the Fixed-Wing and Multicopter drones respectively. These two diagrams provide a comprehensive overview of how data is managed and transformed into commands within the drone system. The communication flow diagram can be seen in Figure 4.10. Furthermore, the connection between the data flows and communications with the software components required for the operation of the swarm is shown in the software block diagram presented in Figure 4.11.

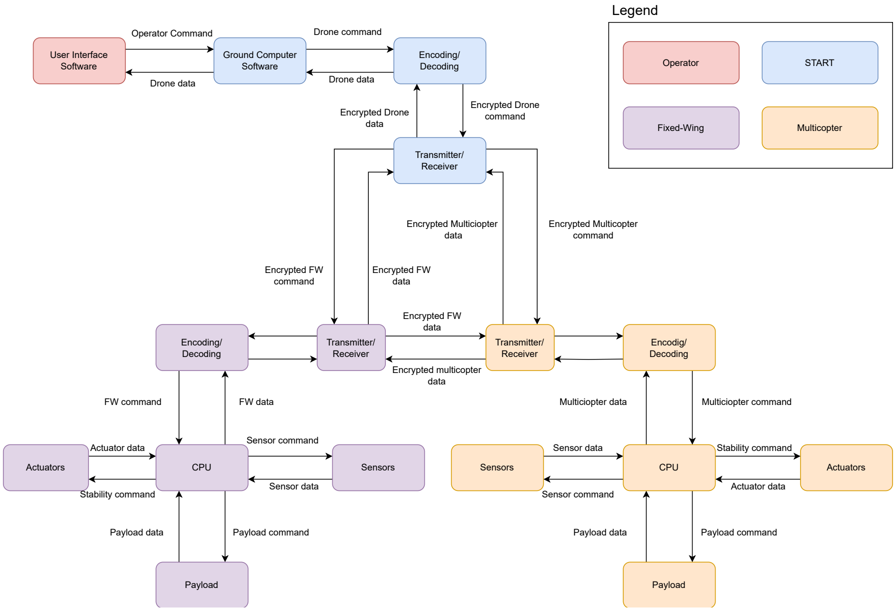

Figure 4.10: Communication flow diagram of the system; operator, START system, Multicopter and Fixed-Wing drone.

As mentioned earlier, the communication system comprises four key components: the ground station (START system) situated on the ship, the two drones, and the operator who controls the autonomous drones. When initiating a mission, such as in the case of an alarm triggered by someone being lost at sea, the operator is responsible for initiating the entire system by issuing a command to the START system. This command serves as the starting point for activating and coordinating the communication system, setting the mission in motion.

Once the command is sent, it is directed to either the Fixed-Wing drone or the Multicopter. The command is received by the CPU, which ensures that it is routed to the appropriate subsystem of the drone. Both the Multicopter and the Fixed-Wing drone also have inter-drone communication capabilities, which is crucial for the autonomous functioning of the system. This communication enables collaboration and coordination between drones during various operations such as the docking and landing sequence.

Effective communication among the drones and with the ship during the landing procedure is very important. This communication ensures that the drones can approach each other mid-air and safely land, ultimately allowing the system to return to the ship. The ability to communicate and synchronize actions between the drones and the ship is essential for the successful completion of the landing procedure.

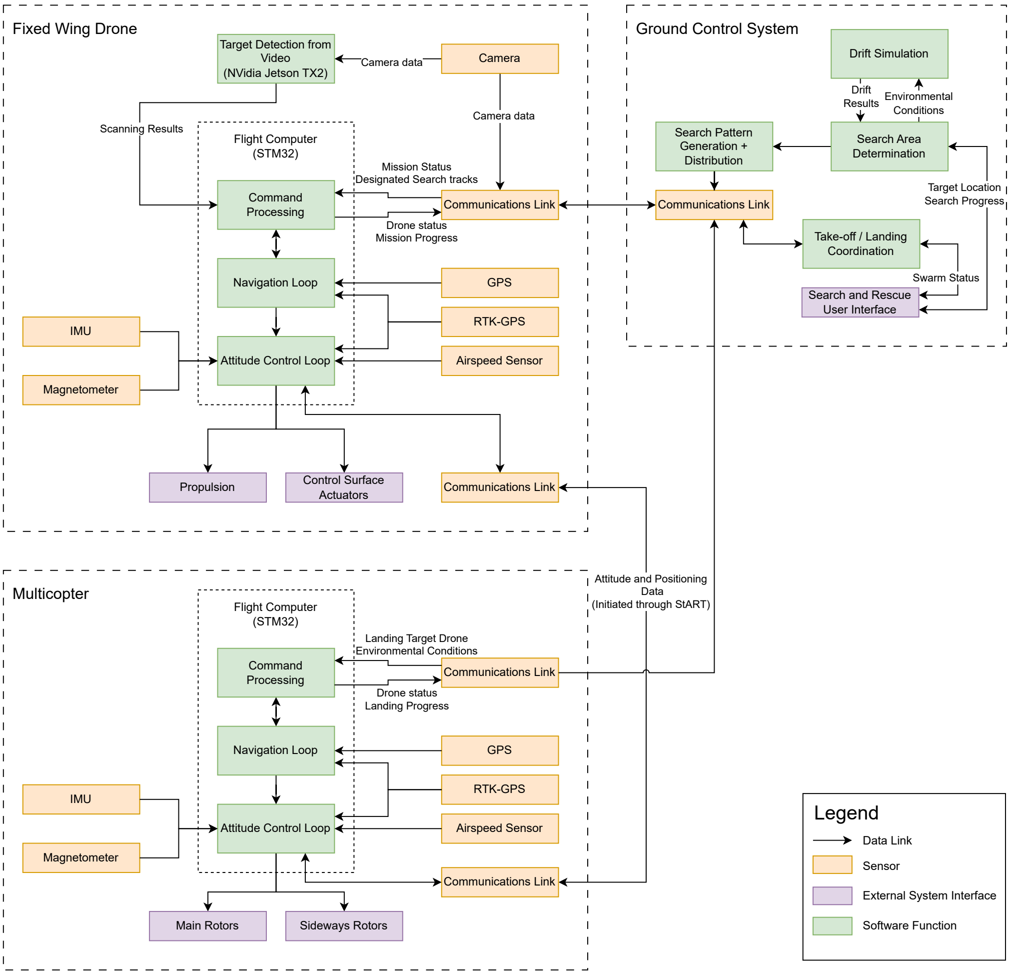

Figure 4.11: Software block diagram of the swarm system.

4.4. Conclusion

In this section, the performance and behaviour of the swarm has been analysed along with the interactions between different components of the swarm. To compare the impact of various swarm characteristics, a purpose built 2D swarm simulation was created and various tests were configurations were tested. From these tests, it was found that the scanning swarm would have an active size of 10 simultaneous scanning drones. It was found that the most efficient search pattern is either a spiral search pattern, or a line sweep pattern, depending on the shape of the search area and the drift parameters of the search area. Furthermore, diagrams have been constructed to show the data flow within the swarm and show interdependencies.

5

Fixed-Wing Drone

This chapter aims to present the preliminary Fixed-Wing drone system design. The Fixed-Wing aircraft is the system responsible for the majority of the search and rescue mission, therefore, performing a detailed analysis of the system is of great importance. In section 5.1 the main wing sizing of the Fixed-Wing is presented, which is followed by the fuselage and empennage design in section 5.2 and section 5.3. The aforementioned three sections finalise the initial configuration of the system, this is followed by performing an aerodynamic and stability analysis in section 5.4 and section 5.5 respectively. Diving deeper into the subsystems required to perform the search and rescue mission successfully, the power and propulsion system is described in section 5.6. The Fixed-Wing system is subjected to a variety of loading cases and environmental factors, the structural system that has to cope with this is highlighted in section 5.7. In section 5.8 a description of the different available engineering budgets is presented. Finally, section 5.9 aims at presenting the hardware, electrical and data handling block diagrams of the Fixed-Wing drone system.

5.1. Main Wing

The main wing of an aircraft is one of the most important subsystems of the aircraft. Its main function is to generate the lift for the aircraft in order to stay airborne throughout the whole flight phase at varying flight speeds. Careful consideration needs to be taken in order to ensure optimal aerodynamic, structural and stability performance. In order to size the wing, first the surface area needs to be determined. This is done in subsection 5.1.1 with the use of a wing loading diagram. In subsection 5.1.2 important geometric parameters for the wing are selected and in Table 5.4 and Table 5.5 the control surfaces of the Fixed-Wing drone are synthesised.

5.1.1. Surface Area Determination

In order to determine the size of the wing, multiple factors have to be taken into consideration. Given the fact that a lot of parameters are unknown at this stage of the design process a lot of assumptions have to be made. In order to narrow the design space, the ratios of power to weight (P/W) and weight to surface area (W/S) have to be determined. This is done by rearranging some equations in terms of these ratios and plotting them on a graph. A total of six ratio lines can be used to narrow down the wing loading diagram for propeller aircraft. These are in relation to:

- Stall Speed
- Cruise Speed
- Climb Rate
- Climb Gradient
- Take-off Distance
- Landing Distance

Given the fact that the Fixed-Wing drone utilizes an assisted take-off and landing procedure, the ratios for the take-off and landing distance are not necessary in this case.

Stall Speed

To size the stall speed ratio Equation 5.1 [37] is used. A V_{Stall} of 19.5 [ms^{-1}] and a conservative estimate for $C_{Lmax,Clean}$ of around 1.3 [-].

$$\frac{W}{S} = \frac{1}{2} \cdot \rho \cdot V_{Stall}^2 \cdot C_{Lmax,Clean} \tag{5.1}$$

Where ρ is the air density, V_{Stall} is the stall speed for the clean configuration and $C_{Lmax,Clean}$ is the maximum lift coefficient of the Fixed-Wing drone in clean configuration.

Cruise Speed

For the cruise speed line Equation 5.3 [37] is used. A P_{sett} of 90% is used, an η_P of 63% is used from an assumed propeller and electrical motor efficiency of 70% and 90%. For C_{D0} the value of 0.028 [-] for a single propeller aircraft was assumed and for e Equation 5.2 was used. [41]

$$e = \frac{1}{1.05 + 0.007 \cdot \pi \cdot AR} = 0.778[-] \tag{5.2}$$

$$\frac{W}{P} = P_{sett}\cdot\eta_{\mathsf{P}}\left(\frac{\rho}{\rho_0}\right)^{3/4}\left[\frac{C_{\mathsf{D}_0}\frac{1}{2}\rho V^3}{(\mathsf{W/S})} + \left(\frac{W}{S}\right)\frac{1}{\pi ARe\frac{1}{2}\rho V}\right]^{-1} \tag{5.3}$$

WhereP_{sett} is the power setting, η_{P} is propulsion efficiency, ρ_0 is sea level air density, ρ is air density at cruise height, C_{D_0} is the zero lift drag coefficient, V is cruise speed, AR is aspect ratio and e is Oswald efficiency factor.

Climb Rate

To obtain the climb rate line Equation 5.4 [37] is used. A value of 3 $[ms^{-1}]$ for c_{rate} is used.

$$\frac{W}{P} = \eta_P\cdot\left[\frac{c_{rate}+\sqrt{\frac{W}{S}}\cdot\sqrt{2}}{\frac{C_L^{3/2}}{C_D}\cdot\sqrt{\rho}}\cdot P_{sett}\right]^{-1} \tag{5.4}$$

Where ρ is air density, η_{P} is propulsion efficiency, c_{rate} is the climb rate, C_L is the lift coefficient, C_D is the drag coefficient, V is cruise speed and P_{sett} is the Power Setting.

Climb Gradient

For the climb gradient line Equation 5.5 [37] is used. A value of 17/100 [-] for c_{grd} was used, meaning that for every 100 $[m]$ horizontally, the drone is able to climb 17 $[m]$ vertically.

$$\frac{W}{P} = \left[\left(c_{grd}+\frac{C_D}{C_L}\right)\cdot\left(\frac{\sqrt{\frac{(W/S)^2}{\rho\cdot C_L}}}{\eta_P}\right)\cdot P_{sett}\right]^{-1} \tag{5.5}$$

Where c_{grd} is the climb gradient, C_D is the drag coefficient, C_L is the lift coefficient, ρ is the air density, η_{P} is propulsion efficiency and P_{sett} is the Power Setting.

Parameter	Symbol	Value	Units
Stall Speed	V_{Stall}	19.5	$[ms^{-1}]$
Cruise Speed	V_{Cruise}	30	$[ms^{-1}]$
Climb Rate	c_{rt}	3	$[ms^{-1}]$
Climb Gradient	c_{grd}	17/100	[-]

Table 5.1: Important wing loading diagram parameters.

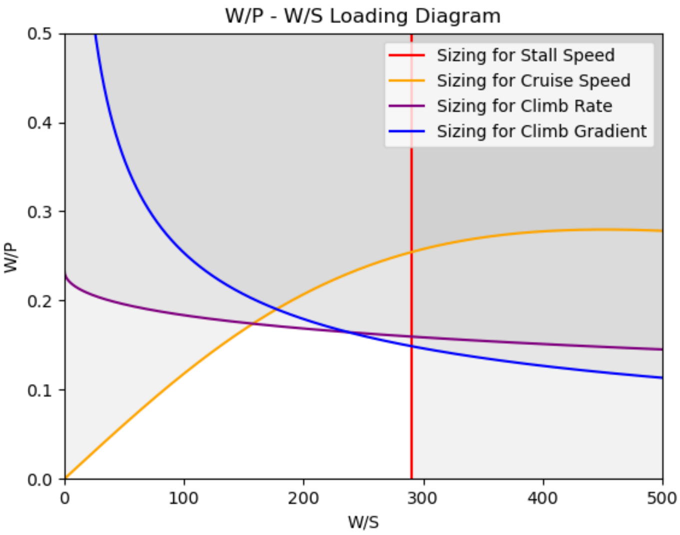

Table 5.2: Wing loading diagram.

Among all the W/P and W/S combinations that allow to meet the mission performance requirements, the design point that yields the aircraft with the lowest cost and weight needs to be selected. That is the point with:

- The highest possible wing loading
- The highest possible power loading

This corresponds to the point in Table 5.2 that is located in the top right white area, in the intersection between the stall speed and climb gradient line. This point gives a W/S value of 286.4 $[Nm^{-2}]$ and a W/P value of 0.147 $[Nm^{-2}]$. This means that given the fact that the weight of the Fixed drone is 245.2 $[N]$ the Wing surface area is 0.845 $[m^2]$ and the corresponding power is 1647.9 $[W]$.

5.1.2. Wing Geometric Parameters

In order to progress in the design of the Fixed-Wing drone, it is important to have an initial estimation of the various parameters that dictate the wing planform. Given the fact that these geometric values were subject to change due to various design iterations, a Python file was procured in order to easily modify these values. Furthermore the HLDs and ailerons in subsection 5.1.3 and subsection 5.1.4 can also be displayed using the Python program.

Wing Span

The wingspan was calculated using Equation 5.6 [37].

$$b = \sqrt{S \cdot AR} = \sqrt{0.845 \cdot 10.7} = 3[m] \tag{5.6}$$

Where b is the wing span, S is the wing surface area and AR is the aspect ratio.

When performing the Class I weight estimation, the aspect ratio of similar aircraft was taken as a reference. Given the fact that the Fixed-Wing drone was not allowed to be larger than 3 $[m]$, an aspect ratio to match this length was selected. It was decided to aim for the highest aspect ratio possible given the beneficial properties of high aspect ratio aircraft:

- Decreased Induced Drag
- High lift curve slope requires low changes of AoA with airspeed
- Increased stall angle
- High L/D_{max} ratio

Sweep Angle

Given the fact that the Fixed-Wing drone will fly at a cruise speed of around 30 $[ms^{-1}]$, no sweep angle is required to increase the critical mach number as the cruise speed falls way within the subsonic flight regime. Furthermore higher sweep angles would decrease the maximum lift coefficient and lead to higher structural weight.

Wing Twist

Applying a wing twist of -3 [°] at the tip chord reduces the wing incidence angle of the wing tips at higher angles of attack, preventing tip stall.

Dihedral

Given the fact that a negative $C_{l\beta}$ is beneficial to lateral stability, a positive dihedral of 5 [°] (Equation 5.7) was applied to aid in this and prevent spiral instability. Furthermore given the fact that the drone will use a low-wing configuration, the dihedral will counteract the positive $C_{l\beta}$ contribution of this configuration.

$$\Gamma = 3 - \frac{\Lambda_{c/4}}{10} + 2 = 5[^{\circ}] \tag{5.7}$$

Γ is the dihedral and $\Lambda_{c/4}$ is the quarter chord sweep angle. There is also an adjustment for low wing configurations, such as this case, whereby 2 degrees must be added to the dihedral.

Taper Ratio

Having no Sweep angle means that a taper ratio of 0.4 is optimal to obtain an elliptical wing distribution by Equation 5.8 [37] .

$$\lambda = 0.2\left(2 - \Lambda_{c/4}\frac{\pi}{180}\right) = 0.4[-] \tag{5.8}$$

In this equation λ is the taper ratio and $\Lambda_{c/4}$ is the quarter chord sweep angle.

Thickness to Chord Ratio

The thickness to chord ratio of the Clark-Y selected airfoil in subsection 5.4.1 is 11.7 [%].

Root and Tip Chords

The root chord length can be calculated using Equation 5.9 [37]

$$c_r = \frac{2 \cdot S}{(1+\lambda) \cdot b} = \frac{2 \cdot 0.845}{(1+0.4) \cdot 3} = 0.401[m] \tag{5.9}$$

Where c_r is the root chord, S is the wing surface area, λ is the taper ratio and b is the wing span. Given the taper ratio, the tip root chord can be calculated in Equation 5.10

$$c_t = \lambda \cdot c_r = 0.4 \cdot 0.401 = 0.161[m] \tag{5.10}$$

Mean Aerodynamic Chord

The mean aerodynamic chord is an important wing parameter that is used in many calculations. To compute the mean aerodynamic chord length, the following formula [37] can be used:

$$c_{MAC} = c_r \cdot \frac{2}{3} \cdot \frac{1+\lambda+\lambda^2}{1+\lambda} = 0.401 \cdot \frac{2}{3} \cdot \frac{1+0.4+0.4^2}{1+0.4} = 0.298[m] \tag{5.11}$$

The spanwise location of the MAC is given by Equation 5.12

$$y_{MAC} = \frac{b}{6} \cdot \frac{1+2\cdot\lambda}{1+\lambda} = \frac{3}{6} \cdot \frac{1+2\cdot 0.4}{1+0.4} = 0.644[m] \tag{5.12}$$

And finally the distance between the leading edge of the wing and the leading edge of the mean aerodynamic chord (LEMAC) can be determined using geometry in Equation 5.13 [37]

$$\tan(\Lambda_{LE}) = \frac{x}{y_{MAC}} \rightarrow x = 0.644 \cdot \tan(4.58) = 0.0516[m] \tag{5.13}$$

Overview of Wing Geometric Parameters

With all these parameters an initial wing shape can be devices. In Table 5.3 as summary of the relevant parameters is provided and in Figure 5.1 a top view of the wing can be easily visualised.

Table 5.3: Wing geometric parameters.

Parameter	Symbol	Value	Units
Wing Surface Area	S	0.845	$[m^2]$
Wing Span	b	3	$[m]$
Aspect Ratio	AR	10.7	[-]
Taper Ratio	λ	0.4	[-]
Wing Sweep	$\Lambda_{c/2}$	0	[°]
Wing Twist	α_{twist}	-3	[°]
Dihedral Angle	$\Gamma_{c/2}$	5	[°]
Thickness-to-Chord Ratio	t/c	0.117	[-]
Root Chord Thickness	t_r	0.072	$[m]$
Tip Chord Thickness	t_{tip}	0.029	$[m]$
Root Chord Length	c_r	0.401	$[m]$
Tip Chord Length	c_t	0.161	$[m]$
Mean Aerodynamic Chord	c_{MAC}	0.298	$[m]$
spanwise MAC location	y_{MAC}	0.644	$[m]$

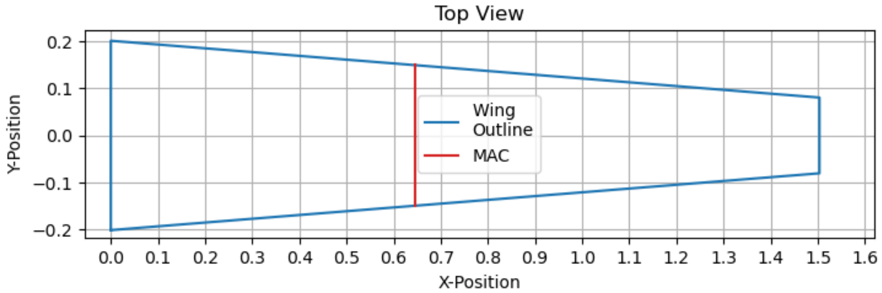

Figure 5.1: Top view of right wing.

5.1.3. High Lift Devices Sizing

High lift devices (HLDs) are moving surfaces that are used at both the leading and trailing edge of the wing during take-off and landing to increase the lift generated. Thus, in order to ensure that the Fixed-Wing drone performance during these important phases of the flight is at an acceptable level, the HLDs have to be properly chosen and sized, which will be done in the coming section. The $\Delta C_{L\,\text{max}}$ that the HLDs can provide is calculated using Equation 5.14. [37]

$$\Delta C_{L\,\text{max}} = 0.9\Delta C_{l\,\text{max}}\frac{Swf}{S}\cos\Lambda_{\text{hinge-line}} \tag{5.14}$$

In this equation $\Delta C_{l\,\text{max}}$ is a function of the selected HLD technology, Swf is the reference flapped surface area as seen in Figure 5.3, S is wing surface area of $0.845[m^2]$ and Λ_{hinge} is either the angle at the leading edge spar located at $0.15c$ or the trailing edge spar located at $0.7c$. The $\Delta C_{l\,\text{max}}$ for different HLDs can be seen in Figure 5.2.

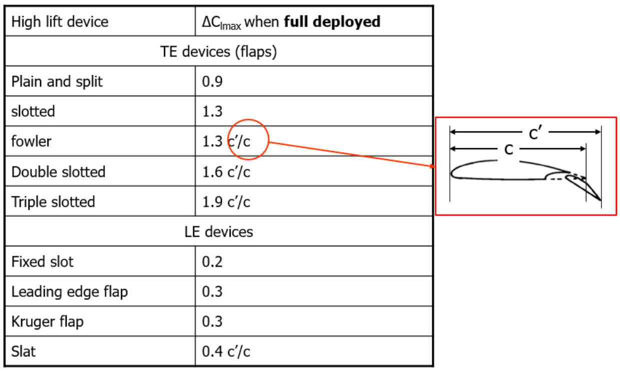

High lift device	$\Delta C_{l\text{max}}$ when **full deployed**
TE devices (flaps)	
Plain and split	0.9
slotted	1.3
fowler	1.3 c'/c
Double slotted	1.6 c'/c
Triple slotted	1.9 c'/c
LE devices	
Fixed slot	0.2
Leading edge flap	0.3
Kruger flap	0.3
Slat	0.4 c'/c

Figure 5.2: $\Delta C_{l\,\text{max}}$ of different HLDs technologies.

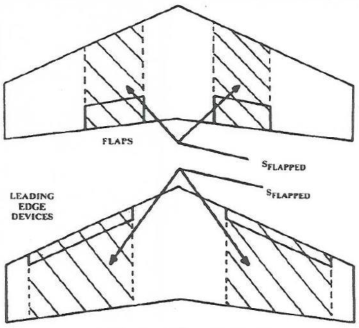

Figure 5.3: Reference wing flapped surface area for LE and TE HLDs.

The leading edge HLD that was selected was the Kruger flap due to the fact that it has a small footprint and thus a less complex deploying mechanism than the leading edge flap and slat. It also has a higher performance-to-weight ratio than the fixed slot leading edge HLD.

(a) Leading edge slot. (b) Slat. (c) Kruger flap. (d) Leading edge flap.

Figure 5.4: Leading Edge High Lift devices.

For the trailing edge HLDs only the plain, split and slotted HLDs were considered. Given the fact that the thickness-to-chord ratio of 11.7 [%] is relatively thin, implementing Fowler, double slotted or even triple slotted flaps would be quite difficult due to the fact the extra mechanism required to both rotate and translate the airfoil is quite complex and thus very heavy. The split flap was selected because it is less complex than the plain and slotted flaps and has an appropriate performance.

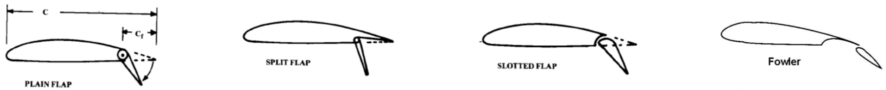

(a) Plain flap.

(b) Split flap.

(c) Single slotted flap.

(d) Fowler flap.

Figure 5.5: Trailing edge High Lift Devices.

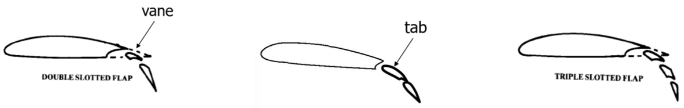

(a) Double slotted flap (vane).

(b) Double slotted flap (tab).

(c) Triple slotted flap.

Figure 5.6: Trailing edge High Lift Devices.

The most relevant values used in the calculations can be observed in Table 5.4 and the initial layout can be seen in Figure 5.7

Table 5.4: High Lift Devices parameters.

Parameter	Symbol	Value	Units
Location of LE Hinge-line wrt. Wing LE	$H_{line,LE}$	0.15	[-]
Location of TE Hinge-line wrt. Wing LE	$H_{line,TE}$	0.7	[-]
Reference Flapped Surface / S Ratio (LE HLDs)	$Swf_{LE,HLDs}$	0.824	[-]
Reference Flapped Surface / S Ratio (TE HLDs)	$Swf_{LE,HLDs}$	0.452	[-]
$\Delta C_{L_{max}}$ for fully deployed LE Kruger Flap	$C_{Lmax,LE}$	0.222	[-]
$\Delta C_{L_{max}}$ for fully deployed TE Plain Flap	$C_{Lmax,TE}$	0.366	[-]
$\Delta C_{L_{max}}$ for fully deployed HLDS	$C_{Lmax,HLDs}$	0.588	[-]
Stall Speed Clean Configuration	$V_{Stall,clean}$	19.5	[m/s]
Stall Speed for only LE deployed HLDs	$V_{Stall,HLDs}$	18.0	[m/s]
Stall Speed for only TE deployed HLDs	$V_{Stall,HLDs}$	17.2	[m/s]
Stall Speed for LE and TE deployed HLDs	$V_{Stall,HLDs}$	16.2	[m/s]

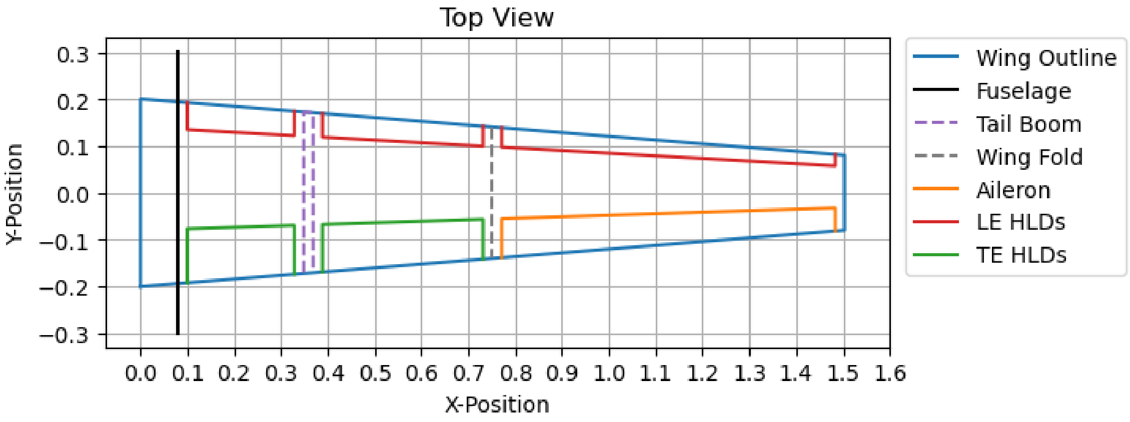

Figure 5.7: Top view of wing with LE and TE HLDs and ailerons.

After analysing the results of the calculations, the design team came to the conclusion that only the leading edge HLDs are really needed if the top speed of the recovery multi-copter was increased from 18 $[ms^{-1}]$ to 25 $[ms^{-1}]$. Although the stall speed of the Fixed-Wing with only leading edge HLDs is 18 $[ms^{-1}]$ some margin is required around the stall speed during recovery operations. This would result in considerable weight savings in the wing structure due to the fact that the wing would need less reinforcement to accommodate the rear moving surfaces as you would no longer need a rear spar at $0.7c$ near the root chord whereas the increased weight of the multi-copter to handle the new top speed was not as drastic. The final updated control surface layout can be found in Figure 5.9, where the size of the ailerons is further narrowed down.

5.1.4. Aileron Sizing

Ailerons are used to provide roll control over an aircraft. They should provide a sufficient roll rate, minimise the effect of adverse yaw and avoid the effects of aileron reversal.

The aileron that deflects downwards increases the local angle of attack, increasing the lift force. The one that deflects upwards creates a downwards lift vector. This two forces create a moment that rolls the aircraft in the desired direction. However aileron deflection gives rise to counter-productive effects too. The aileron that deflects upwards increases the induced drag at that location of the wing, resulting in a yaw movement in the direction of the up going wing. This effect should be minimised by the aileron design. One way to accomplish this is to place the ailerons closer to the fuselage. This results in a decrease in the moment arm that leads to the yawing moment. Another counterproductive effect induced by aileron deflection is aileron reversal also known as adverse yaw. At high speeds, the torque moment on the wing can twist the wing such way that the increased lift generated by this new incidence angle counteracts the extra lift generated by the aileron, thus creating a rolling moment in the opposite direction.

In order to size the ailerons, first the spanwise locations of the start and end positions of the aileron are selected. Then the aileron chord to wing chord ratio is computed, taking into consideration that some room between the aft wing spar and the aileron leading edge needs to be left out to accommodate the mechanism needed to move them. Finally, An estimation is made regarding the maximum aileron deflection is made, the value selected is 20 [°]. The next step to size the ailerons is to calculate the rolling moment coefficient. This is done with Equation 5.15. [37] The rolling moment coefficient is a measure of how much the rolling moment changes with a change in aileron deflection, that is why this derivative is also commonly known as the aileron effectiveness.

$$C_{l_{\delta a}} = \frac{2c_{l\alpha}\tau}{S_{ref}b}\int_{b_1}^{b_2} yc(y)dy \tag{5.15}$$

Another important coefficient that can be calculated is the roll damping coefficient. When the aircraft rolls, the vertical speed of the wing induces an increase in the angle of attack at the down-going wing and a decrease at the up-going wing. This creates a change in lift that counteracts the rolling moment. The roll damping coefficient can be calculated using Equation 5.16. [37]

$$C_{l_P} = -\frac{4(c_{l\alpha} + c_{d_0})}{S_{ref}b^2}\int_{0}^{b/2} y^2c(y)dy \tag{5.16}$$

In Equation 5.15 [37] and Equation 5.16 [37] C_{l_P} is the roll damping coefficient, and $C_{l_{\delta a}}$ is the rolling moment coefficient, also known as aileron effectiveness. $c_{l\alpha}$ is slope of the airfoil lift curve, and c_{d_0} the airfoil zero lift drag coefficient. S_{ref} is the area of the portion of the wing where the ailerons are placed and b is the wingspan. τ is the aileron effectiveness, which depends on the aileron chord to wing chord ratio, which can be obtained from Figure 5.8. $c(y)$ is the wing chord at a certain spanwise location y.

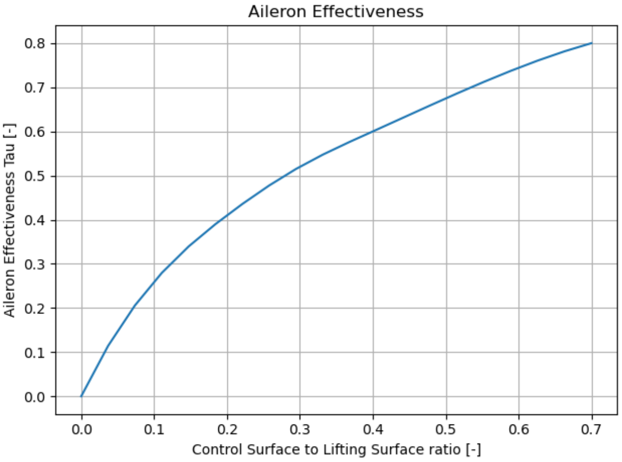

Figure 5.8: Aileron effectiveness versus control surface to lifting surface ratio.

Once these two derivatives are known, the roll rate of the Fixed-Wing drone can be computed. This is done using Equation 5.17. [37] In this equation P is the roll rate, V is the flight speed, and δa_{max} is the maximum deflection of the ailerons.

$$P = \frac{-C_{l_{\delta a}}}{C_{l_P}} \delta a_{max} \frac{2V}{b} \tag{5.17}$$

Knowing the roll rate, the time take to roll a certain angle can be computed by simply dividing the angle by the roll rate. It is important to note that one has to be aware of the units used given the fact that the roll rate is computed in radians and the aileron deflection is commonly expressed in degrees.

Table 5.5: Aileron sizing parameters.

Parameter	Symbol	Value	Units
Aileron spanwise start Position	$ail_{y,b1}$	0.567	[-]
Aileron spanwise end Position	$ail_{y,b2}$	0.934	[-]
Control Surface to Lifting Surface Ratio	$Cs_{to}Ls$	0.288	[-]
Aileron Deflection	ail_θ	20	[°]
Aileron Control Derivative	$C_{l_{\delta a}}$	0.5907	[-]
Roll Damping Coefficient	C_{l_P}	-2.5282	[-]
Roll Rate	P	1.628	$[rads^{-1}]$
Time to Roll 90°	$t_{roll,90^\circ}$	0.965	$[s]$

The final layout of the control surfaces can be seen in Figure 5.9. Important to note is that the aileron length is smaller than the one displayed in Figure 5.7. This is due to the fact that the performance of the smaller aileron was deemed acceptable and thus some weight savings can be made on the wing structure.

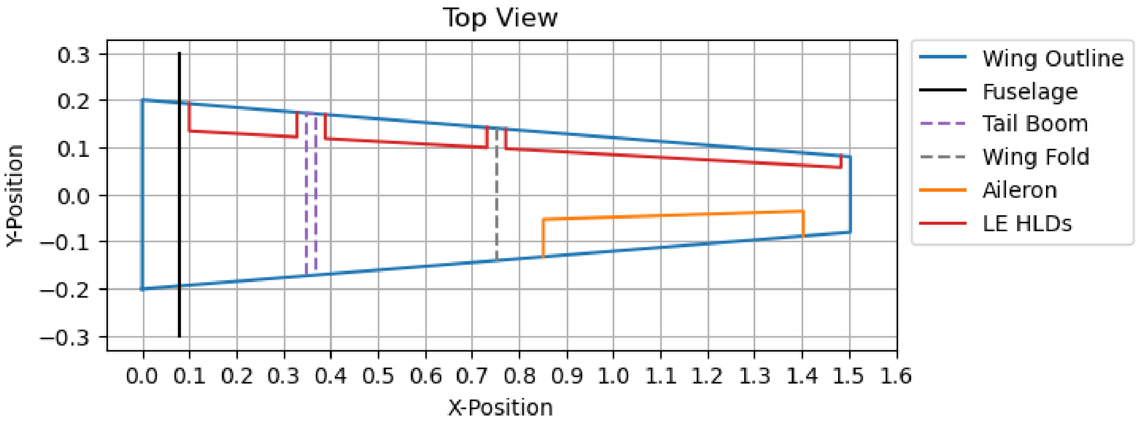

Figure 5.9: Top view of wing with final layout of the control surfaces.

5.2. Fuselage

The fuselage of an aircraft serves several important functions. It mainly provides structural integrity, acts as a streamlined body to reduce aerodynamic drag and it houses the internal components of the Fixed-Wing such as the battery, sensors and computing units, ensuring the proper functioning and integration of various subsystems.

5.2.1. Payload Placement & Integration

There are three main placement options to integrate a rotating camera into a drone fuselage to ensure the widest possible field of view. The camera can either be placed on the centreline of the nose/tail-cone, at the belly of the fuselage or a mixture of both such as the pan-tilt configuration. This can be better visualised in Figure 5.10.

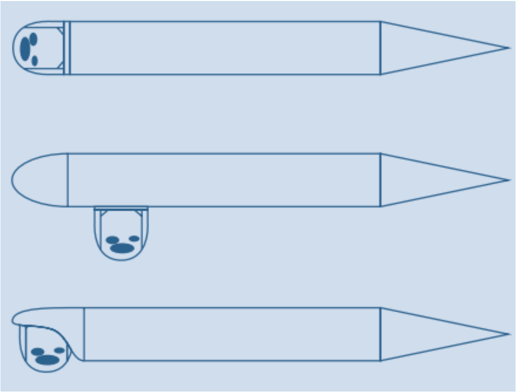

Figure 5.10: Possible camera placements; Integrated Roll-tilt, Belly pan-tilt and Partially faired pan-tilt Configuration.

Given the fact that the Mantis camera lacks an appropriate aerodynamic housing, placing it at either the nosecone or at the belly of the fuselage would cause a lot of drag. Therefore the next logical option is to place it at the tail. This is more aerodynamic given the fact that a lightweight partial housing for the camera can be designed without resulting in a large increase in fuselage diameter since the whole camera does not need to be fully enclosed. This is also compatible with the propeller placement as it can be either placed at the front or at the wings. Placing the camera at the back is also compatible with the $45[^\circ]$ scanning angle. The camera can rotate forwards at $40[^\circ]$, $70[^\circ]$ side to side and more than $90[^\circ]$ backwards with respect to the downwards direction, with no interference between the sensors and the fuselage.

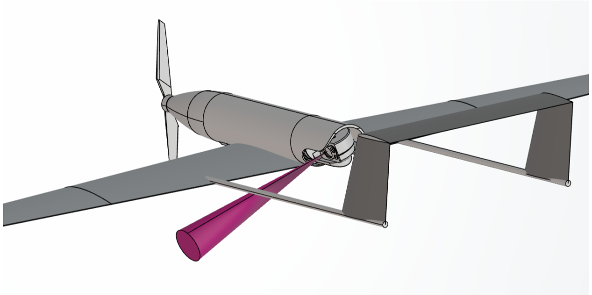

Figure 5.11: Camera tilted at $70[°]$ with the $11[°]$ FOV cone displayed in red.

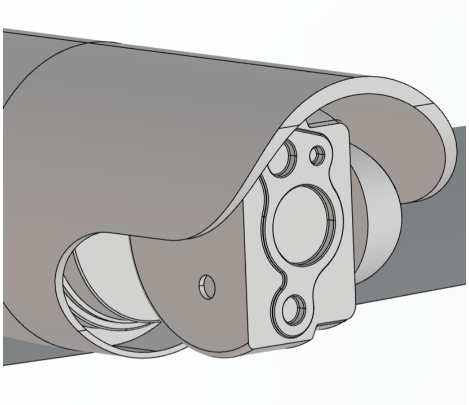

Figure 5.12: Camera housing.

5.2.2. Fuselage Shape

The layout of the internal components of the Fixed-Wing is the main factor determining the dimensions of the fuselage. The main component driving the diameter of the fuselage is the Mantis camera, with a diameter of around 131 $[mm]$. The main component driving the length of the fuselage is the battery with a length of 525 $[mm]$. This leads to an overall fuselage length of 990 $[mm]$ and a fuselage diameter of 160 $[mm]$. A cylindrical shape for the fuselage was selected to reduce the external surface area and thus reduce skin friction drag. An external view of the fuselage can be seen in Figure 5.13. Special care was also taken to ensure that there were no drastic changes in curvature to prevent flow separation.

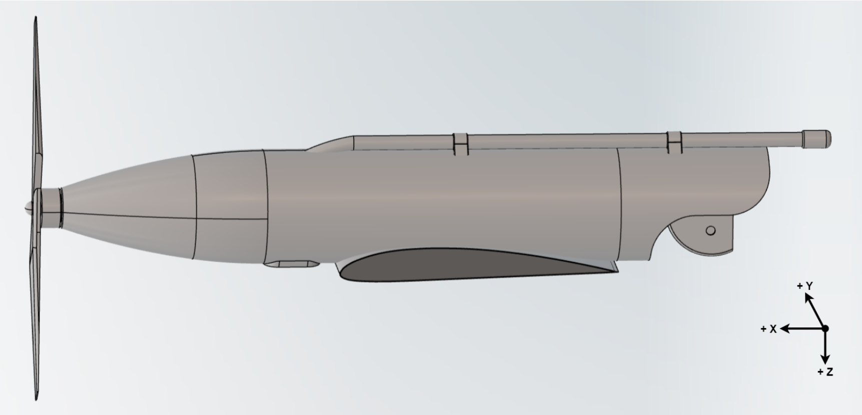

Figure 5.13: External view of fuselage.

5.2.3. Internal Component Layout

When sizing the fuselage, one has to also take into consideration the placement of the rest of the inner components and the layout of the structural support. In Figure 5.14 one can get a better view of the internal placement of the components. The rationale behind their positioning is the following:

- The internal space needs to be taken advantage of as much as possible
- There should be no interference between components

An example of this is the positioning of the magnetometer. The magnetometer is used to determine the relative orientation of the drone with the magnetic north pole, therefore it needs to be positioned far away from strong magnetic fields. This is why it is placed far away from the electrical motor and the metal plate used for coupling with the Multi copter. Another example of this is the antenna positioning. It was decided that an external placement was needed due to the fact that the carbon fibre skin of the fuselage would block the transmission if the antenna was placed inside.

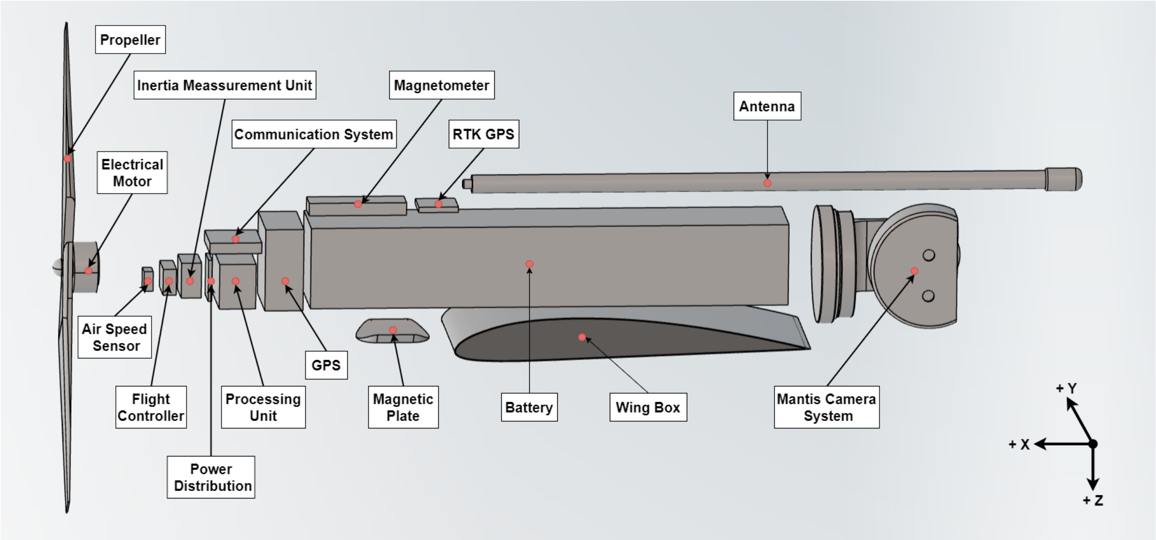

Figure 5.14: Internal view of fuselage components.

5.3. Empennage

The main functions of the empennage are establishing longitudinal stability, and providing yaw and pitch control during flight. The sizing of the empennage is performed following the initial sizing of the main wing, this sizing encompasses both the horizontal and vertical stabiliser. The methods used for the initial sizing have been taken from the course Aerospace Design and Systems Engineering Elements I, taught in the Bachelor in Aerospace Engineering at the Delft University of Technology [60].

The starting point of the empennage sizing is determining the centre of gravity location of the Fixed-Wing, as this position is a crucial factor in ensuring longitudinal stability. The position of the centre of gravity is calculated using Equation 5.18.

$$X_{cg} = \frac{\sum m \cdot x_{cg}}{\sum m} \tag{5.18}$$

Firstly, all the components and equipment required to perform the mission have to be identified. In Table 5.6 the individual subsystems, including their dimensions, mass and distance of the center of gravity of the component with respect to the nose cone of the Fixed-Wing, which is taken as the datum, are presented.

Table 5.6: Fixed-Wing system operational components and equipment.

Subsystem component	**Dimensions (wxlxh) [mm]**	**Weight [g]**	**Distance from datum [mm]**
Inertial Measurement Unit (IMU)	39x45x22	70	109.5
Magnetometer	33x14x107	15	283.5
Airspeed Sensor	22x22x22	3.5	61
Onboard Computer and Processing Unit	50x50x87	85	155
Power Distribution and Management	46x36x4	9	143
Flight Controller	44x29x14.5	22	92
GPS	91x42x91	332	225.5
RTK-GPS	43.5x43.5x3	6.8	225.5
Communication system	65x57x12	78	152.5
Battery	525x90x90	11700	492.5
Propulsion system	28x27.8x27.8	300	-10
Mantis i45N	187.4x64.03x64.03	750	848
Wing	401x3000x46.92	4990	580
Fuselage	170x780x170	2908	390

It is important to note that the empennage subsystem is omitted in the determination of the center of gravity location, the reason for this is that the weight and position of the empennage is a direct function of the center of gravity location. The resulting center of gravity location, X_{cg}, of the Fixed-Wing is 0.496 [m], considered from the nose cone.

The known position of the center of gravity enables the sizing of the horizontal and vertical stabiliser. In the Aerospace Design and Systems Engineering Elements I lecture slides[60] the method for calculating the empennage surface areas is presented. In Equation 5.19 and Equation 5.20 the respective formulas are shown.

$$V_h = \frac{(X_h - X_{cg}) \cdot S_h}{S \cdot \bar{c}} \tag{5.19}$$

$$V_v = \frac{(X_v - X_{cg}) \cdot S_v}{S \cdot b} \tag{5.20}$$

The horizontal and vertical tail volume coefficients, V_h and V_v respectively, have been obtained from literature. In Table 5.7 the volume coefficients for a number of aircraft categories can be seen, the average value of these has been used for the empennage sizing of the Fixed-Wing system.

Table 5.7: Horizontal and vertical tail volume coefficients of different aircraft categories.

Aircraft category	V_h	V_v
Sailplane	0.500	0.0190
Civil props		
Homebuilt	0.484	0.0380
Personal	0.593	0.0601
General aviation - single engine	0.672	0.0443
Average values	0.56225	0.04035

In order to obtain the initial surface areas, the longitudinal position of both the horizontal and vertical, X_h and X_v, tail have to be assumed. The position of the empennage will determine the moment arm, which influences the longitudinal stability characteristics of the Fixed-Wing. The value assumed for the position of the horizontal stabiliser is 1.53 [m], and for the vertical stabiliser, it is assumed that the position is slightly more forward at 1.43 [m] both with respect to the nose cone. With the positioning of the stabilisers finalised, the surface areas can be computed, this is done by rewriting Equation 5.19 and Equation 5.20.

The planform of the empennage is the final step in the horizontal and vertical stabiliser design. The equations presented in subsection 5.1.2 are used for this, as these both hold for main wings and stabilisers. In Table 5.8 the resulting parameter values for the horizontal and vertical stabiliser size can be found. The values for aspect ratio, taper ratio and leading edge sweep angle have been obtained by averaging out the ranged values presented in [60]. Additionally, the taper ratio of the horizontal stabiliser equalling 1.0, which dictates a rectangular wing planform, results from an empennage design choice that will be highlighted upon in subsection 5.3.1.

Table 5.8: Horizontal and vertical stabiliser size parameters.

Empennage parameter	**Horizontal stabiliser**	**Vertical stabiliser**
Aspect ratio [-]	4.0	1.5
Taper ratio [-]	1.0	0.5
Surface area [m^2]	0.13	0.052
Span [m]	0.72	0.279
Root chord [m]	0.18	0.248
Tip chord [m]	0.18	0.124
Leading edge sweep angle [°]	0	25

5.3.1. Tail Layout

The final step in the empennage design is opting for a suitable tail layout. Tail designs come in a large variety, each optimised for a different aspect of flight or mission. In Figure 5.15 an overview of a selection of different tail designs is shown.

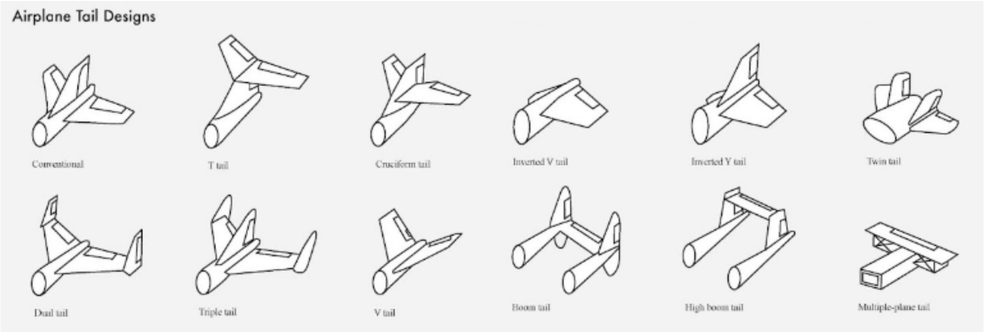

Figure 5.15: Variety of possible tail design layouts [14].

In section 5.2 it is described that the fuselage embodies all of the required hardware to perform the mission, additionally, the positioning of the propulsion system in the front and the Mantis i45N payload aft in the fuselage is justified. Considering the preliminary layout of the fuselage, a number of tail layout designs are deemed infeasible, this is mainly due to the limited space for connecting structures between the fuselage and empennage, and the possible obstruction of the field of view of the camera due to such structural components.

In order to have a clear view of the search area, it has been decided by the team that the boom tail designs would have the highest probability of being successful in this aspect. Additionally, the booms aid in distributing the forces generated by the control surfaces present on the empennage, hence making the Fixed-Wing system more controllable [1].

For these reasons, the conventional tail designs have been disregarded for the rest of the design phases. The remaining tail design options are the boom configurations, which consider either the boom tail or the high boom tail. The team has selected the high boom tail for the preliminary design of the Fixed-Wing system, mainly because it does not have the horizontal stabiliser obstructing the view of the camera in any way. In addition, with this design choice, the horizontal stabiliser will be clear of the wake created by the propeller, which increases the effectiveness of the control surfaces on the empennage.

5.4. Aerodynamic Analysis

Performing an aerodynamic analysis is essential in assessing the aerodynamic characteristics of the Fixed-Wing system, it also allows the justification of first-order calculations performed for a number of aircraft parameters such as lift and drag coefficients.

5.4.1. Aerofoil Selection

The aerofoil selection is the first step in deriving the aerodynamic features, in achieving this, the team has selected a set of aerofoils from literature that will be analysed in more detail. The selected aerofoils are widely used in radio-controlled aircraft designs, thus opting for these seems appropriate due to the similar dimensions and operating conditions. The chosen aerofoil set consists of the following:

- *Clark Y*
- *SD7037-092-88*
- *MH 32*
- *S3010-103-84*
- *E205*
- *NACA 2412*

The operational conditions have to be considered in order to compare the capabilities of the aerofoils and select the most suitable for the Fixed-Wing system. The Reynolds number is a useful quantity describing the flow

---

[1] URL:https://simpleflying.com/twin-boom-aircraft-pros-cons-guide/ [Cited: 19-06-2023]

regime over objects, it can be calculated using Equation 5.21, where L describes the characteristic length of the object, which in the case of aircraft is taken as the chord length, and μ being the dynamic viscosity in Pascal-seconds $[Pa \cdot s]$.

$$Re = \frac{\rho \cdot L \cdot V}{\mu} \tag{5.21}$$

In the light of selecting the most suitable aerofoil for the main wing, there are three chord lengths of interest, namely the root chord, the tip chord and the mean aerodynamic chord. The freestream velocity, V, is taken to be 30 $[ms^{-1}]$, which is the cruise velocity of the Fixed-Wing system. The fluid's density is taken equal to the density of air at the operational altitude of the Fixed-Wing, the air density at an altitude of 450 $[m]$ is equal to 1.173 $[kg \cdot m^{-3}]$. The resulting Reynolds numbers at the three chord lengths of interest are presented in Table 5.9.

Table 5.9: Reynolds number for the different chord lengths of interest.

Chord description	**Chord length [m]**	**Reynolds number [-]**
Root chord	0.401	780424.94
Mean aerodynamic chord	0.298	579744.24
Tip chord	0.161	312169.98

The aerofoils are analysed using the XFLR5 software, which is used to design and simulate the performance of wings and aircraft at low Reynolds numbers. The aerofoils are analysed for the aforementioned range of Reynolds numbers, and for a sequence of angles of attack between -10 [°] and 20 [°]. The lift coefficient versus angle of attack and the lift coefficient versus drag coefficient polars are shown in Figure 5.16.

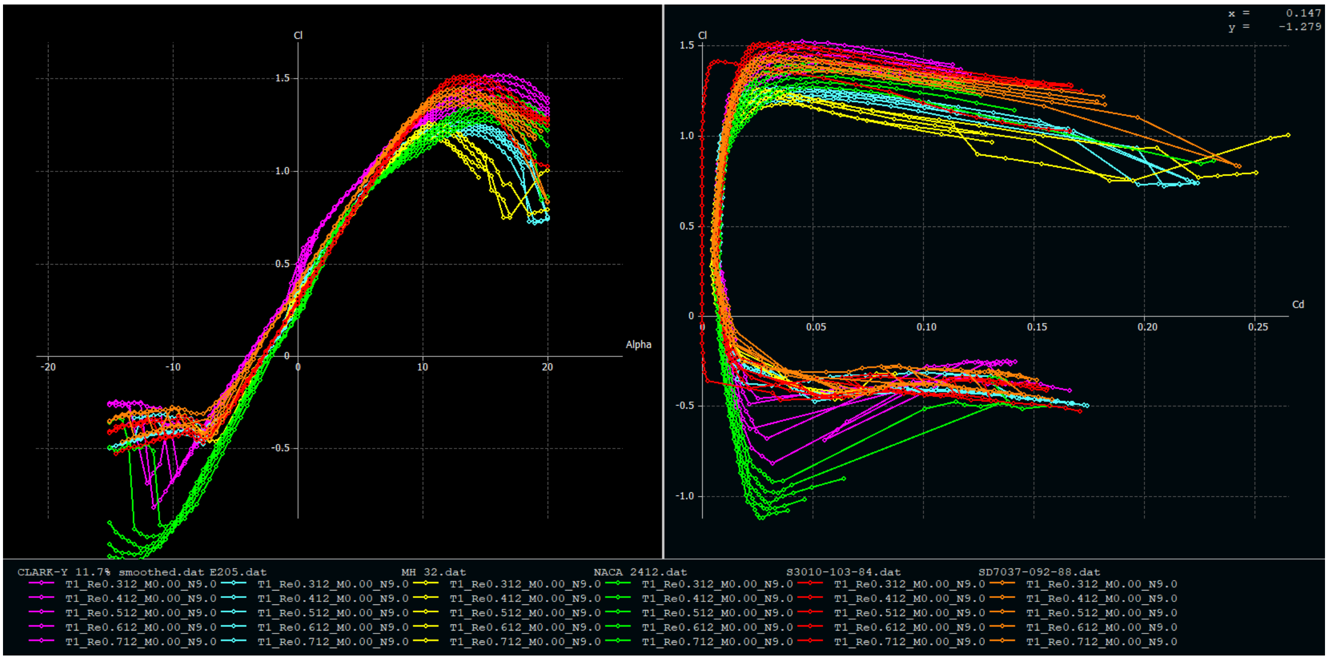

Figure 5.16: C_l versus angle of attack and C_l versus C_d polars for a range of aerofoils.

Based on the initial aerodynamic analysis performed on the aerofoils, the selected aerofoil for the main wing of the Fixed-Wing is the Clark Y. The reason for this is that it outperforms the rest of the aerofoils based upon stall characteristics, it has the highest lift coefficient in combination with the highest stall angle of attack. In addition, the Clark Y aerofoil has been widely used in aeronautical applications, and radio-controlled aircraft designs, and is much studied in aerodynamics [44].

Following the aerofoil selection for the main wing, the aerofoil that will operate on the empennage is selected. The function of the horizontal stabiliser is to provide longitudinal stability and control in the pitch direction. To ensure longitudinal control in both positive and negative directions, the horizontal stabiliser has to be able to provide both positive lift and negative downforce. The common method to achieve this is opting for an aerofoil that is symmetric around its chord, this enables the horizontal stabiliser to provide lift at positive angles of attack, and downforce at negative angles of attack. To comply with the aforementioned requirements, the team has chosen the NACA 0010 aerofoil for the empennage.

In Figure 5.17 the lift coefficient versus angle of attack, and the lift coefficient versus drag coefficient polars are shown for the NACA 0010 aerofoil, the considered operational conditions are equivalent to the conditions used in Figure 5.16. In addition, a cross-sectional view of the two chosen aerofoils can be seen in Figure 5.18.

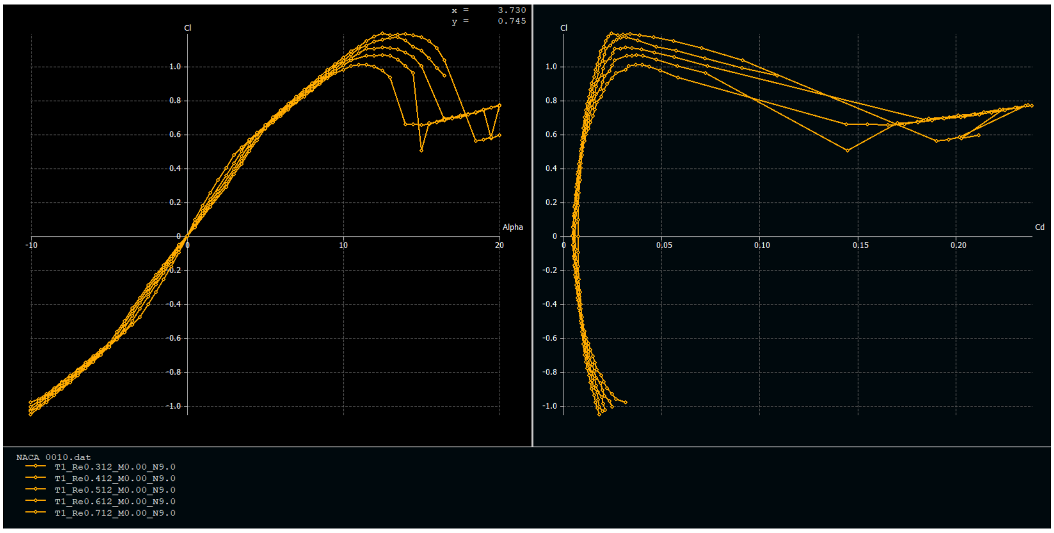

Figure 5.17: C_l versus angle of attack and C_l versus C_d polars for the NACA 0010 aerofoil.

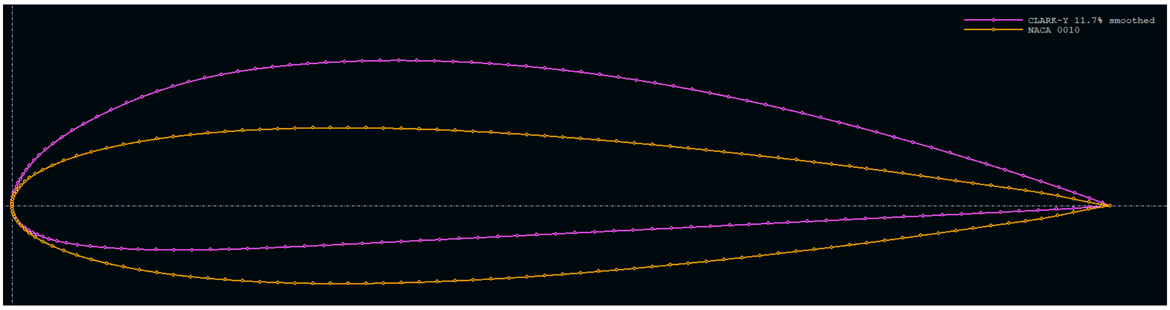

Figure 5.18: Cross-sectional view of the chosen Clark Y and NACA 0010 aerofoils.

5.4.2. Wing Aerodynamic Analysis

Firstly, the wing by itself is analysed, the main reason for this is to reduce the risk of any discrepancies induced by the interaction of the main wing with the empennage. Having completed the aerofoil selection, the wing planform can be included in the aerodynamic analysis software XFLR5. The wing has first been discretised into a large number of panel sections. The three possible analysis methods are then applied to the discretised surfaces, these include the lifting line theory (LLT), vortex lattice method (VLM) and the 3D panel method. The three analysis modes can both be applied taking into account the fluid's viscous effects, or these can be neglected resulting in an inviscid analysis. Flow separation resulting in stall behaviour of the wing can only be calculated and visualised if the flow is viscous. In order to obtain the most accurate aerodynamic results, all of the subsequent analyses have been performed using the viscous flow configuration.

In Figure 5.19, the resulting polars for the three-dimensional wing are presented. The conditions for the polars are taken equally as the ones considered in the aerofoil selection as discussed in subsection 5.4.1. Some interesting results can be obtained from the polars, considering the CL/CD versus alpha curve it can be seen that the optimal lift-to-drag ratio is obtained at small angles of attack ranging between 1.0 [°] and 1.5 [°]. Furthermore, dissimilarities between the three methods are also visible in the polars. Especially, the shortcoming of the 3D panel and vortex lattice method in the C_L versus alpha curve, at angles of attack above 10 [°] is obvious. This is the result of the working principles behind these two modes, the limitations of these analyses will be discussed therefore briefly.

First considering the vortex lattice method, this algorithm is linear and assumes an inviscid flow. The viscous variables are obtained by interpolation of the calculated parameters that can be derived by integrating the surface forces on the panels. Unfortunately, this method poses some issues for angles of attack approaching the stall regime, which can be clearly seen in Figure 5.19. Secondly, the 3D panel method is a more sophisticated version of the vortex lattice method. The 3D panel method incorporates the wing's thickness, whereas the VLM only considers the mean camber line. However, the working principle behind the 3D panel method is the same as used in VLM, therefore, the stall characteristics of the wing are not properly accounted for. In general, the lifting line theory provides the best insight into viscous drag and is, therefore, able to provide a better estimate of the behaviour around stall conditions at higher angles of attack [61].

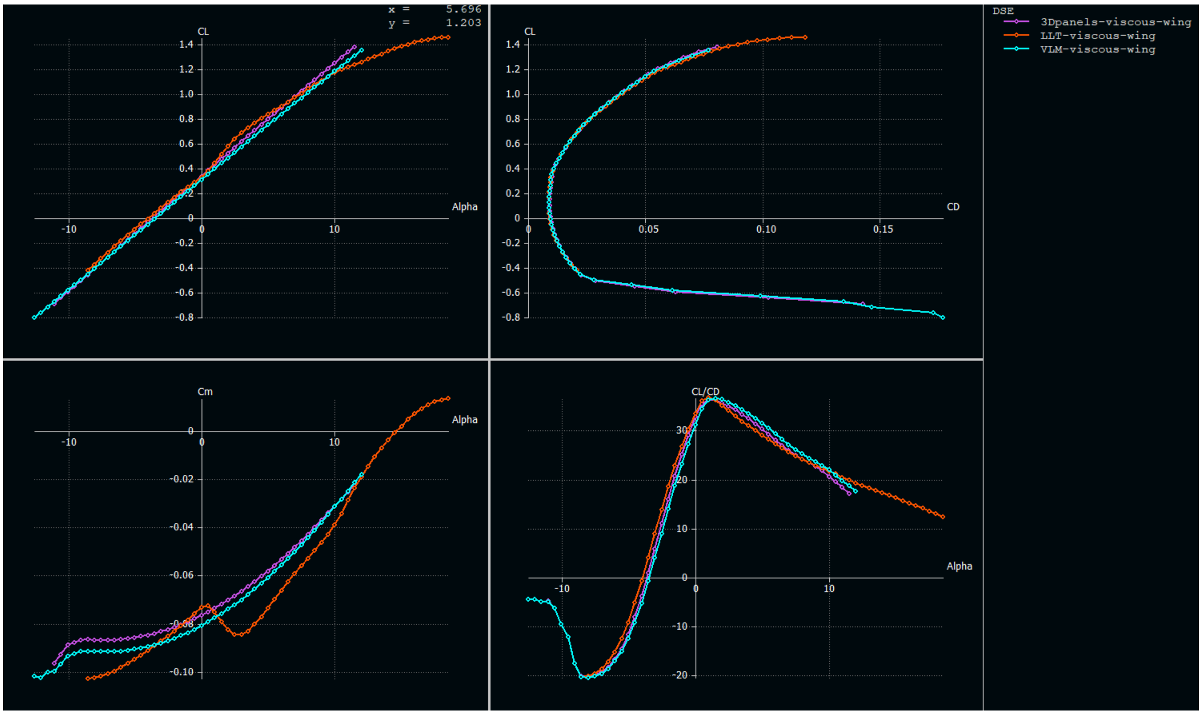

Figure 5.19: Set of aerodynamic polars for the three-dimensional wing.

5.4.3. Wing and Empennage Aerodynamic Analysis

The final step in the aerodynamic analysis is including the empennage in the XFLR5 software. The analysis modes are rather limited when the empennage is included, the only possible algorithm that can be applied is the vortex lattice method.

In Figure 5.20 similar polars as seen in Figure 5.19 are presented. The two figures show a lot of similarities, the most interesting graph to highlight is the C_m versus alpha curve. This curve possesses a positive gradient for all three analysis methods in Figure 5.19, while in Figure 5.20 it is a negative gradient. This exact difference is actually one of the fundamental reasons for including an empennage to an aircraft, and it is the working principle of longitudinal stability for the Fixed-Wing system, this will be discussed in more detail in section 5.5. In Figure 5.21 the main wing including the empennage is visualised, the purple lines indicate the stream flow around the wing and the coloured arrows present the pressure forces acting.

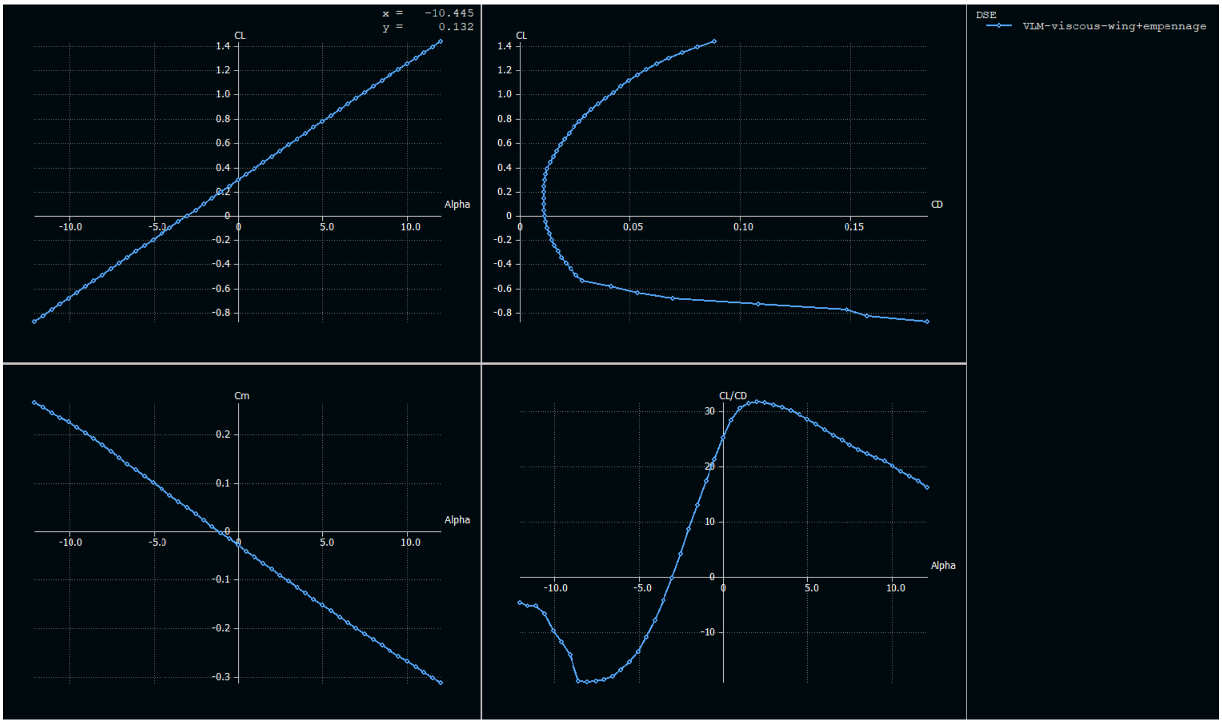

Figure 5.20: Set of aerodynamic polars for the three-dimensional wing including empennage.

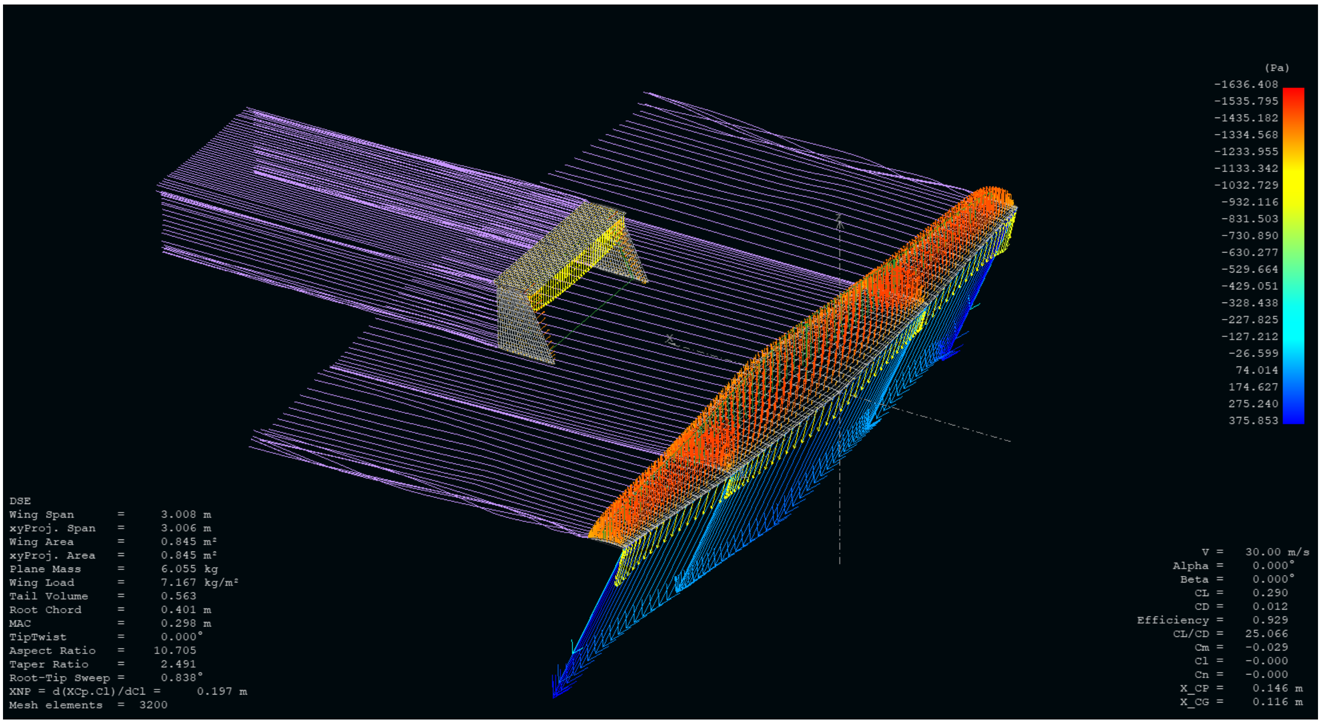

```
DSE
Wing Span      =    3.008 m
xyProj. Span   =    3.006 m
Wing Area      =    0.845 m²
xyProj. Area   =    0.845 m²
Plane Mass     =    6.055 kg
Wing Load      =    7.167 kg/m²
Tail Volume    =    0.563
Root Chord     =    0.401 m
MAC            =    0.298 m
TipTwist       =    0.000°
Aspect Ratio   =   10.705
Taper Ratio    =    2.491
Root-Tip Sweep =    0.838°
XNP = d(XCp.Cl)/dCl =     0.197 m
Mesh elements  =  3200
```

```
         V =   30.00 m/s
     Alpha =    0.000°
      Beta =    0.000°
        CL =    0.290
        CD =    0.012
Efficiency =    0.929
     CL/CD =   25.066
        Cm =   -0.029
        Cl =   -0.000
        Cn =   -0.000
      X_CP =    0.146 m
      X_CG =    0.116 m
```

Figure 5.21: Visualisation of the wing and empennage in a stream flow.

5.5. Stability Analysis

Ensuring static longitudinal and lateral stability is of great importance in the preliminary design phases of a Fixed-Wing aircraft. In this section, a detailed analysis of the stability characteristics of the Fixed-Wing system is presented. The XFLR5 software is used for this, as it has a built-in stability analysis tool.

5.5.1. Stability Prerequisites

In order to verify whether the Fixed-Wing system shall be able to provide stability, two prerequisites for stability can be identified and checked in previously shown polars. The two prerequisites that should be verified before running the stability analysis in XFLR5 are the following:

- Negative gradient in the C_m versus angle of attack curve.
- Positive C_m value at C_L equal to zero.

Firstly, the negative gradient in the C_m versus angle of attack curve. The pitching moment coefficient C_m is defined such that a positive moment would lead to a pitch up rotation of the Fixed-Wing system. To achieve static longitudinal stability, the Fixed-Wing aircraft needs to produce a nose down pitching moment, hence negative, if the angle of attack is increased. Therefore, the gradient in the C_m versus angle of attack curve has to be negative [43].

Secondly, the positive value for the moment coefficient at the point where the lift coefficient is equal to zero is the second prerequisite for longitudinal static stability of the Fixed-Wing aircraft. This indicates that if the wing is not generating any lift, the aircraft still maintains a positive pitching moment, hence a nose up rotation [43]. The two polars that are used to verify the prerequisites are presented in Figure 5.22. Both the initial static stability requirements are met, hence the more thorough stability analysis is performed using XFLR5.

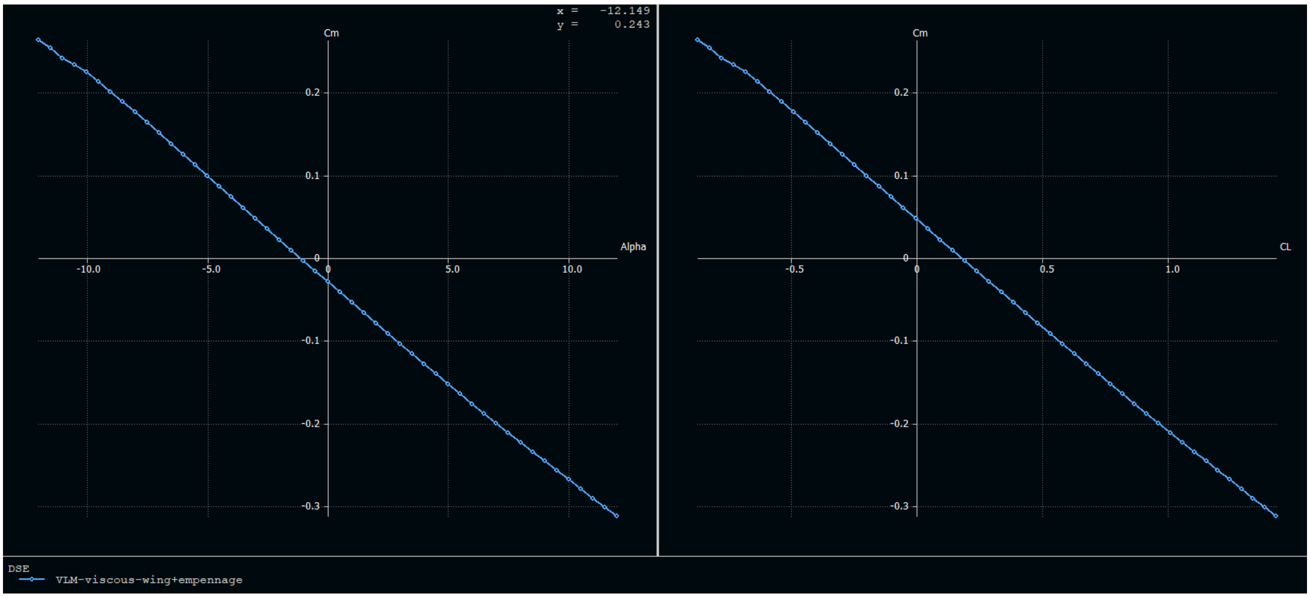

Figure 5.22: C_m versus angle of attack, and C_m versus C_L curve used to verify initial static longitudinal stability.

5.5.2. XFLR5 Stability Analysis

The built-in XFLR5 stability analysis tool provides stability coefficients for both longitudinal and lateral motion. In aircraft's stability analysis, five different eigenmodes can be characterised, these are the following:

- **Longitudinal eigenmodes:**
- Phugoid
- Short period
- **Lateral eigenmodes:**
- Dutch roll
- Spiral
- Aperiodic roll

The five eigenmodes depict different types of behaviour of an aircraft, the eigenmodes and stability characteristics of Fixed-Wing systems have been widely studied. The Bachelor Aerospace Engineering course Flight

Dynamics presents a very in-depth analysis of the numerous eigenmodes, based on the lecture notes, a brief description of the eigenmodes shall be given to gain a better understanding of the stability of Fixed-Wing aircraft [39].

Firstly, the two longitudinal eigenmodes. The phugoid manoeuvre is characterized by long, slightly damped oscillations of velocity and pitch while maintaining a constant angle of attack. The motion is induced by a small elevator deflection for around five seconds.

The short period manoeuvre is a very short response, in the order of a few seconds, to an elevator deflection input. The response is heavily damped, resulting in almost no visible oscillations. Due to the short period's brief time, this eigenmode has no effect on the velocity of the aircraft. Following the two aforementioned longitudinal eigenmodes, the three remaining lateral eigenmodes are also briefly highlighted to gain a better understanding of the working mechanism of the XFLR5 stability analysis.

The Dutch roll manoeuvre is an asymmetric response to an oscillatory rudder defection. This input into the rudder system causes a yawing motion, which in turn, induces roll. The manoeuvre should be stable and oscillate rapidly.

The aperiodic roll is induced by a deflection of the ailerons, causing a steady, constant rolling motion. The ailerons are however not returned to their neutral position, at 0 [°] deflection, but the pilot deflects the ailerons in the opposite direction to not induce a spiral motion. Instead, the aircraft steadily rolls back, this eigenmode does not show any oscillatory behaviour.

Finally, the spiral manoeuvre, is the only unstable manoeuvre that is allowed to be performed. This eigenmode, in which the ailerons are deflected induces a roll motion of the aircraft, which causes a yaw motion as well. The ailerons are deflected slightly resulting in a constant increase in roll angle. The eigenmode is unstable because, without any action undertaken, the roll angle would increase until non-recoverable angles. The aircraft is allowed to have an unstable spiral motion, mainly as the period of this motion is very long, hence the pilot can easily recover as soon as this eigenmode is induced.

The abovementioned eigenmodes are simulated using the XFLR5 software. The results of this analysis will be discussed in subsection 5.5.3

5.5.3. XFLR5 Stability Analysis Results

The easiest way to identify stability, or possibly instability, is by considering the corresponding eigenvalues to the individual eigenmodes. The eigenvalues of a system are equal to the poles known in control theory, the location of poles dictates the stability behaviour of the system. The eigenvalues that have a positive real part, hence they are located on the right-hand side of the imaginary axis, will result in instability. The eigenvalues for the longitudinal and lateral eigenmodes are presented in Table 5.10, for visualisation purposes the poles-zero plot of these eigenvalues are given in Figure 5.23a and Figure 5.23b.

Table 5.10: Static longitudinal and lateral eigenvalues corresponding to five characterising eigenmodes.

Longitudinal eigenmodes:	Eigenvalue
Phugoid	-0.00225 ± 0.242i
Short period	-10.343 ± 19.349i
Lateral eigenmodes:	
Dutch roll	-1.568 ± 10.799i
Spiral	0.0107 ± 0.0i
Aperiodic roll	-27.170 ± 0.0i

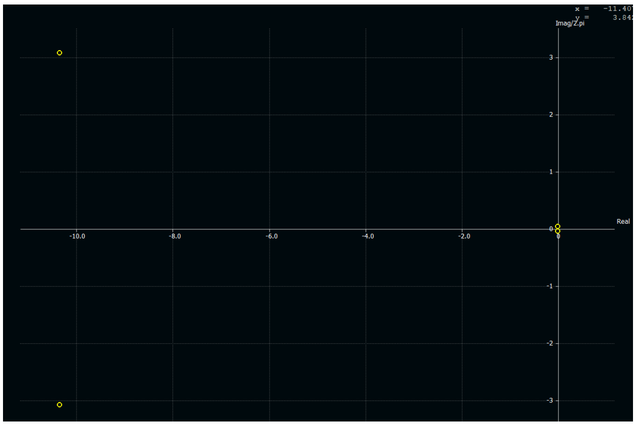

(a) Static longitudinal eigenmode corresponding eigenvalues.

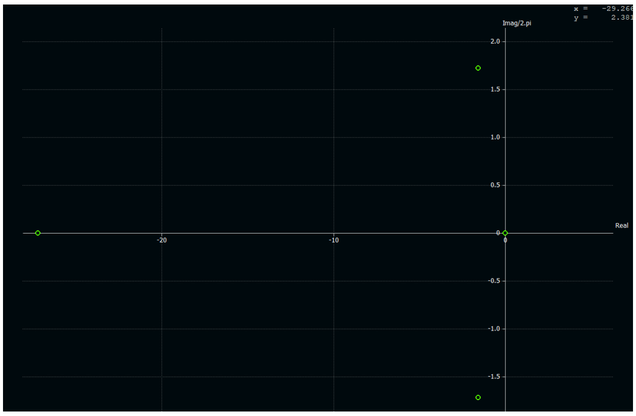

(b) Static lateral eigenmode corresponding eigenvalues.

Considering the presented eigenvalues, a number of interesting remarks can be made. It can be seen that the phugoid, short period and Dutch roll eigenmodes all have a non-zero imaginary part, this indicates that these eigenmodes show oscillatory behaviour over time. The spiral and aperiodic roll are purely real values, hence these eigenmodes are not oscillatory, as described previously. The final remark is with regards to the spiral eigenmode, as it can be seen, this eigenvalue is real and positive, hence it is unstable. This particularity is described previously and is in line with what is expected of this lateral eigenmode.

Concluding, it can be seen that the Fixed-Wing system ensures both static longitudinal and lateral stability.

5.6. Power and Propulsion System Sizing

5.6.1. Propulsion System

Thrust calculation

The propulsion system must be capable of providing the necessary thrust during cruise and other manoeuvres. The Fixed-Wing is specifically sized for level flight during cruise flight, serving as an assumption for propeller sizing. To initiate the initial sizing of the propulsion subsystem, the thrust required during cruise conditions is calculated based on the assumption of level flight. Given a constant airspeed assumption, the Fixed-Wing is in equilibrium. The cruise lift coefficient is then determined using Equation 5.22. The Fixed-Wing's cruise velocity is set at 30 [$m \cdot s^{-1}$], and the air density at the operational altitude of 450 m is 1.173 [kg$\cdot m^{-3}$]. The weight considered during cruise conditions is the maximum take-off weight of the Fixed-Wing. The calculated cruise lift coefficient amounts to 0.5479.

$$C_{L_{cruise}} = \frac{2W}{\rho V_{cruise}^2 S} \tag{5.22}$$

From this calculated C_L the corresponding C_D can be found from the C_L vs C_D curve in Figure 5.19. From the graph, the corresponding value of C_D at the cruise conditions is 0.0394. In Equation 5.23, the relation for calculating the required thrust at level flight is presented. With the values known, the thrust required during cruise can be calculated, assuming steady and symmetrical flight, is 17.57 [N].

$$T_{req} = \frac{C_D}{C_L} \cdot W \tag{5.23}$$

From this thrust value, a rough estimate of power consumption during cruise conditions can be calculated using Equation 5.24

$$P_{motor} = \frac{T_{req} V_{cruise}}{\eta_{motor} \eta_{prop}} \tag{5.24}$$

Assuming a total system efficiency of 0.6, the required power is found to be 878.5 [W]. From this power value, a statistical relationship between the power consumption and the propeller diameter can be calculated using Equation 5.25 [48]:

$$D = 0.55\sqrt[4]{\frac{P_{motor}}{1000 \cdot N}} \tag{5.25}$$

where N is the number of propellers and D is the diameter of the propeller. With only 1 propeller present and the power consumption known, it is estimated that the propeller diameter will be around 53.2 $[cm]$. A literature study is then conducted to review COTS available for our design criteria. A list of propulsion systems, all complete with a motor, propeller, and electrical speed controller (ESC), fitting the design requirements was created to evaluate the options available to be used in the drone.

Component Selection

After the required thrust calculation and the rough propeller diameter estimate, the components of the propulsion system can be chosen. The components are selected based on efficiency, thrust generation and weight. As this required thrust is an estimate, it should not equal the maximum throttle thrust of the propulsion system in order to leave redundancy in the system. The components that there were found on the market are presented in Table 5.11. The components are compatible and can generate the required thrust at 40% throttle. The motor efficiency of the system is 0.80. The diameter of the propellers is 22 $[in]$, which is equal to 55.88 $[cm]$ and the pitch of the propellers is 6 $[in]$ which is 15.24 $[cm]$ [58].

Table 5.11: A table showcasing the components for the propeller and its weight [49].

Component	Description	Weight $[g]$
Motor	T-Motor MN501S	170
Propeller	T-Motor NS22x66	34
ESC	KDE Direct KDEXF-UAS55	32

Regarding the battery, the Amprius Lithium-Ion Silicon Battery [2] is used. The commercially available battery has a specific energy density of 450 $[Wh \cdot kg^{-1}]$ and 1150 $[Wh \cdot L^{-1}]$. This technology outperforms the other battery technologies and is more flexible than fuel cell technology. With battery packs, the power requirements can be adjusted by modifying the number of batteries in series and/or parallel. In contrast, fuel cells lack this capability. Furthermore, fuel cells require storing hydrogen in pressurized tanks, adding complexity to the system. Hence it was decided by the design team to use lithium-ion batteries rather than hydrogen fuel cells.

Propulsion Paramaters

As the components are defined for the propulsion system, the power and endurance calculations can be performed. The equations that are used are Equation 5.26 and Equation 5.27.

$$P_{motor} = \frac{T_{req}V_{cruise}}{\eta_{motor}\eta_{prop}} \tag{5.26}$$

$$endurance = \frac{E_{batteries}}{P_{motor}} \tag{5.27}$$

The efficiency of the propeller is based on statistical data, resulting in a total motor power of 878.5 $[W]$. To calculate the total energy of the battery, the specific energy is multiplied by the total battery mass, which amounts to 11.7 kg. This yields a total energy of 5265 $[Wh]$ and corresponds to a battery volume of 4.12 $[L]$. It is assumed that 90 [%] of the energy is utilized by the propeller system, while the remaining 10 [%] powers the other components. Consequently, 4738.5 $[Wh]$ is allocated to the propeller system, while 526.5 $[Wh]$ is assigned to the remaining components. In conclusion, the Fixed-Wing has an endurance of 5.39 $[h]$ and an excess power of 97.62 $[W]$. A summary of the relevant parameters is showcased in Table 5.12.

---

[2] URL: https://amprius.com/technology/ [Cited: 19-06-2023]

Table 5.12: A table showcasing the relevant propulsion parameters and their values.

Parameter	Value
$C_{l_{cruise}}$	0.5974
$C_{d_{cruise}}$	0.0394
Motor Efficiency	0.80
Propeller Efficiency	0.75
T_{req}	17.57 $[N]$
Motor Power	878.55 $[W]$
Battery Mass	11.70 $[kg]$
Battery Volume	4.12 $[L]$
Endurance	5.39 $[h]$
Excess Power	97.62 $[W]$

5.7. Structural and Vibrations Analysis

Throughout its operational lifetime, the drones will experience a variety of loading cases and environmental effects. It is then essential to ensure that the structures of the drones can endure the loads and the stresses applied to them and that they are within the allowable range. Where the loads and stresses are higher than what's allowed, reinforcements have to be made to the structure to allow the drone to withstand the loads. In this section, the analysis of how can the drone sustain its structural integrity is analysed.

5.7.1. Load and Stress Analysis

To begin the structural analysis of the Fixed-Wing drone design, first, the external loads experienced by the drone have to be identified. As a design criterion, it was decided that the drones have to endure a maximum load factor of n = 5 and a minimum load factor of n= -3 as elaborated on in subsection 5.7.2. The main loads identified on the drone are the weight distribution of the fuselage structure, the lift of the wing and the tail boom, the drag of the wing, the moment induced by the wing, and the weight of the individual internal components in the drone. The structural analysis and the stress calculations of the drone are therefore made with consideration of these loads. Using the identified loads free body diagrams can be made for the fuselage, the wing, and the tail boom.

After the main loads and the locations of these loads are identified, the next step is to analyze how these loads induce stresses on the structural components of the drone. To start the analysis, internal loading diagrams are constructed to identify the largest internal loads experienced by the structures. The design of the components can then be performed according to these ultimate load cases. During the design, the axial loads on the fuselage, wing and tail boom are not analysed in detail as they are deemed to be not significant in magnitude compared to the other loads on the structure. During the design, the most important failure modes of the structure are analysed in detail: exceeding the material's ultimate stress due to stresses, buckling of the skin due to these same stresses, and failure in shear due to internal shear loads.

5.7.2. Load factor

Maneuver Loading

The load factor is defined by Equation 5.28 [37]

$$n = \frac{L}{W} = \frac{C_L \frac{1}{2}\rho V^2 S}{W} = \frac{q \cdot C_L}{W/S} \tag{5.28}$$

where L is the lift force, W is the weight of the aircraft, C_L is the lift coefficient, ρ is air density, V is airspeed, S is surface area and q is dynamic pressure.

For example, if the load factor is 3, as seen in the manoeuvre diagram in Figure 5.24, it means that the lift generated is 3 times greater than the weight, which if you actually put on a scale it would mean the drone weight would go from 25 $[kg]$ at $n = 1$ to 75 $[kg]$.

The logic of the manoeuvre diagram located in Figure 5.24, from left to right is the following:

- When the Fixed-Wing has zero velocity it would fall straight down so it would have a load factor of 0.
- As the velocity of the Fixed-Wing increases, the load factor would increase quadratically with respect to V^2 as the faster you travel, the more lift the wing is able to generate.
- At the stall speed the load factor is equal to 1 because there is a force equilibrium between lift and weight.
- On the lower side of the graph you have a similar quadratic line with a negative load factor that can be generated by performing a manoeuvre going downwards.
- If you keep increasing the velocity of the Fixed-Wing you would end up generating higher load factors which would greatly affect the structure of the drone. Although the Fixed-Wing is designed to handle higher load factors during shorter periods of time, a manoeuvring limit of $n_{max} = 3$ was set to reduce the fatigue of the structure throughout the lifespan of the drone.
- On the lower side of the graph manoeuvring there is a $n_{min} = -1.2$. This limit was set as 0.4x the one of n_{max}, according to CS23 regulations for utility aircraft[17].
- Finally the green vertical line represents the maximum speed the drone can go, which is achieved when performing a diving manoeuvre. This was approximated using Equation 5.29 [37], where V_D is dive speed and V_C is cruise speed.

$$V_D = \frac{V_C}{0.8} = 37.5[m/s] \tag{5.29}$$

Gust Loading

For the gust loading diagram located at the right of Figure 5.24. When the FW drone is subjected to a wind gust, the angle of attack is temporarily increased resulting in a change in the lift force and therefore a δn. This change in load factor can be computed using Equation 5.30 [37]:

$$\delta n = \frac{\rho V C_{L_\alpha} u}{2(W/S)} \tag{5.30}$$

Where ρ is the air density, V is airspeed, C_{L_α} is the gradient of the lift polar, W is the weight of the aircraft, S is Surface area and $u = U_{ref} \cdot K$. U_{ref} is the reference gust speed where the maximum gusts considered are 15.24 [ms^{-1}] at cruise, and 7.62 [ms^{-1}] at maximum dive speed [17] and K is a correctional factor (depending on whether the flight regime is sub/trans/supersonic) defined in Equation 5.31 [17]:

$$K = \frac{0.88\mu}{5.3 + \mu} \tag{5.31}$$

Where μ is the aircraft mass ratio defined in Equation 5.32 [17]

$$\mu = \frac{2 \cdot W/S}{\rho \cdot c \cdot C_{L_\alpha} \cdot g} \tag{5.32}$$

By computing μ and inputting the velocities, one can calculate the required load factor for each velocity by: $n_{req} = 1 + \delta n$, since the drone is already flying at a force equilibrium at n=1.

Maneuver and Gust Loading Diagrams

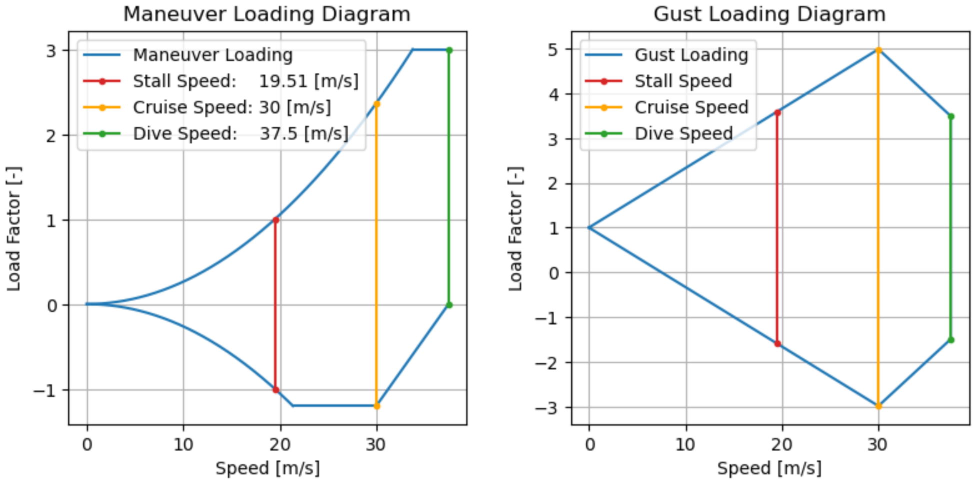

Figure 5.24: Maneuver and Gust Loading Diagrams.

5.7.3. Wing Loading Analysis

Bending

The vertical forces on the wing caused by the lift of the wing and the attachment to the multicopter lead to a bending moment in the wing. This bending moment leads to both compressive and tensile stresses in the skin surface along the spanwise direction. All forces that are identified to contribute to the bending moment in the wing are shown in the free body diagram of the wing, shown in Figure 5.25.

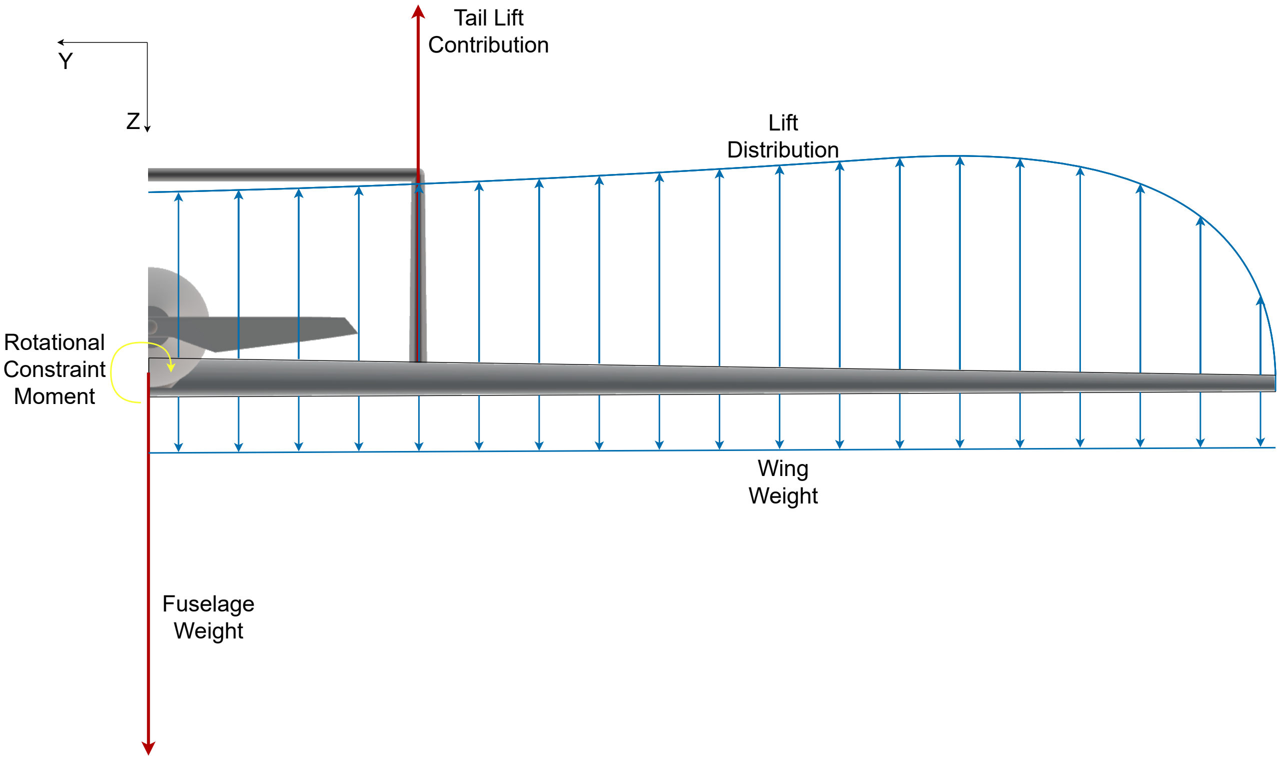

Figure 5.25: Free Body Diagram (FBD) of the FW drone wing.

For the case where the drone is attached to the multicopter, the free body diagram would not have the lift gradient acting on the wing. In this case, this load would be replaced with a vertical point load acting at the half span of the wing. Taking the maximum of either scenario, the internal shear and bending diagram shown in

Figure 5.26 can be constructed.

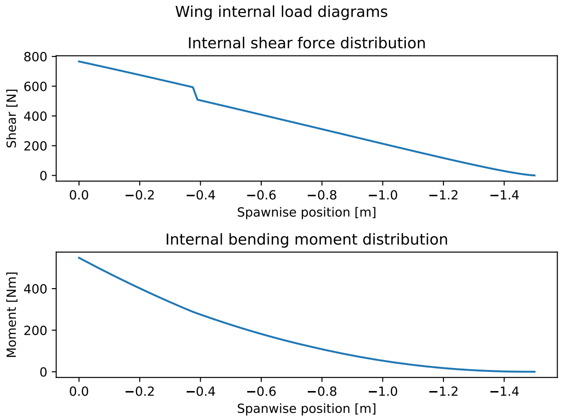

Figure 5.26: Internal load diagram of the FW drone wing.

The stresses in the wing skin can be related to the applied loading and wing cross-section according to Equation 5.33.

$$\sigma_z = \frac{M_y I_{xx} - M_y I_{xy}}{I_{xx} I_{yy} - I_{xy}^2}(x - x_0) + \frac{M_x I_{yy} - M_y I_{xy}}{I_{xx} I_{yy} - I_{xy}^2}(y - y_0) \tag{5.33}$$

In Equation 5.33, x_0 and y_0 denote the position of the centroid of the wing. To calculate the centroid and area moments of inertia of the wing, due to the complexity of the aerofoil shape making an analytical solution difficult, a numerical approach is used instead. For this approach, the wing is assumed to be a thin-walled structure, meaning its thickness is assumed to be significantly smaller than the smallest feature on the aerofoil. For the numerical analysis, the aerofoil is split into many small rectangular sections following the circumference of the wing. The total area moment of inertia can then be computed by summing up the contributions of each individual rectangular section. Using this method, it was found that for a skin thickness of 1 $[mm]$, the airfoil without any internal strengthening components has area moment of inertia values as laid out in Table 5.13.

Parameter	Value [m^4]
I_{xx}	$4.11 \cdot 10^{-6}$
I_{xz}	$-1.73 \cdot 10^{-6}$
I_{zz}	$1.76 \cdot 10^{-4}$

Table 5.13: Area moments of inertia of the airfoil.

Plugging these values for the moment of inertia into Equation 5.33 leads to lift-induced stress distribution in the wing as shown in Figure 5.27.

During the mission of the Fixed-Wing, there are two load cases that must be considered for causing bending in the main wing. Firstly, there is the vertical force introduced by the lift of the wing itself. For the moment calculations of this mode, the C_L distribution of the wing is first determined using XFLR 5. As the lift distribution along the span stays effectively constant for varying values for angles of attack and airspeed, this lift distribution is then multiplied with the load factor determined in subsection 5.7.2 to find the limit lift force distribution along the wing. This distribution can then be integrated along the span to find the moment caused on the wing. The second load case occurs when the drone is attached to the multicopter, which then carries all the load. In this case, all vertical load is assumed to be applied at the connection points halfway along the wings, with the fuselage-mounted connection point only serving to maintain the stability of the drone. During the design, the most constraining of these load cases should then be used to size the structure of the wing. The maximum stresses found along key positions of the wing are laid out in Table 5.14.

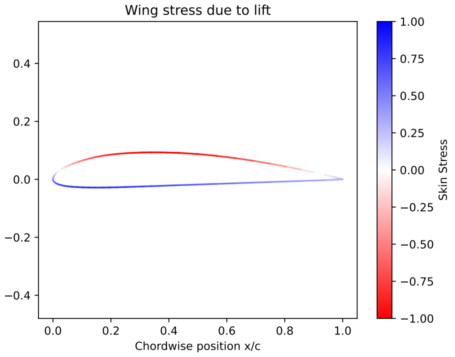

Figure 5.27: Stress gradient due to lift.

Position [m]	Compressive Stress [MPa]	Tensile Stress [MPa]
0 (Wing root)	62.42	-51.21
0.75 (Half span rib)	29.04	-23.82

Table 5.14: Bending stresses in the wing skin.

These stresses are significantly below the failure stress of the material, meaning the material itself will not fail, the stresses could however still lead to a failure of the structure through buckling of the skin surface, as discussed in Equation 5.7.3.

Finite Element Analysis

To verify the bending analysis performed, FEM was used on the wing skin. To do this, first, the CAD model was imported into the FEM software FEMAP. Then, a mesh was applied on the surface, and the root was constrained. Finally, the loads were distributed over the wing surface, and the analysis was run. The stresses on the top surface of the wing can be observed in Figure 5.28.

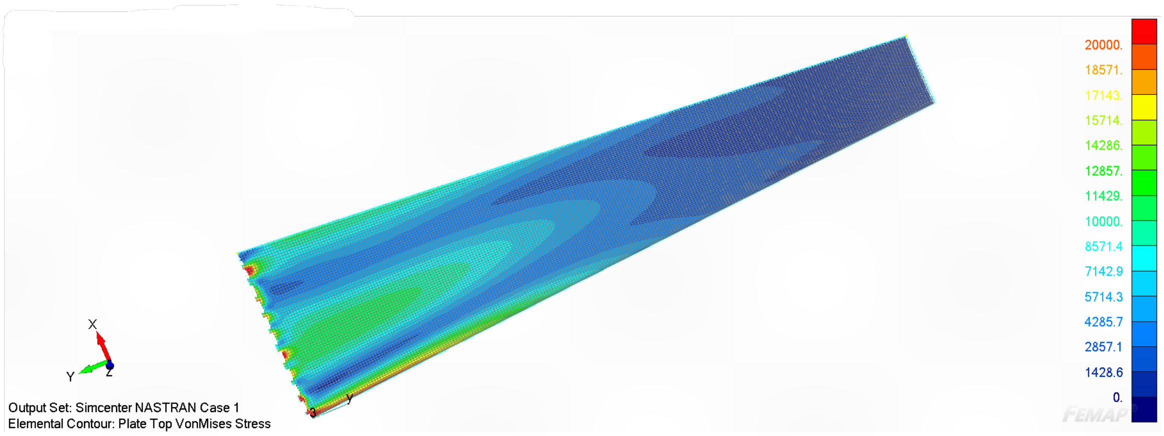

Figure 5.28: Top plate stresses.

It is important to note that the stresses displayed in Figure 5.28 are in [psi] and must be multiplied by 0,00689476 to obtain a value in [MPa]. It is also noteworthy to mention that the stresses near the root show some red sections, this is where the model is constrained, and should therefore be ignored, as they are not an accurate representation of the stresses. Figure 5.28 shows the highest stresses to be present towards the centre of the top surface, near the root, these stresses have a value of approximately 14000 [psi], or 96.5 [MPa]. These values are a bit higher than those calculated in the analysis but of a similar order of magnitude. This loading diagram further proves that the wing skin alone is able to withstand the bending moments experienced by the wing.

Shear Stress

The vertical lift force and the horizontal drag induce internal shear forces in the structure. These shear forces correspond to shear flows through the wing skin. The shear flows inside the structure depend on the shear force magnitude, the location of the load applied, and the geometry of the cross-section. The shear flows inside a closed cross-section can be calculated using Equation 5.34:

$$q_b = -\frac{S_x I_{xx} - S_y I_{xy}}{I_{xx} I_{yy} - I_{xy}^2} \int_0^s tx\,ds \; - \frac{S_y I_{yy} - S_x I_{xy}}{I_{xx} I_{yy} - I_{xy}^2} \int_0^s ty\,ds \tag{5.34}$$

To simplify the shear flow analysis, a simplification of the aerofoil cross section is used. A visualisation of the simplified aerofoil is provided in Figure 5.29. Since the largest internal shear force is experienced at the root of the wing, the cross-sectional geometry of the root and the internal shear loads at the root are considered for the analysis.

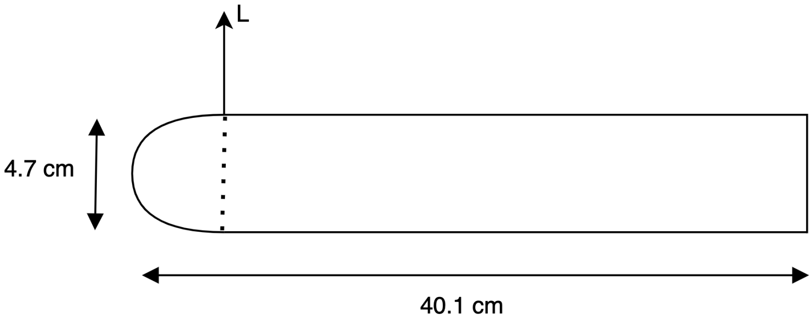

Figure 5.29: A simplified schematic of the wing cross-section used in the shear flow analysis (not to scale).

It was analysed that the lift force is much larger than the drag force, hence the drag force was assumed to be negligible to further simplify the the analysis. With these assumptions the shear flow along the airfoil was calculated and it was found out that the maximum shear flow along the skin was found to be 724.5 $[N \cdot m^{-1}]$. The relationship between the shear flow, skin thickness, and the shear stress is given with Equation 5.35.

$$\tau = \frac{q}{t} \tag{5.35}$$

With the initial design assumption of skin thickness of 1 [mm], the maximum shear stress experienced along the airfoil skin is calculated to be $\tau = \frac{724.5}{0.001} = 724500[Pa] = 724.5[kPa]$.

Buckling

The most constraining failure mode of the wing is buckling. Buckling is a phenomenon that occurs when a structure fails due to instability, induced by compression forces. For a wing, this situates at the upper skin which has the possibility to buckle due to the upwards bending of the lift force. A visual representation of how the internal stresses act due to the lift is shown in Figure 5.30. The wing possesses a high slenderness ratio due to its significantly high ratio of wing span to cross-sectional area. Therefore, without internal components, the wing is most likely to buckle.

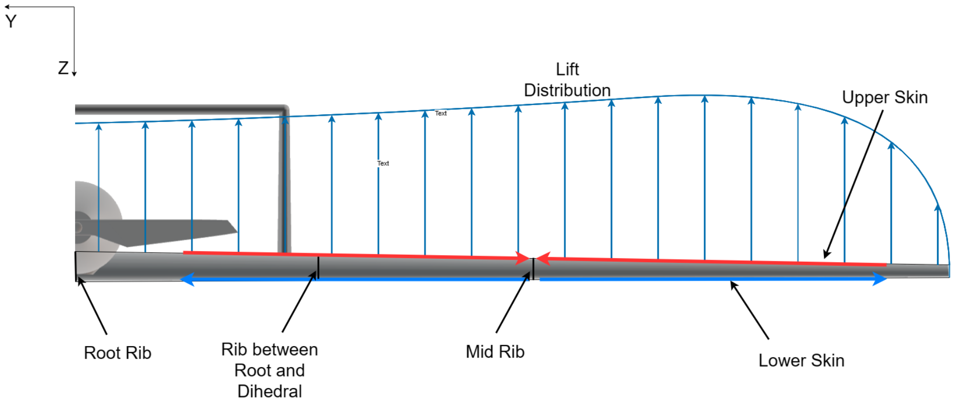

Figure 5.30: A visual representation of the lift distribution on one side of the wing. The internal forces induced by the lift in the upper and lower skin. The upper skin is in compression (red) and the lower skin is in tension (blue).

The spar inside the wing acts as a stiffener along the wing span, and increases the maximum buckling stress for the wing. The maximum stress of the bare skin of the wing, before buckling occurs, is calculated with Equation 5.36 [45]. The wing skin is made out of Carbon Fibre T800S and has a Young's Modulus of 163 $[GPA]$. The Poisson ratio is assumed to be 0.33 and the skin thickness of the wing is assumed to be 1 $[mm]$. The buckling ratio is dependent on the boundary layer condition of the wing. The wing is assumed to be clamped on all sides, translating to a buckling ratio of around 6.98. Concluding, The maximum buckling stress for the bare skin of the wing at the root chord length of 0.401 $[m]$ is 3.74 $[MPa]$.

$$\sigma_{cr_{s}kin} = C\frac{\pi^2 E}{12(1-v^2)(\frac{t}{b})^2} \tag{5.36}$$

The bare skin will fail in buckling if no structural support component is present, as the maximum bending moment far exceeds the stress before buckling occurs. As mentioned before, the spar will act as a stiffener, providing structural integrity and support against buckling. Since the spar serves as a stiffener for the wing, we can perform a stiffened panel analysis to determine the updated buckling stress for the wing. The cross-section of the stiffener is shown in Figure 5.31. We use a constant thickness of 2 $[mm]$, and only 3 sections of the stiffener are considered for the calculation. The bottom flange, which is attached to the lower skin of the wing, is deemed irrelevant for the buckling analysis of the upper skin.

To continue the buckling analysis for the stiffened panel, we need to identify the a/b ratio. The a/b ratio for the three sections is larger than 3, where 'a' represents the length of the section and 'b' represents the thickness of the section. This ratio is further used to calculate the buckling ratio for each section. Additionally, the corners are assumed to be stiff, and the bottom side of section (3) is considered clamped, as it is attached to the lower flange of the stiffener. Figure 5.32 presents the buckling coefficients based on the boundary layer condition and the a/b ratio.

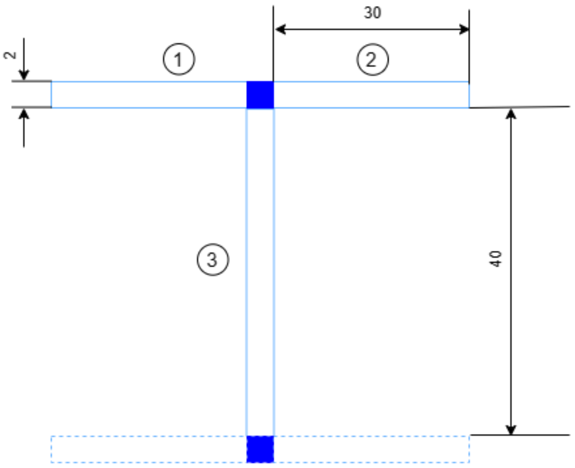

Figure 5.31: A visual representation of the cross-sectional of the spar in the wing. The blue boxes indicate the stiff corners of the spar. The dotted lines indicate the irrelevant sections of the stiffener.

Figure 5.32: A table showcasing the boundary conditions (BC) and buckling ratio's (C) for each relevant section of the stiffener.

Section	BC	C
Section 1	SSFC	1.28
Section 2	SSFC	1.28
Section 3	SSCC	6.98

The next step in the analysis is to find the crippling stress, σ_{cc} of the stiffener. Using Equation 5.37, the crippling stress of the stiffener can be calculated. The material that is used for the stiffener is Al-2024 T3, which has a tensile yield stress of 483 $[MPa]$ and a Young's Modulus of 73.1 $[GPa]$. Assuming α = 0.8, n = 0.6, and a Poisson ratio of 0.33 [-], the calculation is performed for each section. If the ratio exceeds 1, the crippling stress for that section is set equal to the yield stress. Using Equation 5.38, the crippling stress of the whole stiffener can be calculated using the sectional properties of the stiffener. The final crippling stress of the stiffener is 404.68 $[MPa]$.

$$\frac{\sigma_{cc}^{(i)}}{\sigma_y} = \alpha\left(\frac{C}{\sigma_y}\frac{\pi^2 E}{12(1-v^2)}(\frac{t}{b})^2\right)^{1-n} \quad (5.37)$$

$$\sigma_{cc_{stiffener}} = \frac{\sum \sigma_{cc}^{(i)} A^{(i)}}{\sum A^{(i)}} \quad (5.38)$$

Using the prior calculations, the effective width of the sheet was calculated using Equation 5.39 [45]. The effective width of the sheet is an indicator of how much of the skin itself has the same stress as the stiffener. For the structure, an appropriate buckling coefficient of 6.98 was chosen. Using the rule of thumb, the b/t ratio of the wing is bigger than 110 meaning this buckling coefficient is justified. For finding the effective width sheet, the Young's Modulus and thickness of the sheet material is used. Concluding, the effective width ($2w_e$) sheet is 50.94 $[mm]$. This is smaller than the width of the stiffener ($2w_s$), which was expected and justifies the boundary condition.

$$2w_e = t\sqrt{\frac{C\pi^2}{12(1-v^2)}\frac{E}{\sigma_{cc_{stiffenner}}}} \quad (5.39)$$

By implementing the effective width sheet, the new final buckling stress of the stiffened wing can be derived. The final calculation is shown in Equation 5.40. Neglecting the corner of the stiffener, the new buckling stress including support is 171.15 $[MPa]$.

$$\sigma_{cc} = \frac{\sigma_{cc_{stiffener}} \cdot (A_{stiffener} + 2w_e t_{skin}) + \sigma_{cr_{skin}} \cdot (b - 2w_e)t_{skin}}{A_{stiffener} + bt_{skin})} \quad (5.40)$$

The revised buckling stress is significantly higher than the maximum compression strength in the upper skin of the wing. However, the inclusion of stiffeners significantly increases the weight of the wing. The incorporation of the spar has raised the total buckling strength from 3.74 $[MPa]$ to 171.15 $[MPa]$, resulting in a relative increase of 4476 [%].

In terms of weight, the initial cross-sectional area at the root chord measures 401 $[mm^2]$. The relevant sections of the spar have a cross-sectional area of 405 $[mm^2]$. The spar is constructed from aluminium, which has a density of 2.78 $[g \cdot cm^{-3}]$, while the carbon fibre T800s possess a density of 1.544 $[g \cdot cm^{-3}]$. Consequently, there is a relative weight increase of 182 [%], which is quite substantial. Typically, such a significant weight increase is avoided, however, the absence of internal components would almost certainly lead to the skin failing in buckling.

The weight analysis is performed under the assumption that the wing and the spar gradually decrease in area at the same rate.
The spar is placed until the dihedral of the wing starts. The wing would fail in buckling if no internal structure was present after the dihedral. However, there are two stringers running through the wing span at 33 [%] and 66 [%] chord lengths. The stringers separate the wing into three sections. The chord length at the dihedral point is 0.281 $[m]$ and separating the wing in three sections converts to a spacing of 93.7 $[mm]$. Using Equation 5.36 and the properties of the sheet results in a buckling stress of 68.6 $[MPa]$, which is significantly larger than the compression force at the dihedral point. This justifies using the spar until the half-wing span.

5.7.4. Fuselage Loading Analysis

In the design of conventional aircraft, one of the most critical design constraints is the stress caused by the pressurisation of the fuselage. The skin thickness is often designed with the hoop stress and the axial stress due to the pressure difference in mind. However unmanned drones do not need to be pressurised in their fuselage so this reduces the stresses present on the fuselage. So the only remaining relevant loads on the fuselage are the shear flow due to the lift and weight forces and the bending moment induced by these forces. Due to the circular shape of the fuselage cross-section and the relatively small side force that induces torsion, torsion is not considered in the analysis.

Structural idealisation

To begin the structural analysis of fuselage loading, the structure is initially idealised, as depicted in Figure 5.33. This idealisation allows for simplifications in stress analysis. In the structural idealisation, the skin thickness is assumed to be negligible, and the structure is represented by concentrated areas known as booms.

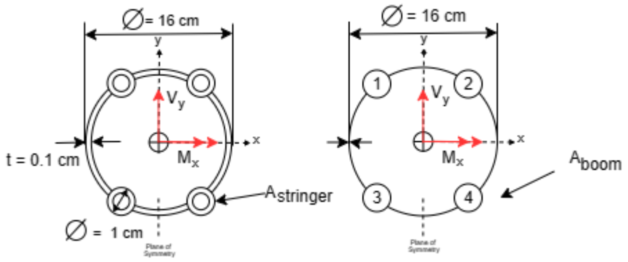

Figure 5.33: Cross-section of the fuselage before the structural idealisation (left) and after the structural idealisation (right). The internal bending moment, M_x, and internal shear force, V_y, are indicated in red.

In the initial stage of the structural idealisations, the areas of the booms were determined. These boom areas are derived based on the skin area and the area of the stringer. The calculated boom areas are subsequently employed in the stress analysis. The relationship between the boom area, skin area, and stringer area is represented by Equation 5.41.

$$A_{boom} = A_{stringer} + \frac{t_{skin}}{3}(\pi r_{fuselage} - 2D_{outer_{stringer}}) \tag{5.41}$$

Bending of the Fuselage

The primary sources of bending stress in the fuselage arise from the distribution of lift and weight throughout the aircraft. Several assumptions are made in this analysis. Firstly, the bending moment caused by side forces (represented by M_y) is neglected due to its significantly smaller magnitude compared to the lift and weight forces. Additionally, a simplifying assumption is made that the fuselage cross-section possesses an axis of symmetry, resulting in a product of inertia (I_{xy}) of zero. These assumptions and simplifications are incorporated, leading to the final equation used for calculating the bending stress, as illustrated in Equation 5.42.

The maximum bending stress in the fuselage can be determined by relating it to the maximum bending moment and the moment of inertia. By analysing the loading diagrams provided in Figure 5.35, it has been found that the maximum bending moment in the fuselage is 56.17 $[Nm]$. Using Equation 5.42 and Equation 5.43, the maximum bending stress is calculated. The properties of the boom and bending stress are displayed in Table 5.15.

$$\sigma_z = \frac{M_x y}{I_{xx}} \quad (5.42) \qquad\qquad I_{xx} = \sum B_r y^2 \quad (5.43)$$

Table 5.15: Relevant boom properties regarding bending stress.

Boom	**Boom Area** [mm^2]	**y** [mm]	**Steiner Term** [mm^4]	**Bending Stress,** σ_z [MPa]
Boom 1	136.01	56.57	435244.80	-1.825
Boom 2	136.01	56.57	435244.80	-1.825
Boom 3	136.01	-56.57	435244.80	1.825
Boom 4	136.01	-56.57	435244.80	1.825
		I_{xx}	1740979.20	

The maximum bending stress in the fuselage is determined to be $\sigma_z = |1.825[MPa]|$, indicating that the fuselage is capable of withstanding the bending loads encountered during operation. It is important to note that this analysis simplifies the actual scenario, neglecting certain factors in the process. Nevertheless, the results provide valuable insight, suggesting that the fuselage has a considerable safety margin before its structural integrity is compromised.

Shear on Fuselage

Apart from the internal bending moment, the distribution of lift and weight in the fuselage also generates shear stress. All forces identified that contribute to this shear stress are shown in the free body diagram shown in Figure 5.34.

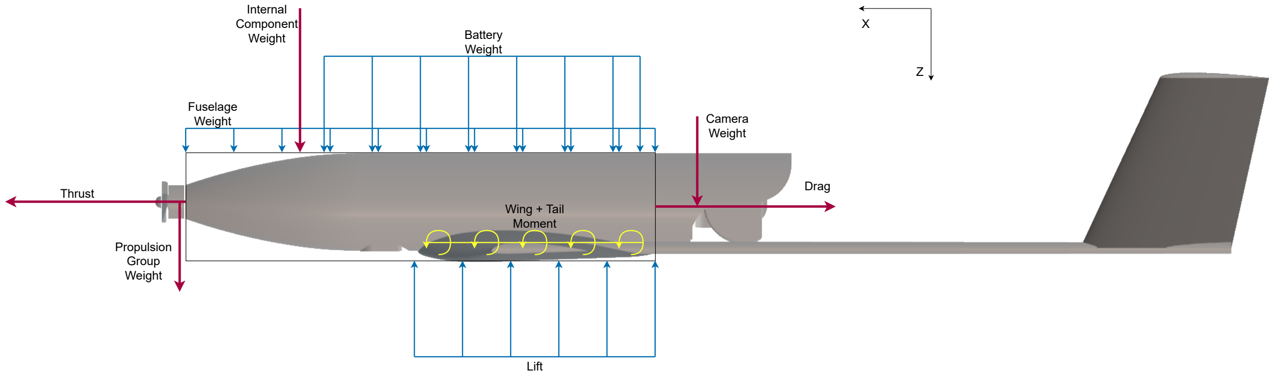

Figure 5.34: Free Body Diagram of the FW drone fuselage.

Using the loads shown in the free body diagram, the internal load diagram shown in Figure 5.35 can be constructed.

The maximum shear force was determined by the loading diagram in Figure 5.35. The maximum shear force along the shear was -419.98 $[N]$. To perform the shear analysis, the boom area and properties obtained from the previous section are utilised. These parameters are crucial for calculating the shear flow distribution and evaluating the shear stress experienced by the fuselage. The maximum shear force experienced by the fuselage can be obtained from Figure 5.35

As only the shear force in the y-axis is considered, V_x = 0. Using the simplification of I_{xy} = 0 too, the equation for the change in shear flow is shown in Equation 5.44. The shear flow is constant between the booms since the skin between the booms has a thickness of zero. The boom properties for the shear stress analysis are presented in Table 5.16.

$$\Delta q = -\frac{V_y}{I_{xx}} B_r y \quad (5.44)$$

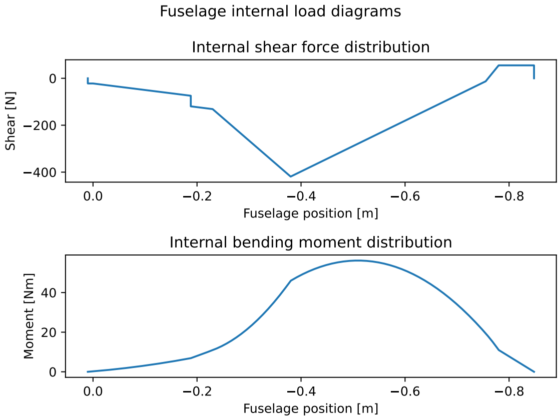

Figure 5.35: Internal load diagram of the FW drone fuselage.

Table 5.16: Relevant boom properties regarding shear stress.

Boom	**y** $[mm]$	$Steinerterm$ $[mm^4]$	Δq $[N \cdot \mathrm{mm}^{-1}]$
Boom 1	56.57	435244.80	0.8019
Boom 2	56.57	435244.80	0.8019
Boom 3	-56.57	435244.80	-0.8019
Boom 4	-56.57	435244.80	-0.8019
	I_{xx}	1740979.20	

The maximum shear flow in the idealised structure is 801.9 $[N \cdot m^{-1}]$. To calculate the maximum shear stress in the structure, the shear flow is multiplied by the original thickness, which is 1 $[mm]$. By performing this calculation, a maximum shear stress of 801.9 $[kPa]$ is obtained. This indicates that the structure is capable of withstanding the applied shear stress. The use of structural idealisation simplifies the shear stress analysis meaning that factors such as the variable shear flow and the curvature of the fuselage are neglected in the analysis. However, the low maximum shear stress indicates that the structure has enough margin to withstand the shear stresses in the fuselage.

5.7.5. Material Selection

As a result of the structural analysis, a material has been selected that directly impacts the weight and strength of the Fixed-Wing. The structure is distinguished between external and internal components for the material selection. The external components of the wing are the skin of the wing, the fuselage skin, and the empennage. The internal components include all the support structure components of the Fixed-Wing. Prior to conducting a material trade-off analysis, considerations were undertaken to assess the suitability of different materials.

Material Considerations

After prioritizing the ability to withstand loads without failure, the selection of the material took additional factors into account. Firstly, considering the operational environment being at sea, it was crucial for the material to possess water and corrosion resistance. The absorption of water can lead to swelling, deformation, and the loss of structural integrity. To prevent this, the application of an additional coating becomes necessary, adding complexity and maintenance requirements to the structure. Furthermore, in saltwater environments, the material should ideally exhibit resistance to salt. Additionally, a high strength-to-weight ratio and durability are desirable qualities for the chosen material. The selection of an appropriate material prioritizes a prolonged lifespan, thereby necessitating the mitigation of chemical degradation and corrosion processes. Considering the operation of drones in a swarm configuration, minimizing maintenance requirements is desirable.

Following careful consideration of these factors, it is determined that balsawood and triplex are unsuitable for the structural components of the aircraft. These materials lack the required environmental resistance to withstand operational conditions and fail to meet the structural requirements of a Fixed-Wing drone. Similarly, ceramics are not suitable due to their fragility and low tensile strength. Moreover, ceramics generally have a lower specific strength-to-weight ratio compared to metals and composites. While natural materials such as rubber could be an option if there is a strict weight constraint, their lower strength in comparison to other materials limits their suitability. However, polymers are not considered in the analysis due to their low strength, aligning with the same reasoning as natural materials. A visual representation of the density and strength of the materials is shown in Figure 5.36.

Material Trade-Off

A selected amount of materials were selected after the considerations. The respective composites are carbon fibre-reinforced polymers (CFRPs) and Kevlar. For the carbon fibre-reinforced polymers, a combination of 60 [%] fibre volume and 40 [%] epoxy resin is used. The epoxy resin has a density of 1160 [$kg \cdot m^{-3}$]. The density of the composite is calculated by using the rule of mixture. CFRPs are known for their exceptional strength-to-weight ratio and are commonly used for drones. Composites exceed in tensile strength, characterised by fibre properties.

Metals are valued for their isotropic properties and excellent mechanical performance. They typically possess higher shear strength compared to composites. While metals tend to have a higher density than composites, they are often more cost-effective.

The quantitative criteria for the trade-off were the ultimate tensile strength (UTS), shear strength, Young's Modulus, density, and the price per kg. The properties of the selected materials are shown in Table 5.17. There are two materials allocated for the structural components. The selected composite is used for the external components defined prior. Similarly, the selected metal is used for the internal component. As composites are less dense, weight can be saved if composites are used for the external structure. Metals are more usable for internal structures, as they are easier to manufacture and complex shapes are easier to make.

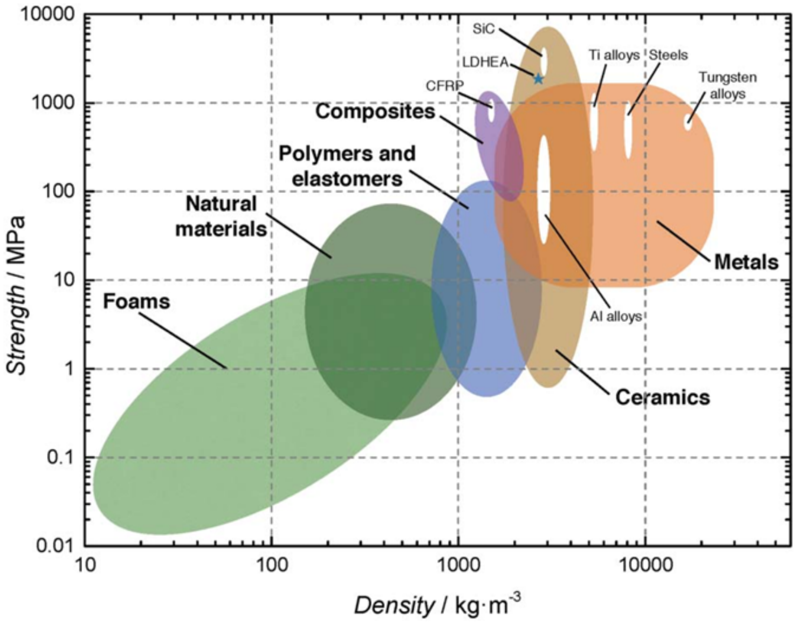

Figure 5.36: Graphic overview of strength versus density for engineering materials [62]

For the composite material, the trade-off led to CFRP T800s as the final selection. Compared to the other two materials it has the highest Young's Modulus and is cheaper than Kevlar 49. Kevlar 49 proportionally increases in price when the mechanical properties increase based on the form of the material. As buckling is more constraining than the bending stresses for the structure of the Fixed-Wing drone, the small advantage of the higher Young's Modulus is preferred over the advantage in the ultimate tensile strength. Carbon fibre is also more commonly used in similar drone designs which augments the confidence in the selection.

For the metal, aluminium-2024 T3 has been selected. Mainly because of weight priorities. Steel is way too heavy and cannot be used for aluminium-2024 T3, however, it is more heavy and expensive than aluminium.

Aluminium-2024 T3 has the strength to withstand the estimated loads on every axis, which justifies the trade-off.

Table 5.17: Material properties of relevant options. The highlighted materials in green are selected for the final design.

Material	UTS [MPa]	Shear Strength [MPa]	Young's Modulus [GPa]	Density [kg $\cdot m^{-3}$]	Price [EU/kg]
CFRP T300	1860	98	135	1520	20-50
CFRP T800s	3290	135	163	1544	90
Kevlar 49	3600	50-150	124	1440	20-200
Al-2024 T3	483	283	73.1	2780	9
Ti-6Al-4V	950	550	113.8	4430	22
Steel (304L)	564	275	193	8000	2

5.7.6. Internal Layout of Structural Components

After the internal stresses have been analysed, the next step of the design is to design the internal structural layout of the Fixed-Wing drone. From the stress analysis conducted, it was concluded that aside from the buckling of the wing skin, the stresses realized on the structural components of the Fixed-Wing drone are significantly lower than the yield stress of the carbon fibre composite that is going to be used for the skin of the aircraft. This implies that the carbon fibre composite wing skin alone can withstand the axial and shear stresses occurring during the drone's operational lifetime.

It was decided to use 3 aluminium ribs on each side of the wing to aid with the buckling of the wing skin and an I-beam-shaped spar going spanwise until the kink point of the wing, which is at the halfway point of the wingspan. To further reinforce the structural integrity of the wing shape and prevent it from losing its geometry throughout its operational lifetime, 2 aluminium stringers at the leading edge and the trailing edge along the whole span of the wing are placed. To transfer the lift of the wings to the fuselage, a wingbox structure is designed that is placed towards the bottom side of the fuselage to make space for the other internal subsystems in the fuselage. It was analysed that a simple aluminium box shape of 16x16x3 [cm^3] with an aluminium I-beam stiffener placed spanwise is sufficient to withstand the loads experienced by the wing. With these considerations and design choices, the total mass of the wing including the wingbox, wing skin and, the internal structural components is 5 [kg].

For the internal structure of the fuselage, it was decided to use 1 bulkhead to attach the nosecone and the propulsion system to the fuselage, 4 frames to keep the structural shape of the fuselage and to attach the wingbox, and 4 longerons along the fuselage to distribute the loads along the fuselage and carry the internal components in the fuselage. The bulkhead and the frames are designed as simple circular aluminium structures with holes in the middle to allow for the placement of internal components and longerons are designed as simple circular aluminium tubes. With these considerations and design choices, the total mass of the fuselage including the fuselage skin and the internal structural components is 2.95 [kg].

The empennage of the aircraft produces relatively low lift and side force compared to the lift of the wing, so the carbon fibre composite skin is sufficient enough to withstand the internal loads during flight. However, it was deemed beneficial by the design team to include stringers on the leading edge and the trailing edge of both the horizontal stabilizer and the vertical stabilizer. The stringers used in the empennage are the same stringers designed for the wing. Considering the Fixed-Wing drone has 2 vertical stabilisers, there are 6 stringers in total placed in the empennage. With these considerations and design choices, the total mass of the empennage including the empennage skin and the internal structural components accounts for 1.07 [kg].

The last structural component that needs to be designed are the booms that connect the empennage to the wing. The primary loads acting on the boom are shown in Figure 5.37.

In the Internal Load Diagram shown in Figure 5.38, derived from the free body diagram, it can be seen that the maximum bending moment experienced by the booms is 76.72 [Nm] while the maximum shear force experienced is 100 [N] and hence the booms are designed according to this loading criteria. Due to weight constraints, it was decided to use the same carbon fibre composite used in the skin of the Fixed-Wing drone. The booms are designed to have a diameter of 2 [cm] with a hollow hole diameter of 1 [cm]. The total mass of

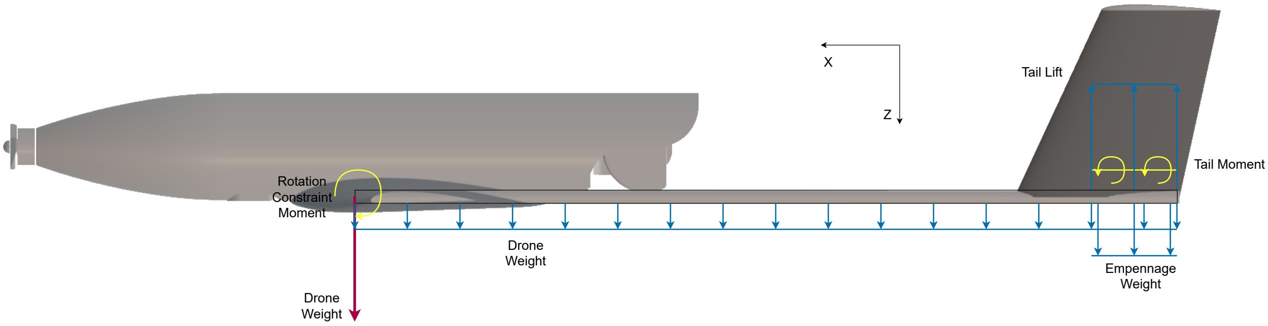

Figure 5.37: Free Body Diagram of the FW drone tail boom.

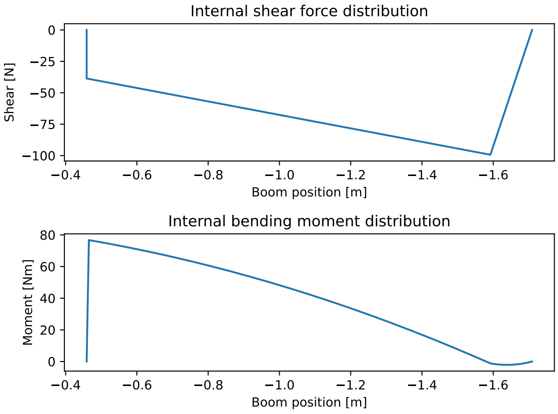

Figure 5.38: Internal Load Diagram of the FW drone tail boom.

the booms is 0.910 $[kg]$.

With these design choices, the total mass of the structural subsystem totals 9.93 $[kg]$. A schematic of the internal structural components of the drone is presented in Figure 5.39

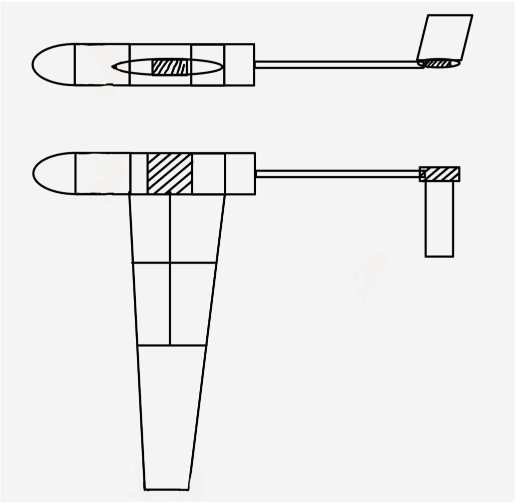

Figure 5.39: Free Body Diagram of the FW drone tail boom.

5.8. Budget Breakdown

A preliminary budget breakdown for the FW drone has been presented in [10]. Since the design has progressed to a significantly more detailed phase, it is important to revisit how the design of each subsystem relates to the provided budgets to see where improvements and changes in the margin are required. These budgets however were still made with the assumption that the FW drone would autonomously perform the launch and landing on the ship deck. Because the concept has evolved drastically since the conception of those specific breakdowns, it is required to create a revised budget breakdown.

5.8.1. Power Breakdown

The power distribution of the Fixed-Wing drone is among the primary factors determining the endurance and range of the Fixed-Wing. To improve insight on the power distribution of the drone, and prevent excessive power use, a revised power budget is presented in Table 5.18 and Table 5.19. Table 5.18 contains the contributions of the primary power-consuming components, as visually displayed in Figure 5.40a. The propulsion segment of this power breakdown consists of the power used by the engine and losses in the ESC. From the breakdown, it can be seen that the propulsion is by a significant margin the largest consumer of power on the drone, with a total power fraction of 90%. The payload, including both the scanning camera and command and data handling subsystem trails with a power fraction of only 7.5% of the total available power. The remaining $\approx$25 $[W]$ is reserved as a margin for potential future changes. If more additional power is required than available in the margin, this will require a redesign of one or more subsystems to prevent cutting into the endurance of the drone.

Table 5.18: Power breakdown of major components.

Component	Power [W]	Relative Power [%]
Propulsion	879	90.0
Payload	72.9	7.5
Excess Power	24.3	2.5
Total	976.2	100

The payload is further split up and worked out in more detail in Table 5.19 and Figure 5.40b. In this breakdown, the sensors encompass all sensors that are not designated for the scanning of the search area. The on-board computing group consists of the flight controller, based on an STM32, and the camera data processing runnng on the Nvidia Jetson TX2.

Table 5.19: Power breakdown of minor components.

Component	Power [W]	Relative Power [%]
Actuators	1.0	1.4
Camera: Mantis i45N	40	54.9
Sensors	2.1	2.9
On-board computing	15.8	21.7
Communication	14	19.2
Total	72.9	100

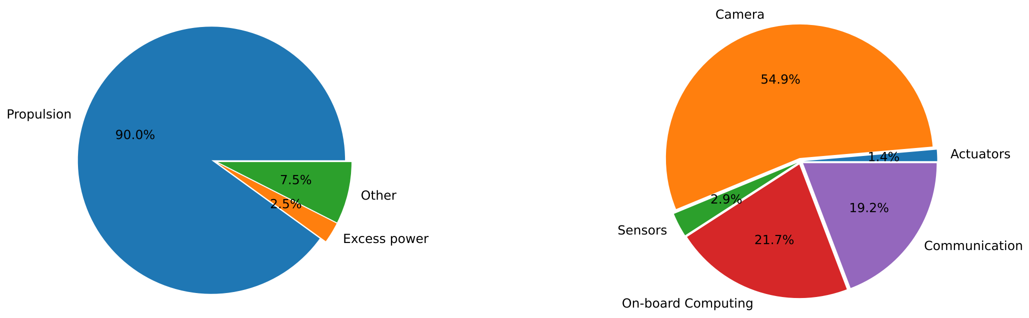

(a) Major contributor power budget.

(b) Minor contributor power budget.

Figure 5.40: Power budget pie chart for the Fixed Wing drone.

When compared to the power budget breakdown in [10], a noticeable difference is a decrease in the total power available to the system due to tightened performance targets set by the team. This decrease was primarily realised due to a reduced power requirement for the propulsion subsystem. The payload power on the other hand has seen a significant increase since the preliminary design due to an underestimation of the required power of the camera gimbal system which was not expected to play as significant of a role as it does in the current state of the design.

5.8.2. Mass Breakdown

The components for the mass breakdown of the Fixed-Wing are the battery, payload, propulsion, wing, empennage, and fuselage. As expected, the battery is the main component of the weight. The Fixed-Wing is designed for long endurance operations for cruise conditions. The other main contributors to the weight are the structural components. All structural components include the skin and support structures. The support structures support against stresses and failure modes by adding extra weight to the component. The wing is significantly heavier than the empennage and fuselage. Mainly because the wing has a large wing span compared to the fuselage and empennage. Two main requirements in the mass budget were presented: the maximum payload mass is 3 $[kg]$ (REQ-STK-SYS-05) and the maximum take of weight of the node is 25 [kg] (REQ-STK-SYS-03). In Table 5.20, the components are presented with their mass and relative mass to the total mass. Further, the mass components are visualised by the pie chart in Figure 5.41.

Table 5.20: Mass Breakdown for the Fixed-Wing drone.

Component	Mass [kg]	Relative Mass [%]
Battery	11.7	46.8
Payload	2.5	10.0
Propulsion	0.3	1.2
Wing	5.0	20
Empennage	2.5	10.0
Fuselage	2.9	11.6
Excess Mass	0.1	0.4
Total	5	100

Based on the results presented in Table 5.20, a small margin of 0.1 $[kg]$ was observed in the mass breakdown of the Fixed-Wing drone. It is important to note that no mass was allocated to the landing gear of the drone due to the unnecessary requirement for take-off and landing mechanisms. Additionally, in comparison to the reference [10], the fuselage was designed to be smaller than expected, and the batteries were under-designed in the previous iteration. As a result, the design underwent significant structural changes as the design progressed and a more detailed analysis was conducted. In conclusion, the design exhibited notable transformations as the level of detail increased.

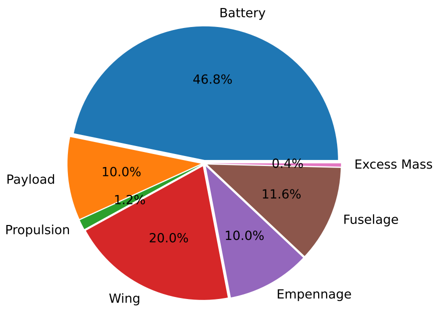

Figure 5.41: Mass budget pie chart for the Fixed-Wing drone.

5.9. Block Diagrams

The hardware block diagram for the Fixed-Wing, shown in Figure 5.42, showcases the components of the Fixed-Wing and their relationship. The main systems are the communication system, power system, propulsion system and payload. The power system regulates the power input of the components through the power distribution and management system. This system is directly connected to the battery pack which feeds the system. The battery discharge rate, battery life and battery performance are monitored and regulated by the battery management system (BMS). Any component that relies on a direct source of power is connected to the battery distribution and management system for its power supply. The red blocks in the diagram indicate the components that are part of the communication system which transmits and receives data from the Guardian ship and other drones. As the mesh radio can only compress and transmit data, the antennas can receive any form of input from the Guardian ship. The Video Processing Unit (VPU) receives the data from the Mantis i45N camera and processes it. The flight controller is the hub of the communication between the various components. It receives data from the VPU and all sensors such as the Inertial Measurement Unit (IMU), Magnetometer, Pitot tube, airspeed sensor, and GPS. Based on these inputs, the flight controller gives commands to the actuators and the ESC. The actuators are connected to the control surfaces of the wing and empennage. The ESC controls the motor input which is directly connected to the propeller.

The electrical block diagram for the Fixed-Wing drone, shown in Figure 5.43, shows the electrical and data connections required for the system to function. The ground connection is omitted from the diagram to limit the complexity of the diagram, since every component is to be connected to the ground plane regardless. The power for all components will be provided by either the 19 $[V]$ converter, or the 5 $[V]$ converter present in the system. The RTK-GPS, being the only component that requires a 3.3 $[V]$ power source, will be connected to the 3.3 $[V]$ output of the flight controller provided by its on-board power converter. To reduce the complexity of the wiring, all components that are connected to the flight controller over the I2C protocol, being the airspeed sensor, the RTK-GPS, and Nvidia Jetson, will be connected to the same data bus. Where voltage levels do not match, logic level converters are introduced to convert the voltage levels between different components to compatible levels.

The electrical block diagram for the Fixed-Wing, shown in Figure 5.43, shows the electrical and data connections required for the system to function. The ground connection is omitted from the diagram to limit the complexity of the diagram, since every component is to be connected to the ground plane regardless. The power for all components will be provided by either the 19 $[V]$ converter, or the 5 $[V]$ converter present in the system. The RTK-GPS, being the only component that requires a 3.3 $[V]$ power source, will be connected to the 3.3 $[V]$ output of the flight controller provided by its on-board power converter. To reduce the complexity of the wiring, all components that are connected to the flight controller over the I2C protocol, being the airspeed sensor, the RTK-GPS, and Nvidia Jetson, will be connected to the same data bus. Where voltage levels do not match, logic level converters are introduced to convert the voltage levels between different component compatible levels.

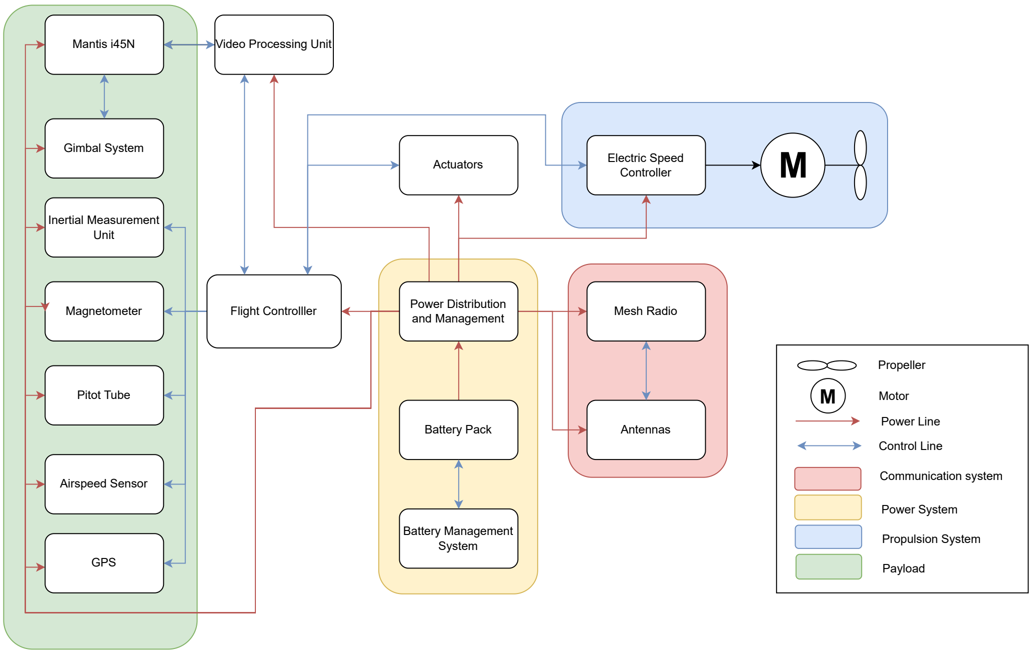

Figure 5.42: Hardware Block Diagram of the FW drone.

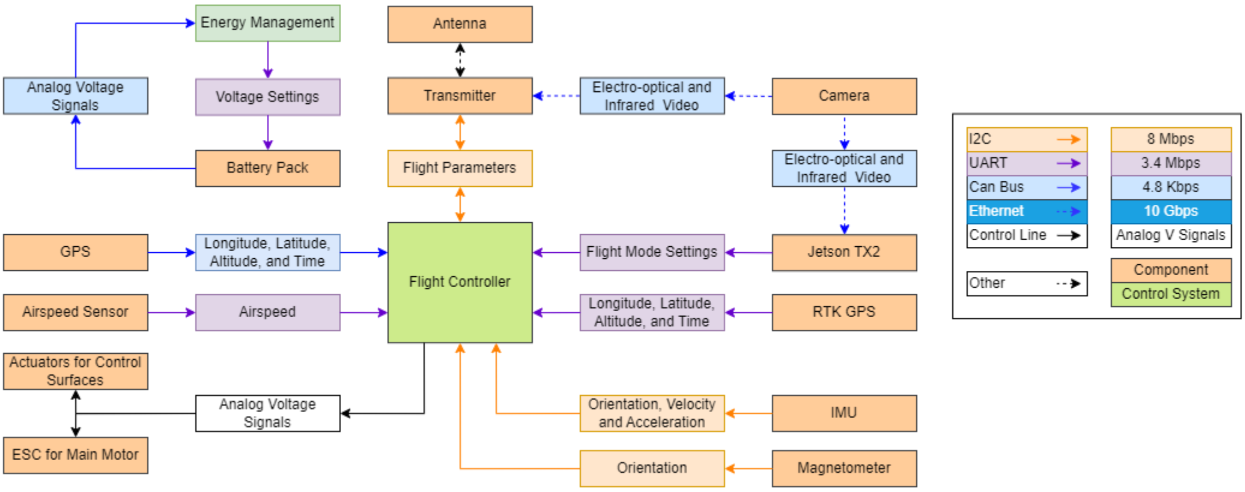

Figure 5.44: Data Handling Diagram of the FW drone.

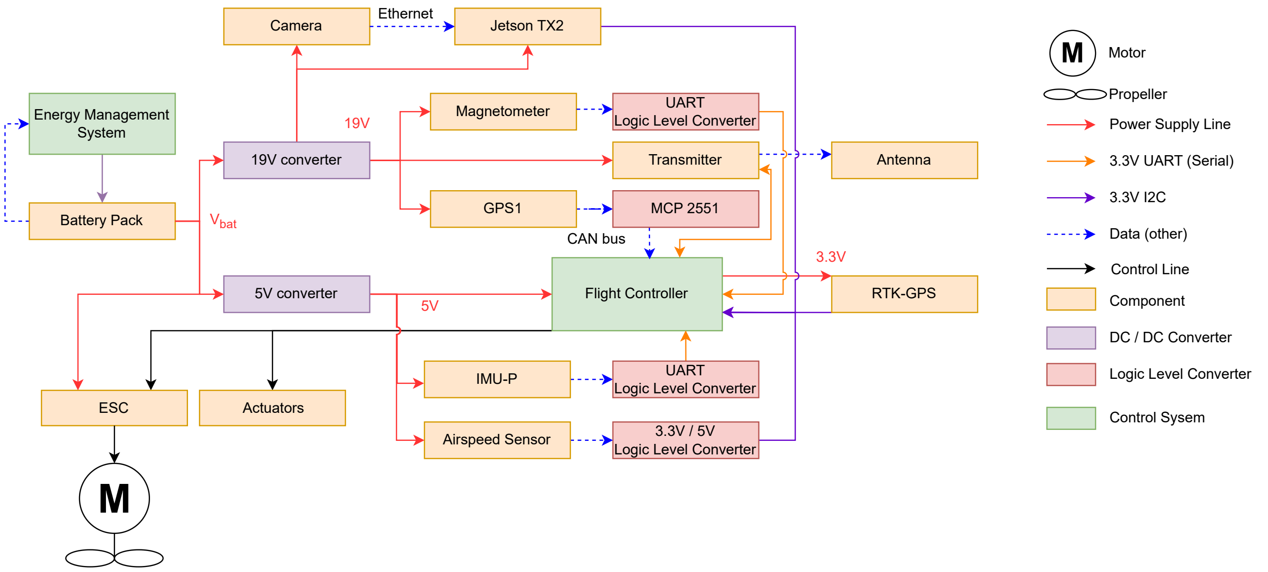

Figure 5.43: Electrical Block Diagram of the FW drone.

5.10. Conclusion

This chapter detailed the design phases undergone to finalise the initial configuration of the Fixed-Wing mission drone system. The main aspects that have been taken into account in all of the design iterations is the autonomous element of the system, being able to withstand the stormy operational conditions and successfully performing the search and rescue mission within the proposed timeframe. These considerations led to a Fixed-Wing design embodying all of the required components, configured in such a way that there is no form of obstruction for the payloads, while obtaining a center of gravity position allowing statically stable longitudinal and lateral characteristics. Additionally, the structural components of the Fixed-Wing have been designed such that the system is able to withstand the severe conditions expected during operation. Finally, the interaction between all of the internal hardware and software systems is considered on the basis of the presented hardware, electrical and data handling block diagrams.The final Fixed-Wing design is showcased in Figure 5.45.

Figure 5.45: The final design of the Fixed-Wing drone.

6
Landing Sequence & Multicopter

Autonomy introduces new challenges in all aspects of the search and rescue mission. One of the most challenging is the safe recovery of the drones to the ship, post-mission. The procedure has to withstand the harsh atmospheric conditions without human intervention. This chapter aims to outline the detailed design of the landing phase.

The landing procedure from an operational point of view will be presented in section 6.1. This is followed by an elaborate overview of the docking mechanism for the mid-air interception of the Fixed-Wing drone in section 6.2. Thereafter, in section 6.3 the detailed design of the resulting optimized Multicopter, whom will retrieve the Fixed-Wing, shall be discussed. After that, block diagrams will be provided in section 6.4 to show interactions between different subsystems. A stability analysis for the coupled system and as a result, joint control during the descent back to the ship is presented in section 6.5, followed by a budget breakdown of the system in section 6.6 to conclude the chapter.

6.1. Landing Procedure for the Fixed-Wing

This section aims to outline the the landing phase: from the point when the Fixed-Wing is approaching back from its mission, up to its safe return onto the ship deck. It details all stages of Phase 4 of the operations and logistics flow diagram in Figure 3.1.

6.1.1. Landing Procedure Selection Summary

The method that shall be implemented for the landing procedure was selected in the preliminary design phase [11]. Before documenting the detailed design of this system, it is important to re-iterate the reasoning as to why this specific landing procedure was selected.

From all the design options, it was decided upon to intercept the Fixed-Wing mid-air by using an untethered Multicopter. This design choice resulted from several options listed below:

1. Untethered Multicopter interceptor
2. Tethered Multicopter interceptor
3. Cable catching system
4. Net catching system

The cable catching system (3) and net catching system (4), were omitted first due to the requirement that the mission has to be fully autonomous. With these systems, once the drone has been caught and brought onto the ship deck, the need for human intervention to ultimately remove the drones from the system is inevitable. In other words, the automation of such systems is very difficult. Moreover, these options require a lot of additional structures on the ship, which would also have difficulties operating in the weather conditions namely, sea state 5 and wind state 7. For instance, a cable catching system such as in [51], requires structural columns several meters tall. With a sea state of 5, These columns would not be stationary and therefore make the interception of the Fixed-Wing drone near impossible.

The reason for a tether would be primarily to provide additional power to the Multicopter such that it can carry out its function with no power limitations. Additionally, it would allow for a more controlled retrieval as, by creating a tensioned cable, additional stability is provided and the drone can be pulled back to a desired location on the ship. It was decided however not to implement the tether as it would induce a lot of disturbances on the Multicopter due to its interaction with high wind gusts (up to 18 [ms^{-1}]). Furthermore, the use of several Multicopters for the landing procedure could be required for higher-volume landings. This could arise the problem that such tether cables would entangle, jeopardizing the safety of the procedure. It is for these reasons that the team opted for an untethered Multicopter interceptor (1).

6.1.2. Landing Requirements

Along with the aforementioned key and driving requirements stated in chapter 2, some further requirements necessary for the design of the landing system are presented in Table 6.1. These requirements only apply to this section and as such, are presented here. As can be seen, some of them are still to be quantified, which will be handled in this chapter, but are already mentioned due to their anticipation.

Table 6.1: Additional requirements for the landing phase.

Requirement code	*Description*
	Landing Requirements
REQ-SYS-LAN-01	The system shall perform the docking at an altitude of 100 [m]
REQ-SYS-LAN-02	The system shall be able to reach a horizontal velocity of at least 25 [ms^{-1}]
REQ-SYS-LAN-03	The system shall be able to withstand 18 [ms^{-1}] wind gusts in any direction.
REQ-SYS-LAN-04	The system shall have an ascent speed of 5 [ms^{-1}]
REQ-SYS-LAN-05	The system shall be able to carry its own weight as well as the weight of the Fixed-Wing.
REQ-SYS-LAN-06	The system shall have enough battery power for at least one landing phase cycle.
REQ-SYS-LAN-07	The system shall have a thrust-to-weight ratio (T/W) of 2.

The requirements displayed in Table 6.1 have been introduced with reason. It is important to discuss their relevance and justify why they are necessary to constrain the landing system design. REQ-SYS-LAN-01 is to clear the turbulent air of the air corridor close near the ship and the ocean surface. REQ-SYS-LAN-02 is to ensure that Multicopter can catch up to the Fixed-Wing when it flies at a stall speed of $V_{stall} = 18[ms^{-1}]$ (a margin will be added later to make this value $V_{1.25 \cdot stall} = 22.5[ms^{-1}]$). REQ-SYS-LAN-03 is derived from the requirement that the drone swarm shall be able to operate in wind state 7 conditions. REQ-SYS-LAN-04 this value was taken from a similar carrier drone that performs the same function [13]. REQ-SYS-LAN-05 this is self evident as it has to carry the Fixed-Wing back to the ship during the landing procedure; its primary function. REQ-SYS-LAN-06 is also self explanatory as it describes also the primary function of the Multicopter. Finally, REQ-SYS-LAN-07 ensures that the Multicopter abides to aerospace design conventions.

6.1.3. Landing Operations and Logistics

The landing phase of the mission entails all stages from the point where the Fixed-Wing drone signals to the ground station (ship) that it is ready for landing, up to the point of its safe retrieval on the ship deck. For this sequence, a mission profile for the Multicopter can be created, which will include three phases: the ascension phase to docking altitude, the interception of the Fixed-Wing drone at docking altitude, and the landing on the ship deck with the Fixed-Wing as seen in Figure 6.1.

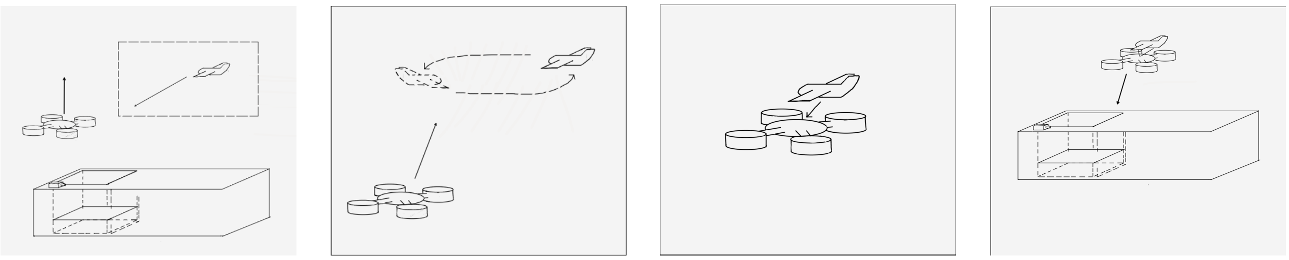

(a) Ascension phase. **(b)** Loiter phase. **(c)** Coupling phase. **(d)** Descent phase.

Figure 6.1: Flight phases of the STORM system.

1. **Ascension Phase:** This phase involves the taking off of the Multicopter from the ship deck up to docking altitude, as mentioned before. The Multicopter shall take off from the START system with maximum thrust

to a predetermined target altitude where it shall intercept incoming Fixed-Wing drone.

2. **Docking phase:** Once the Multicopter has reached the target altitude, it shall adjust its control for docking by adjusting its motion with respect to the relative positioning between itself and the Fixed-Wing drone. After the sequence is complete, the two drones will form one joint coupled system.
3. **Descending Phase:** Once the Multicopter and Fixed-Wing have successfully coupled, the Fixed-Wing will terminate its control and the Multicopter will transition its control to joint control and safely land the Fixed-Wing on the ship (in the START System).

To continue, each one of these three phases will be discussed in detail providing a clear overview of how all three systems (ground station/START System, Fixed-Wing drone, and Multicopter) will work together to successfully carry out the landing procedure.

6.1.4. 1. Ascension Sequence of the Multicopter to Docking Altitude

The ascension manoeuvre of the Multicopter is dependent on the location of the Fixed-Wing drone. It shall be explained in section 6.3 that the battery life of the Multicopter is 5 minutes. This means that to at least satisfy REQ-SYS-LAN-06, the Multicpoter should be as efficient as possible. In other words, it should initiate the landing phase as late as possible.

The Fixed-Wing drone, after it completes its descent from cruise altitude (450 [m]), will enter a loitering track in which it shall be intercepted by the Multicopter. The Fixed-Wing will enter this track (which will be designed under the docking sequence (phase 2)), and cycle through it twice in order to calibrate its control to this flight track and attain the interception velocity; which is essentially the Fixed-Wing stall speed with a safety factor of 1.25. This safety factor was implemented to allow for the slowest speed for docking whilst ensuring the Fixed-Wing does not stall in case of any disturbances. Furthermore, when flying at stall speed, the aircraft will tend to vibrate which is not desired for the docking procedure.

Once the Fixed-Wing enters the loitering track, the START System will initiate the take off of the Multicopter as visualised in Figure 6.2. The Fixed-Wing has, in its flight algorithm, a built in constraint that ensures that it returns to the ship with a remaining battery life of 10 minutes. This has been done to sustain flight during the loiter phase. Once the ground station receives a signal from the Fixed-Wing that it has entered its loitering phase, the START System initiates the ascent of the Multicopter. It shall ascend to an altitude of 100 [m] as prescribed by REQ-SYS-LAN-01 to the docking altitude. The flight profile of this manoeuvre is relatively simple. It shall accelerate at maximum acceleration $a_{V_{max}} = 20.68[ms^{-2}]$ and $a_{H_{max}} = 7.68[ms^{-2}]$ (acceleration values that resulted from the power sizing done in section 6.3), in order to clear the ship, after which it will stabilize and ascend at a constant velocity of $5[ms^{-1}]$. The Multicopter will navigate to the docking entry point where it shall initiate phase two of the landing procedure. This docking entry point is ever-changing, due to the presence of constant wind disturbances and, as such, the unpredictability of a constant loitering track location. The finding of the docking entry point shall be discussed in the docking sequence of the coupling phase. A rendering of the relative positioning of both drones when transitioning from the ascension to docking phase is seen in Figure 6.3.

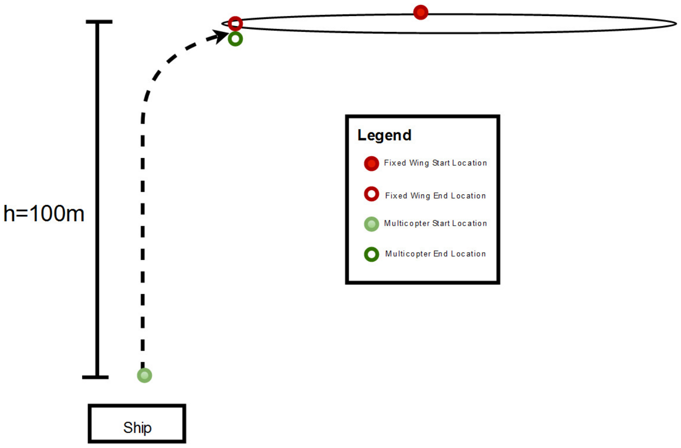

Figure 6.2: Ascension phase visualisation.

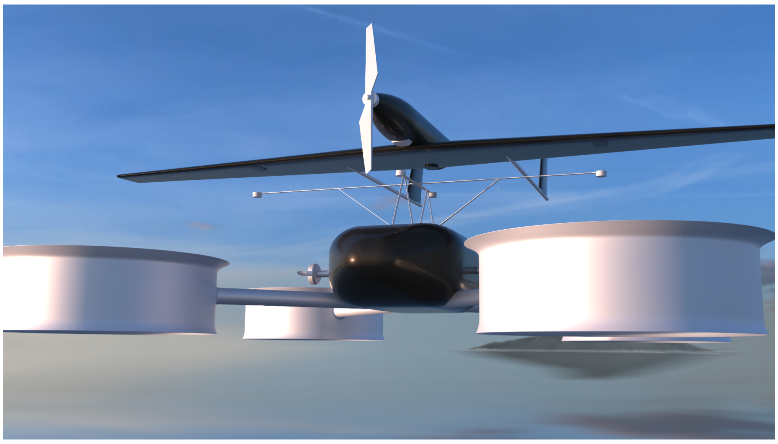

Figure 6.3: Render of the entry point to the docking phase.

6.1.5. 2. Docking Sequence of Coupling Phase

The most complicated stage of the landing phase is the interception of the Fixed-Wing drone. This process requires high precision due to the fact that the clamping mechanism in itself requires high accuracy, as shall be explained in section 6.2, and not to forget the tempestuous conditions make it even more challenging.

The Multicopter will have to locate the Fixed-Wing. An option for this would be that the Fixed-Wing has a predetermined flight path to follow during the landing phase. This route would be a known input for the Multiroter, to which it can then adjust its own flight profile and intercept the Fixed-Wing at a specific velocity, v altitude, h and latitude and longitude. This would work in ideal circumstances, where there are no disturbances to any system. as aforementioned, given the harsh weather conditions, the level of unpredictability is high and even if flight profiles follow the same shape, they will never be the exact same. For this reason, the two drones should communicate with each other such that the Multicopter can adjust its motion to that of the Fixed-Wing drone.

Selection of Communication Method

It is evident that there needs to be a means of communication between the two drones for successful docking. Several methods have been proposed of which one option has been selected. The methods are listed below:

1. **GPS + Aruco Markers:** The two need to work in conjunction due to the fact that Aruco Markers only work with limited detection range and, as such, need a navigation system that brings them into functional range. Once the GPS gets the Multicoper in feasible range, an IR camera will initiate the marker detection feeding

images to an algorithm. This algorithm will estimate the markers' pose in 3D space continuously allowing the tracking of the markers and, as a result, the Fixed-Wing [30].

2. **RTK-GPS:** This GPS is a subcategory of differential GPS systems. It is a newer technology as compared to the traditional GPS, allowing for centimeter accuracy [1]. Differential GPS allows for more accurate positioning by taking into account the difference between the positions obtained from a reference station and the positions obtained from the mobile receivers in the vehicles.

The communication system that was chosen for implementation is the RTK-GPS. As mentioned before, Real-Time Kinematics (RTK) is a specific type of DGPS. It has an increased accuracy over GPS by an order of magnitude of 10^2 [2]. This level of accuracy is beneficial in the precise positioning of the drones. Furthermore, RTK provides real time data, as is hinted in its name. With a real-time stream of data, the Multicopter will be able to know the exact accurate position of the Fixed-Wing instantly; enabling it to adjust its controls and ultimately positioning quickly.

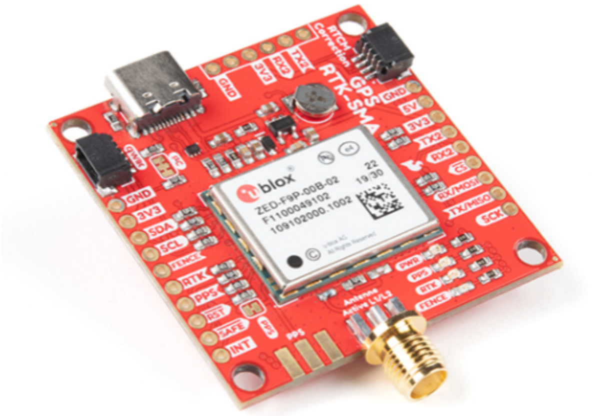

Figure 6.4: Image of the SparkFun GPS-RTK-SMA Breakout - ZED-F9P [52].

Each of the three options are feasible in theory, however for this application RTK-GPS is the best. The combination of Aruco Markers and GPS in itself is less efficient as it requires two different techniques to achieve docking. This is due to the fact that GPS is not accurate enough (meter-level accuracy) and Aruco markers have limited detection range [30]. This detection range heavily depends on factors such as the size of the markers, the lighting conditions and further distortions. Furthermore, The markers need to be placed such that they are visible to the Multicopter with a high level of stability. This would be difficult to achieve if the Fixed-Wing is constantly susceptible to wind gusts. Finally, this technique requires the use of a high-resolution infrared camera by the Multicopter. Adding a sensor to a system that is not a key sensor (the system can achieve its tasks without it) would then rather not be added.

The RTK-GPS that was decided upon is the *SparkFun GPS-RTK-SMA Breakout - ZED-F9P* [52]. This is one of the latest releases of powerful RTK boards and allows for 10mm three-dimensional accuracy. It will provide knowledge of the X,Y,Z location of both the Multicopter itself and the Fixed-Wing drone as well.

Fixed-Wing Drone Landing Track

As mentioned under the ascension phase (phase 1), the Fixed-Wing will enter a loitering track. The exact shape and size of this track needs to be determined. It was tailored to optimize the ease of docking with the additional constraint of finite battery power. To be more specific, the drones each have a limited battery life. The Multicopter has a battery life of 5 minutes and the Fixed-Wing 10 minutes as mentioned in subsection 4.1.2. As such, the loitering track cannot be too long in case of a missed interception.

---

[1] URL: https://gssc.esa.int/navipedia/index.php/Differential_GPS [accessed on 15-06-2023]

[2] URL: https://globalgpssystems.com/gnss/rtk-gps-understanding-real-time-kinematic-gps-technology/ [accessed on 15-06-2023]

It was chosen to opt for an oval shaped loiter phase. The reason behind this is to aid the docking. The docking manoeuvre needs to occur in straight horizontal flight as shall be explained in section 6.2 due to the clamping method used. Furthermore, the distance of this straight phase needs to accommodate for a long enough window such that there is enough time to dock. By field research conducted at the MAVlab at the Delft University of Technology, a 10 [s] window was found to be viable for a successful docking manoeuvre when using the clamping mechanism designed in section 6.2. The velocity of the fixed wing during loiter is $V_{1.25 \cdot stall} = 22.5[ms^{-1}]$. With this speed, a 225 [m] stretch is needed for successful docking. Adding a small margin of 1 [s] to account for any misalignment of the Multicopter when it enters the docking track, makes this length 250 [m]. This was deemed viable as the Multicopter has maximum horizontal velocity, $V_{H_{max}} = 25[ms^{-1}]$ according the propeller sizing in section 6.3. This manoeuvre shall only be carried out when there is headwind. If there is a tailwind, the drones will have a larger ground speed due to the added wind velocity vector and, as such, cover the 250 [m] stretch in < 11[s].

The next step, is to size the circular sections of the oval. According to [50], this turn can be sized in multiple ways. It was decided to size for the minimum turn radius to keep the track flight distance as short as possible. The limiting factor for this is the load factor the Fixed-Wing can sustain. In subsection 5.7.2 it has been calculated that the maximum manoeuvre load factor is 3. Taking a margin on this, it was decided to size the turn using a load factor of 2. Using equation Equation 6.1 from [50], where $V = V_{1.25 \cdot stall}$ and n = 2, the turn radius $R_{turn} = 29.79[m]$. A visualisation containing the loiter trach shape and dimensions is presented in Figure 6.5.

$$R_{turn} = \frac{V^2}{g \cdot \sqrt{n^2 - 1}} \tag{6.1}$$

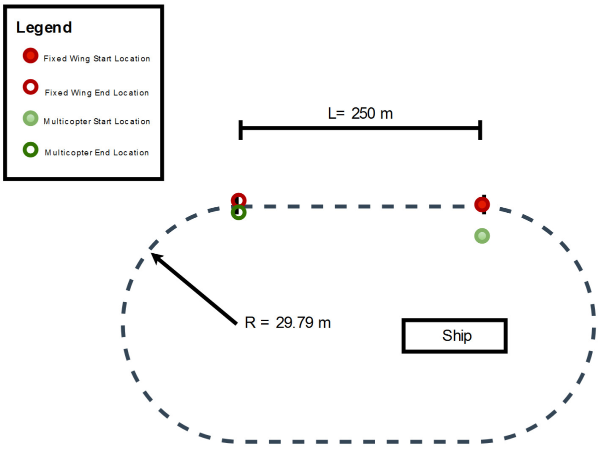

Figure 6.5: Docking phase loiter track visualisation.

Docking Sequence

The docking sequence is visualised in Figure 6.5, where it is shown that the entry point for the Multicopter into the loitering. It has been explained that Real-Time Kinematics (RTK) GPS shall be used for the inter-communication of the two drones. During the ascension phase (phase 1), the Multicopter will use its RTK-GPS to track the Fixed-Wing in order to position itself at the correct docking entry point. This portrays one of the reasons for the loitering drone to perform two calibration laps of the loiter track. It not only does it for itself, but also to relay real-time data of its loiter tracks to the Multicopter; with which the Multicopter can predict the docking entry point. As highlighted before, these tracks are never the same, even if the differ slightly. As such, along with the stored track data, the differences (misalignments) between each track can be corrected for with a constant flow of real-time positioning data.

The Multicopter will approach the Fixed-Wing from underneath for clearance proposes (so that there is no hindrance from the Multicopter rotors). Once the docking phase has initiated, the Multicopter will use its side rotors (sized for in section 6.3) to provide increments of thrust to ultimately dock with the Fixed-Wing. The required precision of this manoeuvre governs the design and configuration of the rotors/propellers in section 6.3.

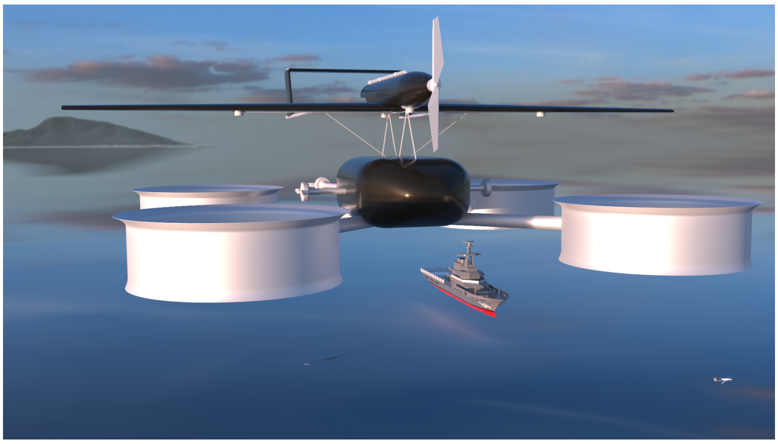

Figure 6.6: Visualisation of the joint system after completion of the docking phase.

6.1.6. 3. Descent and Ship-Deck Landing Sequence

Once the Multicopter has intercepted the Fixed-Wing, forming a joint coupled system, it shall prepare for the descent back to the ship. The Multicopter has a flight controller that is configured for joint control. It is programmed to take into account the combined moments of inertia of the two drones combined as well as all the aerodynamic forces that would act on the system. The mathematical model for this system and the resulting simulation and analysis are presented in subsection 6.5.2.

For the joint control of the system, there is a possibility to use both drones to carry out the control function in conjunction. However, implementation of a simultaneous control with both drones that coordinate the exact same is very difficult. This would require both control systems to be programmed to function the exact same by reacting to the environment equally and at the same instant. They drones will induce forces to each other through the connection points, for which the control systems should be programmed to account for and not interpret as a disturbance. The probability of conflict arising between the two systems, as such, is high which would jeopardize the flight of the joint system. Furthermore, the use of the wing control surfaces to steer the drones back to the ship is inefficient as compared to controlling the system by using the drone rotors. The Multicopter can be over designed for its function and specifically for the landing procedure, meaning it would be more efficient to use its capabilities for this procedure. With this being said, the Multicopter will perform all controls on its own throughout the descent. Therefore, once in coupled state, two important things happen, namely:

1. Fixed-Wing propulsion system shut-off
2. Multicopter braking manoeuvre

The Fixed-Wing will thus be a payload for the Multicopter as it can carry out its function as a ”carrier drone”. The Multicopter will subsequently slow down the system from $V_{1.25 \cdot stall}$, by means of aerodynamic drag and/ or reverse thrust of the side propellers (sizing carried out in section 6.3. From this point onwards the Multicopter will descend by providing a thrust-to-weight ratio (T/W) such that a descent speed of 3 $[ms^{-1}]$ is achieved. A visualisation of the descent phase is displayed in Figure 6.7. In ideal conditions (no resistance), this can be achieved with a T/W of 1. However, due to realism of the situation along with the harsh weather conditions, it is more complex than that. For this reason, the T/W will most likely be lower than 1. During this process, it will communicate with the START System to locate the ship for terminal landing.

Once the system has reached an altitude of 20 [m] above the ship (to clear any turbulence caused by air flow around the ship architecture), the Multicopter will enter a hovering state to calibrate for landing. At this point, the drone will use the real-time positioning data from the START System to gather data on the exact movements of the ship in the ocean. With this data it shall be able to impersonate the movement of the ship to accomodate a safe landing into the START System. Finally, it shall land the Fixed-Wing drone onto the ship (the RTK-GPS location is the landing location) and prepare for another landing phase or recharge its battery in the mean time.

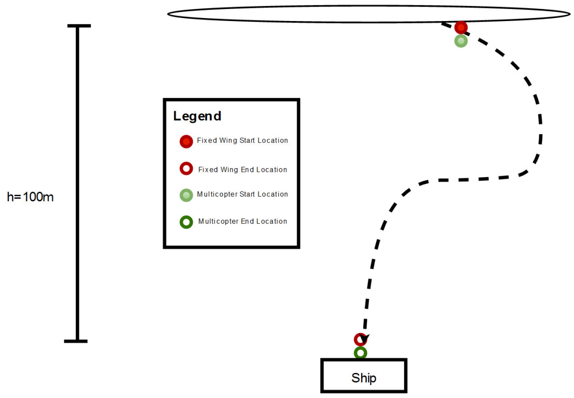

Figure 6.7: Descending phase visualisation.

6.2. Clamping Mechanism for the Docking Phase

As mentioned before, it has been decided to intercept the Fixed-Wing drone mid-air for landing. This arises the necessity to design and conceptualize an interception mechanism. There are multiple ways to achieve this, and therefore the upcoming section will outline the design and selection of the clamping mechanism.

6.2.1. Clamping Mechanism Design Options

Intercepting an aerial vehicle mid-air is not an easy exercise and requires intricate engineering. There are two main categories of clamping methods that were considered: mechanical and non-mechanical clamping. Instead of looking at a variety of different methods, it was decided to branch into one of these categories to narrow down options as much as possible and prevent the need of analysing a wide range of options.

Both categories of clamping are beneficial depending on the application. For this reason, it is important to carefully assess which type would better suit the aerial interception of a drone. Mechanical clamping methods relies on mechanical components. This could be for instance a two components locking into each other (e.g in a ball and socket configuration), or one component clamping itself onto the other. Examples include screw clamps, hinged clamps, toggle clamps etc.... Such mechanical methods are usually used in applications such as machining [3]. The non-mechanical clamping methods do not employ such methods but rather create surface tensions between two objects. Examples would include electromagnetic clamps or vacuum clamps.

Mechanical clamping methods require the engineering of an extra structure, in other words, the mechanical components used for attachment. Moreover, these components would have to integrated into to the *structure of the Fixed-Wing* without compromising the aerodynamic shape and therefore, functionality of the Fixed-Wing. Adding such a structure to the drone whilst not impeding its capabilities but also providing a secure and reliable camping mechanism would require, a lot more capital in research and development. Furthermore, the addition of such a system would increase the drone weight and compromise the flight performance of the Fixed-Wing.

On the other hand, non-mechanical clamps offer attractive benefits for the application at hand. Since most of these methods only require surface contact for clamping, the ease of attachment and detachment is faster than for mechanical methods. There is no need for the actuation of mechanical components to secure themselves, but rather just feasible proximity of two surfaces. Furthermore, methods such as electromagnetic clamping can carry out this attachment and detachment very fast, which allows for a higher success rates during the docking phase and, in case of errors in the joint control, can detach quickly to separate the two drones from each other. Non-mechanical clamping methods are preferred in in cases where attachment is difficult due to exotic shapes

---

[3] URL: https://www.engineeringenotes.com/industrial-engineering/machine-tools/clamping-devices-rules-and-types-fixtures-machine-tools-engineering/23622 [accessed on 07-06-2023]

and sizes of parts [4]; especially of fragile parts. It was for these reasons that non-mechanical clamping was opted for as a clamping mechanism.

From this category, **electromagnetic clamping** was chosen, as it is easier to control as compared to methods such as vacuum clamps. A power supply would be fed to the magnets as they would be built into the electrical system of the Multicopter as presented in Figure 6.13. This supply is regulated and controlled by the on board central processing unit (CPU) and, as such, can be activated/deactivated at any time with precision, allowing for fast control of any attachment/detachment that needs to occur during landing.
The use of electromagnetic was further motivated by the fact that there are no electromagnetic interferences (EMI) at open sea. In congested urban areas, the interference of prominent magnetic fields could interfere with the workings of the clamping method [5].

6.2.2. Selection of Plate Material and Electromagnets

Having decided upon electromagnetic clamping, the next step is to design and select the clamping interface. As mentioned before, this method employs a surface tension between the electromagnet and magnetic material without any mechanical components. As such, the electromagnets and a suitable magnetic material needs to selected.

Figure 6.8: Image of the electromagnet 25kg - 12V DC - JF-XP4020 [56].

Selection of Electromagnets
The electromagnets need no further design as readily existing COTS electromagnets can be used. It is just a matter of which exact one to select. The main driving factor is the *strength of the electromagnetic holding force* that the magnets create. Furthermore, their weight needs to be taken into consideration, as the required thrust-to-weight ratio of the Multicopter must not be compromised.

The Fixed-Wing has a mass of 25 [kg]. Since it is being carried (it lies on top of the Multicopter), the Multicopter does not have to carry its weight. It was however decided, as an initial estimate, to select an electromagnet that has a holding force equal to the Fixed-Wing weight, such that in any mode of failure, it can still carry the load of the Fixed-Wing weight. A further analysis on the impact of aerodynamic forces shall be carried out in subsection 6.2.3 to validate the strength of the electromagnet. The chosen electromagnet is the *Electromagnet 25kg - 12V DC - JF-XP4020*. Its specifications can be found in Table 6.2. As shall be evident in the power budget of the Multicopter in section 6.3, this electromagnets draws very little power (1W), meaning it does not compromise the power distributed to the rotors for thrust.

---

[4] URL: https://www.engineeringenotes.com/industrial-engineering/machine-tools/clamping-devices-rules-and-types-fixtures-machine-tools-engineering/23622 [accessed on -07-06-2023]

[5] URL: https://www.electronicdesign.com/technologies/power/whitepaper/21179428/electronic-design-emi-shielding-for-drones-and-uavs[Accessed 06-06-2023]

Table 6.2: Electromagnet 25kg - 12V DC - JF-XP4020 specifications [56].

Specification Parameter	Value
Height	20 [mm]
Diameter	40 [mm]
Depth Mounting Hole	15 [mm]
Holding Force	25 [kg]
Supply Voltage	12 [v]
Mass	0.150 [kg]

Selection of Magnetic Plate Material

The plates used for the clamping interface need to excel in two main properties: *magnetic permeability* and *corrosion resistance*. Magnetic permeability defines the ease at which it can magnetize and retain this magnetization [6]. Secondly, since the the drones are operating in saline conditions, the material also needs to have a degree of corrosion resistance to prevent degradation and as a result, functionality decline. A material with the optimum coalescence of these two properties was chosen. Iron (Fe) excels in magnetic permeability property, however pure iron is soft and has horrible corrosion resistance. as such iron alloys need to be considered instead. As such, three materials were considered:

1. Permalloy (nickel + iron alloy)
2. Mu-Metal (nickel + molybdenum + balance Iron)
3. 300 Stainless Steel series

Permalloy and Mu-Metal primarily consist of a high percentage of Nickel, which enhance their corrosion resistance. However, as compared to other materials they still do not perform as good when in terms of corrosion resistance, especially against materials designed for marine environments. The saline conditions will degrade the material over time, and reduce their functionality. As such, research one higher corrosion resistant materials was necessary; from which stainless steel (ferritic material) arose. Stainless steel has excellent corrosion resistance due to the presence of chromium [7]. They do have worse magnetic properties as compared to soft magnetic alloys (such as Permalloy and Mu-Metal, and are generally not used for their magnetic properties. The 300 series is shows the best magnetic properties of the stainless steels however require significant deformation for desirable magnetic properties. From result of this analysis was that a more innovative material would be required to maximize the performance required.

In order to accommodate for magnetic properties as well as corrosion resistance, a new material is proposed in [21]. It discussed Fe-based amorphous alloys that exhibit ”excellent corrosion resistance and soft magnetic properties”. A lot of alloys that possess high corrosion resistance contain Chromium (Cr). However, this addition brings a significant reduction in magnetic field strength, B. For this reason, silicon based Fe-based amorphous alloys were explored. The addition of Silicon (Si) as described in [21], provides significant corrosion resistance whilst maintaining good soft magnetic properties (high B). The cost of this raw material is also low, reducing the overall material cost of the drone.

The proposed material is $Fe_{83.3}Si_1B_{15}Cu_{0.7}$ *amorphous alloy*. This material exhibits high magnetic field strength, B up to 1.66T in conjunction with low corrosion resistance. It is a promising alloy for the application of electromagnetic clamping and, as such, is selected in this plate material selection.

6.2.3. Location of Electromagnets and Fe-Based Amorphous Alloy Plates

Having decided upon an electromagnetic clamping mechanism, its integration into the design of both the Multicopter and Fixed-Wing requires good systems engineering. It depends on a lot of factors and must ensure that the workings of both drones is not compromised by any means.

The Fixed-Wing is the driving component on the placement of the attachment points, and the Multicopter will have to be tailored for resulting placements. The main factors that determine their location are the resulting stability of the attached Fixed-Wing (moments from the clamping forces are strong enough to keep the Fixed-Wing steady

---

[6] URL: https://www.engineeringtoolbox.com/permeability-d_1923.html [Accessed on 19-06-2023]

[7] URL: https://blog.thepipingmart.com/metals/chromium-corrosion-resistance-an-overview-2/ [Accessed on 19-06-2023]

on the Multicopter), the fact that they need to be placed at a rigid point, and their distance from magnetically influenced sensors (electromagnetic interference (EMI) avoidance).

Stability of Fixed-Wing in Coupled State

The distribution of plates around the aircraft needs to be such that the aircraft is as stable as possible. In other words, the moments induced by the clamping force need to be strong enough to counteract the aerodynamic moments imposed on the Fixed-Wing. This applies in both the lateral (roll) and longitudinal (pitch) direction: M_x and M_y respectively. If the attachment points are placed along one line (in either direction) then one of these moments will not counteract all possible aerodynamic moments, depending on its relative location to the CoG. For instance, if it induces a positive moment around the CoG but the aerodynamic moment around that axis is also positive, then the Fixed-Wing will tilt around that axis. This already induces a constraint that the attachment points need to at least come in pairs, and be placed on *either side of the CoG*. Since this must be the case in both the x an y directions, it enforces the need of a 2-dimensional spatial layout. From this it can be concluded that there will be two magnets along the y-direction on the wing, and two along the x-direction on the fuselage. It would be ideal that the attachment points are aligned with the CoG in both directions, so that the EM forces do not introduce moments around multiple axes. For the x-direction, this is possible as this axis runs through the middle of the fuselage. In the y-direction it is slightly more complicated. The positioning of the plates in this direction depends on other constraints, which will be discussed hereafter. Sufficiently large moments can be created by increasing the moment arms of the electromagnetic forces as much as possible. This is however, constrained by the structure of the wing and the payloads on the fuselage.

Attachment at Structurally Rigid Points

The attachment locations are points where loads are transferred from one drone to another. These can be both tension and compression loads. It serves as an interface in the joint coupled system through which these forces are introduced into the Fixed-Wing from the Multicopter and vice versa. For this reason, it is vital that these locations are the most rigid of the structure. The steel plates on the wing will be aimed to be placed underneath the spars of the wing (that run spanwise from the root to the tip of the wing as discussed in chapter 5). The fuselage mounted plates should be located where there is a reinforcement structure within the fuselage, such that they are not just placed on the fuselage skin. If the plates would be placed at a structurally weak location, e.g where there is only fuselage or wing skin, it could lead to bending and damage of the structure due to the induced loads.

In subsection 5.1.2 it is explained that a dihedral angle [5 °] is designed for the wing that starts at the midpoint of the wingspan on each side of the wing. In order to make this structurally feasible, in subsection 5.7.6 the internal layout of the wing was designed from which the structural constraints for the plate locations stem. Ribs are placed at the transition from straight wing section to dihedral wing section to provide rigidity. Along with this, a single spar runs from the root of the wing up to the transition point. This spar is necessary to prevent buckling, however its chord percentage location is variable. For this reason, it was decided to position this spar so as to accommodate for the plate locations. It was justified that all attachment points should be in line with the CoG. This location is at $\approx$30% chord. As such, the spar will run at this chord location.

Distance from Magnetic Sensitive Sensors

the Electromagnets on the Multicopter attract the magnetic plates on the Fixed-Wing by creating a magnetic field that will attract, when in close enough proximity, these plates. The problem with the presence of such magnetic fields is that it could interfere with magnetic sensitive instruments or sensors in either drone, more specifically, the Fixed-Wing. The relation between the magnetic field strength, B and the distance from the source has an inversely proportional relation according to the inverse square law : $B \propto 1/r^2$ [23]. In other words, the magnetic fields strength does rapidly weaken the further away from the source. This is in the ideal case, where the magnetic fields are uniform and not influenced by any external factors. The case at hand is of course a non-idealized case where such a relation is not linear. However, even though the magnetic field may not be uniform and difficult to visualise, there are no further materials around the system that have high magnetic permeability. To be more specific, materials with high magnetic permeability can easily be magnetized in the presence of a magnetic field [23]. These materials can amplify the magnetic field, more so known as magnetic induction, which would distort the general relation of the inverse square law. Since this is not the case, as most of the Fixed-Wing consists of carbon fibre and Aluminium 2048 (these materials have low magnetic permeability), the magnetic field strength, B will therefore still reduce the further away from the electromagnets regardless.

As mentioned before, the necessity of a highly accurate docking system, stems from the fact that the magnetic field formed by the electromagnets weakens rapidly. it may be strong near the source, but after centimeters, it is barely felt [23]. As such, it has been concluded that once the magnets are removed from any magnetic sensitive sensor by an order of at least 10 [cm], it can be assumed that there is negligible influence on the functionality of these sensors. On board of the Fixed-Wing, the only magnetic sensitive sensor that could potentially have its functionality compromised, is the *magnetometer*. For this reason, the positioning of both the sensor and the electromagnetic attachment points shall be closely examined.

6.2.4. Resultant Placement of Attachment Points

Selecting a material for the plates is important, however their physical dimensions are equally important. The sizing of the plates depends on two main properties: *aerodynamic interference* and *relative size compared to the electromagnet*. As can be seen in Figure 6.9b the front attachment point is the only one that really protrudes out of the Fixed-Wing shape. For this reason, a fairing was placed around it to minimize its disturbance. The same was done for the wing plates, due to the fact that the airfoil shape is not exactly horizontal, however the the offset is minuscule and, as such, the fairings are small.

The size of the exact plates is sized based off the diameter of the electromagnets (40 [mm]). The size was made sure to be at least double the surface area of the electromagnets. The plate shapes are oval with a length $l = 20[mm]$ and radius $r = 28[mm]$.

Note: The addition of these plates was not incorporated into the aerodynamic analysis, so to get a more concrete prediction on their influences, an iteration of the aerodynamic analysis is necessary.

Having taken into consideration all of the above mentioned, the attachment point locations resulted. The two wing placed plates shall be at the midpoint of the wing at the transition to the dihedral, at 30% chord to align with the CoG. The Fuselage mounted plates will be placed under bulkheads: one at the aft bulkhead and one at the first frame bulkhead (ahead of the battery). Their locations with respect to the CoG are presented in Table 6.3. These dimensions are superimposed for the frame of the Multicopter that shall hold the Fixed-Wing.

Table 6.3: Attachment locations with respect to CoG.

Component	Location [mm]	size [-]
Aft x-axis Plate	230	$\varnothing$ 40
Front x-axis Plate	200	$\varnothing$ 40
Aft y-axis Plate	750	$\varnothing$ 40
Front y-axis Plate	750	$\varnothing$ 40

(a) Fixed-Wing plate locations.

(b) Clamping mechanism in coupled state.

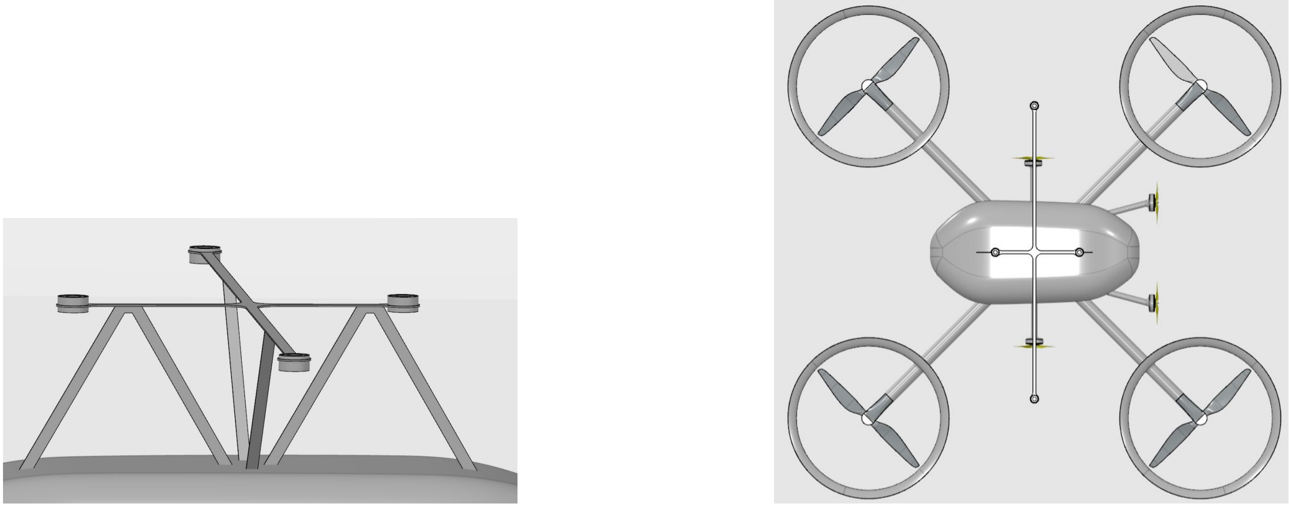

(c) Frame structure with electromagnets.

(d) Frame structure top view on the Multicopter.

Figure 6.9: Visualisation of the electromagnet clamping mechanism with with attachment points on the Fixed-Wing in (a), coupled system attachments in (b), the frame structure in (c), and the frame top view on the Multicopter in (d).

6.3. Multicopter Detailed Design

To counteract the side wind gusts two options were proposed: using eight rotors in co-axial Quadcopter formation, or using four rotors, with a combination of side propellers.

In the first case, the drone would have to tilt at an angle to have a component of lift in the horizontal plane. This would induce a horizontal movement. In the second case, the rotors are solely used for lift production and the side propellers are solely used for horizontal motion.

To aid the manoeuvre and compatibility with the Fixed-Wing drone during the manoeuvre it is best that top of the Quadcopter and the bottom of the fixed drone are parallel with respect to each other. Because of this, it is decided that the landing drone will adopt a Quadcopter formation with side propellers to strafe horizontally while still keeping a constant altitude. (In the case of the Octocopter, tilting would affect the lift produced. This tilt angle and nuanced motion may be detrimental to the clamping mechanism, therefore it is preferred to have a level ”platform”. In addition to this, having separate propellers for sideways motions is less complex than having a combined rotor system which eases the control system). The sizing of this Quadcopter will be outlined in the following sections.

Preliminary Multicopter Design Summary

This section describes the design process the team underwent to determine a Quadcopter formation. To outline the requirements that affect take-off an abridged requirements table is presented below

\textbf{Requirement ID}	\textbf{Requirement Description}
REQ-STK-MIS-02	The drone system shall be able to operate in at least wind force 7
REQ-STK-MIS-04	The drone system shall be able to take-off autonomously from the ship deck
REQ-STK-SAR-02	The system shall not require any personnel near the drone during the operational time
REQ-STK-SYS-03	The individual nodes shall not have a total operational weight exceeding 25 kilograms

To accommodate these requirements and to facilitate a safe and steady landing, a tethered drone that will undergo a mid-air landing manoeuvre with the Fixed-Wing drone was decided upon; where the Fixed-Wing drone would slow down to its stall speed and loiter in a circular motion above the ship [11]. The tethered drone will meanwhile launch from the ship deck and coupled with the drone from behind.

This scenario is ideal when only considering one tethered drone as the tether is unimpeded. However, when considering multiple tether drones, due to the strong wind gusts and the fact that the tether-drone will attempt to match the fixed wing's circular motion, the issue of the tethers tangling with each other arises. Due to the nature of the swarm, it is expected that multiple Fixed-Wing drones return to the ship to land at a time. In order to facilitate this, the tether was removed from the tether drone.

This has a negative effect on battery life as the drone can no longer be considered to have infinite power, however since the landing manoeuvre duration is relatively short compared to the mission duration, it is assumed that the battery life is sufficient for at least one landing manoeuvre. Therefore, it is concluded that the tether-drone is changed to a conventional Quadcopter formation. The sizing of such is elaborated in the following section

6.3.1. Propeller Sizing of the Multicopter

During the initial stage of propeller sizing, the coupling phase is identified as the most constraining phase. This is the case where the Fixed-Wing is now attached to the Quadcopter and the coupled system encounters an 18 $[m \cdot s^{-1}]$ wind gust. The hybrid system is assumed to be a 3x3x1.5 metre cuboid for the preliminary drag calculations. From this, a preliminary required thrust can be deduced using Equation 6.2.

$$T_{req} = m_t g + \frac{1}{2}\rho V^2 C_d A \tag{6.2}$$

Where m_t is the total mass of the coupled system, V is the wind gust velocity, and C_d is the assumed drag coefficient [8].

Following the required thrust, the required rotor diameter is determined from Equation 6.3. Equation 6.3 describes the thrust produced from a rotor with blade area A, thrust coefficient c_t, rotational speed ω, and blade radius R. This is shown in Equation 6.3.

$$T_{rotor} = c_t \rho A(\omega R)^2 \tag{6.3}$$

The expression ωR describes the tip velocity of the blade. The thrust coefficient is a property of the blade shape and characteristics and is determined experimentally. At this point in the design it is not possible to determine a value and a reasonable value based on literature is used. In addition, in order to avoid compressible behaviour of the air, the wing tip velocity is sized to not exceed 80% the speed of sound[9]. With this constraint. The blade area, radius, and rotational velocity can be determined.

6.3.2. Power Sizing of the Multicopter

With the blade dimensions, it is now possible to determine the power required to produce the required thrust; The power drawn from the motor/battery is due to 3 main factors, The power used to climb P_c, the power to hover (Induced Power) P_i, and the power to overcome the profile drag of the rotors P_o, other power losses are assumed to be negligible. [10] The equation for total power consumption to generate a given rotor thrust is given

---

[8] The coupled system is modelled as a 3x3x1.5m cuboid as stated. As such, a drag coefficient of a cube is assumed; As in reality, the coupled systems characteristics will not reflect these assumptions, the required thrust is an overestimation. This assumption, therefore, negates the use of a safety factor

[9] It is assumed that this is in sea-level conditions

[10] As the required thrust already accounts for the body drag of the coupled system this is not considered in the power estimation

in Equation 6.4.

$$P = P_c + P_i + P_o = \left(TV_y - \frac{k_i}{2}TV_y + \frac{k_iT}{2}\sqrt{V_y^2 + \frac{2T}{\rho A}}\right) + \rho A V_{Tip}^3 \left(\frac{\sigma C_d}{8}\right) \tag{6.4}$$

Where Vy is the effective wind speed, k_i is a factor to account for power loss due to ”rotor tip losses, non-uniform inflow, wake swirl, non-ideal wake contraction, and a finite number of blades’ effects on the aircraft” [33], σ is the solidarity; the ratio of actual blade surface area to the area spanned by the blade, and C_d is the drag coefficient of the blade. k_i, σ, C_d are properties of the blade and therefore literature values are used.

It should be noted that the rotors are being sized on the most constraining case in the ”coupling” flight stage. Considering also that the first phase only considers the mass of the Quad-copter alone and the drag overestimation, It is assumed that the thrust of the coupled system in hybrid is sufficient for the first flight phase to climb. The climb rate will be later determined by the excess rotor power.

6.3.3. Propulsion System Selection

Using the values for required power, thrust, and blade, the battery technology, motor, and propeller can be decided upon from commercially available technology. The selected motors are the MN801-S KV120, and V10 KV160 from ”T-motors” (https://store.tmotor.com/goods-1111-V10+KV160.html). In addition, the battery technology chosen is from Amprius [11].

Structural and Vibrations Analysis

A sizing to determine the rod diameter is conducted. Using the free-body diagrams shown below, the rod diameter is given as 6cm with a thickness of 1 mm for a material choice of aluminium 2024. In addition to this, assuming the rod acts as a Newton spring under forced vibrations due to the motor. The natural frequency of the spring is 27% of the forced vibration frequency, meaning that resonance is not a substantial issue and will therefore not be considered.

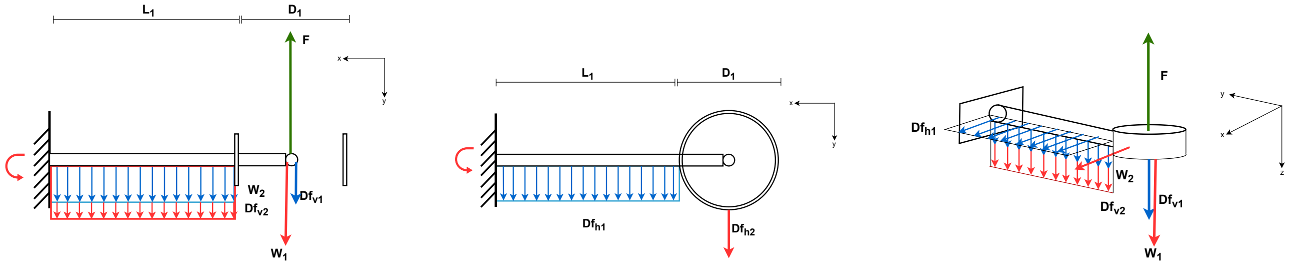

(a) Rotor frame FBD side view.

(b) Rotor frame FBD top view.

(c) Rotor frame FBD three-dimensional view.

Figure 6.10: Free Body Diagrams of the rotor frame structure.

Detailed Design

Using the initial values for the drone, a Catia model can be produced. This allows for a more accurate estimation of the drag. Using visual editing software, it is possible to determine the frontal, side, and top/bottom surface areas of the quadcopter. As seen below in:

---

[11] URL: https://amprius.com/the-all-new-amprius-500-wh-kg-battery-platform-is-here/

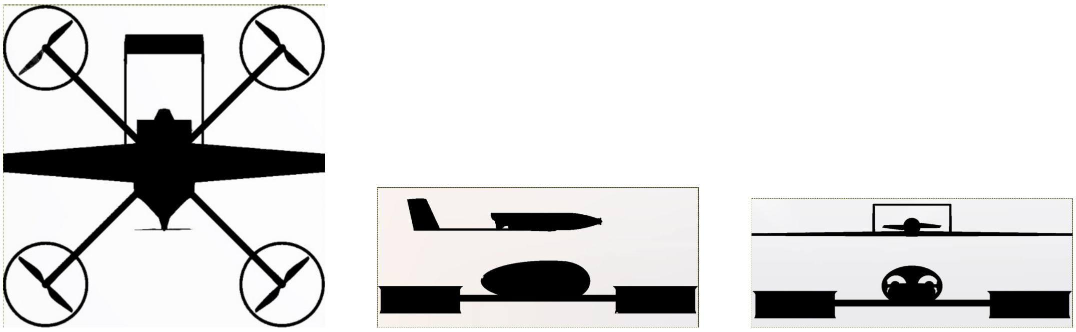

(a) Top Silhouette View **(b)** Side View **(c)** Front View

Figure 6.11: Visualisation of clamped Fixed-Wing and Multicopter system silhouette views

Using these new values for the surface area of each face of the coupled system the sizing process described in 6.3 can be updated. The updated table is presented below:

Table 6.4: Multicopter selected motors, rotors and battery technology.

Parameter	Value Justification	Lift Rotors	Side Prop	Front Prop (2x)
T_req [N]	Determined	517.0	187.5	241.17
T_req (Per rotor/prop) [N]	Determined	129.3	187.5	110.7
R [m]	Determined/Set	0.36	0.1	0.1
A [m^2] (For Drag Estimations)	Determined	Quad: 1.157 Hybrid:1.985	Quad: 0.690 Hybrid:0.899	Quad: 0.604 Hybrid:0.764
C_d Profile [-]	From Literature	1.05	1.05	1.05
C_t [-]	From Literature	0.065	0.065	0.065
\omega [rads^-1]	Determined	761.1	2740	2740
\sigma [-]	From Literature	0.07	0.07	0.07
C_d Blade[-]	From Literature	0.036	0.036	0.036
k_i [-]	From Literature	1.15	1.15	1.15
P_req_Total [kW]	Determined	25.08	42.22	26.2
COTS	-	-	-	-
Motor Thrust (Max Total) [N]	COTS	1098.72	1098.72	118.47
Motor Weight (per rotor) [kg]	COTS	0.865	0.865	0.470
Motor Weight (Total per axis) [kg]	COTS	3.46	1.73	0.94
Battery Weight (Total For Whole System) [kg]	COTS	17.4	17.4	17.4
Battery Capacity [Wh]	COTS	2067.8	3477.6	2159.0

The battery capacity portions are divided proportionally to the power usage of each rotor. The endurance of the quadcopter has a minimum of 5 minutes endurance assuming that 18 m/s wind gust is continuously acting on the quadcopter, a maxumum endurance of 23 minutes assuming no wind gusts act on the drone. Note that the minimum time required to reach 100m and to couple with the fixed wing is 31 seconds total.

Controlling the yaw of the Quadcopter with the Fixed-Wing during wind gusts can be challenging due to the wind gusts. While the Quadcopter can use its four upward rotors to exert control over the yaw by spinning them in opposite directions, this alone provides insufficient to counteract the yaw moment induced by wind gusts. As a solution, the team has opted to offset the propellers in the x-direction, thereby enabling the utilization of a specific propeller for yaw control. This additional propeller provides enhanced manoeuvrability in managing yaw. This will be analyzed using the asymmetric equation of motion in section 6.5.

6.4. Block Diagrams

This section will provide the block diagrams of the Quadcopter to show how all subsystems are connected within the whole Quadcopter system. Figure 6.12 shows the data handling diagram of the Multicopter drone. This needs no further explanation as it has similar functional flow as compared to the Fixed-Wing.

The electrical block diagram of the Quadcopter is displayed in Figure 6.13. It provides an overview of the flow of power through the system with a clear depiction of the systems that control the flow of electricity, the components that receive the power, and the converters that bridge components that require different voltage levels.

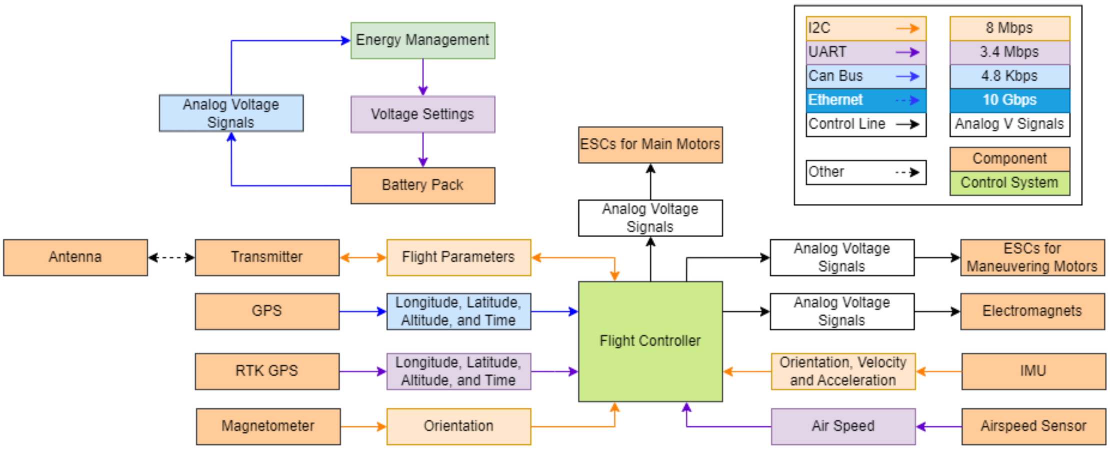

Figure 6.12: Data handling diagram of the Quadcopter drone.

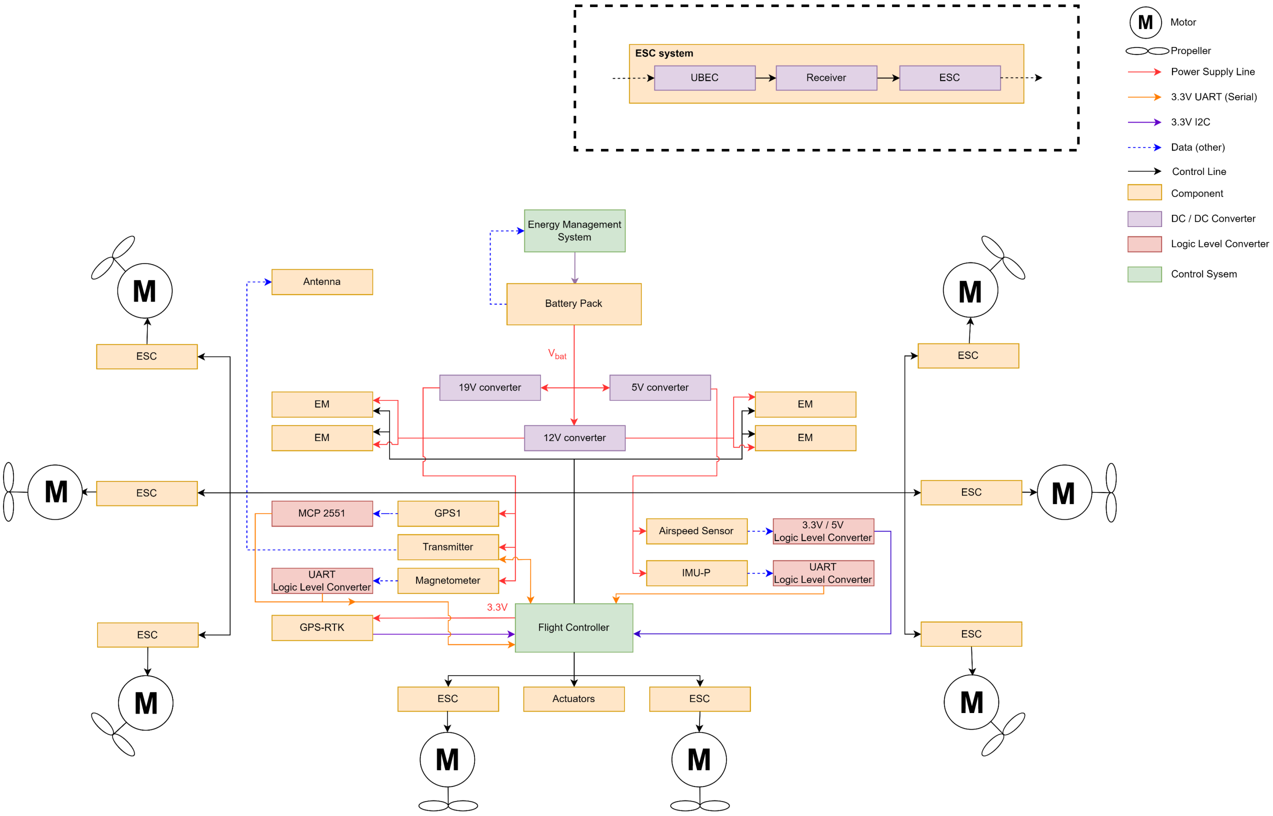

Figure 6.13: Electric block diagram of the Quadcopter drone.

The hardware block diagram of the Quadcopter is seen in Figure 6.14. It shows a schematic of the connections between all hardware components in the system. The functional flow is similar to the hardware diagram of the Fixed-Wing in section 5.9.

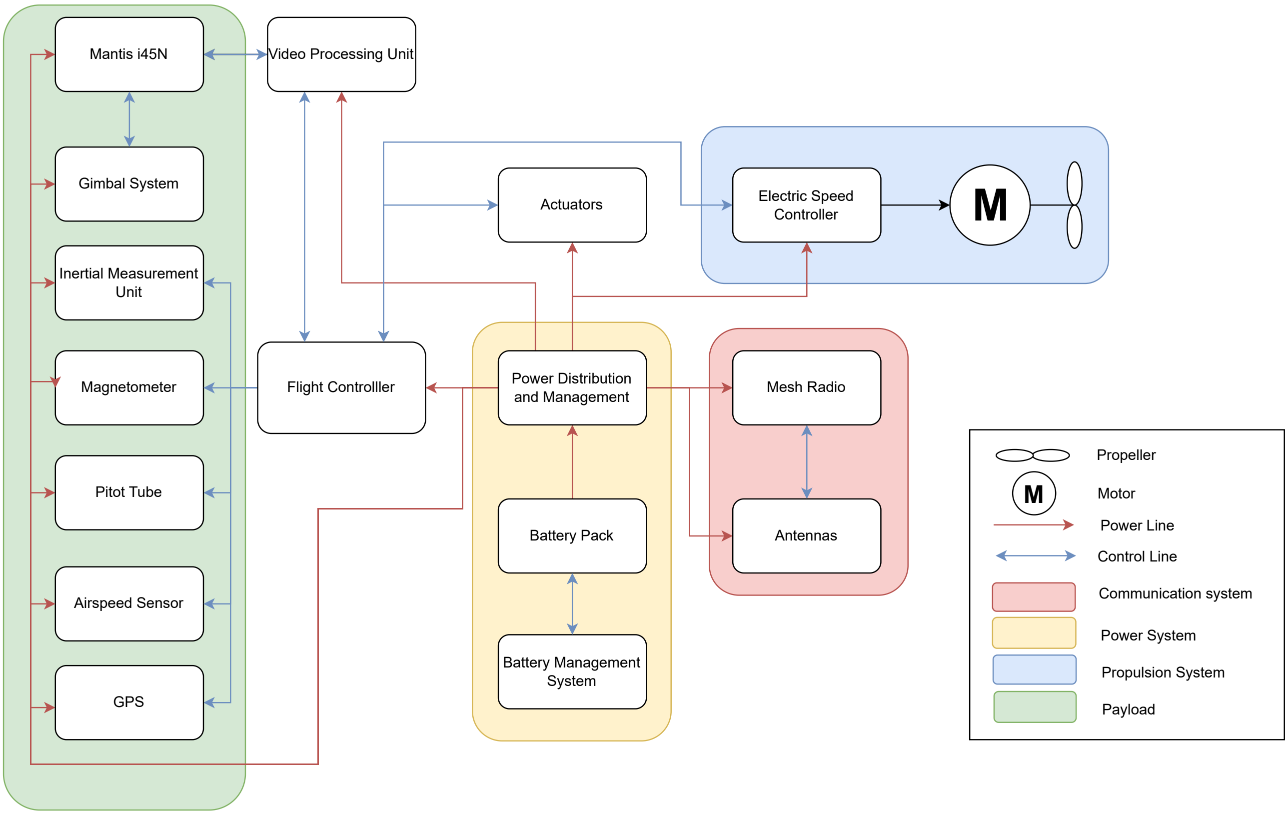

Figure 6.14: Hardware block diagram of the Quadcopter drone.

6.5. Stability Analysis of the Coupled System

Once the Quadcopter catches the Fixed-Wing drone out of the air, they become a coupled system. The stability of this system is crucial for ensuring a safe landing, especially under storm conditions. This coupled system needs to cope with the harsh storm conditions. The stability of the coupled system is explored in this section.

6.5.1. Mathematical Model

This section comprehensively addresses the aspects of stability and control of the hybrid system. Given the substantial weight of the combined system of 50 [kg], the influence of wind gusts on the system's stability and control becomes particularly significant. The first step to see if the system can cope with the wind is to make a free body diagram displayed in Figure 6.15.

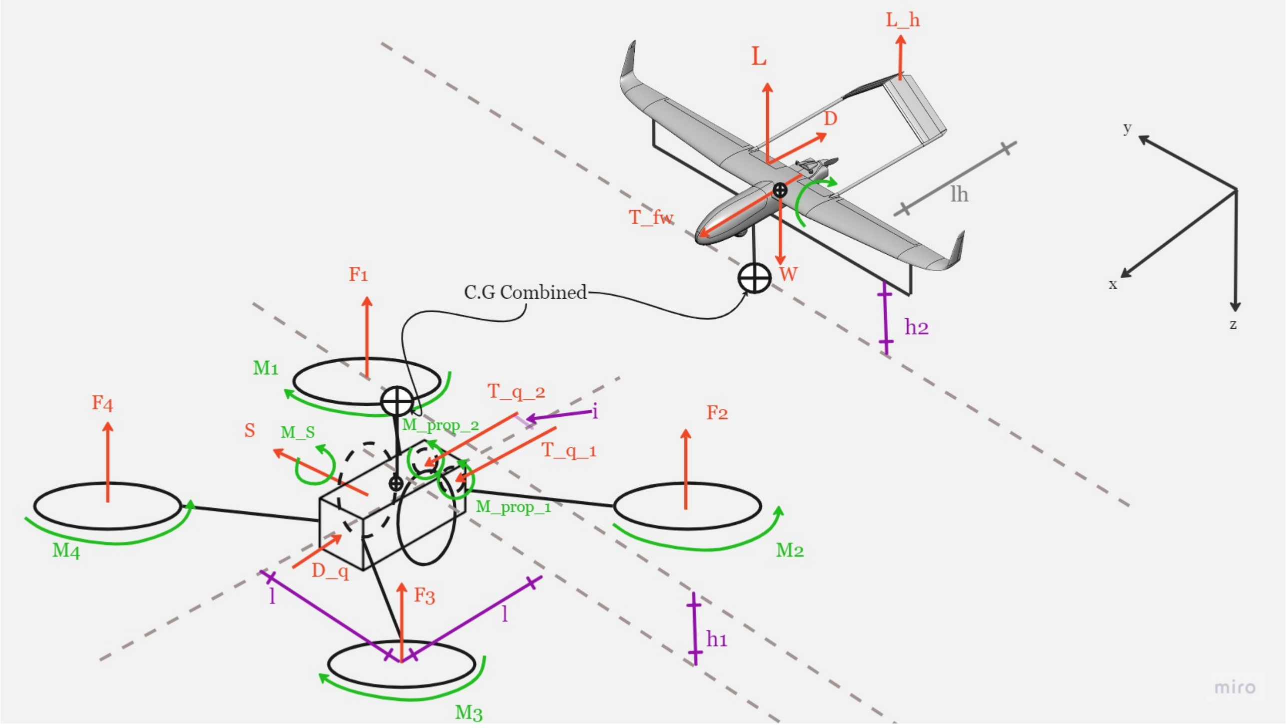

Figure 6.15: Free Body Diagram of the Hybrid Fixed-Wing Octacopter system.

After this, some assumptions are made in order to simplify the model. These include:

1. The thrust of the Fixed-Wing is set to zero when connected. Therefore, only the two forward-facing propellors of the Multicopter is used to translate in the x-direction.
2. The drag generated by the aircraft's horizontal tail is significantly smaller than the drag generated by the main wing [39]. Therefore, the drag of the horizontal tail can be approximated as zero: $D_h \approx 0$.
3. To control the pitch motion of the drone, the thrust produced by the two backward rotors is assumed to be equal to the thrust produced by the two forward rotors, i.e., $F_1 = F_2$ and $F_3 = F_4$.
4. To control the roll motion of the drone, the thrust produced by the two left rotors is assumed to be equal to the thrust produced by the two right rotors, i.e., $F_1 = F_4$ and $F_2 = F_3$.
5. To control the yaw motion of the drone, the thrust produced by the two diagonally opposite rotors is assumed to be equal, i.e., $F_1 = F_3$ and $F_2 = F_4$.
6. The lift force is calculated as the resultant point force of the total lift distribution acting on the aircraft.

The initial step in formulating the state model involves the dynamic equations governing translational and rotational motion, and the kinematic relations These equations are represented in Equation 6.5 respectively [39], where u is the velocity in the X-direction, v is the velocity in the Y-direction, w is the velocity in the Z-direction, p is the roll rate, q is the pitch rate, r is the yaw rate, θ is the pitch angle, ϕ is the roll angle and φ is the yaw angle. The dot on top of the symbols refer to the time derivative of the represented symbols.

$$
\begin{aligned}
m(\dot{u} + qw - rv) &= -mg_{r,0}\sin\theta + X \\
m(\dot{v} + ru - pw) &= mg\sin\phi\cos\theta + Y \\
m(\dot{w} + pv - qu) &= mg\sin\phi\sin\theta + Z \\
I_{xx}\dot{p} + (I_{zz} - I_{yy})\,qr - I_{xz}(\dot{r} + pq) &= L \\
I_{yy}\dot{q} + (I_{xx} - I_{zz})\,rp + I_{xz}\left(p^2 - r^2\right) &= M \\
I_{zz}\dot{r} + (I_{yy} - I_{xx})\,pq - I_{xz}(\dot{p} - rq) &= N \\
\dot{\varphi} &= p + q\sin\varphi\tan\theta + r\cos\varphi\tan\theta \\
\dot{\theta} &= q\cos\varphi - r\sin\varphi \\
\dot{\psi} &= q\frac{\sin\varphi}{\cos\theta} + r\frac{\cos\varphi}{\cos\theta}
\end{aligned}
\tag{6.5}
$$

Where X represents the forces in the X-direction, Y the forces in the Y-direction, Z the forces in the Z-directions, L the moments around the x-axis, M the moments around the y-axis and N the moments around the z-axis. These forces and moments can be obtained from Figure 6.15 and are given by Equation 6.6.

$$
\begin{aligned}
X &= T_{q_1} + T_{q_2} - D_Q - D_w - W\sin\theta \\
Y &= S + W\sin\phi\cos\theta \\
Z &= -4F_1 + W\cos\phi\cos\theta - L - L_h \\
L &= M_{prop} + (2F_2 - 2F_1)\cdot l - Sh_1 \\
M &= (2F_3 - 2F_1)\cdot l - L_h l_h + (T_{Q_1} + T_{Q_2} - D_q)\cdot h_1 + D_w h_2 + M_{ac} \\
N &= (2M_1 - 2M_2) + (T_{q_1} - T_{q_2})\cdot i
\end{aligned}
\tag{6.6}
$$

Where S is the resultant thrust of the side propellors, T_q the thrust of the forward propellers of the Quadcopter, F_i the thrust of each of the rotors and M_i the torques induced due to the rotation of the rotor and propeller. The equation of the thrust force and torques are given by Equation 6.7 and Equation 6.8 respectively [29].

$$
T_{q_i}, F_i = C_t\rho A\omega_i^2 R^2 \tag{6.7}
$$

$$
M_i = k\omega_{1,2}^2 = C_q\rho AR^3\omega_i^2 \tag{6.8}
$$

Next step is to linearize Equation 6.5. The result can be seen in Equation 6.9.

$$
\begin{aligned}
m\dot{u} &= -W\cos\theta_0\theta + X_u u + X_w w + X_q q + X_{\omega_{q_1}^2}\cdot\omega_{q_1}^2 + X_{\omega_{q_2}^2}\cdot\omega_{q_2}^2 \\
m(\dot{v} + rV) &= W\cos\theta_0\phi + Y_v v + Y_{\dot{v}}\dot{v} + Y_p p + Y_r r + Y_{\omega_S^2}\cdot\omega_S^2 \\
m(\dot{w} - qV) &= -W\sin\theta_0\theta + Z_u u + Z_w w + Z_{\dot{w}}\dot{w} + Z_q q + Z_{\omega_1^2}\cdot\omega_1^2 \\
I_{xx}\dot{p} - I_{xz}\dot{r} &= L_v v + L_p p + L_r r + L_{\omega_S^2}\omega_S^2 + L_{\omega_{prop}^2}\omega_{prop}^2 + L_{(\omega_2^2-\omega_1^2)}\cdot(\omega_2^2 - \omega_1^2) \\
I_{yy}\dot{q} &= M_u u + M_{\dot{w}}\dot{w} + M_{\omega_{q_1}^2}\cdot\omega_{q_1}^2 + M_{\omega_{q_2}^2}\cdot\omega_{q_2}^2 + M_{(\omega_3^2-\omega_1^2)}(\omega_3^2 - \omega_1^2) \\
I_{zz}\dot{r} - I_{xz}\dot{p} &= N_v v + N_{\dot{v}}\dot{v} + N_p p + N_r r + N_{(\omega_1^2-\omega_2^2)}\cdot(\omega_1^2 - \omega_2^2) + N_{(\omega_{q_1}^2-\omega_{q_2}^2)}(\omega_{q_1}^2 - \omega_{q_2}^2) \\
\dot{\phi} &= p + r\tan\theta_0 \\
\dot{\theta} &= q \\
\dot{\psi} &= \frac{r}{\cos\theta_0}
\end{aligned}
\tag{6.9}
$$

Next step is to nondimensionalize the equations by dividing all terms by $\frac{1}{2}\rho V^2 S$. This is done with the same methodology as outlined in [39], leading to the derived system for symmetric and asymmetric flight presented in Equation 6.10 and Equation 6.11 respectively.

$$
\begin{bmatrix}
C_{X_u} - 2\mu_c D_c & C_{x_\alpha} & C_{Z_0} & C_{X_q} \\
C_{Z_u} & C_{Z_\alpha} + (C_{Z_{\dot{\alpha}}} - 2\mu_c)D_c & -C_{X_0} & C_{Z_q} + 2\mu_c \\
0 & 0 & -D_c & 1 \\
C_{m_u} & C_{m_\alpha} + C_{m_{\dot{\alpha}}}D_c & 0 & C_{m_q} - 2\mu_c K_{yy}^2 D_c
\end{bmatrix}
\begin{bmatrix}
\frac{u}{V} \\ \alpha \\ \theta \\ \frac{q\bar{c}}{V}
\end{bmatrix}
= \tag{6.10}
$$

$$\begin{bmatrix} -C_{X_{\omega_{q1}^2}} & -C_{X_{\omega_{q2}^2}} & 0 & 0 \\ 0 & 0 & -C_{Z_{\omega_1^2}} & 0 \\ 0 & 0 & 0 & 0 \\ -C_{M_{\omega_{q1}^2}} & -C_{M_{\omega_{q2}^2}} & 0 & -C_{M_{(\omega_3^2-\omega_1^2)}} \end{bmatrix} \begin{bmatrix} \omega_{q1}^2 \\ \omega_{q2}^2 \\ \omega_1^2 \\ \omega_3^2 - \omega_1^2 \end{bmatrix}$$

$$\begin{bmatrix} C_{Y_\beta} + (C_{Y_{\dot\beta}} - 2\mu_b)D_b & C_L & C_{Y_p} & C_{Y_r} - 4\mu_b \\ 0 & -\frac{1}{2}D_b & 1 & 0 \\ C_{l_\beta} & 0 & C_{l_p} - 4\mu_b K_{xx}^2 D_b & C_{l_r} + 4\mu_b K_{xz} D_b \\ C_{n_\beta} + C_{n_{\dot\beta}} D_b & 0 & C_{n_p} + 4\mu_b K_{xz} D_b & C_{n_r} - 4\mu_b K_{zz}^2 D_b \end{bmatrix} \begin{bmatrix} \beta \\ \phi \\ \frac{pb}{2V} \\ \frac{rb}{2V} \end{bmatrix} = \tag{6.11}$$

$$\begin{bmatrix} -C_{Y_{\omega_S^2}} & 0 & 0 & 0 \\ 0 & 0 & 0 & 0 \\ -C_{L_{\omega_S^2}} & -C_{L_{\omega_{prop}^2}} & -C_{L_{(\omega_2^2-\omega_1^2)}} & 0 \\ 0 & 0 & -C_{N_{(\omega_2^2-\omega_1^2)}} & -C_{N_{(\omega_{q1}^2-\omega_{q2}^2)}} \end{bmatrix} \begin{bmatrix} \omega_s^2 \\ \omega_{prop}^2 \\ \omega_2^2 - \omega_1^2 \\ \omega_{q1}^2 - \omega_{q2}^2 \end{bmatrix}$$

As can be observed from Equation 6.10 and Equation 6.11, the control of the coupled system is dependent on the angular velocity of the rotors and propellors of the Quadcopter. Taking the derivatives of the forces and the torques with respect to the angular velocity gives Equation 6.12.

$$\begin{aligned} \frac{\partial F_i}{\partial \omega_i^2} &= C_t \rho A_i R_i^2 \\ \frac{\partial T_q}{\partial \omega_i^2} &= C_t \rho A_q R_q^2 \\ \frac{\partial M_i}{\partial \omega_i^2} &= C_q \rho A_i R_i^3 \end{aligned} \tag{6.12}$$

The torque coefficient, denoted as C_q, is determined by Figure 6.16. In subsection 6.3.1, it was established that the thrust coefficient, C_t, has a value of 0.065. Consequently, the corresponding C_q is approximately 0.0065, as per the established relationship between C_t and C_q.

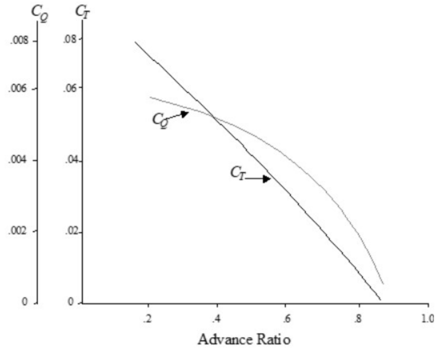

Figure 6.16: Relationship between the thrust coefficient, C_t, and the torque coefficient, C_q [3].

To analyze the stability of the coupled system, the simulation parameters are set to reflect the conditions immediately after the Fixed-Wing drone is captured. At this stage, the velocity of the system is set to the stall velocity, which is 18 [ms^{-1}]. Additionally, the simulation's air density corresponds to the sea level air density, which is 1.225 [kgm^{-3}]. These parameter values are essential for non-dimensionalising the input coefficients in the system. To achieve this, the coefficients are divided by $\frac{1}{2}\rho V^2 S$. One example calculation is shown for the non-dimensionalized force as well as for the torque in Equation 6.13.

$$
\begin{aligned}
C_{X_{\omega^2_{q_1}}} &= \frac{1}{\frac{1}{2}\rho V^2_{stall}S}\frac{\partial X}{\partial \omega^2_{q_1}} = \frac{1}{\frac{1}{2}\rho V^2_{stall}S}\frac{\partial T_{q_1}}{\partial \omega^2_{q_1}} = \frac{C_t\rho A_{q_1}R^2_{q_1}}{\frac{1}{2}\rho V^2_{stall}S} \\
C_{N_{(\omega^2_{q_1}-\omega^2_{q_2})}} &= \frac{1}{\frac{1}{2}\rho V^2_{stall}S}\frac{\partial N}{\partial(\omega^2_{q_1}-\omega^2_{q_2})} = \frac{i}{\frac{1}{2}\rho V^2_{stall}S}\frac{\partial(T_{q_1}-T_{q_2})}{\partial(\omega^2_{q_1}-\omega^2_{q_2})} = \frac{iC_q\rho A_{q_1}R^3_{q_q}}{\frac{1}{2}\rho V^2_{stall}S}
\end{aligned}
\tag{6.13}
$$

The aforementioned calculation is carried out for all the non-dimensional coefficients of the input matrix in Equation 6.10 and Equation 6.11. The computed results are presented in detail in Table 6.5.

Table 6.5: Non-dimensional coefficients in the state space model of the coupled Fixed-Wing Quadcopter: scaling with $k = \frac{1}{\frac{1}{2}\rho V^2 S}$.

Non-Dimensionalized Coefficients	**Formula**
$C_{X_{\omega^2_{q1}}}$	$kC_t\rho A_{q_1}R^2_{q_1}$
$C_{X_{\omega^2_{q2}}}$	$kC_t\rho A_{q_2}R^2_{q_2}$
$C_{Z_{\omega^2_1}}$	$-4kC_t\rho A_1R^2_1$
$C_{M_{\omega^2_{q1}}}$	$h_1kC_t\rho A_qR^2_{q_2}$
$C_{M_{\omega^2_{q2}}}$	$h_1kC_t\rho A_qR^2_{q_2}$
$C_{M_{(\omega^2_3-\omega^2_1)}}$	k$2lkC_t\rho A_2R^2_2$
$C_{Y_{\omega^2_S}}$	$kC_t\rho A_SR^2_S$
$C_{L_{\omega^2_S}}$	$-h_1kC_t\rho A_SR^2_S$
$C_{L_{\omega^2_{prop}}}$	$kC_q\rho A_{prop}R^3_{prop}$
$C_{L_{(\omega^2_2-\omega^2_1)}}$	$2lkC_t\rho A_1R^2_1$
$C_{N_{(\omega^2_2-\omega^2_1)}}$	$-2kC_q\rho A_1R^3_1$
$C_{N_{(\omega^2_{q1}-\omega^2_{q2})}}$	$kiC_t\rho A_{q_1}R^2_{q_1}$

This section presented the mathematical model and presented the formulas for the non-dimensionalized coefficients. The subsequent step involves analyzing the simulations of symmetric and asymmetric motions, as well as assessing the overall stability of the coupled system. This analysis will be conducted in detail in subsection 6.5.2.

6.5.2. Simulation Analysis

After establishing the mathematical model, the next step involves conducting simulations to analyze the symmetric and asymmetric motion of the system. First, the results obtained from the simulations will be presented. Subsequently, an explanation of the verification method utilized will be provided.

Results

The matrices on the left-hand side of Equation 6.10 and Equation 6.11 describe the system's response to initial conditions and inputs. In order to obtain preliminary estimates of the coefficients, the XFLR5 software was employed and the system was analyzed with the coefficients of the fixed wing. Although these values may not be highly accurate, they provide an initial estimation. The obtained results are presented in Table 6.6. For more accurate coefficient values, one could opt for a more comprehensive computational fluid dynamics (CFD) simulation or conduct measurements on a prototype. However, this is outside the scope of this project.

Table 6.6: Non-dimensionalised stability coefficients as an output of the XFLR5 software.

Coefficient	Value
C_{X_u}	-0.0024
C_{Z_u}	0.00012
C_{m_u}	0
C_{X_α}	0.12
C_{Z_α}	0.56
C_{m_α}	-1.45
C_{X_q}	0.078
C_{Z_q}	-3.0
C_{m_q}	-8.78
C_{Y_β}	-0.31
C_{Z_β}	-0.023
C_{n_β}	0.11
C_{Y_p}	-0.022
C_{Z_p}	-0.54
C_{n_p}	-0.040
C_{Y_r}	0.24
C_{Z_r}	0.050
C_{n_r}	-0.082

Due to the limitations of the XFLR5 software, it was not possible to compute all the coefficients required for the system analysis. To address this, coefficients from a hybrid Fixed-Wing drone, as presented in [47], were utilized to supplement the missing values. The total mass and moment of inertia were obtained from the CATIA model of the coupled system. These give the remainder coefficients of the system.

Table 6.7: Remaining non-dimensional stability coefficients.

Coefficient	Value
$C_{Z_{\dot{\alpha}}}$	0.59
$C_{m_{\dot{\alpha}}}$	0.18
$C_{Y_{\dot{\alpha}}}$	0
$C_{n_{\dot{\beta}}}$	0

The simulation conditions are set to the moment immediately after the Quadcopter captures the Fixed-Wing drone mid-air. Specifically, the height is set to 100 $[m]$, the air density is 1.21 $[kg \cdot m^{-3}]$, and the velocity is adjusted to the stall speed of 18 $[ms^{-1}]$ while considering an additional wind gust of 15 $[ms^{-1}]$. Consequently, the total velocity of the system during the simulation is 30 $[ms^{-1}]$. The initial angle of attack is set to the angle of attack at stall speed, which can be obtained from Figure 5.16. The system does not have any input from the rotors. The results of the symmetric motion can be seen in Figure 6.17.

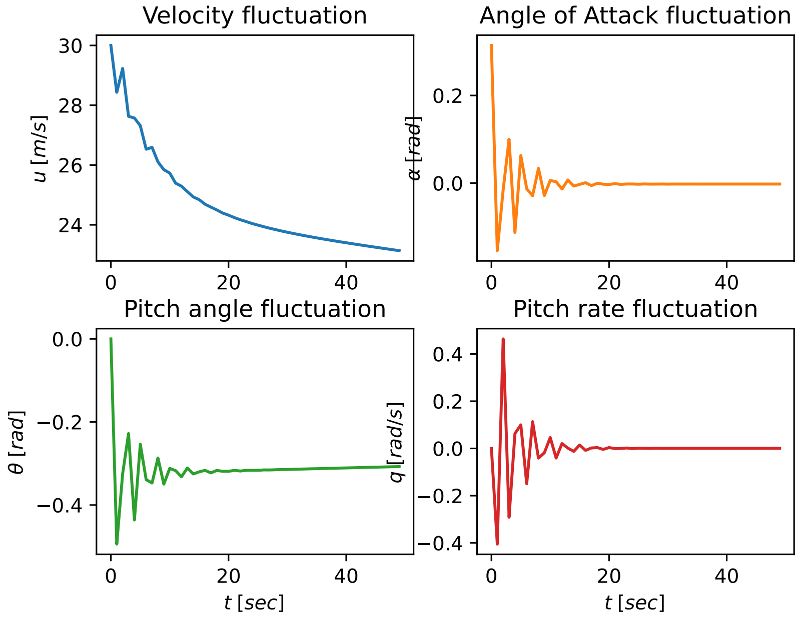

Figure 6.17: Symmetric eigenmotion from the coupled system

As depicted in Figure 6.17, the coupled system exhibits longitudinal stability. The velocity experiences a decrease of approximately 7 [m/s], from 37 [m/s] to 30 [m/s]. Additionally, starting at approximately 18 seconds, the angle of attack, pitch angle, and pitch rate reaches a steady state or remain close to zero. These observations indicate a stable and controlled motion of the system.

The analysis of the coupled system extends to its asymmetric stability as well. By simulating the system with the same initial conditions as described previously, the results of the asymmetric stability analysis are obtained, which are depicted in Figure 6.18.

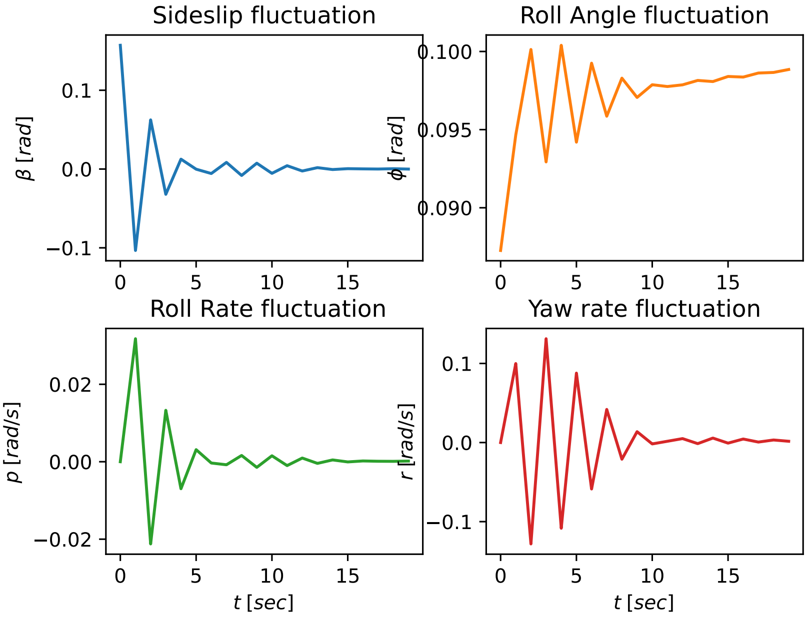

Figure 6.18: Asymmetric eigenmotion from the coupled system.

6.5.3. Verification

To verify that the generated space state is an accurate tool for predicting the behaviour of the drone, a number of tests will be run. In these tests, different inputs are given to the simulation tool, and the results are compared against what would be expected to happen in real life. This verification will also provide insight into the stability of the coupled system.

Longitudinal Stability

There are 3 possible inputs that will alter the longitudinal stability of the system, and will thus cause variation in the produced graphs.

Translational Motion X-axis

The first input that can be altered is the rotational speed of the two forward-facing rotors. If this rotational speed is increased then the whole system will experience an increase in the horizontal velocity component. In addition to this, the aircraft will pitch up, therefore both the angle of attack and the pitch angle will experience a momentary increase.

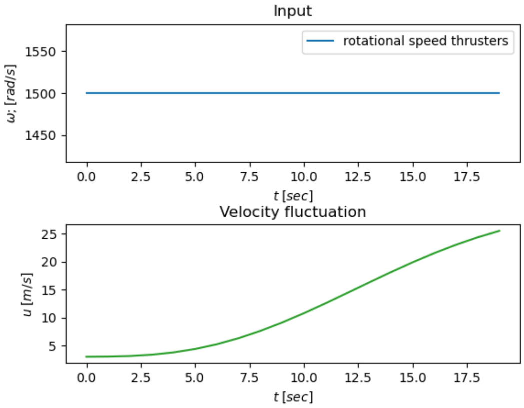

Figure 6.19: 100s Step response positive X-direction.

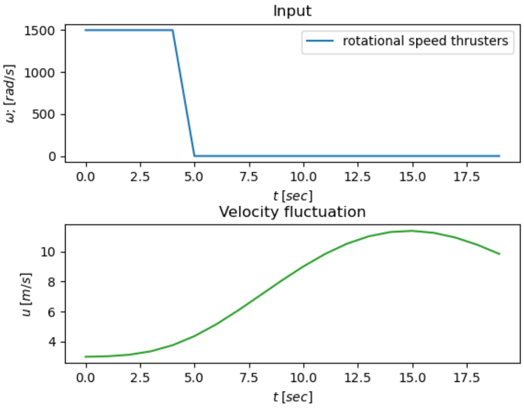

Figure 6.20: 5s Step response positive X-direction.

In Figure 6.19, one can observe the increase in the horizontal velocity in the x-direction as the system is given an input of 1500 $[rad/s]$ in both forwards-facing thrusters for 100 seconds. In contrast, Figure 6.20, shows the response with an equal input only lasting 5 seconds. As expected, the 5 seconds step only causes the velocity to momentarily increase before starting to oscillate back to its original value, meanwhile the 100 second step keeps on increasing in velocity.

Translational Motion Z-axis

The second input that can be changed is the rotational speed of the 4 upwards-facing rotors. This change in rotational speed will cause an increase in the vertical velocity. This can be verified with Figure 6.21 below.

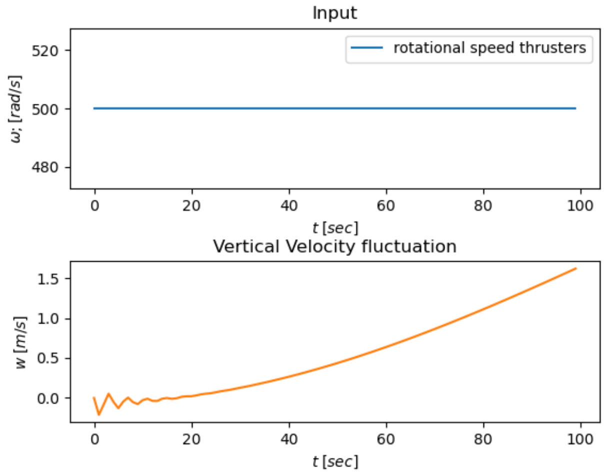

Figure 6.21: Vertical Velocity Step Response

As can be seen in Figure 6.21, if we give the four rotors facing upwards a rotational speed of 500 rad/s, or an equivalent of approximately 5000 rpms per rotor, the vertical velocity increases slowly. A more drastic effect can be seen when the rotational speed given is 1000 rad/s. As it is seen in Figure 6.22, doubling the rotational speed of the rotors, quadruples the effect on the vertical velocity. This further verifies the squared relation between the thrust force produced by the rotors and the angular velocity ω.

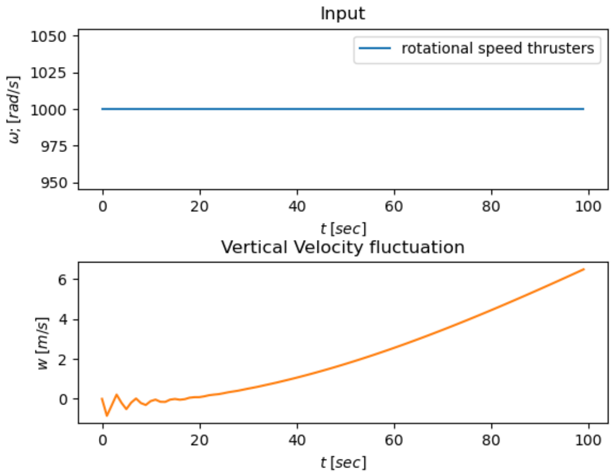

Figure 6.22: Vertical Velocity Step Respons

Pitching Moment

The final input that can be altered is the difference in rotational speeds between the two most forward upwards-facing rotors and the two most backwards forward-facing rotors. This difference in the force along the z-axis will induce a moment about the y-axis, pitching the coupled system up if the forward rotors have the higher rotational speed and pitching down if the forward rotors have the lower rotational speed. It is also important to note, that as long as the coupled system is moving forward, the system will have a naturally induced nose-up motion, so this control will be necessary to counteract the induced increase in pitch when moving forward.

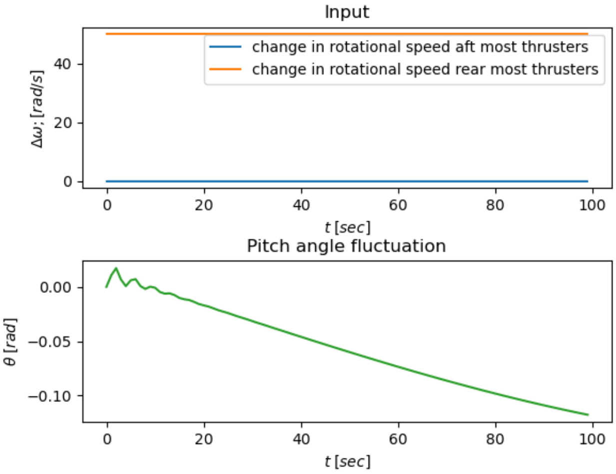

Figure 6.23: Step impulse pitch angle fluctuation.

In Figure 6.23, one can observe that if the rotational speed of the most aft thrusters is increased by 40 rad/s with respect to the most forward thrusters, the system will pitch down. Figure 6.23 shows a step response lasting 100 seconds, where one can observe a linear decrease in the pitch. This is a good characteristic, as it means that if the input is ceased, the system would go back to its equilibrium.

Lateral Stability

Similar to longitudinal stability, lateral stability can be controlled with a set of 3 inputs. The side rotors control the displacement along the y-axis, the forward-facing rotors and the upwards-facing rotors are used to control the yaw, and the forwards facing

Translational Motion Y-Axis

Providing a rotational speed to either the left or the right side rotors, will cause the drone to translate parallel to the y-axis. This means, that given a certain input, the horizontal velocity along the y-axis will increase. This is an important characteristic of the coupled system, as it should be able to land precisely on the ship and counter wind gusts from all directions.

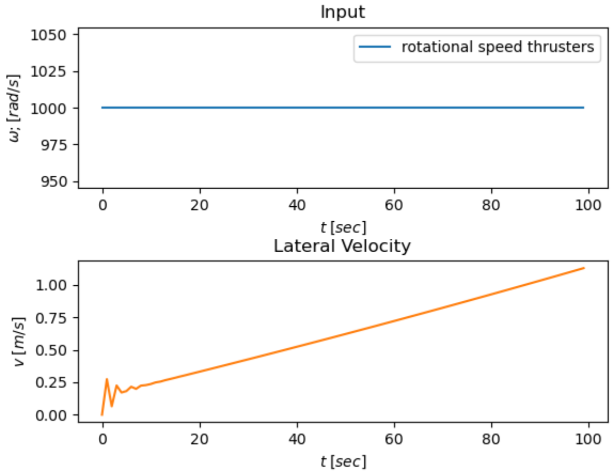

Figure 6.24: Step impulse velocity fluctuation Y-direction.

In Figure 6.24, one can observe the change in velocity along the y-axis, as the system is given an input of 1000 $[rad/s]$. It is important to note that, since only one propeller is available at a time and the side profile is more drag resistant, the effect of the rotational speed of the propeller is not as high as that of the forward-facing propellers. This effect can also be observed in Figure 6.24. It is also important to note, that due to the offset of the side-thrusters with respect to the centre of gravity, a rolling moment will be induced which will have to be countered.

Rolling Moment
To induce a rolling moment, or counter an already induced one, one can simply give different inputs in the rotational speed of the right upwards-facing rotors and to the left ones. This difference will cause the right-most rotors to produce a larger upwards force than the left-most ones, or vice versa, thus inducing a rolling moment.

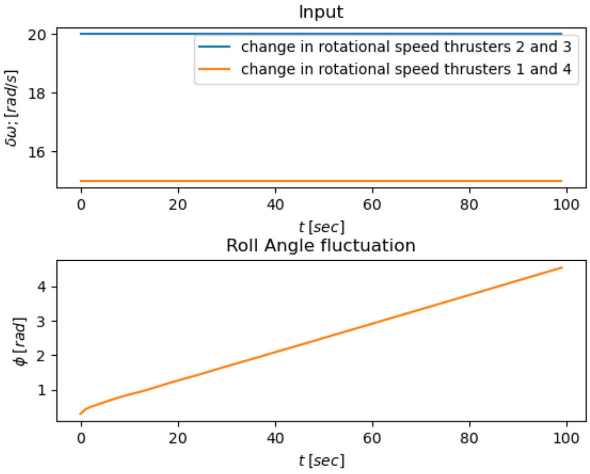

Figure 6.25: Step impulse roll angle.

Figure 6.25 shows the change in roll angle as the rotational speed of the left side thrusters, 2 and 3, is increased by 20 $[deg/s]$ with respect to the rotational speed of thrusters 1 and 4. This small difference in rotational speed will cause a roll angle of 4 radians in just under 100s.

Yawing Moment
The yawing moment can be controlled with two different surfaces, the upwards-facing rotors and the forward-facing rotors. This is due to the fact that rotors 1 and 3 are rotating in different directions than 2 and 4, therefore, an increase in the rotational speed of 1 and 3 will induce a torque around the z-axis causing the coupled system to rotate.

Additionally, the forward-facing rotors can be used to generate a yawing moment, giving a higher value to the rotational speed of one over the other will cause a moment about the z-axis.
The simulation is able to account for both of these phenomena. If the rotational speed of 2 and 4 is increased by the same amount, a positive yawing moment will be induced as observed in the following Figure 6.26

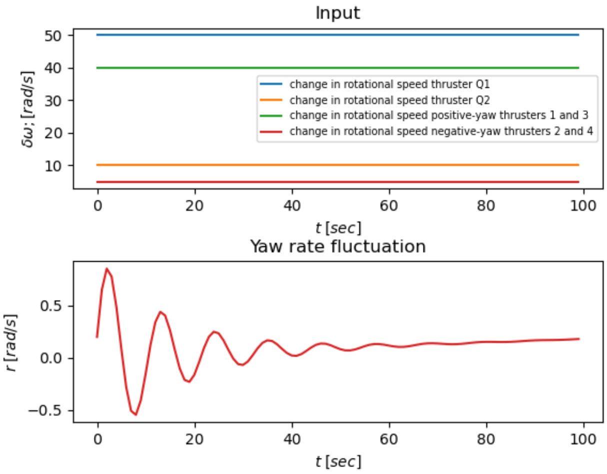

Figure 6.26: Step impulse roll angle.

Figure 6.26 is perhaps the more complicated degree of freedom to maintain control over. Two different control inputs are needed, and even then, the variation in yaw angle is very small. In addition, there are very large oscillations which could result in damage to the system, so a solution to this problem must be found.

6.6. Budget Breakdown

As a final consideration for the Quadcopter, a budget breakdown regarding mass and power was performed. No prior budget breakdown was performed, as the design of the Quadcopter was initiated at the second half of the project. Currently, the relevant components can be identified to analyse the contribution to the mass and power.

6.6.1. Power Breakdown

The power usage of the Quadcopter drone is primarily used for the propulsion system. The most power-demanding and constraining phase of the flight is the take-off in stormy conditions. The Quadcopter is designed for high peak powers during the takeoff in stormy conditions. The available power is directly derived from the available energy from the battery, while using a small fraction of around 1 % for the magnet. As the peak power is around 83.5 $[kW]$, the power usage for components, such as the sensors and control systems, are considered to be negligible. Additionally, since the drone is Consequently, a detailed power breakdown for different components is not relevant for the Quadcopter.

6.6.2. Mass Breakdown

The components for the mass breakdown is the battery, structure, propulsion and remaining components of the Quadcopter. The battery is significantly heavier compared to the other components. This is expected as the Quadcopter has to supply high amount of power in a such period. The structure of the Quadcopter is simplified to 4 similar rods, each weighing 0.25 $[kg]$, that form the frame of the drone. The propulsion system exist out of the motors, lift rotors and propellers, and 2 4-channel electronic speed controllers. The electronic speed controllers are both placed on one side, regulating and providing the power used by the motor. In total there are 4 lift rotors, 2 side propellers and 2 front propeller. Each lift rotor is connected to a large motor that weighs 0.865 $[kg]$. The front and propellers are connected to a small motor that weighs 0.287 $[kg]$. Each lift rotor are weighs 90 $[g]$ and the side and front propellers weighs 20 $[g]$. The other components are similar to the fixed wing except the Quadcopter does not have a pitot tube and actuators. In Figure 6.27, the allocated mass and relative mass to the total mass for the different components. The relative masses are displayed using a pie chart in Figure 6.28. The requirements for the mass REQ-STK-SYS-03 and REQ-STK-SYS-05 also apply for the Quadcopter.

Figure 6.27: Mass breakdown for the Quadcopter.

Component	Mass [kg]	Relative Mass [%]
Battery	17.12	68.4
Structure	1.0	4.0
Propulsion	5.19	18.4
Other	1.69	6.8
Total	25	100

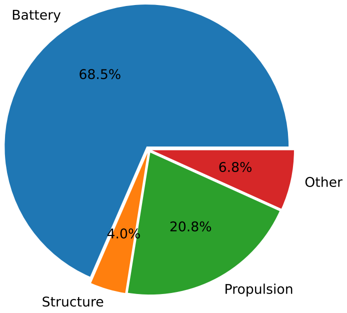

Figure 6.28: Mass budget pie chart for the Quadcopter drone.

6.7. Conclusion

In this chapter, the focus was on the detailed design of the landing sequence for the drone swarm. The goal was to create a mechanism that could safely catch the Fixed-Wing drone mid-air and ensure a secure landing in the storm conditions. To achieve this, a Quadcopter was specifically designed for this purpose. To facilitate the interception of the Fixed-Wing drone, powerful electromagnets were strategically integrated into the design. These magnets created a strong magnetic attraction, effectively clamping the Fixed-Wing drone to the Quadcopter. The magnets were carefully placed on the fixed so that it did not influence the stability of the Quadcopter. The subsystems interaction of the Quadcopter has been provided and the stability of the coupled Fixed-Wing Quadcopter has been analysed. The final design of the Quadcopter, including the clamping mechanism, can be observed in Figure 6.29. This showcases the integration of the clamping mechanism on top of the Quadcopter, ready to catch the Fixed-Wing drone during the landing process.

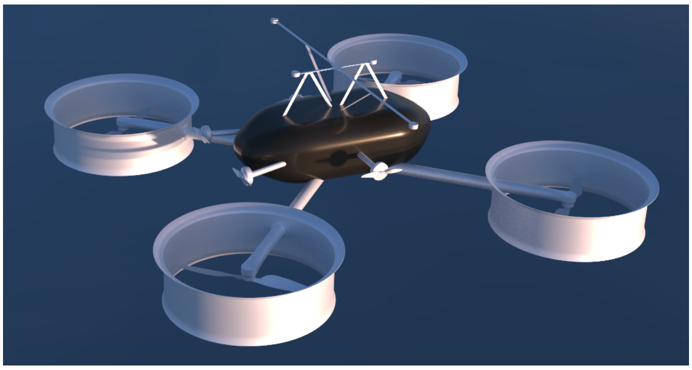

Figure 6.29: Final Quadcopter design with its clamping mechanism to catch the Fixed-Wing.

The upcoming chapter will focus on the potential risks that could arise during the design phase of the project. Furthermore, mitigation strategies will be proposed for the risks deemed significant. In addition to the mitigation strategies, a contingency plan will be presented. This plan serves as a backup in case unforeseen risks or challenges still occur despite the implemented mitigation measures.

7
Risk & Safety

In every design project, a risk analysis is performed to identify the vulnerabilities of the project. By identifying vulnerabilities, the team can mitigate these risks and minimize their severity. In section 7.1, the risks are analyzed and assessed. Furthermore, the critical risks are mitigated in subsection 7.1.1. At last, a contingency plan is presented in subsection 7.1.2.

7.1. Technical Risk Assessment

The technical risk assessment, identifies all the possible risks associated with the operations of the mission, the risks associated with the environments, and the risks associated with the resource management of the mission. After these risks are identified, their impact and likelihood are classified. The distinction between significant and severe is that for a severe risk, the entire mission is compromised. The likelihood ranges from rare to almost certain and the impact ranges from negligible to severe. The risks are characterized by the type of risk they are. The types of risks that are identified are operational, environmental, development, and resource management risk.

Table 7.1: Operational risks.

ID	*Risk code*	*Description*
		Operational Risks
01	RISK-OP-GEN-01	**Failure in battery charging** would result in uncharged batteries, potentially preventing some or all drones from being launched, or launching them at a lower battery level, thus decreasing endurance. This will greatly impact the efficiency of the mission but is unlikely as thorough pre-flight checks are performed. **Likelihood:** Possible, **Impact:** Significant.
02	RISK-OP-GEN-02	**Failure of takeoff and landing mechanisms** Takeoff and landing is a crucial part of the mission. The drones should autonomously take off and land from a ship. When one of the fails, the whole mission would fail, because you either can deploy your drones or you can't get them back on the ship. **Likelihood:** unlikely, **Impact:** Severe.
03	RISK-OP-GEN-03	**Obstruction by airborne and waterborne vehicles** Flying outside the required range could lead to a catastrophic collision with another aircraft or watercraft. However, collisions rarely happen since the location of other nearby vehicles is often known. **Likelihood:** Rare, **Impact:** Significant.
04	RISK-OP-ADCS-01	**Invalid/incorrect input due to sensor error**: error in the attitude determination sensors due to faulty sensor or sensor malfunction, which would lead to incorrect attitude control, and could lead to one drone losing stability and control in storm conditions. Sensor errors are expected due to the operational conditions, however, a new input can be given that nullifies the impact of the invalid input.**Likelihood:** Possible, **Impact:** Moderate.
05	RISK-OP-ADCS-02	**Failure of attitude control actuators**. Attitude actuators fail to initialize or malfunction when a wind gust or disturbance is experienced, this would lead to a lack of attitude control and the potential crashing of the drone. As it is not expected that the actuators fail, the risk seems rather unlikely. **Likelihood:** Unlikely, **Impact:** Significant.
06	RISK-OP-COM-01	**Communication Loss**. This would result in failure to complete the rescue mission if communication is not established, as the ship would not know where to locate the target. This will jeopardize the mission and increase the duration of the mission. If communication is lost between the drones themselves, the flight time is prolonged and there is a possibility of no video feed available to verify the target is a human in distress. As the swarm is redundant, it is unlikely that communication is lost. However, this would greatly hinder the mission.**Likelihood:** Unlikely, **Impact:** Significant.

07	RISK-OP-COM-02	**Transponder malfunction**. If the transponder cannot be dropped at the centre of the search area, ocean drift would not be recorded easily, thus mathematical models would have to be used. If the transponder cannot be dropped at the target location, drone's position relative to the search area centre would have to be used to locate the target. A malfunction of the transponder is unlikely as it is checked before operation. **Likelihood:** Unlikely, **Impact:** Moderate.
08	RISK-OP-EPS-01	**Failure of the power generating unit**. This would result in a lack of power for all the subsystems, including the propulsion subsystem, the payload, and the attitude control and determination. The drone will not be able to fly and would have to be replaced or the swarm profile altered. **Likelihood:** Unlikely, **Impact:** Significant.
09	RISK-OP-EPS-02	**Failure in the power lines**. This could result in a lack of power to any or all of the subsystems of a drone, the drone won't be able to complete the mission. Depending on the swarm configuration, a drone could be repaired or compensated for. **Likelihood:** Unlikely, **Impact:** Significant.
10	RISK-OP-STR-01	**Structural failure during operation**. During operation, the drone experiences heavy gust loads and storm conditions. There is a possibility that the structure was not fully prepared for the loads that it will experience. Resulting in the structural failure of the drone. **Likelihood:** Unlikely, **Impact:** Significant.
11	RISK-OP-PL-01	**Camera malfunction**. The drone will be unable to send footage of survivors to the ground ship. This means that the backup or other camera drone must be used. As the drone is part of a swarm, the malfunction can be compensated for. **Likelihood:** Unlikely, **Impact:** Moderate.
12	RISK-OP-SIM-01	**Error in stability control loop**: A mistake in the control loop due to improper implementation of control would lead to a lack of attitude control for the entire swarm. Meaning the swarm would be unable to fly in a stable manner, and would not resist the weather conditions. **Likelihood:** Unlikely, **Impact:** Severe.
13	RISK-OP-SIM-02	**Error in thrust control loop** A mistake in the control loop would lead to errors when actuating the thrust control, this could have catastrophic consequences for the entire swarm. **Likelihood:** Unlikely, **Impact:** Severe.
14	RISK-OP-SIM-03	**Software error resulting in failure of nodes to follow desired search pattern**. This might cause overlap in search areas, areas left unsearched, or could result in a collision between nodes. The mission might not be completed. **Likelihood:** Unlikely, **Impact:** Significant.
15	RISK-OP-SIM-04	**Incorrect landing software control loop**. If the landing control loop is faulty, no drone would be able to land safely, so the mission would not be completed and would result in the damage or destruction of the swarm. **Likelihood:** Unlikely, **Impact:** Severe.
16	RISK-OP-SIM-05	**Anomaly is falsely interpreted as human**. Resources would be deployed to rescue this target, the mission would be completed incorrectly. Misallocation of resources that should have been used to locate the person in distress. **Likelihood:** Possible, **Impact:** Minor.
		Environmental Risks
17	RISK-ENV-01	**Low visibility due to environmental conditions**. This would hinder communication methods reliant on line-of-sight visibility and would make the footage of the target less recognizable. Thus the rescue boat would not be able to confirm whether the target picked up by the drones is indeed a victim in distress, or something else. **Likelihood:** Likely, **Impact:** Minor
18	RISK-ENV-02	**Parts not reusable due to inflicted damage**. If damage is inflicted by external factors from the drone, there is a risk that parts or components become unusable for future missions. As the drone is designed to withstand such conditions, the lifetime is long enough to **Likelihood:** Possible, **Impact:** Minor

19	RISK-ENV-03	**Environmental Degradation of hardware components**. Due to the rough storm conditions, drones should be water-resistant and weather-resistant. However, after continuous use, parts would need to be fixed or replaced, as components would degrade. This would reduce the sustainability of the project **Likelihood:** Likely, **Impact:** Minor
20	RISK-ENV-04	**Electrical discharge due to storm conditions**. As the drone operates in stormy conditions, the electric power system can discharge due to the storm. This has a big impact on the electric power system as the discharging lowers the endurance of the drone. **Likelihood:** Unlikely, **Impact:** Significant
		Development Risks
21	RISK-DEV-AS-01	**Construction and assembly errors**. An assembly error in one of the parts could result in a decrease in sustainability and an increase in costs for the mission as the part would need to be scrapped and redesigned or replaced. **Likelihood:** Unlikely, **Impact:** Severe
22	RISK-DEV-TEST-01	**Human error when performing pre-flight checks**. As the pre-flight checks are done manually, the risk of human errors is possible. Pre-flight checks can be biased or any issues can be overlooked. **Likelihood:** Possible, **Impact:** Moderate
23	RISK-DEV-TEST-02	**Uncertainties of software testing equipment** Could result in software that acts in an unexpected manner, which could have a range of minor to catastrophic consequences for the mission. **Likelihood:** Likely, **Impact:** Moderate
		Resource Management Risks
24	RISK-RMR-01	**Research and Development costs exceeds allocated budget** An increase in cost would make this project less profitable, thus to decrease costs, corners could be cut, decreasing the quality of the final product. **Likelihood:** Likely, **Impact:** Moderate
25	RISK-RMR-02	**Operation costs exceeds allocated budget**. Unlike the R&D costs, an increase in operational costs could cause the project to be scrapped. **Likelihood:** Unlikely, **Impact:** Moderate
26	RISK-RMR-03	**Deadlines are not met for the assembly processes**. This can be due to inexperience on the engineers' part among other factors. Not meeting deadlines can result in increased costs or a decrease in quality. **Likelihood:** Likely, **Impact:** Minor

To provide a visual representation of the risks above, a table matrix has been created, which is depicted in Table 7.2. The risks are denoted by numbers such as 1.2 or 4.1, these numbers can be found in the last digits of the risk codes. The risk map will show which risks are the most impactful and thus must be mitigated. The mitigation steps can be found in subsection 7.1.1.

Table 7.2: Risk map of the entire project, before mitigation.

Likelihood / **Impact**	Rare	Unlikely	Possible	Likely	Almost Certain
Severe	🟨	🟧 2, 12, 13, 15, 21	🟥	🟥	🟥
Significant	🟩 3	🟨 5, 6, 8, 9, 10, 14, 20	🟧 1	🟥	🟥
Moderate	🟩	🟨 7, 11, 25	🟨 4, 22	🟧 23, 24	🟥
Minor	🟩	🟩	🟨 16, 18	🟨 17, 19, 26	🟧
Negligible	🟩	🟩	🟩	🟩	🟨

The risk map above shows that there are 9 risks in the orange area meaning they can not be ignored. Therefore, there is a need for mitigation. The mitigation strategies to reduce risks are presented in subsection 7.1.1.

7.1.1. Mitigation Strategies for Reducing Risks

It is crucial that the risks in the section above are mitigated, minimizing their negative consequences. After the risks are mitigated, they can be shown in a new risk map shown in Table 7.3. The following minimizing strategies are used:

- **RISK-OP-GEN-01: Failure in battery charging:** To mitigate this risk, redundant batteries will be placed on the ship deck. These can be used when the battery of the drone fails. By doing so, the impact of this risk will be moderate. An important point in this mitigation strategy is that the design shall be compatible with battery swapping, which will require a more in-depth design of this subsystem.
- **RISK-OP-GEN-02: Failure of takeoff and landing mechanisms:** This risk can be effectively mitigated through the implementation of multiple redundant takeoff and landing systems, thereby preventing the occurrence of a single point of failure within the overall system. Additionally, maintenance protocols will be instituted to ensure the optimal functioning of these systems. Consequently, the impact will be significant
- **RISK-OP-SIM-01: Error in stability control loop:** The mitigation of this error can be done during the development process of the stability control loop. An extensive simulation for the required flight condition must be developed. The simulation should account for the extreme conditions the drone will be subject to, the drone during the mission will be subject to high wind speeds and wind gusts, as well as rain and other phenomena. In order to make sure the designed control loop enables the drone to maintain stability in storm conditions, verification of each block in the control loop and each aspect of the simulation must be done. Additionally, this control loop should be validated, this means extensive testing of the drone control loop in the mission conditions to validate the mission will be performed as required. This error mitigation will decrease the likelihood of this failure to rare.
- **RISK-OP-SIM-02: Error in thrust control loop:** Same mitigation strategy as for OP-SIM-RISK-01. This mitigation is necessary so that thrust is enabled in the desired way, and the drone can sweep the search area in the required time and speed. After mitigation, the likelihood of this risk would decrease to rare.
- **RISK-OP-SIM-04: Incorrect landing software control loop:** Same mitigation strategy as for OP-SIM-RISK-8.1 and OP-SIM-RISK-8.2. The drone should be able to visualize the orientation of the landing pad, and based on this input, the control loop will make sure the drone is aligned with this for a safe landing. This must be simulated, and the risk in the control loop will be mitigated by verification and validation strategies. This mitigation would reduce the likelihood of this risk occurring to rare.
- **RISK-DEV-AS-01: Construction and assembly errors**. Construction and assembly errors can be avoided by implementing extra maintenance and making the workstations accessible for easy inspection. As for the complexity of the drones, use experienced workers or provide training sessions for beginning workers. At last, quality control measures and final inspection methods are performed before the pre-flight phase. Although it may be difficult to fully avoid all the construction and assembly errors, implementing these strategies can lower the severity of the potential impact. So this decreases the likelihood of the risk to unlikely and the impact to moderate.
- **RISK-DEV-TEST-02 Uncertainties of software testing equipment**: In order to mitigate this critical risk, the involved parties will conduct thorough test planning to minimize uncertainties during the testing and define boundaries and expectations where the equipment is expected to perform to. Additionally, the utilization of different testing equipment can increase confidence in the results. Alternatively, the testing equipment will go through thorough verification and validation tests. This decreases the likelihood to possible.
- **RISK-RMR-01: Research and Development costs exceeds allocated budget**: To mitigate this risk, the team has to perform a thorough budget management analysis. Therefore, lowering the likelihood of exceeding the allocated budget and hindering the design process. As there is a possibility of rework or planning errors, margins for every process can be implemented as a safety measure which decreases the likelihood to possible.

Table 7.3: Risk map of the entire project, after mitigation.

Likelihood **Impact**	Rare	Unlikely	Possible	Likely	Almost Certain
Severe	12, 13, 15	🟧	🟥	🟥	🟥
Significant	3	2, 5, 6, 8, 9, 10, 14, 20	🟧	🟥	🟥
Moderate	🟩	7, 11, 21, 25	1, 4, 22, 23, 24	🟧	🟥
Minor	🟩	🟩	16, 18	17, 19, 26	🟧
Negligible	🟩	🟩	🟩	🟩	🟨

The risk map above shows the successful mitigation of risks, as there are no more risks in the orange and red areas of the diagram. Even though the risks were made less critical there is still a chance that they can occur. Consequently, a contingency plan is presented in subsection 7.1.2.

7.1.2. Contingency Plan

In this section, the contingency plan is proposed. There is a possibility that risks can unexpectedly still occur. Therefore, it is necessary to have a contingency plan in place to minimize disruption in the event of unexpected critical risks. The narrative of the contingency plan is focused on the critical risks. The guidelines of the contingency plan are listed below.

- If a single drone fails or loses connection with the rest of the swarm, backup drones are used which are present on the ground ship. In this way, the mission can continue and the search area stays manageable.
- The pilots and drone will initiate an emergency landing protocol if an error occurs while landing. After the procedure, the error is quickly identified and validated again. This means there has to be a clear communication line between the software developers and the testers.
- If the research and development budget is exceeded, the areas that exceeded the budget have to be identified. An overview will be made of critical and non-critical departments and areas will be identified where possible costs can be reduced.
- If an uncertainty becomes apparent in the testing equipment, the source of error has to be identified first. Alternative testing equipment will be present on the ship to replace the broken equipment. The new equipment has to be calibrated, and the broken equipment is replaced in parallel to reduce the waste of this process.

8

Design and Development Plan

This chapter showcases the complete design and development plan for the STORM system. In total, seven phases are defined; starting with the design phase and ending with the end-of-life operations of the system. Figure Figure 8.1 below visualises a summary of the seven design and development phases. The phases will be expanded upon in the subsequent sections of this chapter.

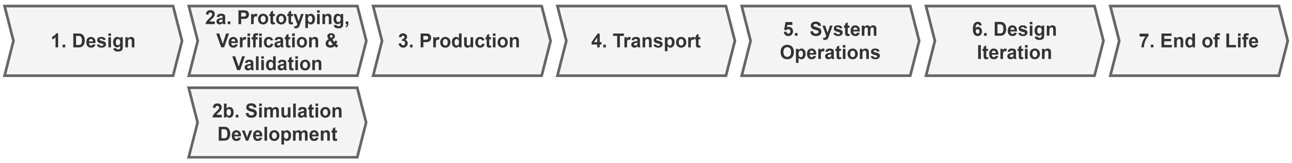

Figure 8.1: The seven design and development phases of the STORM system.

In addition to an explanation of each phase, a functional flow diagram, functional breakdown structure and project Gantt chart are provided at the end of this chapter to give a more detailed overview on the design and development logic of the project during its lifetime. These diagrams, Figure 8.5, Figure 8.6, and Figure 8.7 respectively, are provided in section 8.8.

8.1. Design

Naturally, the first phase of the design and development plan is the design phase. The design phase contains all the previous work done during the Design Synthesis Exercise (DSE) and is concluded by this report.

More specifically, the design phase started with a list of top level user requirements, followed by a determination of the mission need statement and project objective statement. Next, a requirements analysis was performed followed by a preliminary design phase. Lastly, as documented in this report, a detailed design phase is performed which is responsible for defining the characteristics of the required systems and subsystems. These characteristics include but are not limited to the sizing of the propulsion systems, a structural analysis, the swarm and mission profile.

This phase is followed by a testing phase as explained in the subsequent section.

8.2. Prototyping, Verification, Validation and Simulation

Prototyping, verification, validation and simulation of the system will be performed following the detailed design phase of the project. The detailed design phase is concluded with a presentation of the system at the DSE symposium. This phase of the design and development logic is further split up into two subphases. The first subphase contains all activities related to the physical development of the swarm, while the second subphase incorporates all activities related to the development of the simulation of the system as a whole. An overview of this phase can be seen in Figure 8.5 and Figure 8.6.

Phase 2a: Prototyping, Verification and Validation

1. Firstly, the team develops various prototypes for a smaller selection of nodes in the swarm, as opposed to building the entire swarm.
2. After the nodes have been made, the team will implement the steps that are outlined in the verification and validation plan.
3. The team will test the manufactured prototypes in normal conditions. These tests include:
    - Non-Destructive Testing. This test aims to inspect the quality and characteristics of materials, components and systems without causing damage to them.

  - Destructive Testing. This test is used to test the strength, durability and performance of components or systems.
  - Functional Testing. This involves testing the system to ensure that it meets its functional requirements.
  - Performance Testing. This involves testing the system so that it meets the performance requirements.
  - Cybersecurity Testing. This involves testing the system to ensure that it is secure against cyber threats.
  - Safety Testing. This involves testing the system to ensure that it is safe to operate.
4. The results obtained are analysed to determine compliance with the predetermined set of requirements.
5. If the prototype complies with all the requirements, the final product can be manufactured, whereas if not, updated prototypes need to be developed and tested again.
6. Once the final product is manufactured, the operational phase can be initiated in cooperation with the client.
7. During the operational phase, the team can gather a large amount of operational data, which can be analysed to optimise the design even further. This iterative process of data analysis and design optimisation can lead to the development of a more efficient and effective drone swarm.
8. After the optimisation of the current design, the team can shift their focus toward the scalability of the project. By evaluating the scalability of the project, the team can ensure that the design is flexible enough to adapt to changing market demands and achieve sustainable growth.

Phase 2b: Simulation Development

The team also considered the visualisation possibilities post-DSE, which include several phases. These include:

1. Initially, the simulation is subjected to normal conditions to evaluate its ability to accurately replicate the design specifications.
2. The simulation is then subjected to more testing under severe storm conditions, to see if it correctly simulates real-life scenarios.
3. If updates are made to the prototype, the simulation must also be updated accordingly and subsequently tested again.
4. Upon completion of the prototype, a final simulation of the drone swarm can be conducted. This serves to train personnel in the safe operation and usage of the drone swarm.

8.3. Production

After the relevant tests on the prototypes are conducted successfully, the system is verified and validated. The simulation is finalised, going to the next step in the development is the manufacturing of the entire system, and conducting more tests to validate performance of the complete system. A production plan of the system is provided to elaborate on the production phase of the design. In Figure 8.2, the production plan timeline and activities for the construction of the entire system is highlighted upon.

Production Plan

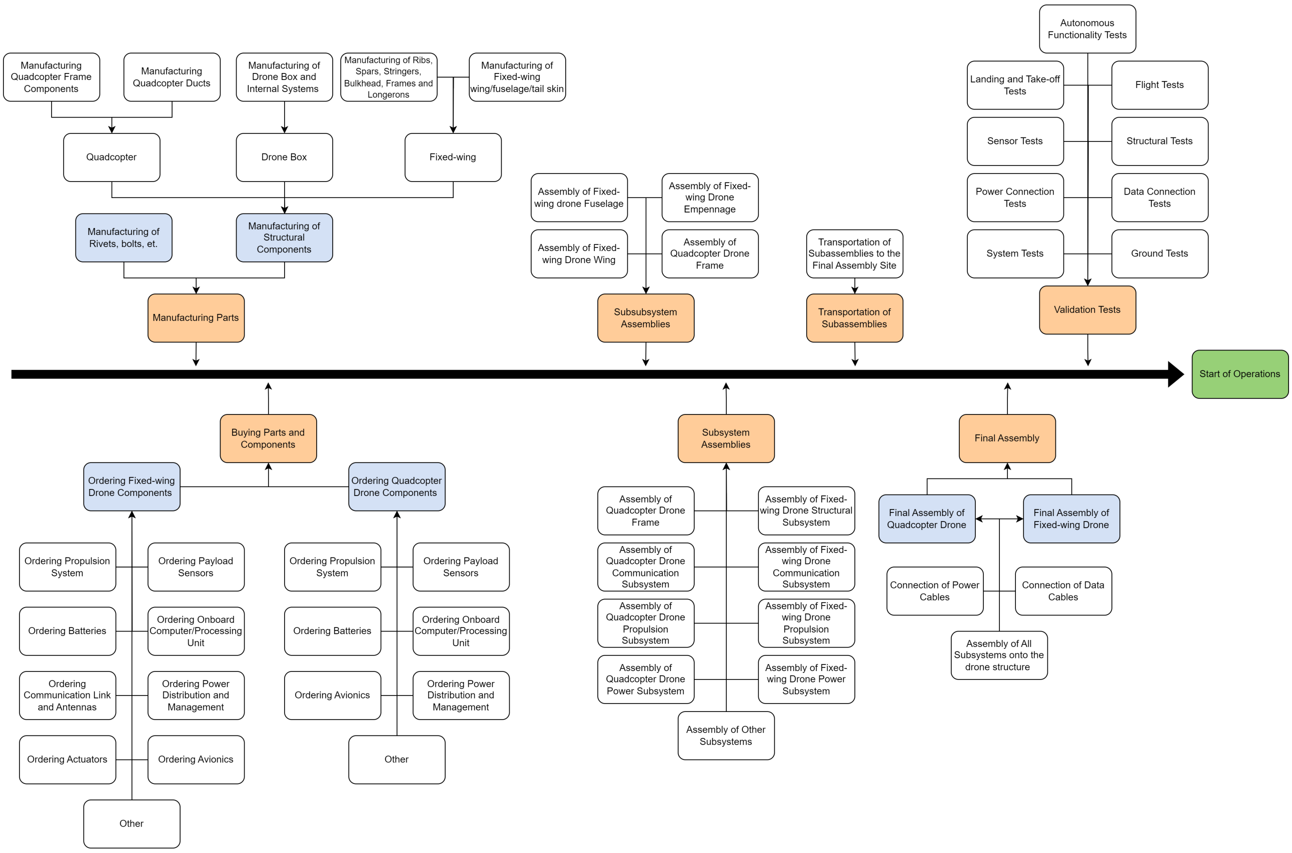

Figure 8.2: The production plan of the STORM system from phase three of the design and development plan.

The production plan outlines the time ordered outline of the required activities to produce the product from its constituent components. A production plan is vital for the timely construction of the product and to avoid unnecessary waiting times. The efficiency of the production phase can be increased by outlining activities that can be conducted simultaneously. For example, some components need to be bought, while some components can be manufactured by the production team. After the manufacturing of the individual components, these need to be assembled into subsystems, which are subsequently assembled to produce the individual drones. These subsystems may be manufactured and assembled in different facilities, so the transportation of all the subsystems into one common facility may be necessary. As soon as all the subsystems are present in the final assembly facility, the final assembly phase can be initiated, and all the subsystems are assembled into the final product. Finally, the testing and validation phase begins. In this phase the functionality of the final product is tested based upon different aspects, additionally, the final product is validated such that it is complying with the set standards. If all of the tests are successful and the standards are met, the systems are ready for use and can start the operation phase.

From Figure 8.2 it can be seen that most of the components of the systems consist of COTS, like the propulsion systems, batteries for the power subsystem, and communication link components. Only the structural components of the drones and the drone hub are manufactured by the team. While the internal structural components like ribs, stringers and spars are easy to manufacture since they are made out of aluminum, the manufacturing of the wing, empennage, fuselage skin and structural booms require more attention. These subsystems are made out of carbon fibre composite, which requires special facilities and equipment to shape the composite into the desired shapes of the aerofoil and the fuselage, which will most likely increase the manufacturing costs.

8.4. Transportation

After the final product has been manufactured in its entirety and has been validated to be in compliance with the set requirements, the next step is to transport the final product to its operational environment. Since the entire system is contained in a standard 20-feet container, transportation does not pose a significant challenge. This phase includes the transportation and the integration of the drone container onto the ship deck, transportation and the initial set-up of the autonomous drone system, and the set-up of the ground station on the ship. The transportation of the system to the client's ship does not require special transportation means as the size and the weight of the system are compatible with standard intermodal transportation containers used in transport ships and trucks.

At the end of this phase, the system should be delivered to the client and fully integrated onto the ship, ready for operations after the final tests and inspections have been conducted.

8.5. Operations and Logistics

The operations and logistics phase of the system contains six mission phases. These phases are described in section 3.1.

8.6. Design Iteration

This phase of the system refers to improvements done to the system product after its performance have been demonstrated and analysed during its operational lifetime. The performance of the system is analysed while the shortcomings and the technical deficiencies are noted and possible improvements are suggested. This phase is similar to the iteration activities conducted during the design phase, while the main difference is that the improvements and changes are intended to be be implemented on the next generation of the system. Data gathered during the operational lifetime of the system forms the basis of this performance analysis.

8.7. End-of-Life Considerations

The end-of-life phase of the STORM system happens at the end of the operational lifetime. During this phase, the system is disarmed, disassembled and recycled. In Figure 8.3 below, the subphases of this part are shown.

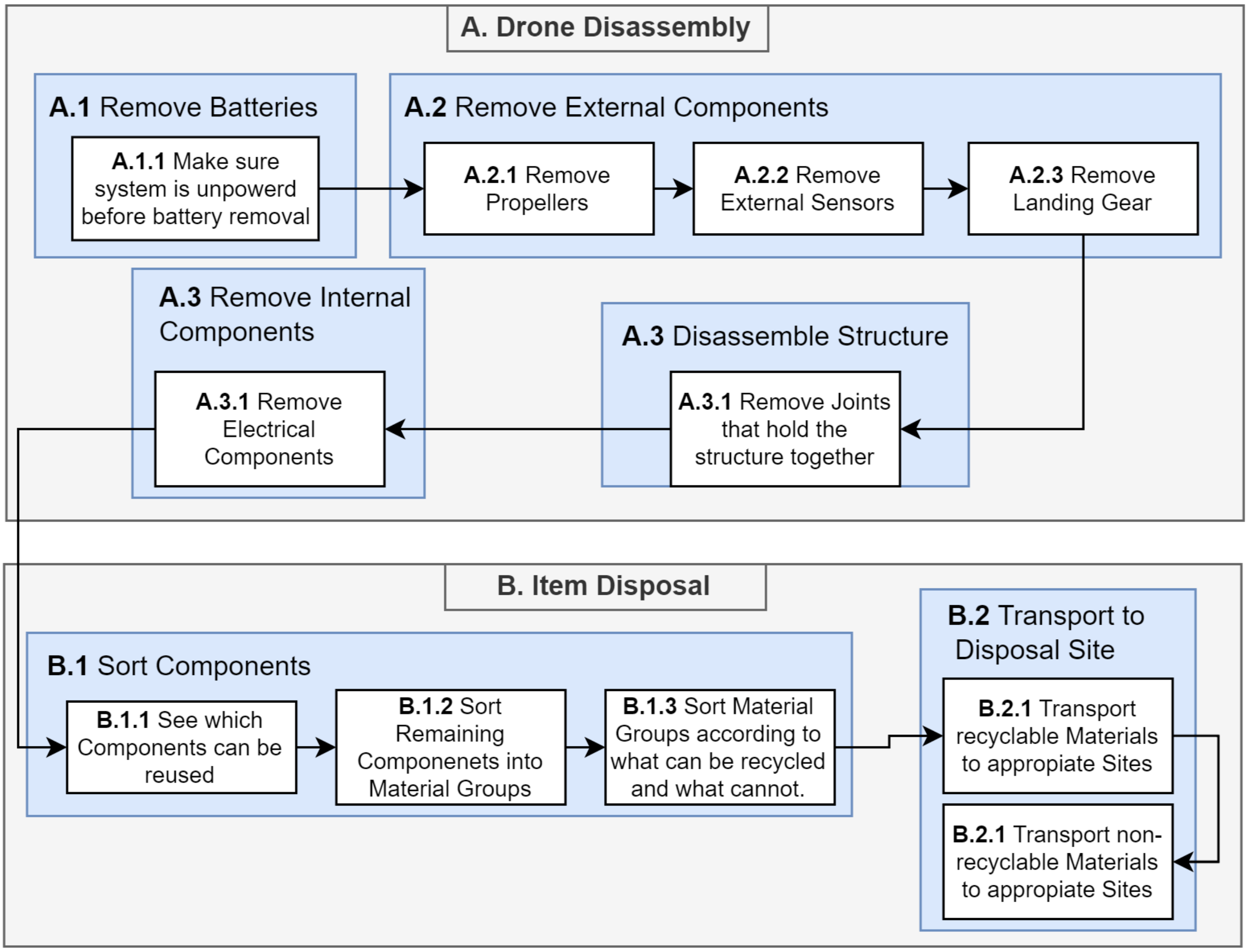

Figure 8.3: End of life operations as part of phase seven of the operations and logistics plan.

Carbon fibre recycling

Since many components of the STORM system are manufactured from carbon fibre, it is important to outline the procedure used to recycle the carbon fibre contained within the STORM subsystems. In Figure 8.4 the steps that are ought to be taken in the recycling procedure used for carbon fibre is visualised.

The high price of carbon fibre material is one of the main driving factors for the need of sustainable and economically viable recycling methods [1]. However, recycling carbon fibre constructed components and composites poses some issues. Firstly, such materials are constructed to be highly durable and non-homogeneous making it inherently more difficult to recycle. Additionally, composites are generally produced in combination with a supportive material such as foams and resins, this leads to mixed waste streams making increasingly more difficult to recycle [2].

---

[1] URL:https://terratechmedia.com/boomtime/ [Cited: 20-06-2023]

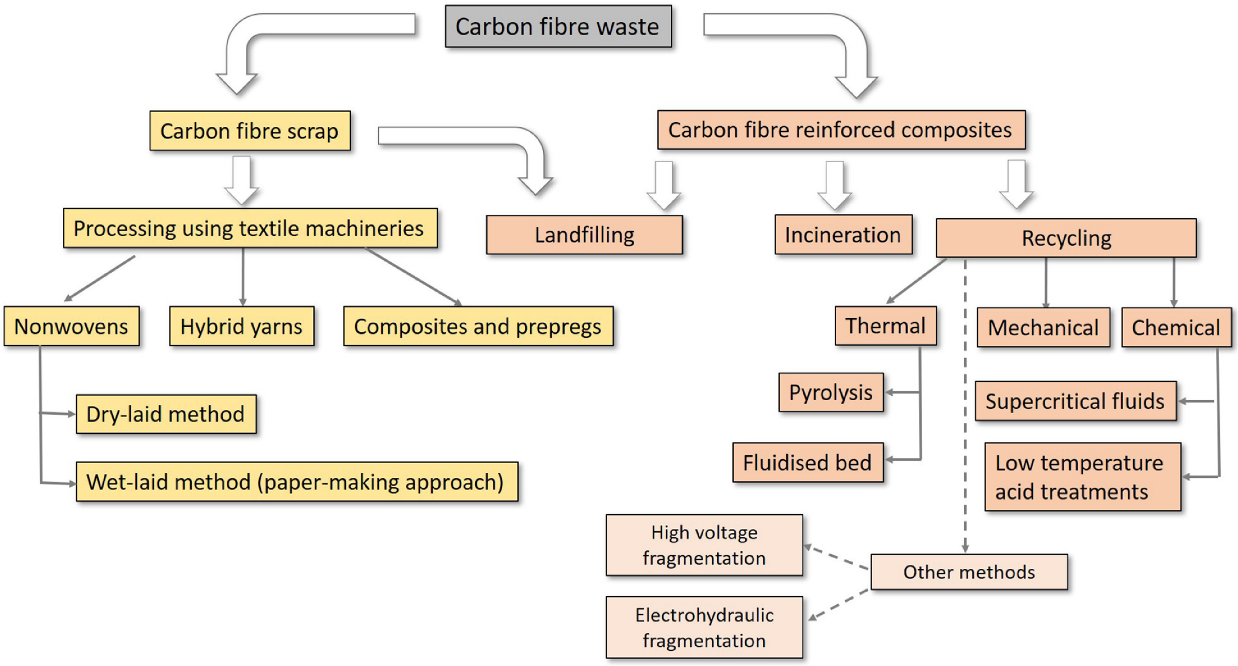

Figure 8.4: Carbon fibre recycling scheme.

8.8. Design and Development Diagrams

The design and development diagrams are used to visually represent the tasks and schedule in a logical order after the detailed design phase. There are three design and development diagrams: the functional flow diagram, the functional flow diagram, and project Gantt chart. The descriptions of these diagrams are shown below.

8.8.1. Functional Flow Diagram

The Design and Development Logic flow diagram is a visual representation that provides the sequence of activities pertaining to work packages and phases. Each work block denotes a distinct work package that is linked with other work packages. The work packages are arranged in a temporal sequence and are executed chronologically. The Design and Development Logic flow diagram can be seen in Figure 8.5.

8.8.2. Functional Breakdown Structure

The Design and Development breakdown structure is a hierarchical decomposition of the activities post-DSE into smaller, more manageable components. This helps to define the work that needs to be done and helps with the organization of the project. The breakdown structure is derived from the flow diagram, but includes more detail with regards to the various tasks that must be executed to complete the project. The blue boxes represent the work packages that need to be finished. Each work package is subdivided into smaller tasks, represented by white boxes, with each task in turn divided into sub-tasks. Each sub-task is accompanied by a duration estimate that facilitates the assessment of the time needed for the completion of each work package. The Design and Development breakdown structure is visualised in Figure 8.6.

8.8.3. Project Gantt Chart

A project Gantt chart is made presenting all of the intended post-DSE activities in a time order. Instagantt will be used to generate the chart. Each row contains the name of the individual tasks, the completion progress as a percentage, and its expected duration in hours. Sufficient detail is provided such that any delays can be quickly spotted and adjusted. The project Gantt chart is derived from the Design and Development Logic flow diagram and Design and Development Logic break-down structure. The project Gantt chart can be seen in Figure 8.7.

Figure 8.5: Design and Development Logic flow diagram.

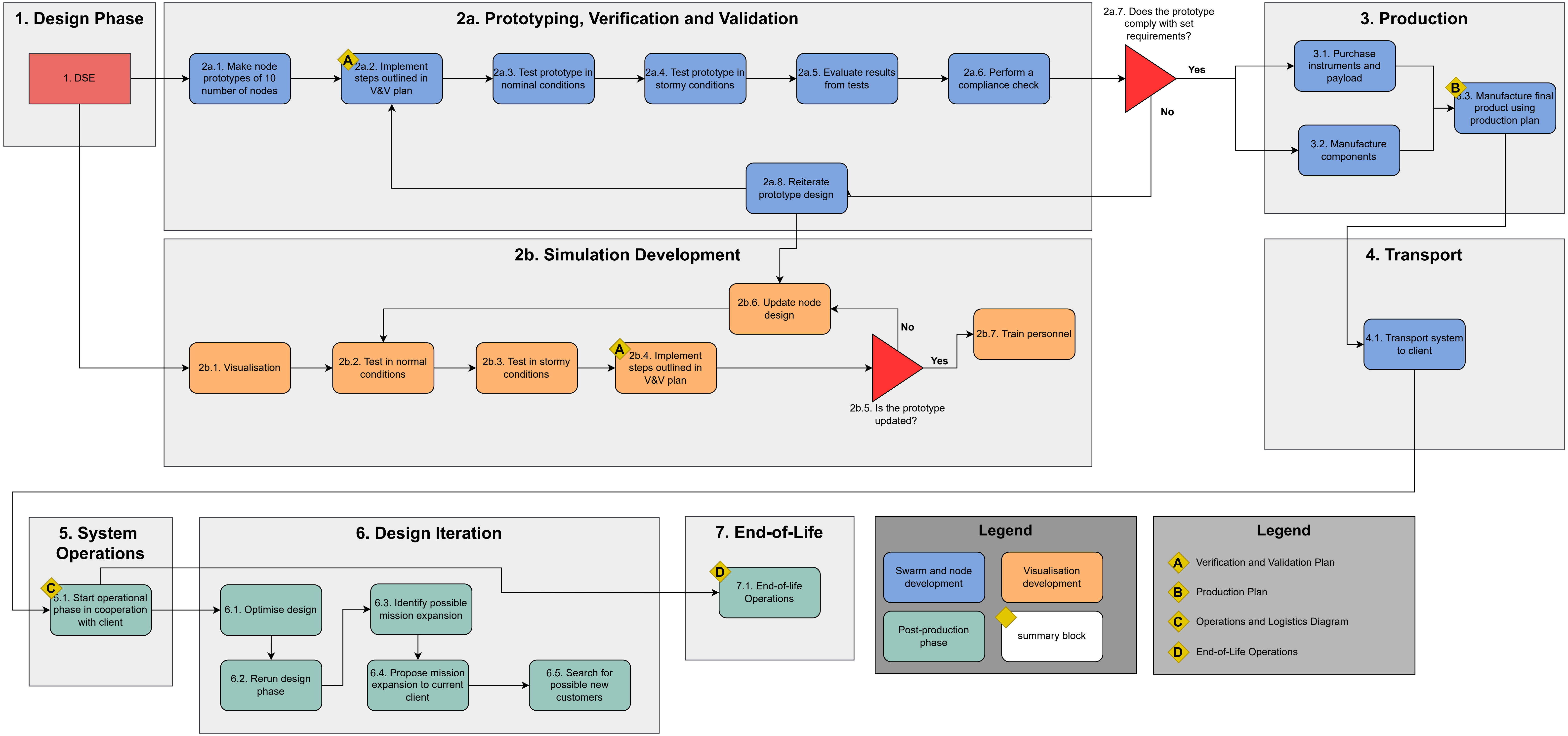

Figure 8.6: Design and Development Logic breakdown diagram.

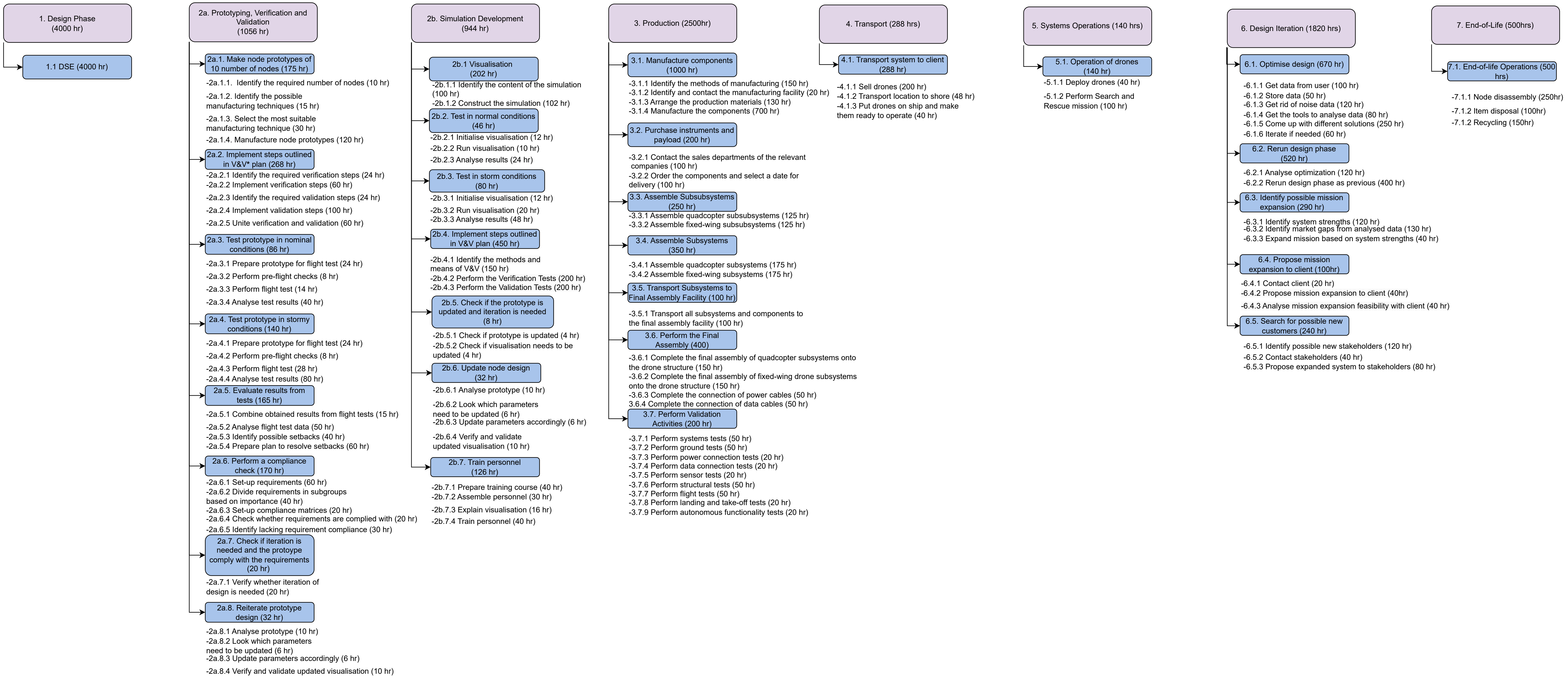

Figure 8.7: Project Gantt Chart.

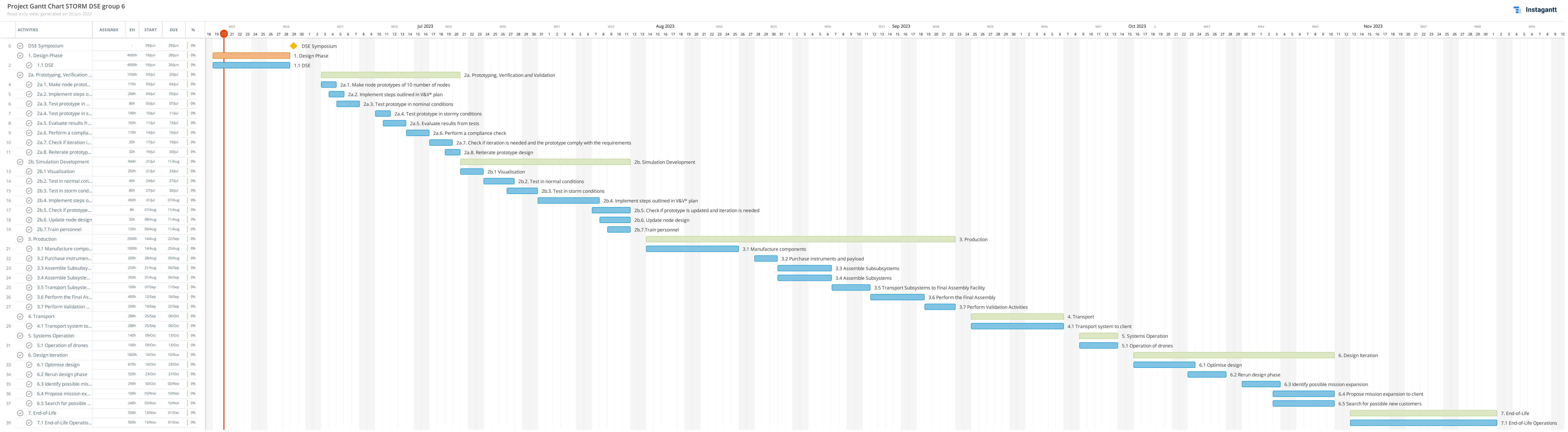

Project Gantt Chart STORM DSE group 6

Read-only view, generated on 20 Jun 2023

	ACTIVITIES	ASSIGNEE	EH	START	DUE	%
0	DSE Symposium		-	29/Jun	29/Jun	0%
	1. Design Phase		4000h	19/Jun	28/Jun	0%
2	1.1 DSE		4000h	19/Jun	28/Jun	0%
	2a. Prototyping, Verification ...		1056h	03/Jul	20/Jul	0%
4	2a.1. Make node protot...		175h	03/Jul	04/Jul	0%
5	2a.2. Implement steps o...		268h	04/Jul	05/Jul	0%
6	2a.3. Test prototype in ...		86h	05/Jul	07/Jul	0%
7	2a.4. Test prototype in s...		140h	10/Jul	11/Jul	0%
8	2a.5. Evaluate results fr...		165h	11/Jul	13/Jul	0%
9	2a.6. Perform a complia...		170h	14/Jul	16/Jul	0%
10	2a.7. Check if iteration i...		20h	17/Jul	19/Jul	0%
11	2a.8. Reiterate prototyp...		32h	19/Jul	20/Jul	0%
	2b. Simulation Development		944h	21/Jul	11/Aug	0%
13	2b.1 Visualisation		202h	21/Jul	23/Jul	0%
14	2b.2. Test in normal con...		46h	24/Jul	27/Jul	0%
15	2b.3. Test in storm cond...		80h	27/Jul	30/Jul	0%
16	2b.4. Implement steps o...		450h	31/Jul	07/Aug	0%
17	2b.5. Check if prototype...		8h	07/Aug	11/Aug	0%
18	2b.6. Update node design		32h	08/Aug	11/Aug	0%
19	2b.7.Train personnel		126h	09/Aug	11/Aug	0%
	3. Production		2500h	14/Aug	22/Sep	0%
21	3.1 Manufacture compo...		1000h	14/Aug	25/Aug	0%
22	3.2 Purchase instrumen...		200h	28/Aug	30/Aug	0%
23	3.3 Assemble Subsubsy...		250h	31/Aug	06/Sep	0%
24	3.4 Assemble Subsyste...		350h	31/Aug	06/Sep	0%
25	3.5 Transport Subsyste...		100h	07/Sep	11/Sep	0%
26	3.6 Perform the Final As...		400h	12/Sep	18/Sep	0%
27	3.7 Perform Validation ...		200h	19/Sep	22/Sep	0%
	4. Transport		288h	25/Sep	06/Oct	0%
29	4.1 Transport system to...		288h	25/Sep	06/Oct	0%
	5. Systems Operation		140h	09/Oct	13/Oct	0%
31	5.1 Operation of drones		140h	09/Oct	13/Oct	0%
	6. Design Iteration		1820h	16/Oct	10/Nov	0%
33	6.1 Optimise design		670h	16/Oct	23/Oct	0%
34	6.2 Rerun design phase		520h	23/Oct	27/Oct	0%
35	6.3 Identify possible mis...		290h	30/Oct	03/Nov	0%
36	6.4 Propose mission ex...		100h	03/Nov	10/Nov	0%
37	6.5 Search for possible ...		240h	03/Nov	10/Nov	0%
	7. End-of-Life		500h	13/Nov	01/Dec	0%
39	7.1 End-of-Life Operatio...		500h	13/Nov	01/Dec	0%

8.8.4. Reliability, Availability, Maintainability and Safety (RAMS) Characteristics

In order for the drones to be used for any mission, especially life-critical missions such as Search and Rescue, it is paramount that the system has high reliability. To ensure this, the swarm as a system will not be allowed to have any single point of failure. This means that any mission-critical system, such as the drone launch and recovery system, must have at least one level of redundancy. Due to the nature of a swarm, the reliability of individual drones is less stringent than that of the swarm, since it is possible to replace failed drones with operational ones to keep the swarm functioning. Still, this procedure will (temporarily) reduce the effectiveness of the drone, and is to be avoided if possible. Therefore, all subsystems critical for the functioning of the drone will also have at least dual redundancy.

The drone swarm is expected to be operational at any point in time. This implies that both scheduled and unscheduled downtime has to be taken into account. Implementing scheduled inspection and repair sessions can complement the readiness of the swarm. On board the ship, there will be spare parts and resources present that can compensate for unexpected failures or downtime. The availability increases with the redundancy of the system. In the storage containers, there will be backup and spare drones available during the operation. This will be necessary, as time is of the essence for search and rescue missions, meaning it will not always be possible to fix a broken drone during the mission duration. Furthermore, there will be protocols in place to respond to any availability issues in a refined way. Following such a structured predetermined plan improves the recovery time of the system and thereby improves availability. The parties involved are expected to be ready to respond to any arising issues at all times, as incidents can occur at unwanted or unexpected moments.

A good maintainability of the drones is important to ensure the cost of operation remains within bounds, as well as to achieve the sustainability goals set out for the project. To achieve this maintainability, a couple of steps will be taken. For the assembly of the drone, standardised bolts and other attachment mechanisms will be used, allowing for access to internal components without the need for specialised equipment. For the assembly, the use of adhesives will be avoided as much as possible, to allow for disassembly to access the components which makes it easier to maintain the drone and repair any damage that may arise. Within the drone, as many subsystems as possible will use standardised parts and components, which will be made available at a reasonable cost for at least as long as the operational life of the drone. To aid customers in their repairs and maintenance procedures, proper manuals and schematics with sufficient detail to perform repairs on the individual subsystems will be published free of charge for any owner or operator of the STORM drones.

At last, safety is paramount for any search and rescue mission. The safety accounts for both the safety of the personnel onboard, and of the people who have to be rescued. Additionally, the safety of any civilians in or near the search area is accounted for in the design and operation of the STORM system. In chapter 7, possible risks were identified and mitigation strategies are set up, which also increases the safety of the drone swarm. To ensure safe operations, no personnel interaction with the swarm is allowed when the outside conditions are not safe to do so. In such cases, the safety protocol urgently advises personnel to stay inside whenever possible. To achieve this goal, the drone swarm will take-off and land autonomously, without requiring human contact. The drones will only be used for finding the target and are not used as rescue vehicles. The drones are not allowed to approach the person within a radius of 10 metres as this increases the risk for the survivor. The rescuing will be done by the ground ship and is accompanied by surrounding rescue boats or emergency tow vehicles. The ground ship always moves alongside the direction of the drift and stays close to the search area.

9
Mission Financial Valuation

A crucial part of the design process is assessing the product's value by comparing it to the available market and calculating potential profits. The mission financial valuation chapter shows the market analysis for the maritime surveillance drone industry. Firstly, in section 9.1 an overview of the design and development, component, manufacturing, operation, and end-of-life costs are shown. Followed by section 9.2, where the current market is analysed to identify the market share for our drones. After the cost breakdown and market analysis is done, the future market demand and investment benefits are explained in section 9.3.

9.1. Cost Breakdown Structure

In order to accurately determine the return on investment, it is necessary to quantify the cost of developing the drone swarm. The costs of the project can be divided into the following groups: design and development costs, component costs, manufacturing costs, operations costs and end-of-life costs. In order to provide an accurate depiction of the current costs, the comparative costs obtained from literature have been adjusted for inflation to align with the standards of 2023. The design and development costs is the same for both the Quadcopter and the Fixed-Wing. However, the components, operations, manufacturing and End-of-life costs are difeerent. These cost groups will be explained in the following sections.

Design and Development Costs
These costs encompass expenses directly associated with the design and development phase of the Quadcopter and Fixed-Wing. This includes wages for employees and engineering roles, as well as costs related to ground station development, software development, and wind tunnel testing. The assumption is made that office rent is provided by TU Delft and therefore does not incur additional expenses for the team.

The wages for employees are assumed to be 30 €/hour, which corresponds to the starting salary of an Aerospace Engineer. The DSE has a total duration of 4000 man-hours. However, since the design is not completed at the end of the DSE, an additional 2000 hours are projected to be required to finalize the design of the drone swarm, resulting in a total duration of 6000 hours.

The ground station development costs include the expenses associated with developing the START system and the entire ground station infrastructure on the ship. It is assumed that the ground station development costs amount to 33000 € per kilogram, as specified in [27]. This cost estimation is based on the ground station development of the DarkStar CGS, and while it may not be entirely accurate for the current mission's ground station, it provides an initial approximation.

The software development costs encompass the development of software components utilized in both the Fixed-Wing drone and the QU drone. This includes various functionalities such as search algorithms, inter-drone communication, and other software components. The estimated cost for software development is assumed to be 8,000 € per kilogram, as indicated in [27].

Wind tunnel testing is a crucial aspect for evaluating aerodynamics and ensuring the proper functioning of the design. However, conducting wind tunnel tests can be costly, which should be considered in the cost breakdown. According to [27], renting a wind tunnel for one week would have a total cost of 136,360 euros. The assumption is made that the team utilizes a wind tunnel for a week to thoroughly test their design.

Component Costs
The component costs refer to the make up of the materials and components of the Quadcopter and Fixed-Wing themselves. As a large portion of the node components are selected commercially available these values are able to be accurate to the order of cents. However, certain costs, such as material costs, need to be accurately listed relative to their specific dependencies on factors such as the local economy, delivery methods, and sourcing logistics. "Off-the-shelf" product costs are taken directly from either quotes from the manufacturer, or at the given cost on their online store. In cases where the costs of specific components were not publicly available, similar components were used as a reference to estimate the price. It should be noted that some components may be potentially sourced from outside the European Union, and therefore may be subjected to trade taxes, artificially increasing the price. For the sake of this breakdown, it is assumed that the components

are not subject to trade taxes.

Manufacturing Costs

These costs pertain to the manufacturing of both the Fixed-Wing drones and the Quadcopters once the detailed design phase is completed. The majority of these costs is dependent on the allocated salary of the employees, specific machine costs and licensing testing fees. To get a first-order estimate of these costs, both parametric relations and values, directly taken from literature, have been used [27].

The estimation of man labour hours utilizes a method introduced in [27]. In accordance with Equation 9.1, the calculation requires the empty weight of the Fixed-Wing or Quadcopter, which is determined as 55.12 lbs. Additionally, a conversion factor is incorporated to account for material usage in the estimation process. It is given that the composite materials used in the construction of the Fixed-Wing possess a value of f_{Matl} equal to 1.98. On the other hand, the majority of the Quadcopter is constructed using aluminum 2024, which has a corresponding f_{Matl} value of 1.0. These f_{Matl} values are indicative of the material's relative contribution to the overall manufacturing process. The resulting labour hours, H_r, equals 233 for the Fixed-Wing system and 118 for the Quadcopter. The aforementioned values are combined with the hourly rate of the technical specialist whom is responsible for the manufacturing process. The corresponding values can be seen in Table 9.2, Table 9.3, and Table 9.4.

$$H_r = 10.4 \cdot W_e^{0.605} \cdot f_{Matl} \tag{9.1}$$

Following the manufacturing, but prior to the operational phase of the STORM system, both the Fixed-Wing and Quadcopter have to be tested and licensed as in accordance with the FAA [46]. The licensing testing fee amounts to €161.00 per system, and is taken into account in the total cost breakdown.

An important remark that has to be made is with regards to the required machines for manufacturing. The team has decided upon an agreement with the Delft University of Technology, by doing so the team is allowed to manufacture the STORM system in-house, greatly reducing the manufacturing costs.

Operation Costs

This refers to any costs incurred onto the then STORM company. These costs includes aspects such as GPS data relay framework (Server and Electricity Costs), drone maintenance services, and battery recharging service. As these costs are only incurred after a drone swarm has been purchased, it is possible to implement a subscription based service at a later stage. Nonetheless, these costs will already be considered in the cost breakdown for the sake of investors. These costs will be estimated using comparable services from engineering companies of roughly the same scale, and the Designing Unmanned Aircraft Systems handbook [27]. The estimated operation costs visualised in Table 9.2 and Table 9.3 are for a singular mission, which has a maximum duration of 48 hours.

The first operational cost that is considered is the recharging of the battery system after completion of a Search and Rescue mission. In Table 5.6.1 it is given that the battery capacity of the Fixed-Wing is equal to 5.265 [kWh], therefore, recharging the ten Fixed-Wing nodes would require a total energy of 52.65 [kWh]. The current electricity price in the Netherlands, which is used as a reference, is given in Table 9.4. The combination of this amounts to €21.06 for Fixed-Wing battery recharging costs. The Quadcopter requires a slightly bigger battery system, with a higher energy rating. By using the same reasoning as previous, the costs to recharge the Quadcopter battery costs €6.16.

The maintenance cost required to keep the the Fixed-Wing system operational are also taken into account. The team has assumed that succeeding every Search and Rescue mission, two hours of maintenance is performed on both the Fixed-Wing and Quadcopter system. The hourly rate for the responsible maintenance technician can be seen in Table 9.4.

Finally, the GPS data relay framework cost aspect is highlighted. In [27] it is given that low-bandwidth systems using a bitrate of tens or hundreds of kbits per second may cost approximately $\$60–500$ per hour, the converted value to euro and adjusted for inflation is given in Table 9.4.

End-of-life Costs

The end-of-life costs concern the costs that arise during the dismantling and recycling processes of the Fixed-Wing system. The exact costs for recycling and dismantling the carbon fibre skin and aluminium structural components is difficult to estimate. Carbon fibre material is still considered a newcomer in the aeronautical industry, which results in some issues [1] in recycling as compared to conventional materials used.

As a first-order approximation it has been assumed that the end-of-life costs are dominated by the recycling costs, which in term is mostly consisting out of the man labour costs. The total required hours to dismantle and recycle a singular Fixed-Wing node is assumed to be equal to the hours required to manufacture one node, equalling 233 hours as calculated using the methods presented in [27]. To get a monetary estimate it has been assumed that the employee responsible for dismantling and recycling is the technical specialist I, which is presented in Table 9.4. The same methodology is applied for the Quadcopter system, however, as the manufacturing man labour hours is lower as compared to the Fixed-Wing system, the dismantling and recycling time will also be reduced. The resulting values can be seen in Table 9.3

The complete breakdown of costs for the Fixed-Wing and Quadcopter are presented in Table 9.1, Table 9.2 and Table 9.3. In Table 9.4, all the assumptions are made regarding the costs in the cost breakdown table. These assumptions help provide clarity and context to the values presented in the cost breakdown table.

Table 9.1: Cost breakdown structure of the design and development of the Quadcopter and the Fixed-Wing drone.

Description	*Amount/Hours*	*Total costs [€]*	*Justification*
	Design and Development		
Design team	6000 hours	180000	section 9.1
Ground station development	1	1614994.38	[27]
Software development	1	403748.60	[27]
Wind tunnel testing	40 hours	136360	[27]
Total costs	-	2335102.98	

Table 9.2: Cost breakdown structure of the Fixed-Wing drone.

Description	*Amount/Hours*	*Total costs [€]*	*Justification*
	Components		
Inertial Measurement Unit (IMU)	1	450	[38]
Magnetometer	1	800	[25]
Airspeed sensor	1	54.95	[16]
CPU	1	183.13	[42]
Power distribution and management	1	27	[1]
Antenna	1	473.3	[55]
Actuators	10	2780	[57]
Flight controller	1	97.06	[35]
GPS	1	150	[12]
RTK GPS	1	275	[52]
Communication system	1	966	[19]
Pitot tube	1	400	[7]
Magnet	4	40	[56]
Carbon fibre skin	2.83 m^2	141.39	[18]
Structural	3.70 kg	33.17	Table 5.17
Battery	1	731.41	[8]
Propulsion system	1	247.22	[54]
Mantis i45N	1	13700	[15]
Total costs per Fixed-Wing system	-	21549.63	-
	Manufacturing		
Man labour per node	233 hours	25630	[27]

---

[1] URL:https://terratechmedia.com/boomtime/ [Cited: 20-06-2023]

Licensing testing fee	1	161.00	[46]
Total costs per Fixed-Wing system	-	25779.98	-
Operations			
Battery recharging	52.65 kWh	21.06	[20]
Maintenance	2 hours	284	section 9.1
GPS data relay	48 hours	19776	[27]
Total costs	-	20081.06	-
Total costs per Fixed-Wing system	-	2008.11	-
End-of-life			
Man labour to recycle node	233 hours	25630	section 9.1
Total costs per Fixed-Wing system	-	25630	-

Table 9.3: Cost breakdown structure of the Quadcopter.

Description	*Amount/Hours*	*Total costs [€]*	*Justification*
Components			
Inertial Measurement Unit (IMU)	1	450	[38]
Magnetometer	1	800	[25]
Airspeed sensor	1	54.95	[16]
CPU	1	183.13	[42]
Power distribution and management	1	27	[1]
Antenna	1	473.3	[55]
Flight controller	1	97.06	[35]
GPS	1	150	[12]
RTK GPS	1	275	[52]
Communication system	1	966	[19]
Magnet	4	40	[56]
Carbon fibre skin	1.13 m^2	56.55	[18]
Structural	1.07 kg	9.63	Table 5.17
Battery	1	1163.46	[8]
Propulsion system	1	247.22	[54]
Total costs per Quadcopter system	-	4993.3	-
Manufacturing			
Man labour per node	118 hours	12980	[27]
Licensing testing fee	1	161.00	[46]
Total costs per Quadcopter system	-	13141	-
Operations			
Battery recharging	15.41 kWh	6.16	[20]
Maintenance	2 hours	284	section 9.1
Total costs	-	290.16	-
Total costs per Quadcopter system	-	145.08	-
End-of-life			
Man labour to recycle node	118	12980	section 9.1
Total costs per Quadcopter system	-	12980	-

Table 9.4: Cost assumptions with justifications; current prices are accounted for inflation (2023)

Description	Assumed numerical value	Source
Low-bandwidth bitrate cost	412.00 €/hour	[27]
Software development	16 378 €/kg	[27]
Windtunnel	185 000 €/week	[27]
Current energy price in the Netherlands	0.40 €/kWh	[20]
Operations engineer	142.00 €/hour	[27]
DSE engineer	30.00 €/hour	[24]
Maintenance technician	89.00 €/hour	[27]
Technical specialist I	110.00 €/hour	[27]

.

9.2. Market Analysis

This section builds up on the preliminary market analysis after having a greater view on the scope of the functionality of the product. First, a cost breakdown structure detailing the distribution of costs for the development of the drown swarm is presented. Then, it discusses the state of the current markets along with a prediction of the state and emergence of new markets. Moreover, a return on investment will be outlined to quantify the success the product shall have and to persuade future investors and companies about the benefits of the drown swarm.

9.2.1. Total Addressable Market for the Drone Swarm

A maritime drone swarm can autonomously perform a plethora of missions in large operational areas in harsh environmental conditions. The Mission Need Statement as stated in chapter 2, and the already provided customer requirements can be extrapolated to determine which market segment the drone swarm appeals to. The feature of autonomy attracts many clients and, as such, the several potential customers that a long range maritime drone swarm with surveillance capabilities could cater are listed as follows.

- **Search and Rescue Operations**: Maritime search and rescue teams can make use of drone swarms to improve their effectiveness in locating and assisting distressed vessels or individuals at sea. Drones equipped with cameras and thermal imaging sensors can cover large areas quickly, increasing the chances of successful rescues.
- **Maritime Security Agencies**: Government agencies responsible for maritime security, such as the coast guard, the Navy, or port authorities could be interested in deploying drone swarms for surveillance purposes. They could use drones to monitor coastal areas, shipping lanes, and ports, enhancing their situational awareness and response capabilities.
- **Fisheries and Aquaculture Industry**[59]: Commercial fisheries or fisheries management agencies could use drone swarms to monitor fishing activities, enforce regulations, track fish stocks, and detect illegal fishing practices.
- **Environmental Monitoring Agencies**: Environmental protection agencies, marine research institutions, or non-profit organizations, might utilize drone swarms to monitor marine ecosystems, detect illegal fishing activities, study wildlife, and assess the impact of pollution or climate change on marine environments.
- **Border Control and Customs Agencies**: Border control and customs agencies responsible for monitoring and securing coastal and maritime borders may find drone swarms useful in detecting and preventing smuggling, illegal immigration, or other illicit activities.
- **Offshore Wind Farm Industry**: The offshore wind farm industry could benefit from the use of surveillance drones to monitor the state of the wind turbines or ships in the area to make sure they keep out of the restricted areas.
- **Offshore Oil and Gas Industry**: The offshore oil and gas industry could benefit from drone swarm surveillance for monitoring platforms, pipelines, and other critical infrastructure. Drones can assist in inspecting equipment, identifying leaks, and ensuring compliance with safety and environmental regulations.
- **Commercial Shipping Companies**: Shipping companies may find value in using drone swarms for monitoring their vessels, cargo, and maritime operations. Drones can provide real-time aerial views, aiding

in identifying any security threats such as piracy, monitoring vessel conditions, and enhancing colliding avoidance measures in busy shipping lanes.

- **Insurance Companies**: Insurance companies that specialize in maritime and cargo insurance could employ drone swarm surveillance to assess risks, inspect vessels, monitor cargo conditions, and investigate any incidents or claims.

9.2.2. Current Market State and Expected Growth

The drone swarm is essentially a surveillance drone swarm that is applied to search and rescue missions. For this reason, to assess the current markets, it was decided to look at the surveillance drone market as a whole, and then specifically the search and rescue market.

Surveillance Drone Market

The current surveillance drone market is estimated to have a value of 5.5 billion US dollars in 2023 [2]. The largest share of this value is located in the European markets, with a total market value of 1.7 billion US dollars. The United States is not far behind, having a market share of 1.6 billion US dollars. East Asia is responsible for the third largest share, with an estimated market value of 1.1 billion dollars.

When split by market segment, it is evident that the primary market is provided by the energy sector. Power plant inspection makes up for 25% of the total surveillance drone market, with another 17% taken up by inspection of wind turbines, and a further 12.5% market share for inspection of solar panels [3]. This leads to a total contribution of 55% for just the electricity generation market to the total surveillance drone market. Offshore platform inspection, such as inspection of oil drilling platforms or research stations, makes up another 21% of the market. The last major market contributor is the inspection of pipelines, coming in at 16.5 % of the market. The remaining contributors, including military demand, and search and rescue missions, make up only 5.7% of the market[4] . The market distribution is summarised in Table 9.5.

Table 9.5: Summary of market distribution.

Continent	Market Share [B US Dollar]	Market Segment	Market Share [%]
Europe	1.7	Electricity Generation Inspection	55
United States	1.6	Offshore Platform Inspection	21
East Asia	1.1	Pipeline Inspection	16.5

In order to asses the future states of the markets, its valuation in the next decade (2033) was estimated. It is expected that the global valuation of the drone surveillance market shall reach US$ 21163.2 million. This is expected to be reached by with at CAGR of 14.4%. The global drone market is expected to be valued, growing at a CAGR of 17.6%, at US$ 33.9 billion. This means that the surveillance drone market shall hold a 62.4% share of the global drone market. These numbers motivate the application of the drone swarm to surveillance missions. This demand can be explained by the rise of new technologies such as AI allowing for more autonomy during inspections. Another component is due to the growth of drones in military applications, which will experience a yearly growth of 12%[22]. As shall be mentioned shortly, it hints to the fact that the implementation of a secondary mission is attractive.

To motivate the implementation of a secondary mission in surveillance further, a bubble graph visualizing the 5 year CAGR and the revenue across those 5 years in Figure 9.1. In this figure it can be seen that Oil and gas inspections have the highest CAGR and electrical power generation has the highest revenue forecast. These energy generation and extraction types can be found in offshore oil rigs and wind farms. Since these are stations in open water (at sea) surveillance missions in the form of inspection would be feasible for the drown swarm proposed.

---

[2] URL: https://www.factmr.com/report/surveillance-drone-market [accessed on 20-06-2023]

[3] URL: https://www.factmr.com/report/surveillance-drone-market [accessed on 20-06-2023]

[4] URL: https://www.factmr.com/report/surveillance-drone-market [accessed on 20-06-2023]

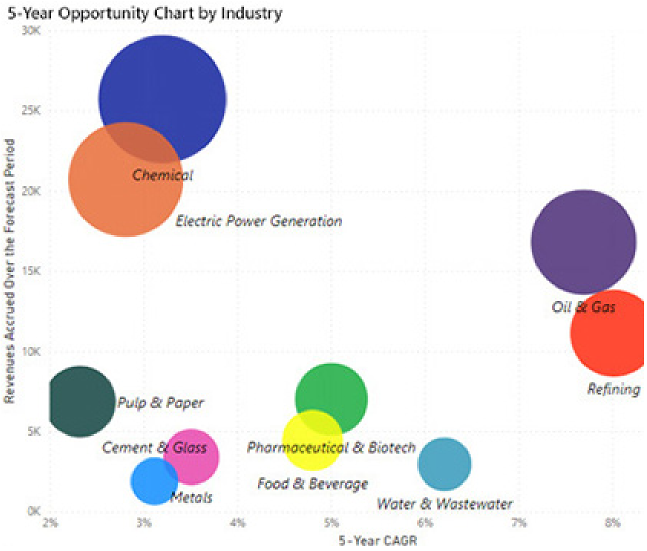

Figure 9.1: Global drone inspection services growth and revenue in 5 years [26].

Search and Rescue Drone Market
The search and rescue drone market segment as of today has an estimated valuation of US$ 547.6 million in 2023 [5]. It is clearly a small percentage of the whole surveillance market, but a vital market to assess for drone swarm product. As for the global surveillance market, the main proportions of the global market are in North America and Europe, with market shares of 30.12% (US$ 164.9 million) and 35.4% (US$ 193.9 million) respectively.

In the next decade, by 2033, the drone rescue service market is expected to reach, at a progression rate of 15.2% CAGR, a valuation of US$ 2254.1 million. This is a 411% increase in total market value, insinuating the opportunities that this market holds.

From this it can be concluded that the search and rescue market is relatively small compared to the other segments such as the energy sector (the inspections thereof). This can be advantageous in two ways: *less competitors* and *large growth*. A smaller market naturally entails the fact that there are less rivals, in which it is easier to excel as a competitor. As for large growth, a small market generally has the potential to grow and expand, as opposed to a large market where contractions are possible; take the oil industry for example. With the importance of sustainability becoming more apparent such a market will inevitably decline. As will be discussed in section 9.3, the expected growth of the search and rescue market is immense and, as such, the opportunities in this market are attractive for the product.

9.3. Return on Investment

This section focuses on assessing the profit margins on the drone swarm as well as motivations as to why the technology represented in this report will add value to future markets and ,as such, reason for investors to invest in the product. The design team expects to sell the drone swarm at a markup of 15% which is in line with comparable aircraft engineering projects profit margins [36]. To justify investment to outside investors, the return on investment shall be explored.

9.3.1. Return on Investment parameters

The return on investment (ROI) is an important parameter for investors as it gives an indication as to how profitable investing in the STORM system is. This indicator ultimately communicates to investors if investing is worth the cost. To calculate ROI, the formula given below is used:

---

[5] URL https://www.factmr.com/report/drones-rescue-service-market [accessed on 20-06-2023]

$$ROI = \left(\frac{\text{Net Profit}}{\text{Investment Cost}}\right) \times 100 \tag{9.2}$$

Net profit is given by 15% of the total unit cost per unit as stated in [36]. At this stage, the total unit cost only considers the manufacturing, component, and end-of-life costs. This amounts to EUR 72959.6 thousand and EUR 31114.3 thousand for the Fixed-Wing and Quadcopter respectively. On top of this a profit margin of 15% [53] was added to estimate an initial price for each node. This then amounts to EUR 83903.6 thousand and EUR 35781.4 thousand for the Fixed-Wing and Quadcopter respectively. As the value of the potential company value increases and further revenue streams are created (For example through the introduction of paid maintenance or paid end-of-life services and general expansion) it is expected that the net profit increases.

Investment cost at this stage is assumed to be the total cost of research and development, component, manufacturing, and sales and marketing costs (making up 17% of all costs as per [53]). The sales and marketing. The team is not a private company, and the investment costs and logistics associated with a publicly traded company as not considered.

At of this stage in time, the lifetime of the nodes and the number of missions a node will undergo are unknown. It is, therefore, difficult to deduce the exact operational costs. This aspect is expected to change in the future. Once this information is known (after testing of the swarm) the operational costs and maintenance costs can be accurately estimated and this cost can be accounted for in the investment cost. In addition to the operational costs, taxes on importing materials and exporting the swarm are not considered in the total cost.

When only considering the aspects mentioned above, the return on investment per unit is simplified as seen in Equation 9.3:

$$\frac{0.15 \times (Manufacturing\ Costs + Component\ Cost + End\ of\ Life\ Costs)}{Research\ and\ Development\ Costs + Sales\ and\ Marketing\ Costs + Manufacturing\ Costs + Component\ Cost} \tag{9.3}$$

9.3.2. Investment Benefits

Along with the profit from sales themselves, investment in such a market can have such benefits on stakeholders. Due to the global COVID-19 pandemic, the autonomous industry has increased with great acceleration [6]. This has shifted a lot of focus towards autonomy in every sector where this technology would be feasible. One of the main autonomous technologies, as discussed in section 9.2, is drones. This industry is going to keep growing regardless of the drone swarm product presented in this report. For this reason, it is important to identify the key benefits as to why this drone swarm is worth investing in to attract investors.

Over the upcoming years, travel over water is expected to increase as globalization increases [11]. From this follows an increase in accidents at sea due to increased vacational and migrational travel. In addition, with the inevitable problem of global warming, harsh weather conditions are going to be more prominent. The Unites States Environmental Protection Agency expects, along with a lot of other climate changes, tropical cyclone activity to increased frequency of category 4 and 5 storms [7]. These facts scratch the surface of a plethora of reasons as to why the importance of search and rescue is evident.

Salary costs will also be saved to the fact that the system is fully autonomous and requires little to none intervention. More importantly, it requires no ship crew members to be on the ship deck during operation, reducing risk by not subjecting responders to dangerous conditions; which is a huge additional safety benefit. The drone swarm is fully packed in the START System. This system resembles the shape and size of a 20 foot container. As such, it is easily transportable by means of conventional transport methods used by trucks and ships. This reduces transport costs as the need for special equipment to transport extraordinary cargo is not needed. It is also modular, meaning that if larger ships want to employ multiple of these system, the wish to do so is an easy implementation. Furthermore, with its conventional shape, many ships will already be able to accommodate its storage and use as compared to other maritime drone systems. Other systems such as

---

[6] URL: https://www.fortunebusinessinsights.com/industry-reports/drone-surveillance-market-100511 [accessed on 20-06-2023]

[7] URL: https://www.epa.gov/climate-indicators/weather-climate [accessed on 20-06-2023]

Catapult launchers, nets, or cable catching systems would require additional structure and interfaces on the ship to accommodate for these methods. These systems would also be susceptible to damage as they are not protected like the START System (which houses the drone swarm in its structure).

With the camera technology in the Mantis i45N, a secondary mission, as explored in section 9.2 for surveillance, is attractive. The Fixed-Wing is designed for this exactly. Thus, when it is not operating a search and rescue mission, the swarm can be used for any surveillance application, including inspections, at sea. Moreover, close proximity inspections of wind farms or oil rigs for example can also be carried out for by the Quadcopter which has hovering abilities. A few design changes would have to occur for this to be a competitive product, as the battery life in ideal conditions (no wind gusts) for this drone is only 23 minutes as designed in section 6.3. This would need to be significantly higher in order to carry out efficient inspection missions.

10
Sustainable Development Strategy

In order to ensure the long-term sustainability of the drone swarm project, the team has implemented strategies to mitigate unsustainable practices and assess the project's current sustainability. This section is divided into three parts, each focusing on a different aspect of sustainability. The first aspect is economic sustainability which is outlined in section 10.1.The second aspect is social sustainability, discussed in section 10.2. Lastly, environmental sustainability will be covered in section 10.3.

10.1. Economic Sustainability

The team will use sustainable manufacturing processes and materials in order to support sustainable development. The order of sustainability can be directly impacted by the use of material and manufacturing processes. For materials, the team will reduce the amount of waste by choosing reusable materials and avoid using materials that can generate toxic waste. Regarding manufacturing processes, the sustainable principle lean manufacturing is the central principle. A good alternative that coincides with this principle is additive manufacturing. This manufacturing process produces low waste and a low amount of tools. In addition, the following practices are used.

Lean Manufacturing
Lean manufacturing is the dynamic, knowledge-driven, and customer-focused process through which all people in a defined enterprise continuously eliminate waste with the goal of creating value. As such, it is an approach that should be implemented throughout every aspect of drone swarm production, from design to actual production. One of the most efficient methods to eliminate waste is the 5S Approach, which involves Sort, Simplify, Shine, Standardize, and Sustain. The 5S approach can significantly enhance the effectiveness of lean manufacturing and contribute to the production of high-quality, sustainable drone swarms and the team should implement this in every stage of the Design Synthesis Exercise.

Green Engineering
Green Engineering is another principle that can be applied to the production of drone swarms. This approach seeks to reduce the environmental impact of engineering activities by designing products and processes that are environmentally sustainable. In the context of drone swarm production, green engineering involves designing drones with materials that are environmentally friendly, as well as minimizing the amount of energy consumed during production and operation. To achieve this goal, the team should implement sustainable manufacturing processes and materials such as the use of biodegradable or recycled materials, as well as energy-efficient components.

Circular Economy
In addition to lean manufacturing and green engineering, the principle of circular economy can also be applied to the production of drone swarms. A circular economy is an approach that seeks to maximize the use of resources by creating closed loops where waste is minimized, and resources are reused and recycled. In the context of drone swarm production, this involves designing drones that can easily be disassembled and used for something else. This approach can also include the use of re-manufacturing of new parts and reparation of the drones, which can extend the lifespan of the drone and reduce the need for new production. It is important that the team applies this approach throughout the entire production process of the drone swarm, from design to end-of-life disposal, to reduce the environmental impact and maximize sustainability.

10.1.1. Production Cost

It is estimated that the cost per unit of the Fixed-Wing and Quadcopter are 21550 and 4993 euros per unit respectively chapter 9. Due to the material choice of aluminium and carbon fibre composite, the total cost is competitive when compared to similar drone systems [1] [2]. Carbon fibre composite required specialized

---

[1] https://www.flyability.com/

[2] https://store.dji.com/nl/product/matrice-300-rtk-and-dji-care-plus?vid=111261

equipment to manufacture adding to cost, however as high volume production of the fixed wing and quadcopter is anticipated, lean manufacturing practices can be exercised. It should be noted however that the Fixed-Wing drone's material choice prioritizes the strength-to-weight ratio and not cost. In contrast, aluminium is a cheap and relatively easy material to work with as well as having effective reusability and recyclability.

10.2. Social Sustainability

To ensure economic costs the following aspects are be considered:

Mission Profile
Our system can replace conventional modes of surveillance or search and rescue. A swarm of drones can be deployed relatively quickly and the swarm can be modified on a per mission basis. This makes it a energy and time efficient system.

Simulation
One of the defining features of our system is the use of a simulation for testing and training purposes. External parties are trained by utilizing a simulation model implemented with relevant parameters. This greatly reduces both the financial and material cost of the system as a whole, by enabling system operators to train without risking material damage or loss of system nodes. Besides that, no fuel for the drones have to be used during training, releasing no greenhouse gases into the air. However, simulating hardware do require a lot of electrical power, so for this reason it is important to ensure that the power they use comes from a sustainable source.

Sustainable Propulsion
As one of the driving requirements, no combustion energy sources are allowed in the process . In the design of the propulsion system, only renewable energy sources such as solar energy, electric energy and thermal energy are considered. These considerations contribute to the environmental sustainability of the drones as there is low to no emission.

Drone Modularity
The drones are heterogeneous meaning that every drone has its own specific task. If the frame of the drone is made modular for every drone, the same product tools and geometry can be used during the manufacturing process. The only difference is the payload as that is specified for each drone.

Smart Grid Technology
A smart grid is an electric power distribution that uses advanced technology to optimize the power efficiency of the system. This system enables two-way communication for improved control of the power supply, providing quick responses towards power demand. This system reduces waste, and is cost and energy-efficient making the power system of the drones more sustainable and reliable.

Multipurpose
by using a swarm of drones with different individual capabilities allows a lot of freedom for mission profiles, giving the option to deploy different types and numbers of drones for a mission-specific swarm makeup. This means a wide variety of missions can be completed with the same system.

10.3. Environmental Sustainability

As the drone is sustainably powered and does not release emissions the major contributor to project emission's is the manufacturing of the drone itself. As mentioned in subsection 5.7.5 and chapter 6 the materials considered are aluminium and carbon fiber composite. It is estimated that 1.7-2.2 kg of carbon dioxide equivalent (CO2e) per kg of aluminum and 2-7 kg of CO2e per kg of carbon fiber. This includes the energy requirements for mining, refining, and smelting processes.In addition, the specific energy consumption for primary aluminum production can range from approximately 13 to 17 MJ/kg of aluminum produced however, the energy consumption for aluminum recycling can be as low as 2-10 MJ/kg. Likewise, the energy consumption for carbon fiber production ranges from 150- 350 MJ/kg (CO2e) [28].

End-of-Life Considerations

To promote sustainability for the drone, the team optimizes the re usability of the drone by making end-of-life considerations. The team will avoid that the drone generates negative environmental impacts at the end of its operational life. Therefore, the drone has to include reusable and recyclable parts and components. This method coincides with the principles of a circular economy, which seeks to minimize waste and maximize the use of resources. Additionally, the drone will exist out of reversible joints for easy reparation and enable the possibility of disassembly.

11

Verification and Validation

The verification and validation is an important process for every design. By verifying the requirement, it is found whether the product meets the requirements. Validation processes include testing processes and checks if the product meets the stakeholder needs. In section 11.1, the verification of the simulaion and state-sapce model is verified. In section 11.2, the mission, swarm, node, and sustainability requirements are verified using a compliance matrix. Lastly, the section 11.3 verification and validation process in the next phase are represented.

11.1. V&V During Development

Verification and validation is a process that is carried out during all stages of the analysis performed in this report. All computations done need to be verified by the theory behind it, all simulations developed must be ran through a large number of tests to ensure the quality of this work. After the development of the software tools required for the simulation of the swarm in chapter 4, the performance analysis of the fixed-wing drone in chapter 5 and the stability simulation of the coupled system and performance analysis of the quadcopter in chapter 6, an in-detail verification and validation procedure was performed. This procedure is necessary to ensure the best quality in the work produce, as well as to fix errors, and avoid computational mistakes that could have been present.

The steps for code verification are as follows:

- Debugging: The most straightforward part of verification done during the programming process. Debugging is done during the developing of the code, when encountering a problem while writing it, or while trying to optimise the efficiency of the code. This approach runs the code line by line and allows the programmer to get a step-by-step guide to their program. For this step, the built-in Python debugger was used.
- Unit Testing: This is a small scale test done when no errors arise when running the code. Unit testing is used to check specific parts of the code, known as units, these units are usually functions. Unit testing has the aim of fixing errors with the logic of the code, the code may run without any interruptions, but there may be small mistake preventing the code from doing what it is supposed to do. Unit tests check the output of each piece of code and compare it with an external calculation, either done by hand or using a different tool. A large number of unit tests have been done using the Pytest framework, these allowed to scan through the code and identify and quickly fix the problems in the first stage of the coding process.
- System Testing: After unit tests have been run, it is important to verify that the program as a whole does as desired. For example, does increasing the drone cruise speed decrease the scanning time? Does increasing thrust increase the drones upwards velocity? These type of ”common-sense” questions are used to verify that the logic behind the overall project is correct. To do these tests, the Pytest framework was used again, and this process was done after the completion of each program.
- Limit Testing: Finally, limit testing makes sure the programme provides the right values and responses at the boundaries. This can be useful to verify the constraints of the programme, as well as assess its limitations.

11.1.1. Verification of Sim.py

Sim.py is the code used in chapter 4. This code is used to compare multiple search patterns, multiple number of drones and multiple atmospheric conditions in order to determine the optimal way to perform a search and rescue mission. This 2D simulation integrated the oceanic drift along with the wind speed to program the atmospheric conditions. In addition, the flight characteristics of a fixed-wing drone were used to give the drone its dynamic characteristics. Finally, a search algorithm was programmed instructing each drone the line segments it should follow while searching, what to do once a target was found and when to return to the ship.

- Unit Tests: For this code unit tests were performed in functions such as a function to determine the sweep are of the camera gimbal, functions to determine the flight time, airspeed and other flight dynamics. All the physics aspects of the search and rescue mission were verified with the theory and checked against hand-made calculations.
- System Testing: The system tests of this simulation were used to determine the optimal search area. The optimal number of drones, the search pattern, and the shape of the search area were all determined by

doing system tests. These tests made it possible to verify that the selected search pattern was the optimal one.

- Limit Testing: These type of tests were less frequent in the development of this code. Since no clear constraints, or boundaries were known, the results of the limit tests ws unpredictable, and thus were not useful tool for verification.

It is important to note, that unfortunately, the simulation tool could not be validated, as there was no experimental data available to validate the results.

11.1.2. Verification of State Space

The state space model developed is used to simulate the stability of the coupled system, i.e the fixed-wing drone attached to the quadcopter.

- Unit Tests: For this code unit tests were performed on the functions used to generate the space state model, the input and output matrices, as well as the control coefficients. This verification was greatly accompanied by hand derivations, which were then implemented using Pytest to check the output of the code.
- System Testing: Perhaps the most important verification to the state space model, these set of tests ensured the system did as desired given the proper inputs. These tests included verifying the step response of the each of the inputs, as well as combinations of these, and ensuring the system would react in the correct manner according to the its stability. For further detail about this please refer back to section 6.5.
- Limit Testing: Throughout the development of this code, limit testing was used as a tool to verify all the inputs. Higher and lower limits were used to get a general sense of direction of whether the code was acting in the right manner. These tests did not yield analysis-worthy results, but were used as a tool to tune the model and improve its accuracy.

11.2. Requirements Compliance Matrix

This section assesses whether the key and driving requirements identified at the beginning of the design stage has been satisfied. The relevant requirements and the status of the requirements are presented in Table 11.1. Requirements that have been met are marked as ”Positive Compliance”. As can be seen, all requirements are met.

Table 11.1: Compliance matrix for the requirements of the STORM system.

Requirement code	*Description*	*Compliance Status*
	Mission Requirements	
REQ-MIS-01	The system shall operate in the least wind force 7 (wind speed between 13.9-17.1 metres per second)	Positive Compliance
REQ-MIS-02	The system shall operate in sea state 5 (wave heights of 2.5 to 4 metres)	Positive Compliance
REQ-MIS-03	The system shall take off autonomously from the ship deck	Positive Compliance
REQ-MIS-04	The system shall land autonomously on the ship	Positive Compliance
REQ-MIS-05	The system shall have an End-of-Life strategy	Positive Compliance
	Swarm Requirements	
REQ-SWM-01	The drone swarm shall be operational for a duration of 48 hours	Positive Compliance
REQ-SWM-02	The swarm shall transmit real-time HD videos at a 100km range from the ground ship	Positive Compliance
REQ-SWM-03	The swarm shall be operationally available at all times	Positive Compliance
REQ-SWM-04	The swarm shall not have a single point of failure	Positive Compliance
REQ-SWM-05	The swarm shall autonomously follow an integrated search pattern	Positive Compliance
REQ-SWM-06	The swarm shall fit in the 1 number of storage units	Positive Compliance
REQ-SWM-07	The swarm shall consist of at least 5 number of drones	Positive Compliance
REQ-SWM-08	The swarm shall be able to scan the whole area successfully within the mission duration	Positive Compliance
	Node Requirements	
REQ-NODE-01	A node shall have a maximum take-off weight of 25 kg	Positive Compliance
REQ-NODE-02	A node shall have a maximum payload weight of 3 kg	Positive Compliance
REQ-NODE-03	A node shall not cost more than 100,000 EU	Positive Compliance
REQ-NODE-04	A node shall have a minimum cruise airspeed of 25 metres per second regardless of the weather conditions	Positive Compliance
	Sustainability Requirements	
REQ-SUS-01	The system shall not cause human and environmental harm	Positive Compliance
REQ-SUS-02	The system shall not require any human interference on the ship during stormy conditions.	Positive Compliance
REQ-SUS-03	The system shall use no combustion propulsion system	Positive Compliance
	Landing Requirements	
REQ-SYS-LAN-01	The system shall perform the docking at an altitude of 100 [m]	Positive Compliance
REQ-SYS-LAN-02	The system shall be able to reach a horizontal velocity of at least 18 [ms^−1]	Positive Compliance
REQ-SYS-LAN-03	The system shall be able to withstand 18 [ms^−1] wind gusts in any direction.	Positive Compliance
REQ-SYS-LAN-04	The system shall have an ascent speed of 5 [ms^−1]	Positive Compliance
REQ-SYS-LAN-05	The system shall be able to carry its own weight as well as the weight of the Fixed-Wing	Positive Compliance
REQ-SYS-LAN-06	The system shall have enough battery power for at least one landing phase cycle	Positive Compliance
REQ-SYS-LAN-07	The system shall have a thrust-to-weight ratio (T/W) of 2	Positive Compliance

11.3. Verification & Validation Next Steps

Although, most of the requirements in Table 11.1 are met at this stage, it is important to continuously meet them as the design process carries on. In order to verify these requirements, a series of methods for verification and validation have been developed. Verification can be done through a series of tests. These methods for product verification are the following:

- Inspection: Inspecting the product to ensure it complies with requirements
- Analysis: Developing a mathematical model to ensure the product complies with requirements.
- Demonstration: Proving a requirement can be met by the system.
- Test: Subjecting the product to testing equipment that is able to proved its compliance with the requirement.

In addition, validation can be performed by replicating the conditions of the mission, and ensuring the system complies with these conditions.

11.3.1. Verification

Table 11.2: Verification Plan

Requirement code	*Verification Method*	*Proposed Verification*
REQ-SWM-02	Demonstration	Fly the drone, or place the drone 100+ [km] away from a control station and verify that an HD video is successfully sent from the drone to the control station
REQ-SWM-03	Inspection	By simple inspection, it should be apparent when the swarm is ready to operate
REQ-SWM-04	Analysis	Perform detailed analysis of swarm operations and run this analysis repeatedly to identify a single point of failure, if none is identified then the requirement is verified
REQ-SWM-05	Analysis	Run simulations of search patterns for random initial conditions and verify the algorithm follows the desired search pattern every time.
REQ-SWM-06	Inspection/Demonstration	Measure size of drones and size of containers, or show drones fit in container
REQ-SWM-07	Inspection	Count the number of drones in the swarm
REQ-NODE-01	Inspection	Measure the weight of the drones
REQ-NODE-02	Inspection	Measure the weight of the payload before placing it in the drone
REQ-NODE-04	Demonstration	Place the drone in a wind-tunnel with a windspeed of 25 [m/s] and 43 [m/s] to account for the most limiting case of 18 [m/s] headwind.
REQ-SUS-03	Inspection	Check no propulsion system is present

The series of verification methods described in Table 11.2 shall be used once the product has been developed and is in the testing phase. These methods will ensure the requirements are met, and thus the system has the required performance characteristics. However, the system must still be validated in mission conditions.

11.3.2. Validation

Validation requires mission-oriented testing. This usually implies simulations, testing the flow of information, testing the operational readiness of the system, and performing mission scenario tests. To validate the product after it has been developed the 5 mission requirements, as well as REQ-SWM-01, REQ-SWM-08, REQ-NODE-03, REQ-SUS-01, and REQ-SUS-02 must be tested. To do so, the recommendation is to perform a ”drill”, where the system is tested in the ocean, preferably in stormy conditions. These tests, however, should only be done after thorough validation and verification have been performed through simulation. An in-depth simulation of the system should be developed, this simulation should be able to mimic to almost perfection all aspects of the system, the fixed-wing flight, the quadcopter control, the coupling, etc. After this simulation has been developed, it will be possible to identify flaws in the design that prevent it from meeting the requirements, this will lead to further design iterations and a finalized deisgn.

12
Conclusions and Recommendations

The team was assigned to design an autonomous drone swarm to perform search and rescue missions for the KNRM and Coast Guard that can survive in stormy conditions. After 10 weeks, the team has come up with a final detailed design for the drone swarm. Among the biggest problems to be solved in this report is the difficulty of combining the endurance requirement when scanning a large search area with the power requirement to take off and land on a ship in stormy conditions. A solution to this problem has been found by splitting the drone swarm system into two specialised designs capable to complete a part of the mission. A Fixed-Wing drone has been designed with enough endurance to complete the search mission. Simultaneously, a Multicopter drone is designed to aid the Fixed-Wing drone during the landing procedure. Furthermore, multiple aspects of the swarm were investigated to optimise the performance of the swarm.

For the swarm, the performance of multiple different search patterns were compared in a variety of conditions. For this purpose, a 2D simulation of the swarm behaviour in a search and rescue procedure has created to model the behaviour of the drone swarm in these conditions. Using this approach, it was found that the most optimal size for the drone swarm consists of up to 10 simultaneously active scanning drones. The most optimal search pattern was found to depend strongly on the shape and drifting conditions of the search area. For a low drift approximately circular search area, the most optimal search pattern was found to be a spiral shape, where the number of tracks is slightly lower than the total number of active drones. For more complex search patterns and drift behaviour, a linear sweep pattern was found to perform more efficiently and with higher consistency.

The Fixed-Wing was designed with a focus on long endurance flight. For this purpose, both an internal and external layout have been designed. The primary and supporting structures were designed using a bending, shear and torsion analysis. During the structural analysis, a conservative approach was used, adding an extra level of redundancy. The structures can be optimised for further analysis using advanced tools such as CFD and FEM. For the Fixed-Wing and the Multicopter, an advanced lithium-ion silicon battery technology was used, which is a state-of-the-art technology that has an extremely high specific densities of 450 $[Wh \cdot kg^{-1}]$ and 1150 $[Wh \cdot L^{-1}]$. An high endurance of 5.39 hours at a constant power output of 878.55 $[W]$. For the aerodynamic and stability analysis, XLFR5 is used which was able to conclude that the Fixed-Wing drone was longitudinal and lateral stable.

The Multicopter has been designed with as its primary purpose to assist the Fixed-Wing drones during their landing operations. The Multicopter accomplishes this by attaching itself to the Fixed-Wing drone, after which it can use its superior manoeuvrability to touch down on the ship. To allow the Multicopter to catch up and connect with the Fixed-Wing drone, the Multicopter needs to be able to match the horizontal speed of the Fixed-Wing drone while maintaining level. For this purpose, the Multicopter is fitted with 4 horizontally facing propellers to allow the Multicopter to have full control over all axis of motion, as well as drastically improving the yawing performance of the Multicopter. The main rotors of the Multicopter are sized thus to provide a sufficient thrust to weight ratio not only in free flight, but also when carrying the Fixed-Wing drone, consuming up to a peak power of 83.15 $[kW]$. The motors are powered by on-board lithium-ion silicon batteries, as using a tether to connect the drone to ground power was found to be unfeasible due the strong wind force and logistical constraints. The clamping of the Multicopter to the Fixed-Wing drone occurs using electromagnets for their reliability, simplicity and efficiency compared to other systems such as physical contact connectors. A rendering of the Fixed-Wing drone and Multicopter clamped is shown in Figure 12.1.

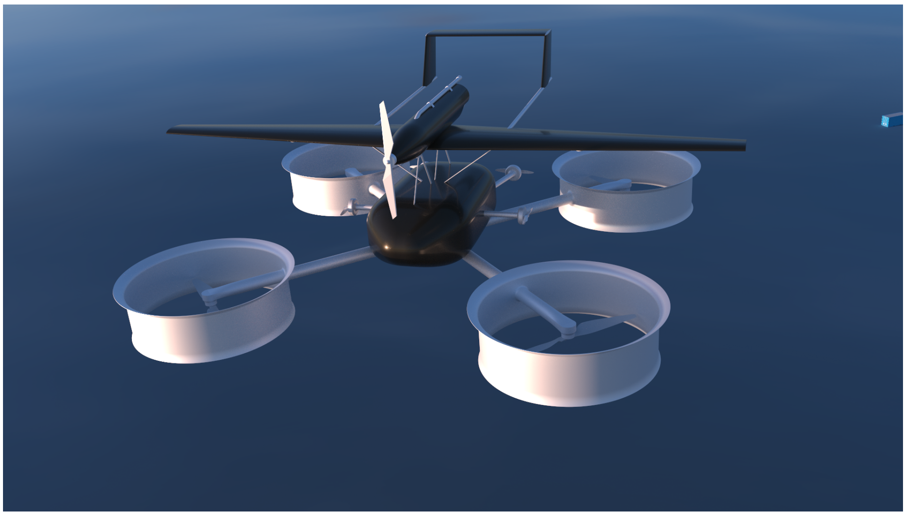

Figure 12.1: Rendering of the clamped system of the Fixed-Wing drone and Multicopter in a 3D environment.

As it was found that landing without equipment was impossible and dangerous for the personnel on deck, the START system was implemented where the drones can be safely stored, launched and retrieved. The take-off sequence was performed using a catapult, implying that no landing gear was required for the Fixed-Wing. The use of the START systems enables the possibility that no human interference during the operations is necessary, while concurrently retrieving the Fixed-Wing drones. The designed clamping system could, however, cause interference with the magnetometer due to the magnet and was therefore placed at a safe distance. Charging systems are also present in the storage systems, which can be used to reach the total mission of 48 [h].

In addition, the development process sustainable implemented approaches across the different design phases. Three main areas of sustainability - economic, social, and environmental - were taken into account. The main implementations focused on green engineering, lean manufacturing, and end-of-life considerations. Reliability, availability, maintainability, and safety (RAMS) characteristics were analyzed to assess the system's performance and non-technical aspects to complete the assessment of the system. Additionally, the critical risks were mitigating, improving confidence in its operation. By adopting these measures, the project aimed to promote sustainable development and ensure long-term viability.

Moreover, a thorough market analysis showed that there are significant opportunities for the sale of the drone swarm systems in search and rescue operations. The drone swarm will have great capabilities for the nearby future and further research is inevitable for the drone swarm.

Further recommendations regarding the system are in place as improvements are possible at some areas of the design. At first, more research for the swarm capabilities and coordination at both the long range as well as close proximity flight should be done. Research into long range swarm interactions will allow for a more efficient use of the available drones, which can help reduce the cost and complexity of operating a drone swarm and reduce the barrier to entry. Better understanding on the interactions of close proximity flight will help in performing the docking manoeuvre and improve the resilience of the extreme swarm to wind and ocean conditions allowing the system to function in a wider range of environmental conditions. The main cause for the currently limited knowledge and research on these topics can be traced back to the fact that the technology required for these concepts have only recently hit the mainstream market. Because of this, the use of drone swarms especially in search and rescue missions is still very immature and little is known about the use of large scale swarms.
Moreover, the loads during the clamping of the drones were not taken into account of the system. For a more accurate representation of the possible loads acting on the drone, this analysis has to be accounted for. Additionally, a vibrational and flutter analysis will make the structural analysis of the drones more complete. A point that is especially relevant for close proximity flight performance is the implementation of the control loop of the drones. Although many control loops exist, a lot is still unknown about their exact performance and behaviour in different circumstances. A promising improvement which deserves special attention is the implementation of an INDI controller into the drones involved in the docking sequence. This controller is a state-of-the-art control algorithm, which is more effective at rejecting disturbances due to for example wind gusts

than many other control technique such as PID loops as the INDI controller can model non-linear and difficult to predict behaviour. The operational environment of the Multicopter suggests that such a control technique is more beneficial as wind gusts can happen at any time. Another aspect of the control and navigation loop that deserves more attention is the use of reinforcement learning. Using reinforcement learning can aid to pinpoint the location of the loitering Fixed-Wing drone by allowing a better prediction of the movement of the drone, improving the interception performance of the Multicopter.

The use of existing modelling and simulation tools was minimal due to the unfamiliarity of the tools. 3D Simulation tools and environments such as Flightmare, Unity, and AirSim can provide valulable insight into the design by helping to simulate and validate the behaviour of the detailed design. For the structural and aerodynamic analysis, complex tools such as FEM and CFD could help to optimize the shape, design and weight of the structure, as the approach used in this report likely resulted in a notably over designed design. Better use of such engineering tools can help to create simpler and more efficient designs that still meet all requirements.

For future possibilities, search and rescue missions are like other surveillance and reconnaissance operations. The general purpose of the drone swarm is to scan an area and identify the target. Surveillance and reconnaissance operations have the same outline as the search and rescue operations. Therefore, the research of the team's project can be used for similar operations too. Consequently, the components will mainly be dependent on the environmental, operational conditions and endurance as this will directly impact the payload and propulsion system. However, the swarm operations and coordination can be implemented for such operations too. As sustainability is gradually increasing its influence in the design process, more sustainable high-strength materials and manufacturing process will be available and can also be implemented in the design.
Concluding, the most constraining factor was time. With more time, the design could become more detailed and refined and more concepts could be researched. However, the findings of the detailed design after 10 weeks look promising. A tangible result of the simulation was programmed, a detailed design of the drones including the relevant components and the Fixed-Wing drone was presented, and a feasible take-off and landing mechanism was identified. The team was able to comply with the key and driving requirements of the systems, making the final design align with the intended purpose of the stakeholders.

References

[1] 123Materialen. *matek fchub-6s hub stroomverdeelbord 5v & 10v bec ingebouwde 184a stroomsensor voor rc drone*. 2023. URL: https://www.123materialen.com/products/matek-fchub-6s-hub-stroomverdeelbord-5v-10v-bec-ingebouwde-184a-stroomsensor-voor-rc-drone_1147591?gclid=CjwKCAjw-b-kBhB-EiwA4fvKrIxI2yvkMiLQ6HMlvBWllXvEeUqEBeKjN50Ud9L_O6lcZB5wQOhBnBoCPdoQAvD_BwE (visited on 06/20/2023).

[2] A.A. van Oudheusden. *Recycling of composite materials*. 2023. URL: https://repository.tudelft.nl/islandora/object/uuid:0749ed5c-7aeb-4275-abee-0f904a08ea4d/datastream/OBJ/download%5C%20 (visited on 06/20/2023).

[3] Al Lawless et al. *Flight Test Engineering Reference Handbook*. 3rd. Lancaster, California: The National Test Pilot School, 2013.

[4] A. A. Allen. *Leeway Divergence*. technical report NTIS 200524. Groton, CT: Coast Guard Research and Development Center, 2005.

[5] A. A. Allen and J. V. Plourde. *Review of Leeway: Field Experiments and Implementation*. technical report NTIS 199924. Groton, CT: Coast Guard Research and Development Center, 1999.

[6] Eric E. Alley. *Problems of search and rescue in disasters*. Accessed: June 6th, 2023. URL: https://link.springer.com/content/pdf/10.1007/978-0-585-33973-3_27.pdf.

[7] Bas Part Sales. *PITOT TUBES*. 2023. URL: https://baspartsales.com/pitot-tubes/ (visited on 06/19/2023).

[8] BloombergNEF. *Lithium-ion Battery Pack Prices Rise for First Time to an Average of $151/kWh*. 2023. URL: https://about.bnef.com/blog/lithium-ion-battery-pack-prices-rise-for-first-time-to-an-average-of-151-kwh/ (visited on 06/19/2023).

[9] Brinkbox. *20FT Zeecontainer*. 2023. URL: https://www.brinkbox.nl/assortiment/20ft/20ft-zeecontainer (visited on 06/19/2023).

[10] D. Çelebi & M. de Bruijn & J. de Wit& P. Garcia de Vinuesa Garcia & O. Heukelom & J. Louro Fuentes & M. Rombouts & M. van Opstal & M. Wolf & J.IJ. Verhoeff. *DSE Group 6 Baseline Report*. 1st ed. Delft, Netherlands: TU Delft, 2023.

[11] D. Çelebi & M. de Bruijn & J. de Wit& P. Garcia de Vinuesa Garcia & O. Heukelom & J. Louro Fuentes & M. Rombouts & M. van Opstal & M. Wolf & J.IJ. Verhoeff. *DSE Group 6 Midterm Report*. 1st ed. Delft, Netherlands: TU Delft, 2023.

[12] Campbell scientific. *GPS16X-HVS GPS Receiver with Integrated Antenna*. 2023. URL: https://www.campbellsci.eu/gps16x-hvs (visited on 06/20/2023).

[13] Defense One. *Insitu's new shipboard drone launches and catches other drones*. 2023. URL: https://www.defenseone.com/business/2023/04/insitus-new-shipboard-drone-launches-and-catches-other-drones/384710/ (visited on 05/17/2023).

[14] Tail Design. *what-when-how In Depth Tutorials and Information*. 2023. URL: http://what-when-how.com/flight/tail-designs/.

[15] DJI Store. *Zenmuse H20N Worry-Free Plus Combo*. 2023. URL: https://store.dji.com/nl/product/zenmuse-h20n-and-dji-care-enterprise-plus-h20n?vid=112851 (visited on 06/19/2023).

[16] DroneshopNL. *MATEKSYS DIGITAL AIRSPEED SENSOR ASPD-4525*. 2023. URL: https://droneshop.nl/mateksys-digital-airspeed-sensor-aspd-4525 (visited on 06/20/2023).

[17] EASA. *Certification Specifications and Acceptable Means of Compliance for Normal, Utility, Aerobatic, and Commuter Category Aeroplanes. Amendment 4*. EASA, July 2015.

[18] EasyComposites. *Component Prepreg*. 2023. URL: https://www.easycomposites.eu/component-prepreg (visited on 06/19/2023).

[19] Echo Mav. *Doodle Labs Embedded Radio*. 2023. URL: https://echomav.com/product/doodle-labs-embedded-radio/ (visited on 06/19/2023).

[20] EnerData. *The Netherlands introduces an electricity and gas price cap for 2023*. 2022. URL: https://www.enerdata.net/publications/daily-energy-news/netherlands-introduces-electricity-and-gas-price-cap-2023.html#:~:text=For%5C%20the%5C%20year%5C%202023%5C%2C%5C%20prices,kWh%5C%20and%5C%201%5C%2C200%5C%20cm%5C%20respectively. (visited on 06/10/2022).

[21] Yanzhou Fan, Suo Zhang, and Xiaofei Xu. “Effect of the substitution of Si for B on thermal stability, magnetic properties and corrosion resistance in novel Fe-rich amorphous soft magnetic alloy”. In: *Intermetallics* 138 (2021), pp. 107–306.

[22] Market Research Future. *Military Surveillance Drone Market to Capture a CAGR of 11.96% Between 2020 and 2030 While Touching Approximately USD 28.96 Billion by 2030 Research Future (MRFR)*. 2023. URL: https://www.globenewswire.com/news-release/2023/04/07/2643218/0/en/Military-Surveillance-Drone-Market-to-Capture-a-CAGR-of-11-96-Between-2020-and-2030-While-Touching-Approximately-USD-28-96-Billion-by-2030-Research-Future-MRFR.html (visited on 05/02/2023).

[23] Dr.ir. M.I. Gerritsma. *Electromagnetic Induction and Faraday’s Law*. 1st ed. Delft, Netherlands, 2021.

[24] glassdoor. *How much does an Aerospace Engineer make in Germany?* 2023. URL: https://www.glassdoor.com/Salaries/germany-aerospace-engineer-salary-SRCH_IL.0,7_IN96_KO8,26.htm (visited on 05/15/2023).

[25] GMW Associates. *Magnetometers A Comprehensive Guide*. 2023. URL: https://gmw.com/magnetometers/ (visited on 06/20/2023).

[26] ARC Advisory Group. *Drone Inspection Services*. 2023. URL: https://www.arcweb.com/market-analysis/drone-inspection-services (visited on 01/01/2023).

[27] Jay Gundlach. *Designing Unmanned Aircraft Systems, A comprehensive Approach*. Blacksburg, Virginia: AIAA Education Series, 2012.

[28] International Aluminium Institute. *Life Cycle Assesment*. 2023. URL: https://international-aluminium.org/resources/lifecycle/.

[29] Erwhin Irmawan, Agus Harjoko, and Andi Dharmawan. “A Model, Control, and Realistic Visual 3D Simulation of VTOL Fixed-Wing Transition Flight Considering Ground Effect.” In: *Drones* (2023). URL: https://www.mdpi.com/2504-446X/7/5/330.

[30] Ho Chuen Kam, Ying Kin Yu, and Kin Hong Wong. *An Improvement on ArUco Marker for Pose Tracking Using Kalman Filter*. 2018, pp. 65–69. DOI: 10.1109/SNPD.2018.8441049.

[31] Kustwacht. *NH90-helikopter*. 2023. URL: https://kustwacht.nl/eenheden/nh90-helikopter/ (visited on 06/19/2023).

[32] Kustwacht. *Reddingboot Klasse NH1816*. 2023. URL: https://www.knrm.nl/reddingboten/nh-1816-klasse (visited on 06/19/2023).

[33] Yuchen Leng et al. “An analytical model for propeller aerodynamic efforts at high incidence”. In: *54th 3AF International Conference on Applied Aerodynamics*. Paris, France, Mar. 2019. URL: https://hal.science/hal-03385734.

[34] Mantis. *Mantis i45*. 2023. URL: https://www.avinc.com/images/uploads/product_docs/Mantis_i45_Datasheet_v2.1.pdf.

[35] Matek. *Matek H743-WLITE Flight Controller Ingebouwde OSD 2-6S ArduPilot INAV voor FPV Drone RC-vliegtuig*. 2023. URL: https://www.banggood.com/nl/Matek-H743-WLITE-Flight-Controller-Built-in-OSD-2-6S-ArduPilot-INAV-for-FPV-Drone-RC-Airplane-p-1967742.html?utm_source=googleshopping&utm_medium=cpc_organic&gmcCountry=NL&utm_content=minha&utm_campaign=aceng-pmax-nl-nl-pc&currency=EUR&cur_warehouse=CN&createTmp=1&utm_source=googleshopping&utm_medium=cpc_us&utm_campaign=aceng-pmax-allcat2-nl-220418-meruem&utm_content=meruem&ad_id=&gclid=CjwKCAjw-IWkBhBTEiwA2exyO4me3slHPtbFwGXuePd06O0hDOcwlDNB2eZEJ4GcKXIiRcQxt6_o9hoCuH4QAvD_BwE (visited on 06/20/2023).

[36] Andrea Matrone. *PERFORMANCE-BASED PRELIMINARY SIZING OF AIRCRAFT WITH DISTRIBUTED PROPULSION*. 2019. URL: https://www.politesi.polimi.it/bitstream/10589/151631/3/Andrea%5C%20Matrone%5C%27s%5C%20MSc%5C%20thesis.pdf.

[37] J. Melkert. *ADSEE-I*. 2023. URL: https://brightspace.tudelft.nl/d2l/le/content/292964/viewContent/1762698/View (visited on 06/01/2023).

[38] Mouser Electronics. *6-axis IMU’s*. 2023. URL: https://nl.mouser.com/c/sensors/motion-position-sensors/imus-inertial-measurement-units/?sensor%5C%20type=6-axis (visited on 06/20/2023).

[39] J.A. Mulder et al. *FlightDynamics2013_V3*. https://https://brightspace.tudelft.nl/d2l/le/content/512959/viewContent/3072267/View. 2013. (Visited on 08/06/2023).

[40] Multraship. *Multraship Commander*. 2023. URL: https://www.multraship.com/images/Multraship_Commander_HR.pdf (visited on 06/19/2023).

[41] Mihaela Ni□ă and Dieter Scholz. “Estimating the Oswald Factor from Basic Aircraft Geometrical Parameters”. In: 2012.

[42] Nvidia Developer. *NVIDIA Jetson TX2 Delivers Twice the Intelligence to the Edge*. 2023. URL: https://developer.nvidia.com/blog/jetson-tx2-delivers-twice-intelligence-edge/#:~:text=The%5C%20CPU%5C%20complex%5C%20combines%5C%20a,watts%5C%20of%5C%20typical%5C%20energy%5C%20usage. (visited on 06/20/2023).

[43] OCW.TUDelft. *Longitudinal Static Stability*. 2023. URL: https://ocw.tudelft.nl/wp-content/uploads/Hand-out-Stability_01.pdf (visited on 06/17/2023).

[44] Albert C. Piccirillo. “The Clark Y Airfoil: A Historical Retrospective”. In: *2000 World Aviation Conference* 1.1 (2000).

[45] Walter D. Pilkey, Deborah F. Pilkey, and Zhuming Bi. John Wiley & Sons, 2020. ISBN: 978-1-119-53251-4. URL: https://app.knovel.com/hotlink/toc/id:kpPSCFE029/petersons-stress-concentration/petersons-stress-concentration.

[46] Pilotinstitute. *How Much Does It Cost to Get an FAA Part 107 Drone License?* 2023. URL: https://pilotinstitute.com/drone-license-cost/#:~:text=The%5C%20Part%5C%20107%5C%20exam%5C%20costs,that%5C%20will%5C%20cost%5C%20approximately%5C%20%5C%24149. (visited on 06/19/2023).

[47] Timothy W. McLain Theory Randal W. Beard and Practice. *Small Unmanned Aircraft*. 8th ed. Princeton, New Jersey: Princeton University Press, 2012.

[48] D. Raymer. *Aircraft Design: A Conceptual Approach*. 2nd ed. American Institute of Aeronautics and Astronautics, Inc., 1992.

[49] Rick. *T-Motor MN501S-240 with T-Motor NS22x66*. 2023. URL: https://database.tytorobotics.com/tests/gyyq/t-motor-mn501s-240-with-t-motor-ns22x66.

[50] P.C. Roling and Dr.Mark Voskuijl). *Turning flight*. 1st ed. Delft, Netherlands, 2020.

[51] Stephen Shankland. “Take a look at Zipline’s new drone delivery system”. In: (Apr. 2018).

[52] SparkFun. *SparkFun GPS-RTK-SMA Breakout - ZED-F9P (Qwiic)*. 2023. URL: https://www.sparkfun.com/products/16481?_ga=2.244290893.919293222.1686577925-1622562738.1686577925 (visited on 06/20/2023).

[53] Philipp Stahl, Christian Roessler, and Mirko Hornung. “Performance and Life Cycle Cost Comparison of Optimized Fixed-Wing VTOL UAV Configurations”. In: Jan. 2020. DOI: 10.25967/490207.

[54] T-Motor. *MN501-S KV240*. 2023. URL: https://store.tmotor.com/goods-695-MN501-S+KV240.html (visited on 06/19/2023).

[55] tessco. *1350-1390 MHz 7dBi Fiberglass Omni Antenna*. 2023. URL: https://www.tessco.com/product/1350-1390-mhz-7dbi-fiberglass-omni-antenna-525821 (visited on 06/20/2023).

[56] TinyTronics. *Electromagnet 25kg - 12V DC - JF-XP4020*. 2023. URL: https://www.tinytronics.nl/shop/en/mechanics-andactuators/electromagnets/electromagnets/electromagnet-25kg-12v-dc-jf-xp4020 (visited on 06/19/2023).

[57] transmotec. *Lineaire actuator 12VDC*. 2023. URL: https://nl.transmotec.com/product/dla-12-10-a-250-ip65/?gclid=CjwKCAjw-b-kBhB-EiwA4fvKrH8Zybo-XGOv3QrczZuocA5yjGF45pHx1pnLWvZgfDAHTec-6A5lzxoCQ2MQAvD_BwE (visited on 06/20/2023).

[58] Tyto Robotics Inc. URL: https://www.tytorobotics.com/ (visited on 06/19/2023).

[59] Naomi A. Ubina and Shyi-Chyi Cheng. “A Review of Unmanned System Technologies with Its Application to Aquaculture Farm Monitoring and Management”. In: *Department of Computer Science and Engineering, National Taiwan Ocean University, Keelung City 202, Taiwan* (2021), pp. 1182–1193. DOI: https://doi.org/10.3390/drones6010012. URL: https://www.mdpi.com/2504-446X/6/1/12.

[60] R. Vos and J.A. Melkert. *Aerospace Design and Systems Engineering Elements I (AE1222-II) - Empennage and Gear design*. 1st ed. Delft, Netherlands, 2019.

[61] XFLR5. *Analysis of foils and wings operating at low Reynolds numbers*. 2009. URL: https://engineering.purdue.edu/~aerodyn/AAE333/FALL10/HOMEWORKS/HW13/XFLR5_v6.01_Beta_Win32%5C%282%5C%29/Release/Guidelines.pdf (visited on 06/16/2023).

[62] Khaled M. Youssef et al. “A Novel Low-Density, High-Hardness, High-entropy Alloy with Close-packed Single-phase Nanocrystalline Structures”. In: *Materials Research Letters* 3.2 (2015), pp. 95–99. DOI: `10.1080/21663831.2014.985855`. eprint: `https://doi.org/10.1080/21663831.2014.985855`. URL: `https://doi.org/10.1080/21663831.2014.985855`.

A
Appendix A: Task Division

Table A.1: Distribution of the workload.

	Task	Student Name(s)
Preface	-	Mathieu
Executive Overview	Pablo	Marnix
Chapter 1	Introduction	Jan IJmte, Marley
Chapter 2	Mission Architecture	Marnix, Mathieu, Max, Olivier, Marley
Chapter 3	Mission Operations and Logistics	Olivier, Mathieu, Max, Marley
Chapter 4	Drone Swarm	Jarno, Jorge, Pablo
Chapter 5	Fixed-Wing Drone	Doruk, Jan IJmte, Jarno, Jorge, Mathieu, Pablo
Chapter 6	Landing Sequence & Multicopter	Max, Marnix, Marley, Pablo
Chapter 7	Risk & Safety	Marnix, Mathieu
Chapter 8	Design and Development Plan	Doruk, Jan IJmte, Olivier
Chapter 9	Mission Financial Valuation	Doruk, Jan IJmte, Marnix, Max, Marley
Chapter 10	Sustainable Development Strategy	Mathieu, Marley, Max
Chapter 11	Verification and Validation	Doruk
Pablo		
Chapter 12	Conclusions and Recommendations	Jarno, Mathieu
	Document Design, Layout and Reporting	Everyone